

Sensitivity Optimization for NV-Diamond Magnetometry

John F. Barry,^{1,2,3,4,*}† Jennifer M. Schloss,^{4,5,*}‡ Erik Bauch,^{3,*} Matthew J. Turner,^{3,4} Connor A. Hart,³ Linh M. Pham,^{1,2} and Ronald L. Walsworth^{2,3,4,§}

¹*Lincoln Laboratory,
Massachusetts Institute of Technology,
Lexington, Massachusetts 02421,
USA*

²*Harvard-Smithsonian Center for Astrophysics,
Cambridge, Massachusetts 02138,
USA*

³*Department of Physics,
Harvard University, Cambridge,
Massachusetts 02138,
USA*

⁴*Center for Brain Science,
Harvard University, Cambridge,
Massachusetts 02138,
USA*

⁵*Department of Physics,
Massachusetts Institute of Technology,
Cambridge, Massachusetts 02139,
USA*

(Dated: June 23, 2022)

Solid-state spin systems including nitrogen-vacancy (NV) centers in diamond constitute an increasingly favored quantum sensing platform. However, present NV ensemble devices exhibit sensitivities orders of magnitude away from theoretical limits. The sensitivity shortfall both handicaps existing implementations and curtails the envisioned application space. This review analyzes present and proposed approaches to enhance the sensitivity of broadband ensemble-NV-diamond magnetometers. Improvements to the spin dephasing time, the readout fidelity, and the host diamond material properties are identified as the most promising avenues and are investigated extensively. Our analysis of sensitivity optimization establishes a foundation to stimulate development of new techniques for enhancing solid-state sensor performance.

CONTENTS

I. Introduction	2	IV. Methods to increase readout fidelity	23
A. Magnetometry with ensemble NV-diamond	2	A. Spin-to-charge conversion readout	23
B. DC and AC sensing	4	B. Photoelectric readout	26
C. Magnetic field sensitivity	4	C. Ancilla-assisted repetitive readout	27
D. Alternatives to Ramsey magnetometry	6	D. Level-anticrossing-assisted readout	28
1. CW-ODMR	6	E. Improved photon collection methods	28
2. Pulsed ODMR	7	F. Near-infrared absorption readout	29
E. Parameters limiting sensitivity	10	G. Green absorption readout	31
II. Limits to relaxation times T_2^* and T_2	11	H. Laser threshold magnetometry	31
A. Motivation to extend T_2^*	11	V. Diamond material engineering	32
B. Ensemble and single-spin T_2^*	12	A. Conversion efficiency	32
C. Dephasing mechanisms	13	B. NV charge state efficiency	32
D. Nitrogen limit to T_2^*	14	1. Non-optical effects on NV charge state efficiency	33
E. Nitrogen limit to T_2	15	2. Optical effects on NV charge state efficiency	33
F. ^{13}C limit to T_2^*	16	C. Diamond synthesis and high pressure high temperature treatment	34
G. NV^- limit to T_2^*	17	D. Electron irradiation	36
III. Methods to extend T_2^* and T_2	18	E. Low pressure high temperature annealing	37
A. Dynamical decoupling for AC magnetometry	18	F. Other common impurities in synthetic or treated single crystal diamond	38
B. Double-quantum coherence magnetometry	20	G. Preferential orientation	40
C. Spin bath driving	21	VI. Miscellaneous sensing techniques	40
D. Transverse strain and electric field suppression	22	A. Rotary echo magnetometry	40
		B. Geometric phase magnetometry	40
		C. Ancilla-assisted upconversion magnetometry	40
		D. Techniques for the strong NV^- - NV^- interaction regime	41
		VII. Conclusion and outlook	43
		Acknowledgments	44
		A. APPENDIX	44

* These authors contributed equally

† john.barry@ll.mit.edu

‡ jschloss@mit.edu

§ rwalsworth@cfa.harvard.edu

1. Derivations	44
a. Ramsey DC magnetic field measurement	44
b. Spin-projection-noise-limited sensitivity	46
c. Photon-shot-noise-limited sensitivity	46
d. Overhead time	48
2. Optimal precession time	48
3. Considerations for increasing sensor number	48
4. Choosing nitrogen concentration in diamond samples	49
5. Spin resonance linewidth and T_2^*	49
6. Estimating T_2^* from spin resonance linewidths of N_S^0	50
7. Stretched exponential parameter	50
8. Isotopic purity confusion in the literature	51
9. Linear Stark and Zeeman regimes	52
10. Example annealing calculations	53
11. The diamond type classification system	54
References	58

I. INTRODUCTION

A. Magnetometry with ensemble NV-diamond

Quantum sensors encompass a diverse class of devices that exploit quantum coherence to detect weak or nanoscale signals. As their behavior is tied to physical constants, quantum devices can achieve accuracy, repeatability, and precision approaching fundamental limits (Budker and Romalis, 2007). As a result, these sensors have shown utility in a wide range of applications spanning both pure and applied science (Degen *et al.*, 2017). A rapidly emerging quantum sensing platform employs atomic-scale defects in crystals. In particular, magnetometry using nitrogen vacancy (NV) color centers in diamond has garnered increasing interest.

The use of NV centers as magnetic field sensors was first proposed (Degen, 2008; Taylor *et al.*, 2008) and demonstrated with single NVs (Balasubramanian *et al.*, 2008; Maze *et al.*, 2008) and NV ensembles (Acosta *et al.*, 2009) circa 2008. In the decade following, both single- and ensemble-NV-diamond magnetometers (Doherty *et al.*, 2013; Rondin *et al.*, 2014) have found use in applications spanning condensed matter physics (Casola *et al.*, 2018), neuroscience and living systems biology (Schirhagl *et al.*, 2014; Wu *et al.*, 2016), nuclear magnetic resonance (NMR) (Wu *et al.*, 2016), earth and planetary science (Glenn *et al.*, 2017), and industrial vector magnetometry (Grosz *et al.*, 2017).

Solid-state defects such as NV centers exhibit quantum properties similar to traditional atomic systems yet confer technical and logistical advantages for sensing applications. NVs are point defects composed of a substitutional nitrogen fixed adjacent to a vacancy within the rigid carbon lattice (see Fig. I.1a). Each NV center's symmetry axis is constrained to lie along one of the four $[111]$ crystallographic directions. While NVs are observed to exist in three charge states (NV^- , NV^0 and NV^+), the negatively charged NV^- center is favored for quantum sensing and quantum information applications (Doherty *et al.*, 2013). The NV^- defect exhibits a spin-1 triplet electronic ground state with long spin lifetimes at room temperature: longitudinal relaxation times $T_1 \approx 6$ ms (Jarmola *et al.*, 2012; Rosskopf *et al.*, 2014) are typical and coherence times T_2 up to a few ms are achievable (Balasubramanian *et al.*, 2009). The defect's

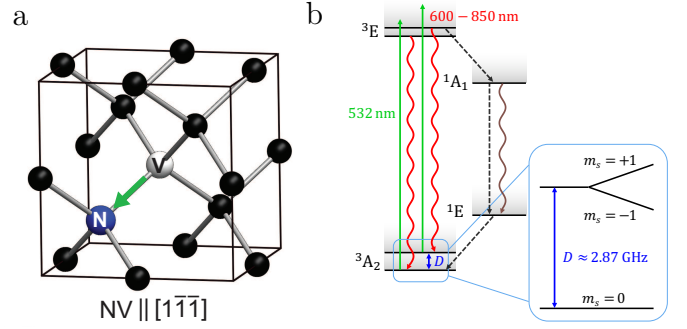


FIG. I.1 Overview of the NV^- center quantum system. a) Diagram of diamond lattice containing a nitrogen vacancy (NV) center, which consists of a substitutional nitrogen adjacent to a lattice vacancy. The green arrow marks the NV^- symmetry axis, oriented along the $[1\bar{1}\bar{1}]$ diamond crystallographic axis for the particular NV^- center shown here. From Ref. (Pham, 2013). b) Energy level diagram for the negatively charged NV^- center in diamond, with zero-field splitting D between the ground-state electronic spin levels $m_s=0$ and $m_s=\pm 1$. The $m_s=\pm 1$ energy levels experience a Zeeman shift in the presence of a magnetic field \vec{B} , which forms the basis for NV^- magnetometry. Adapted from Ref. (Schloss *et al.*, 2018).

spin energy levels are sensitive to magnetic fields, electric fields, strain, and temperature variations (Doherty *et al.*, 2013), allowing NV^- to operate as a multi-modal sensor. Coherent spin control is achieved by application of resonant microwaves (MWs) near 2.87 GHz. Upon optical excitation, a spin-state-dependent intersystem crossing (Goldman *et al.*, 2015a,b) combined with decay through a primarily non-radiative pathway allows for both spin-state-dependent fluorescence contrast and optical spin initialization into the NV^- center's $m_s = 0$ ground state (see Fig. I.1b).

Relative to alternative technologies (Grosz *et al.*, 2017), sensors employing NV^- centers excel in technical simplicity and spatial resolution (Arai *et al.*, 2015; Grinolds *et al.*, 2014; Jaskula *et al.*, 2017). Such devices may operate as broadband sensors with bandwidths up to ~ 100 kHz (Acosta *et al.*, 2010b; Barry *et al.*, 2016; Schloss *et al.*, 2018) or as high frequency detectors for signals up to \sim GHz (Aslam *et al.*, 2017; Boss *et al.*, 2016, 2017; Cai *et al.*, 2013; Casola *et al.*, 2018; Hall *et al.*, 2016; Loretz *et al.*, 2013; Lovchinsky *et al.*, 2016; Pelliccione *et al.*, 2014; Pham *et al.*, 2016; Schmitt *et al.*, 2017; Shao *et al.*, 2016; Shin *et al.*, 2012; Steinert *et al.*, 2013; Tetienne *et al.*, 2013; Wood *et al.*, 2016). Importantly, effective optical initialization and readout of NV^- spins does not require narrow-linewidth lasers; rather, a single free-running 532 nm solid-state laser is sufficient. NV^- -diamond sensors operate at ambient temperatures, pressures, and magnetic fields, and thus require no cryogenics, vacuum systems, or large applied bias fields. Furthermore, diamond is chemically inert, making NV^- devices biocompatible. These properties allow sensors to be placed within ~ 1 nm of field sources (Pham *et al.*, 2016), which enables magnetic field imaging with nanometer-scale spatial resolution (Arai *et al.*, 2015; Grinolds *et al.*, 2014; Jaskula *et al.*, 2017). NV^- -diamond sensors are also operationally robust and may function at pres-

sures up to 60 GPa (Doherty *et al.*, 2014; Hsieh *et al.*, 2018; Ivády *et al.*, 2014) and temperatures from cryogenic to 700 K (Plakhotnik *et al.*, 2014; Toyli *et al.*, 2013, 2012).

Although single NV⁻ centers find numerous applications in ultra-high-resolution sensing due to their angstrom-scale size (Balasubramanian *et al.*, 2008; Casola *et al.*, 2018; Maze *et al.*, 2008), sensors employing ensembles of NV⁻ centers provide improved signal-to-noise ratio (SNR) at the cost of spatial resolution by virtue of statistical averaging over multiple spins (Acosta *et al.*, 2009; Taylor *et al.*, 2008). Diamonds may be engineered to contain concentrations of NV⁻ centers as high as 10^{19} cm^{-3} (Choi *et al.*, 2017a), which facilitates high-sensitivity measurements from single-channel bulk detectors as well as wide-field parallel magnetic imaging (Le Sage *et al.*, 2013; Pham *et al.*, 2011; Steinert *et al.*, 2010, 2013; Taylor *et al.*, 2008). These engineered diamonds typically contain NV⁻ centers with symmetry axes distributed along all four crystallographic orientations, each sensitive to a different magnetic field component; thus, ensemble-NV⁻ devices provide full vector magnetic field sensing without heading errors or dead zones (Le Sage *et al.*, 2013; Maertz *et al.*, 2010; Pham *et al.*, 2011; Schloss *et al.*, 2018; Steinert *et al.*, 2010). NV⁻ centers have also been employed for high-sensitivity imaging of temperature (Kucsko *et al.*, 2013), strain, and electric fields (Barson *et al.*, 2017; Dolde *et al.*, 2011). Recent examples of ensemble-NV⁻ sensing applications include optical magnetic detection of single-neuron action potentials (Barry *et al.*, 2016); magnetic imaging of living cells (Le Sage *et al.*, 2013; Steinert *et al.*, 2013), malarial hemozoin (Fescenko *et al.*, 2018), and biological tissue with subcellular resolution (Davis *et al.*, 2018); nanoscale thermometry (Kucsko *et al.*, 2013; Neumann *et al.*, 2013); single protein detection (Lovchinsky *et al.*, 2016; Shi *et al.*, 2015); nanoscale and micron-scale NMR (Bucher *et al.*, 2018; DeVience *et al.*, 2015; Glenn *et al.*, 2018; Kehayias *et al.*, 2017; Loretz *et al.*, 2014; Rugar *et al.*, 2015; Staudacher *et al.*, 2013; Sushkov *et al.*, 2014); and the study of meteorite composition (Fu *et al.*, 2014) and paleomagnetism (Farchi *et al.*, 2017; Glenn *et al.*, 2017).

Despite demonstrated utility in a number of applications, the present performance of ensemble-NV⁻ sensors remains far from theoretical limits. Even the best demonstrated ensemble-based devices exhibit readout fidelities of ~ 0.01 (Itano *et al.*, 1993), $\sim 100\times$ worse than the spin projection limit. Additionally, reported dephasing times T_2^* in NV-rich diamonds remain 100 to $1000\times$ shorter than the theoretical maximum of $2T_1$ (Levitt, 2008; Myers *et al.*, 2017). As a result, whereas present state-of-the-art ensemble-NV⁻ magnetometers exhibit pT/ $\sqrt{\text{Hz}}$ -level sensitivities, competing technologies such as superconducting quantum interference devices (SQUIDs) and spin-exchange relaxation-free (SERF) magnetometers exhibit sensitivities at the fT/ $\sqrt{\text{Hz}}$ -level and below (Kitching, 2018). This $\sim 1000\times$ sensitivity discrepancy corresponds to a $\sim 10^6\times$ increase in required averaging time, which precludes many envisioned applications. For example, the sensing times required to detect weak static signals with an NV-diamond sensor may be unacceptably long; e.g., biological systems

may have only short-term viability. In addition, many applications, such as spontaneous event detection and time-resolved sensing of dynamic processes (Marblestone *et al.*, 2013; Shao *et al.*, 2016), are incompatible with signal averaging. Realizing NV-diamond magnetometers with improved sensitivity could enable a new class of scientific and industrial applications poorly matched to bulkier SQUID and vapor-cell technologies. Examples include noninvasive, real-time magnetic imaging of neuronal circuit dynamics (Barry *et al.*, 2016), high throughput nanoscale and micron-scale NMR spectroscopy (Bucher *et al.*, 2018; Glenn *et al.*, 2018; Smits *et al.*, 2019), nuclear quadrupole resonance (NQR) (Lovchinsky *et al.*, 2017), human magnetoencephalography (Hämäläinen *et al.*, 1993), subcellular magnetic resonance imaging (MRI) of dynamic processes, precision metrology, and tests of fundamental physics (Kirschner *et al.*, 2018; Rajendran *et al.*, 2017).

This review accordingly focuses on understanding present sensitivity limitations for ensemble-NV⁻ magnetometers to best guide future research efforts. We survey and analyze methods for optimizing magnetic field sensitivity, which we divide into three broad categories: (i) improving spin dephasing and coherence times; (ii) improving readout fidelity; and (iii) improving quality and consistency of host diamond material properties. Given the square-root improvement of sensitivity with number of interrogated spins, we primarily concentrate on ensemble-based devices with $\gtrsim 10^4$ NV⁻ centers (Acosta *et al.*, 2009; Barry *et al.*, 2016; Clevenson *et al.*, 2015; Le Sage *et al.*, 2012; Wolf *et al.*, 2015). However, we also examine single-NV⁻ magnetometry techniques in order to determine their applicability to ensembles. Moreover, while this work primarily treats broadband, time-domain magnetometry from DC up to ~ 100 kHz, narrowband AC sensing techniques are also analyzed when judged relevant to future DC and broadband magnetometry advances. Alternative phase-insensitive AC magnetometry techniques such as T_1 relaxometry (Ariyaratne *et al.*, 2018; Casola *et al.*, 2018; Hall *et al.*, 2016; Pelliccione *et al.*, 2014; Romach *et al.*, 2015; Shao *et al.*, 2016; Tetienne *et al.*, 2013; van der Sar *et al.*, 2015) are not treated.

This document is organized as follows: Sec. I.B summarizes differences between DC and AC sensing approaches and focuses subsequent discussion on DC sensing; Sec. I.C introduces the mathematical formalism governing magnetic field sensitivity for ensemble-NV⁻ magnetometers; Sec. I.D reviews common DC magnetometry alternatives to Ramsey protocols; Sec. I.E overviews key parameters determining magnetic field sensitivity. Section II examines the NV⁻ spin ensemble dephasing time, T_2^* , and coherence time, T_2 . In particular, Sec. II.A motivates efforts to extend T_2^* ; Sec. II.B highlights relevant definitional differences of T_2^* for ensembles and single spins; Sec. II.C characterizes various mechanisms contributing to NV⁻ ensemble T_2^* ; and Secs. II.D-II.G investigate limits to T_2^* and T_2 from dipolar interactions with specific paramagnetic species within the diamond. Section III analyzes methods to extend the NV⁻ ensemble dephasing and coherence times using DC and radiofrequency (RF) magnetic fields. Section IV analyzes

a variety of techniques demonstrated to improve the NV⁻ ensemble readout fidelity. Section V reviews progress in engineering diamond samples for high-sensitivity magnetometry, primarily focusing on increasing the NV⁻ concentration while maintaining long T_2^* times and good readout fidelity. Section VI analyzes several additional NV-diamond magnetometry techniques not covered in previous sections. Section VII provides concluding remarks and an outlook on remaining areas where further study is needed. We note that this document aims to comprehensively cover relevant results up through mid-2017 and provides limited coverage of papers published thereafter.

B. DC and AC sensing

Quantum sensing approaches may be divided into two broad categories based on the spectral characteristics of the fields to be detected, summarized in Table I.1. In particular, DC sensing protocols are sensitive to static, slowly-varying, or broadband near-DC signals, whereas AC sensing protocols typically detect narrowband, time-varying signals at frequencies up to ~ 10 MHz (Boss *et al.*, 2016, 2017; Cai *et al.*, 2013; Loretz *et al.*, 2013; Pham *et al.*, 2016; Schmitt *et al.*, 2017; Shao *et al.*, 2016; Shin *et al.*, 2012; Steinert *et al.*, 2013; Wood *et al.*, 2016), although AC sensing experiments of ~ 100 MHz signals have also been demonstrated for niche applications (Aslam *et al.*, 2017). Both DC and AC sensors employing NV⁻ ensembles exhibit sensitivities limited, in part, by the relevant NV⁻ spin relaxation times. DC sensitivity is limited by the ensemble's inhomogeneous dephasing time T_2^* , which is of order 1 μ s in most present implementations. AC sensitivity is limited by the coherence time T_2 , which is typically one to two orders of magnitude longer than T_2^* (Bauch *et al.*, 2019; de Lange *et al.*, 2010), and which can be extended through use of dynamical decoupling protocols to approach the longitudinal spin relaxation time T_1 (see Sec. III.A). Additionally, alternative forms of T_1 -limited AC sensing such as T_1 relaxometry allow phase-insensitive detection of signals at frequencies in the \sim GHz regime (Casola *et al.*, 2018; Hall *et al.*, 2016; Pelliccione *et al.*, 2014; Shao *et al.*, 2016; Tetienne *et al.*, 2013). In general, the enhanced field sensitivities afforded by longer AC sensor coherence times coincide with reduced sensing bandwidth as well as insensitivity to static fields, restricting the application space of AC sensors (see Table I.1). This review concentrates primarily on DC sensing protocols with particular focus on sensors designed to detect broadband time-varying magnetic fields from DC to ~ 100 kHz.

C. Magnetic field sensitivity

The spin-projection-noise-limited sensitivity of an ensemble magnetometer consisting of N non-interacting $S = 1/2$ spins is approximately given by (Budker and Romalis, 2007; Taylor *et al.*, 2008)

$$\eta_{\text{sp}}^{\text{ensemble}} \approx \frac{\hbar}{g_e \mu_B} \frac{1}{\sqrt{N} \tau}, \quad (1)$$

where $g_e \approx 2.003$ is the NV⁻ center's electronic g-factor (Doherty *et al.*, 2013), μ_B is the Bohr magneton, \hbar is the reduced Planck constant, and τ is the free precession (i.e., interrogation) time per measurement. To generalize to higher-multiplicity spins ($S \geq 1$) where the m_s states used for the interferometry measurement differ by $\Delta m_s \geq 2$, the expression for $\eta_{\text{sp}}^{\text{ensemble}}$ is multiplied by the factor $1/\Delta m_s$.

To achieve projection-noise-limited sensitivity, the tools for manipulating and measuring the spins (MW fields and optical photons in the case of NV⁻ centers) must not interfere with the magnetic field interrogation. This requires use of pulsed magnetometry schemes such as Ramsey's separated oscillatory field method (Ramsey, 1950), henceforth called Ramsey magnetometry. In this method, which is depicted schematically in Fig. I.3a, the spins interrogate the magnetic field for a free precession interval during which no external electromagnetic fields are applied. The free precession time is chosen for optimal sensitivity at a value close to the characteristic decay time T_2^* of the Ramsey fringes (see Fig. I.3b and Appendix A.2). The state evolution and projection-noise-limited sensitivity for a Ramsey magnetometry measurement are derived in Appendices A.1.a and A.1.b. However, even when employing Ramsey protocols, NV⁻ ensemble magnetometers suffer from at least three major experimental non-idealities, which deteriorate the achievable magnetic field sensitivity.

First, for NV⁻ ensemble magnetometers, the spin-state initialization time t_I and readout time t_R may be significant compared to the field interrogation time τ . By decreasing the fraction of time devoted to spin precession, the finite values of t_I and t_R deteriorate the sensitivity by the factor

$$\sqrt{\frac{t_I + \tau + t_R}{\tau}}. \quad (2)$$

Second, the conventional NV⁻ optical readout technique (Doherty *et al.*, 2013), which uses 532 nm light to address each NV⁻ center and read out its quantum state using photoluminescence (PL) in the 600-850 nm band, does not allow single-shot determination of the NV⁻ spin state to the spin projection limit (also known as the standard quantum limit). An NV⁻ center in the electronically excited spin-triplet state will decay either directly to the spin-triplet ground state or indirectly through a cascade of spin-singlet states (Rogers *et al.*, 2008) via an inter-system crossing (Goldman *et al.*, 2015a,b; Thiering and Gali, 2018). Conventional NV⁻ optical readout exploits the $m_s = \pm 1$ states' higher likelihood to enter the singlet-state cascade more often than the $m_s = 0$ state (see Table A.3). An NV⁻ center that enters the singlet state cascade does not fluoresce in the 600-850 nm band, whereas an NV⁻ center decaying directly to the spin-triplet ground state can continue cycling between the ground and excited triplet states, producing fluorescence in the 600-850 nm band. The $m_s = \pm 1$ excited states are more likely than the $m_s = 0$ state to decay into the singlet state cascade, and produce on average less PL in the 600-850 nm band, as shown in Fig. I.2. Unfortunately the $\sim 140 - 200$ ns (Acosta *et al.*, 2010b; Gupta *et al.*, 2016; Robledo *et al.*, 2011) spin-singlet cascade lifetime and limited differences in $m_s = \pm 1$ and $m_s = 0$ decay

	Broadband DC sensing	AC sensing
Common techniques	Ramsey (Sec. I.C), CW-ODMR (Sec. I.D.1), pulsed ODMR (Sec. I.D.2)	Hahn echo, dynamical decoupling (Sec. III.A)
Sensitivity	Limited by inhomogeneous spin dephasing (T_2^*)	Limited by homogeneous spin decoherence (T_2) and longitudinal relaxation (T_1)
Frequency/bandwidth	0 to ~ 100 kHz (pulsed), 0 to ~ 10 kHz (CW)	Center frequency: ~ 1 kHz to ~ 10 MHz; bandwidth: $\lesssim 100$ kHz
Example magnetic sensing applications	Biocurrent detection, magnetic particle tracking, magnetic imaging of rocks and meteorites, imaging of magnetic nanoparticles in biological systems, magnetic imaging of electrical current flow in materials, magnetic anomaly detection, navigation	Single biomolecule and protein detection, nanoscale nuclear magnetic resonance, nanoscale electron spin resonance, magnetic resonant phenomena in materials, noise spectroscopy

TABLE I.1 Performance metrics and selected applications of broadband DC and AC sensing protocols employing NV^- ensembles in diamond. T_1 relaxometry methods are not considered.

behavior allows for only probabilistic determination of the NV^- initial spin state. Following Ref. (Shields *et al.*, 2015), we quantify the added noise from imperfect readout with the parameter σ_R , such that $\sigma_R = 1$ corresponds to readout at the spin projection limit. This parameter is the inverse of the measurement fidelity: $\mathcal{F} \equiv 1/\sigma_R$. For imperfect readout schemes, the value of σ_R can be calculated as (Shields *et al.*, 2015; Taylor *et al.*, 2008)

$$\sigma_R = \sqrt{1 + \frac{2(a+b)}{(a-b)^2}} \quad (3)$$

$$= \sqrt{1 + \frac{1}{C^2 n_{\text{avg}}}}, \quad (4)$$

where a and b respectively denote the average numbers of photons detected from the $m_s = 0$ and $m_s = \pm 1$ states of a single NV^- center during a single readout. In Eqn. 4 we identify $C = \frac{a-b}{a+b}$ as the measurement contrast (i.e., the interference fringe visibility), and $n_{\text{avg}} = \frac{a+b}{2}$ as the average number of photons collected per NV^- center per measurement. Although sub-optimal initialization and readout times t_I and t_R can degrade the value of C , it is henceforth assumed that t_I and t_R are optimized to avoid this effect.

Third, the sensitivity η is degraded for increased values of τ due to spin dephasing during precession. For Ramsey-type pulsed magnetometry, (i.e., with no spin echo), the dephasing occurs with characteristic time T_2^* so that η is additionally deteriorated by the factor

$$\frac{1}{e^{-(\tau/T_2^*)^p}}, \quad (5)$$

where the value of the stretched exponential parameter p depends on the origin of the dephasing (see Appendix A.7). NV^- spin resonance lineshapes with exactly Lorentzian profiles correspond to dephasing with $p = 1$, and spin resonance lineshapes with Gaussian profiles correspond to $p = 2$ (see Appendix A.5).

Combining Eqns. 1, 2, 3, and 5 gives the sensitivity for a Ramsey-type NV^- broadband ensemble magnetome-

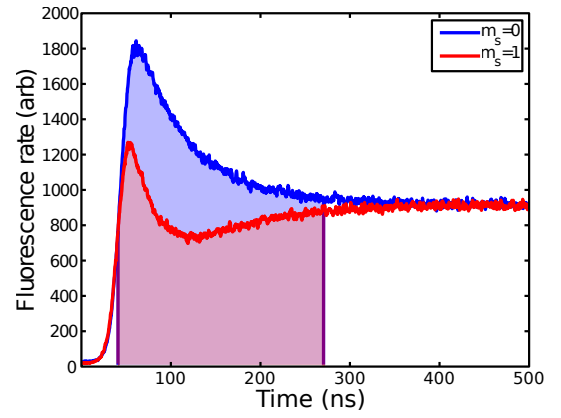


FIG. I.2 Fluorescence of the NV^- spin states. NV^- centers prepared in the $m_s = 0$ state emit more photons than centers prepared in the $m_s = \pm 1$ states. This spin-dependent fluorescence forms the basis of conventional NV^- readout. Data courtesy of Brendan Shields.

ter (Popa *et al.*, 2004) as

$$\eta_{\text{Ramsey}}^{\text{ensemble}} \approx \frac{\hbar}{g_e \mu_B} \times \frac{1}{\Delta m_s} \times \frac{\sigma_R}{\sqrt{N}} \times \frac{1}{e^{-(\tau/T_2^*)^p}} \times \frac{\sqrt{t_I + \tau + t_R}}{\tau}, \quad (6)$$

where N is the number of NV^- centers in the ensemble and $\Delta m_s = 1$ for the effective $S = 1/2$ subspace employed for NV^- magnetometry. However, in the limit of measurement contrast $C \ll 1$ and when the number of photons collected per NV^- center per optical readout is much less than one, σ_R is dominated by photon shot noise and can be approximated as $\sigma_R \approx \frac{1}{C \sqrt{n_{\text{avg}}}}$. Defining $\mathcal{N} = N n_{\text{avg}}$ to be the average number of photons detected per measurement from the ensemble of N NV^- centers yields the following shot-noise-limited sensitivity equation for a Ramsey scheme (Pham, 2013):

$$\eta_{\text{Ramsey}}^{\text{ensemble,shot}} \approx \frac{\hbar}{g_e \mu_B} \frac{1}{\Delta m_s} \frac{1}{C e^{-(\tau/T_2^*)^p} \sqrt{\mathcal{N}}} \frac{\sqrt{t_I + \tau + t_R}}{\tau}. \quad (7)$$

Henceforth we assume broadening mechanisms produce Lorentzian lineshapes, so that $p = 1$. For negligible t_I and t_R , the optimal measurement time is $\tau = T_2^*/2$, whereas

for $t_I + t_R \gg T_2^*$, the optimal τ approaches T_2^* (see Appendix A.2). Equation 7 illustrates the benefits attained by increasing the dephasing time T_2^* , the measurement contrast C , the number of NV⁻ spin sensors N , and the average number of photons detected per NV⁻ per measurement n_{avg} . Table I.2 depicts example values of σ_R and \mathcal{N} achieved using conventional optical readout in pulsed and CW magnetometry measurements, with both single NV⁻ centers and ensembles. At present, conventional optical readout is insufficient to reach the spin projection limit for both single- and ensemble-NV⁻ sensors. Appendix A.1 derives the sensitivity for a Ramsey-type magnetometer in both the spin projection and shot noise limits.

In addition to Ramsey-type methods, other protocols allow measurement of DC magnetic fields. These alternative methods, including continuous-wave and pulsed optically detected magnetic resonance, offer reduced sensitivity compared to Ramsey-type sequences (for a fixed number of NV⁻ centers addressed), as discussed in the following sections.

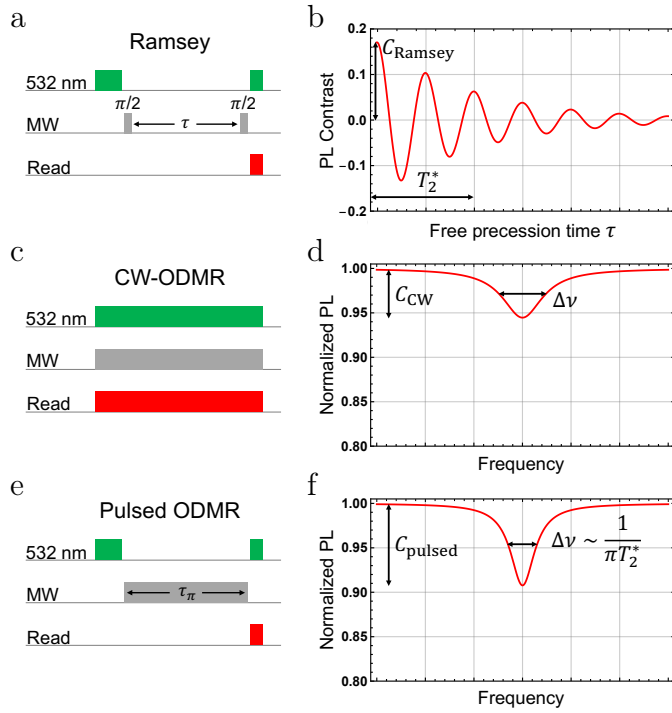


FIG. I.3 Overview of Ramsey, CW-ODMR, and pulsed ODMR magnetometry protocols. a) Schematic of Ramsey magnetometry protocol. b) Cartoon of free induction decay associated with a Ramsey protocol versus free precession time τ . Fringes exhibit contrast C_{Ramsey} and decay exponentially with dephasing time T_2^* . c) Schematic of CW-ODMR sensing protocol. d) Cartoon of CW-ODMR spectrum with contrast C_{CW} and linewidth $\Delta\nu$. e) Schematic of pulsed ODMR sensing protocol with MW π -pulse time $\tau_\pi \sim T_2^*$. f) Cartoon of pulsed ODMR spectrum with contrast C_{pulsed} and linewidth $\Delta\nu \sim 1/(\pi T_2^*)$.

D. Alternatives to Ramsey magnetometry

1. CW-ODMR

Continuous-wave optically detected magnetic resonance (CW-ODMR) is a simple and widely employed magnetometry method (Acosta *et al.*, 2009; Barry *et al.*, 2016; Dréau *et al.*, 2011; Fuchs *et al.*, 2008; Schloss *et al.*, 2018; Schoenfeld and Harneit, 2011; Tetienne *et al.*, 2012) wherein the MW driving and the optical polarization and readout occur simultaneously (see Fig. I.3c). Laser excitation continuously polarizes NV⁻ centers into the more fluorescent $m_s = 0$ ground state while MWs tuned near resonance with one of the $m_s = 0 \leftrightarrow m_s = \pm 1$ transitions drive NV⁻ population into the less fluorescent $m_s = \pm 1$ state, reducing the emitted light. A change in the local magnetic field shifts the ODMR feature with respect to the MW drive frequency, causing a change in the detected fluorescence, as illustrated in Fig. I.3d.

The shot-noise-limited sensitivity of an NV⁻ magnetometer employing CW-ODMR is given by (Barry *et al.*, 2016; Dréau *et al.*, 2011)

$$\eta_{\text{CW}} = \frac{4}{3\sqrt{3}} \frac{h}{g\mu_B} \frac{\Delta\nu}{C_{\text{CW}}\sqrt{R}} \quad (8)$$

with photon detection rate R , linewidth $\Delta\nu$ and CW-ODMR contrast C_{CW} . The prefactor $4/(3\sqrt{3})$ originates from the steepest slope of the ODMR lineshape when assuming a Lorentzian resonance profile, and is achieved for a detuning of $\frac{\Delta\nu}{2\sqrt{3}}$ from the linecenter (Vanier and Audoin, 1989).

CW-ODMR is technically easier to implement than pulsed measurement schemes such as Ramsey and may yield sensitivities similar to Ramsey when a larger number of sensors are interrogated with the same optical excitation power (Barry *et al.*, 2016). However, CW-ODMR is not envisioned for many high-sensitivity applications for multiple reasons. First, CW-ODMR precludes use of pulsed methods to improve sensitivity, such as double-quantum coherence magnetometry (see Sec. III.B), and many readout-fidelity enhancement techniques. Second, CW-ODMR methods suffer from MW and optical power broadening, degrading both $\Delta\nu$ and C_{CW} compared to optimized Ramsey sequences. Optimal CW-ODMR sensitivity is achieved approximately when optical excitation, MW drive, and T_2^* dephasing contribute roughly equally to the ODMR linewidth (Dréau *et al.*, 2011). In this low-optical-intensity regime, the detected fluorescence rate per interrogated NV⁻ center is significantly lower than for an optimized Ramsey scheme, which results in readout fidelities $\sim 10^3$ below the spin projection limit (Barry *et al.*, 2016). This low optical intensity requirement becomes more stringent as T_2^* increases, meaning that CW-ODMR sensitivity largely does not benefit from techniques to extend T_2^* .

Reference	Readout method	Single NV ⁻ /ensemble	σ_R	\mathcal{N} [counts/measurement]
(Shields <i>et al.</i> , 2015)	conventional	single	10.6	$9.45 \times 10^5 \text{ cps} \times t_R$
(Shields <i>et al.</i> , 2015)	spin-to-charge conversion	single	2.76	-
(Lovchinsky <i>et al.</i> , 2016)	conventional	single	35	$\sim 10^5 \text{ cps} \times t_R$
(Lovchinsky <i>et al.</i> , 2016)	ancilla-assisted	single	5	-
(Fang <i>et al.</i> , 2013)	conventional	single	80	0.01
(Hopper <i>et al.</i> , 2016)	conventional	single	48	0.04
(Hopper <i>et al.</i> , 2016)	spin-to-charge conversion	single	3	-
(Jaskula <i>et al.</i> , 2017)	conventional	single	54	0.022
(Jaskula <i>et al.</i> , 2017)	spin-to-charge conversion	single	5	-
(Neumann <i>et al.</i> , 2010a)	ancilla-assisted	single	1.1	-
(Le Sage <i>et al.</i> , 2012)	conventional	ensemble	67	2×10^8
(Wolf <i>et al.</i> , 2015)	conventional	ensemble	~ 1000	10^{12}
(Chatzidrosos <i>et al.</i> , 2017)	NIR absorption [†]	ensemble	65	-
(Barry <i>et al.</i> , 2016)	conventional [†]	ensemble	~ 5000	-
(Schloss <i>et al.</i> , 2018)	conventional [†]	ensemble	~ 5000	-

TABLE I.2 Example literature values for readout schemes employing conventional optical readout or alternative techniques. The parameter σ_R characterizes the factor above spin projection noise and \mathcal{N} is the average number of photons collected per measurement. Conventional NV⁻ readout is unable to reach the spin projection limit ($\sigma_R = 1$), whereas alternative schemes can allow readout to approach this limit. The best demonstrated pulsed readout methods with ensembles are presently $\sim 100\times$ away from the spin projection limit. The symbol [†] denotes non-pulsed schemes for comparison, and dashed lines (-) indicate values not reported (or not applicable to non-pulsed schemes).

2. Pulsed ODMR

Pulsed ODMR is an alternative magnetometry method first demonstrated for NV⁻ centers by Dréau *et al.* in Ref. (Dréau *et al.*, 2011). Similar to Ramsey and in contrast to CW-ODMR, this technique avoids optical and MW power broadening of the spin resonances, enabling nearly T_2^* -limited measurements. In contrast to Ramsey magnetometry, however, pulsed ODMR is linearly sensitive to spatial and temporal variations in MW Rabi frequency. When such variations are minimal, pulsed ODMR sensitivity may approach that of Ramsey magnetometry without requiring high Rabi frequency (Dréau *et al.*, 2011), making the method attractive when high MW field strengths are not available.

In the pulsed ODMR protocol, depicted schematically in Fig. I.3e, the NV⁻ spin state is first optically initialized to $m_s = 0$. Then, during the sensing time τ , a resonant MW π -pulse is applied with duration equal to the sensing time, $\tau_\pi = \tau$, where the Rabi frequency $\Omega_R = \pi/\tau_\pi$. Finally, the population is read out optically. A change in the magnetic field detunes the spin resonance with respect to the MW frequency, resulting in an incomplete π -pulse and a change in the population transferred to the $m_s = \pm 1$ state prior to optical readout.

For a Lorentzian ODMR lineshape (see Appendices A.5 and A.6), the expected shot-noise-limited sensitivity may be calculated starting from the shot-noise-limited CW-ODMR sensitivity given by Eqn. 8. For pulsed ODMR, the resonance profile is given by a convolution of the natural T_2^* -limited line profile and additional broadening from the NV⁻ spin's response to a fixed-duration, detuned MW π -pulse, as shown in Fig. I.4. When the sensing time τ_π is set to

$\approx T_2^*$, these two broadening mechanisms contribute approximately equally to the resonance linewidth (Dréau *et al.*, 2011). Assuming $\tau_\pi \approx T_2^*$, we write the pulsed ODMR linewidth $\Delta\nu$ as $\Delta\nu \approx \Gamma = 1/(\pi T_2^*)$ (see Fig. I.3f), while noting that this approximation likely underestimates the linewidth by $\lesssim 2\times$.

Choosing initialization and readout times t_I and t_R and sensing time $\tau_\pi = T_2^*$ reduces the time-averaged photon collection rate R by the readout duty cycle $t_R/(t_I + T_2^* + t_R)$. Then, defining $\mathcal{N} = Rt_R$ to be the mean number of photons collected per optical readout cycle and replacing C_{CW} with the pulsed-ODMR contrast C_{pulsed} yields the pulsed-ODMR sensitivity

$$\eta_{\text{pulsed}} \approx \frac{8}{3\sqrt{3}} \frac{\hbar}{g_e \mu_B} \frac{1}{C_{\text{pulsed}} \sqrt{\mathcal{N}}} \frac{\sqrt{t_I + T_2^* + t_R}}{T_2^*}. \quad (9)$$

The value of C_{pulsed} under optimized conditions is expected to be higher than C_{CW} (for the same number of interrogated NV⁻ centers and same mean photon collection rate R) because pulsed ODMR enables use of high optical intensities that would degrade C_{CW} (Dréau *et al.*, 2011). Although C_{pulsed} may approach the Ramsey contrast C_{Ramsey} (see Fig. I.3a,b), $C_{\text{pulsed}} < C_{\text{Ramsey}}$ is expected in practice for several reasons: First, because the technique requires Rabi frequencies to be of the same order as the NV⁻ natural linewidth, the MW drive may be too weak to effectively address the entire inhomogeneously-broadened NV⁻ ensemble. Second, while the high Rabi frequencies $\sim 2\pi \times 10$ MHz commonly employed in Ramsey sequences effectively drive all hyperfine-split NV⁻ transitions of ¹⁴NV⁻ or ¹⁵NV⁻ (Acosta *et al.*, 2009), the weaker π -pulses required for pulsed ODMR cannot effectively drive all hyperfine transitions with a single tone. Pulsed ODMR

Sensitivity optimization		
Parameter optimized	Method	Method description and evaluation
Dephasing time T_2^*	Double-quantum coherence magnetometry (Sec. III.B)	Doubles effective gyromagnetic ratio. Removes dephasing from mechanisms inducing shifts common mode to the $ m_s = \pm 1\rangle$ states, such as longitudinal strain and temperature. Minor additional MW hardware usually required. Generally recommended.
	Bias magnetic field (Sec. III.D)	Operation in a bias magnetic field of several gauss or higher suppresses dephasing from transverse electric fields and strain. Generally recommended.
	Spin bath driving (Sec. III.C)	Mitigates or eliminates dephasing from paramagnetic impurities in diamond. Each impurity's spin resonance must be addressed, often with an individual RF frequency. Additional RF hardware is required. Recommended for many applications.
	Dynamical decoupling (Sec. III.A)	Refocuses spin dephasing using one or more MW π -pulses, extending the relevant relaxation time from T_2^* to T_2 , with fundamental limit set by $2T_1$. Recommended for narrowband AC sensing; generally precludes DC or broadband magnetic sensing.
	Rotary echo magnetometry (Sec. VI.A)	MW pulse scheme extends measurement time but offers reduced sensitivity relative to Ramsey. Not recommended outside niche applications.
	Geometric phase magnetometry (Sec. VI.B)	MW spin manipulation method offers increased dynamic range but reduced sensitivity relative to Ramsey. Not recommended outside niche applications.
Readout fidelity $\mathcal{F} = 1/\sigma_R$	Ancilla-assisted upconversion magnetometry (Sec. VI.C)	Method employs NV^- hyperfine interaction to convert DC magnetic fields to AC fields to be sensed using dynamical decoupling. Operates near ground-state level anticrossing (10^3 gauss) and offers similar or reduced sensitivity relative to Ramsey. Not generally recommended.
	Spin-to-charge conversion readout (Sec. IV.A)	Maps spin state to charge state of NV^- , increasing number of photons collected per measurement. Allows $\sigma_R \approx 3$, and initial results show improvement over conventional readout for ensembles. Substantially increased readout time likely precludes application when $T_2^* \lesssim 3 \mu s$. Requires increased laser complexity. Technique is envisioned as promising; hence, further investigation is warranted.
	Ancilla-assisted repetitive readout (Sec. IV.C)	Maps NV^- electronic spin state to nuclear spin state, enabling repetitive readout and increased photon collection. Allows σ_R to approach 1 for single NV s; no fundamental barriers to ensemble application. Substantially increased readout time likely precludes application when $T_2^* \lesssim 3 \mu s$. Requires high magnetic field strength and homogeneity. Technique is envisioned as promising, although further investigation is warranted.
	Improved photon collection (Sec. IV.E)	Improves σ_R by reducing fractional shot noise contribution, subject to unity collection and projection noise limits. Near-100% collection efficiency is possible in principle, making this mainly an engineering endeavor. While many schemes are incompatible with wide-field imagers, the method is generally recommended for optical-based readout of single-channel bulk sensors.
	NIR absorption readout (Sec. IV.F)	Probabilistic readout of initial spin population using optical absorption on the $^1E \leftrightarrow ^1A_1$ singlet transition. Demonstrated σ_R values are on par with conventional ensemble readout, and prospects for further improvement are unknown. Technique is best paired with dense ensembles and an optical cavity but is hindered by non- NV^- absorption and non-radiative NV^- singlet decay. Further investigation is warranted.
	Photoelectric readout (Sec. IV.B)	Spin-dependent photoionization current is detected. Best for small 2D ensembles; has not yet demonstrated sensitivity improvement with respect to optimized conventional readout.
	Level-anticrossing-assisted readout (Sec. IV.D)	Universal technique increases number of spin-dependent photons collected per readout by operation at the excited-state level anticrossing. At best offers a $\sqrt{3}$ improvement in σ_R . Not recommended outside niche applications.
	Green absorption readout (Sec. IV.G)	Probabilistic readout of initial spin state using optical absorption on the $^3A_2 \leftrightarrow ^3E$ triplet transition. Performs best with order unity optical depth. Demonstrations exhibit contrast below that of conventional readout by $3\times$ or more. Prospects are not envisioned as promising.
	Laser threshold magnetometry (Sec. IV.H)	Probes magnetic field by measuring lasing threshold, which depends on NV^- singlet state population. Moderately improved collection efficiency and contrast are predicted compared to conventional readout. Challenges include non- NV^- absorption and system instability near lasing threshold. Prospects are not envisioned as promising.
	Entanglement-assisted magnetometry (Sec. VI.D)	Proposed techniques harness strong NV^- dipolar interactions to improve readout fidelity beyond the standard quantum limit. Existing proposals require 2D ensembles, impose long overhead times, and exhibit unfavorable coherence time scaling with number of entangled spins. While existing protocols are not envisioned as promising, further investigation toward developing improved protocols is warranted.

TABLE I.3 Summary analysis of approaches to optimize ensemble- NV -diamond magnetic sensitivity

Diamond material optimization		
Parameter optimized	Method	Method description and evaluation
N-to-NV conversion efficiency χ (Sec. V.A)	CVD synthesis (Sec. V.C)	Common synthesis method that can produce high-quality ensemble-NV-diamonds. Relatively easy to control dimensions and concentrations of electronic and nuclear spins. May introduce strain and unwanted impurities, which can limit achievable ζ , χ , and T_2^* . Effective for producing NV ⁻ -rich layer diamonds.
NV-to-NV ⁻ charge state efficiency ζ (Sec. V.A)	HPHT synthesis (Sec. V.C)	Common synthesis method that can produce high-quality ensemble-NV-diamonds with lower strain and fewer lattice defects than CVD. Control over doping and impurity concentration may be more difficult than CVD. Not intrinsically amenable to creating NV ⁻ -rich layer diamonds. Ferromagnetic metals may incorporate into diamond.
Unwanted paramagnetic impurities (Sec. V.F)	Irradiation (Sec. V.D)	Diamond treatment method that, combined with subsequent annealing, converts substitutional nitrogen to NV centers. Electrons are preferred irradiation source. Dose should be optimized for diamond's nitrogen concentration to create high ζ without degrading χ . Generally recommended with annealing for producing NV ⁻ -rich diamonds.
Strain (Sec. II.C)	LPHT annealing (Sec. V.E)	Low-pressure annealing that, combined with prior irradiation, converts substitutional nitrogen to centers. Heals some diamond lattice damage. NV ⁻ centers are created effectively at ~ 800 °C; additional treatment at ~ 1200 °C may eliminate some unwanted impurities. Generally recommended with irradiation for producing NV ⁻ -rich diamonds.
Nuclear spins (Sec. II.F)	HPHT treatment (Sec. V.C)	High-pressure annealing may reduce strain and eliminate some unwanted impurities. May enable increases in ζ and χ . Recommended for diamonds with balanced aspect ratios.
	Isotopic enrichment (Sec. II.F)	Diamond synthesis with isotopically enriched source (gas for CVD and typically solid for HPHT) allows reduction of unwanted nuclear spin concentration (e.g., ^{13}C) and selection of nitrogen isotope incorporated into NV ⁻ (^{14}N or ^{15}N). CVD diamonds with $[^{13}\text{C}] \approx 20$ ppm have been synthesized. Recommended for achieving long T_2^* .
	Surface treatment (Sec. V.A)	Surface termination can stabilize the desired NV charge state near the surface and extend relaxation times. Generally recommended.
	Preferential orientation (Sec. V.G)	CVD synthesis of diamond with NV centers preferentially oriented along a single axis. At present, preferential orientation is only maintained in unirradiated diamonds, largely hindering its capability to produce NV ⁻ -rich diamonds. Not generally recommended.

TABLE I.4 Summary analysis of diamond engineering parameters and methods for high-sensitivity ensemble-NV⁻ magnetometry. Colored lines indicate methods that may be employed to optimize each parameter.

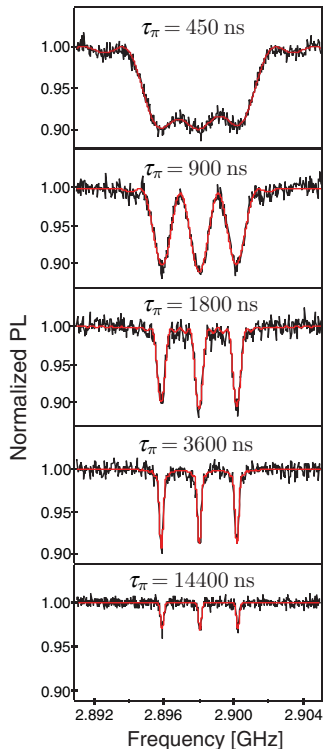


FIG. I.4 Pulsed ODMR spectra for various π -pulse durations τ_π . When $\tau_\pi \ll T_2^*$, the ODMR lineshape is Fourier-broadened beyond the natural linewidth. When $\tau_\pi \gg T_2^*$ the photoluminescence (PL) contrast is diminished due to spin dephasing. Choice of $\tau_\pi \sim T_2^*$ ($\approx 3 \mu\text{s}$ here) allows nearly- T_2^* -limited linewidths while preserving PL contrast. From Ref. (Dréau *et al.*, 2011).

operation at the excited state level anticrossing (Dréau *et al.*, 2011) or utilizing multi-tone MW pulses (Barry *et al.*, 2016; El-Ella *et al.*, 2017; Vandersypen and Chuang, 2005) could allow more effective driving of the entire NV^- population and more optimal values of C_{pulsed} . However, when multi-tone pulses are employed, care should be taken to avoid degradation of C_{pulsed} due to off-resonant MW cross-excitation, which may be especially pernicious when the natural linewidth (and thus MW Rabi frequency) is similar to the hyperfine splitting.

Although pulsed ODMR may sometimes be preferable to Ramsey, the technique ultimately provides inferior sensitivity. Several factors of order $\sqrt{2}$, (which arise from a lineshape-dependent numerical prefactor (Dréau *et al.*, 2011), MW Fourier broadening, nonuniform ensemble driving, and hyperfine driving inefficiencies), combine to degrade the pulsed ODMR sensitivity with respect to that of Ramsey. Furthermore, unlike double-quantum Ramsey magnetometry (see Sec. III.B), pulsed ODMR has not been experimentally demonstrated to mitigate line broadening from temperature fluctuations or other common-mode dephasing mechanisms. Hypothetical double-quantum analogs to pulsed ODMR (Fang *et al.*, 2013; Taylor *et al.*, 2008) might likely require, in addition to the sensing π -pulse, high-Rabi-frequency MW pulses to initialize the $|\pm 1\rangle$ superposition states similar to those employed for double-

quantum Ramsey, which would negate pulsed ODMR's otherwise attractive low MW Rabi frequency requirements.

A generalization of pulsed ODMR is Rabi beat sensing (Fedder *et al.*, 2011; Rabi, 1937), wherein the spins are driven through multiple Rabi oscillations during the field interrogation time. Under optimal conditions, Rabi beat magnetometry, like the specific case of pulsed ODMR, may exhibit sensitivity approaching that of Ramsey magnetometry. For the regime wherein the Rabi frequency Ω_R is large compared to the ODMR linewidth ($\sim 1/T_2^*$), sensitivity is optimized when the detuning is chosen to be similar to the Rabi frequency, ($\Delta \sim \Omega_R$), when the interrogation time is similar to the dephasing time, ($\tau \sim T_2^*$, see Appendix A.2), and when τ is chosen to ensure operation at a point of maximum slope of the Rabi magnetometry curve. However, Rabi beat magnetometry is sensitive to spatial and temporal variations in the MW Rabi frequency Ω_R (Ramsey, 1950). For high values of Ω_R , MW field variations may limit the Rabi measurement's effective T_2^* . Hence, practical implementations of Rabi beat magnetometry on NV^- ensembles likely perform best when $\Omega_R \sim 1/T_2^*$, i.e., when pulsed ODMR is employed.

E. Parameters limiting sensitivity

Examination of Eqn. 6 reveals the relevant parameters limiting magnetic field sensitivity $\eta_{\text{Ramsey}}^{\text{ensemble}}$: (i) the dephasing time T_2^* ; (ii) the readout fidelity $\mathcal{F} = 1/\sigma_R$; (iii) the sensor density $[\text{NV}^-]$ and the interrogated diamond volume V , which together set the total number of sensors $N = [\text{NV}^-] \times V$; (iv) the measurement overhead time $t_O = t_I + t_R$; and (v) the relative precession rates of the two states comprising the interferometry measurement. Sensitivity enhancement requires improving one or more of these parameters. As we will discuss, parameters (i) and (ii) are particularly far from physical limits and therefore warrant special focus.

(i) Dephasing Time T_2^* | In current realizations, dephasing times in application-focused broadband NV^- ensemble magnetometers (Barry *et al.*, 2016; Chatzidrosos *et al.*, 2017; Clevenston *et al.*, 2015; Kucsko *et al.*, 2013) are typically $T_2^* \lesssim 1 \mu\text{s}$. Considering the physical limit $T_2^* \leq 2T_1$ (Levitt, 2008; Myers *et al.*, 2017) where the longitudinal relaxation time is $T_1 \approx 6 \text{ ms}$ for NV^- ensembles (Jarmola *et al.*, 2012), a maximum $T_2^* \approx 12 \text{ ms}$ is theoretically achievable, corresponding to a sensitivity enhancement of $\approx 100\times$. Although the feasibility of realizing T_2^* values approaching $2T_1$ remains unknown, general improvement of T_2^* is believed to be an effective approach to enhancing sensitivity (see Sec. II.A). While the stretched exponential parameter p can provide information regarding the dephasing source limiting T_2^* , its value (typically between 1 and 2 for ensembles) does not strongly affect achievable sensitivity (Bauch *et al.*, 2018).

(ii) Readout Fidelity | Increasing readout fidelity

$\mathcal{F} = 1/\sigma_R$ is another effective method to enhance sensitivity, as fractional fidelity improvements result in equal fractional improvements in sensitivity. With conventional 532 nm fluorescence readout, current NV⁻ ensemble readout fidelities \mathcal{F} are a factor $\gtrsim 67\times$ removed from the spin projection limit $\sigma_R = 1$ (Le Sage *et al.*, 2012), indicating large improvements might be possible. For comparison, multiple readout methods employing single NV⁻ centers achieve \mathcal{F} within $5\times$ of the spin projection limit, i.e., $\sigma_R < 5$ (Ariyaratne *et al.*, 2018; Hopper *et al.*, 2016, 2018b; Jaskula *et al.*, 2017; Lovchinsky *et al.*, 2016; Shields *et al.*, 2015) with Ref. (Neumann *et al.*, 2010a) achieving $\sigma_R = 1.1$.

In contrast, we believe prospects are modest for improving sensitivity by engineering parameters (iii), (iv), and (v).

(iii) Sensor Number, Density, or Interrogation Volume | In theory, the number of sensors N can be increased without limit. However, practical considerations prevent this approach. First, the higher SNR associated with higher N is expected to translate to more stringent noise and timing jitter requirements (for device electronics) in order to reach the shot noise limit. Second, large values of N can require impractically high laser powers, since the number of photons needed for NV⁻ spin initialization scales linearly with N . While larger N can be achieved either by increasing the NV⁻ density or increasing the interrogation volume, both approaches exhibit distinct difficulties. Increasing N by increasing the interrogation volume with fixed [NV⁻] may increase the diamond cost and creates more stringent uniformity requirements for both the bias magnetic field (to avoid degrading the dephasing time T_2^*) and the MW field (to ensure uniform spin manipulation over the sensing volume). Furthermore, increasing interrogation volume is incompatible with high-spatial-resolution sensing and imaging modalities (Fu *et al.*, 2014; Glenn *et al.*, 2017, 2015; Le Sage *et al.*, 2013; Pham *et al.*, 2011; Simpson *et al.*, 2016; Steinert *et al.*, 2010; Tetienne *et al.*, 2017). In the alternative approach, increasing NV⁻ density will increase dephasing from dipolar coupling and decrease T_2^* unless such effects are mitigated. Finally, because sensitivity scales as $1/\sqrt{N}$, increasing N is expected to allow only modest enhancements (e.g., $\lesssim 5\times$) over standard methods. To date no demonstrated high sensitivity bulk NV-diamond magnetometer (Barry *et al.*, 2016; Chatzidrosos *et al.*, 2017; Clevenston *et al.*, 2015; Wolf *et al.*, 2015) has utilized more than a few percent of the available NV⁻ in the diamond, suggesting limited utility for increasing sensor number N in current devices. See Appendix A.3 for additional analysis.

(iv) Overhead Time | Although measurement overhead time can likely be decreased to $\sim 1\ \mu\text{s}$, in the regime where $T_2^* \sim t_I + t_R$, maximum sensitivity enhancement is expected to be limited to order unity,

e.g., $\lesssim 3\times$. See Sec. II.A for a more detailed discussion.

(v) Precession Rate | Use of the NV⁻ center's full $S = 1$ spin can allow $\Delta m_s = 2$ in Eqns. 6 and 7, i.e., a $2\times$ increase in the relative precession rate of the states comprising the interferometry measurement compared to use of the standard $S = 1/2$ sub-basis (see Sec. III.B) (Bauch *et al.*, 2018; Fang *et al.*, 2013). However, further improvement is unlikely, as the NV⁻ spin dynamics are fixed.

We note that the derivation of Eqn. 6 makes certain assumptions (e.g., the N sensors are independent) that neglect additional elaborate approaches such as exploiting strong NV⁻-NV⁻ interactions via Floquet techniques and harnessing entanglement for sensing (see Sec. VI.D) (Choi *et al.*, 2017).

Table I.3 summarizes our analysis of present and proposed techniques to optimize ensemble-NV⁻ magnetic field sensitivity. Table I.4 summarizes our review of engineering methods for producing optimized diamond samples for high-sensitivity ensemble-NV⁻ magnetometry.

II. LIMITS TO RELAXATION TIMES T_2^* AND T_2

A. Motivation to extend T_2^*

A promising approach to enhance DC sensitivity focuses on extending the dephasing time T_2^* (Bauch *et al.*, 2018). The effectiveness of this approach may be illustrated by close examination of Eqns. 6, 7. First, optimal sensitivity is obtained when the precession time τ is similar to the dephasing time T_2^* (see Appendix A.2), so that the approximation $\tau \sim T_2^*$ is valid for an optimized system. Therefore, for the simple arguments presented in this section, we assume that T_2^* extensions translate to proportional extensions of the optimal τ . When the dephasing time T_2^* is similar to or shorter than the measurement overhead time ($T_2^* \lesssim t_O \equiv t_I + t_R$), which may be typical for Ramsey magnetometers employing ensembles of NV⁻ centers in $[\text{N}^\text{T}] = 1\text{-}20$ ppm diamonds, the sensitivity enhancement may then be nearly linear in T_2^* , as shown in Fig. II.1.

The above outlined sensitivity scaling can be intuitively understood as follows: when the free precession time is small relative to the overhead time, i.e., $\tau \sim T_2^* \ll t_O$, doubling T_2^* (thus doubling τ) results in twice the phase accumulation per measurement sequence and only a slight increase in the total sequence duration; in this limit, magnetometer sensitivity is enhanced by nearly $2\times$. This favorable sensitivity scaling positions T_2^* as an important parameter to optimize when $T_2^* \lesssim t_O$.

Typical NV⁻ ensemble T_2^* values are ~ 500 ns in $[\text{N}^\text{T}] \approx 20$ ppm chemical-vapor-deposition-grown diamonds from Element Six, a popular supplier of scientific diamonds. Even when employing maximally optimistic values of $t_I = 1\ \mu\text{s}$ and $t_R = 300$ ns in Ramsey sequences performed on such ensembles, only roughly one quarter of the total measurement time is allocated to free precession.

In this regime, as discussed above, the sensitivity scales as $\sim 1/T_2^*$. Although values of t_I and t_R vary in the literature (see Table II.1), the use of longer t_I and t_R , which may achieve better spin polarization and higher readout fidelity, will only increase the relative sensitivity improvement from extending T_2^* . Notably, initialization times are typically longer for NV⁻ ensembles than for single NV⁻ defects, as spatial non-uniformity in the optical intensity applied to the ensemble (e.g., with a Gaussian illumination profile) can be compensated for by increasing the initialization time (Wolf *et al.*, 2015).

Longer dephasing times T_2^* offer additional benefits beyond direct sensitivity improvement. For example, higher T_2^* values, leading to lower duty cycles for specific experimental protocol steps, may relax certain technical requirements. In a standard Ramsey-type experiment, the optical initialization and optical readout occur once per measurement sequence. Assuming a fixed mean number of photons are required to both spin polarize and read out the NV⁻ ensemble, the time-averaged optical power and resulting heat load are expected to scale as $1/T_2^*$. Reducing heat loads is prudent for minimizing temperature variation of the diamond, which couples to individual NV⁻ resonances like a spurious magnetic signal and may require correction (see Sec. III.B). Minimizing heat load is also important for many NV-diamond sensing applications, particularly in the life sciences. Assuming a fixed overhead time t_O , the realization of higher values of T_2^* , and thus τ , necessitates processing fewer photons per unit time, which may relax design requirements for the photodetector front end and associated electronics (Hobbs, 2011).

Extended T_2^* times can provide similar benefits to the MW-related aspects of the measurement. A standard Ramsey-type measurement protocol employs a MW $\pi/2$ -pulse before and after every free precession interval. If the length of each $\pi/2$ -pulse is held fixed, the time-averaged MW power and resulting heat load will scale as $1/T_2^*$. Additionally, higher T_2^* values can allow for more involved, longer-duration MW pulse sequences in place of simple $\pi/2$ -pulses to mitigate the effects of Rabi frequency inhomogeneities (Angerer *et al.*, 2015; Nöbauer *et al.*, 2015; Vandersypen and Chuang, 2005) or allow for other spin-manipulation protocols. Finally, higher T_2^* values could make exotic readout schemes that tend to have fixed time penalties experimentally feasible, such as spin to charge conversion readout (Shields *et al.*, 2015) (see Sec. IV.A) and ancilla-assisted repetitive readout (Jiang *et al.*, 2009; Lovchinsky *et al.*, 2016) (see Sec. IV.C).

B. Ensemble and single-spin T_2^*

As discussed previously, the dephasing time T_2^* is a critical parameter for broadband DC magnetometry. Importantly, T_2^* is defined differently for a single spin than for a spin ensemble. While an ensemble's T_2^* characterizes relative dephasing of the constituent spins, a single spin's T_2^* characterizes dephasing of the spin with itself, i.e., the distribution of phase accumulation from repeated measure-

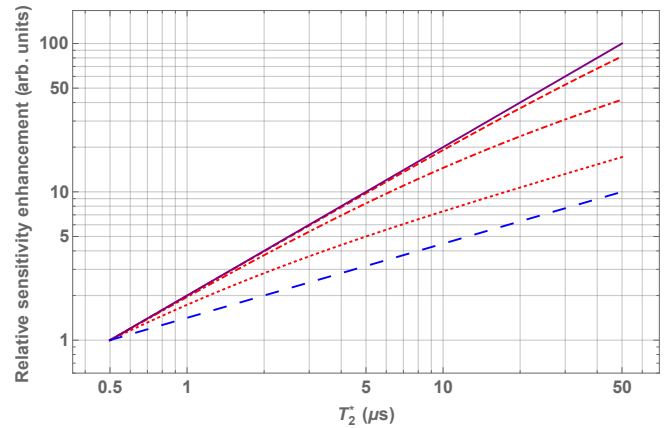


FIG. II.1 Sensitivity enhancement scaling with dephasing time T_2^* for a Ramsey-type magnetometer normalized to the same device with $T_2^* = 500$ ns. The different curves assume overhead times ($t_O = t_I + t_R$) of 1 μ s (\cdots), 10 μ s ($---$), and 100 μ s ($- \cdot -$). The sensitivity enhancement is bounded by either the fractional T_2^* improvement ($-$) or the square root ($---$) of the fractional T_2^* improvement. For simplicity the precession time τ is set to T_2^* . See Appendix A.2 for details on determining the optimal precession time.

Reference	No. NV ⁻ probed	t_I	t_R
(Shields <i>et al.</i> , 2015)	single	150 ns	-
(de Lange <i>et al.</i> , 2012)	single	600 ns	600 ns
(Hopper <i>et al.</i> , 2016)	single	1 μ s	200 ns
(Fang <i>et al.</i> , 2013)	single	2 μ s	300 ns
(Maze <i>et al.</i> , 2008)	single	2 μ s	324 ns
(Neumann <i>et al.</i> , 2009)	single	3 μ s	-
(Le Sage <i>et al.</i> , 2012)	ensemble	600 ns	300 ns
(Bauch <i>et al.</i> , 2018)	ensemble	20 μ s	-
(Wolf <i>et al.</i> , 2015)	ensemble	100 μ s	10 μ s
(Mrózek <i>et al.</i> , 2015)	ensemble	1 ms	-
(Jarmola <i>et al.</i> , 2012)	ensemble	1 ms	-

TABLE II.1 Initialization and readout times in the literature used for conventional optical readout of NV⁻ defects. In general, NV⁻ ensembles require longer initialization times than single NV⁻ defects, in part to account for the often non-uniform optical excitation intensity applied to the ensemble (Wolf *et al.*, 2015). Dashed lines (-) indicate values not reported.

ments on the spin over time (Ishikawa *et al.*, 2012; de Sousa, 2009). Since this work focuses on ensemble-based sensing, single-spin dephasing times are herein denoted T_2^{single} , while the term T_2^* is reserved for ensemble dephasing times.

Values of T_2^{single} are affected by slow magnetic, electric, strain, and temperature fluctuations. Variations in the magnetic environment may arise from dipolar interactions with an electronic or nuclear spin bath. The strength of these fluctuations can vary spatially throughout a sample due to the microscopically nonuniform distribution of bath spins. As a result, different NV⁻ centers in the same sample display different T_2^{single} values (Dobrovitski *et al.*, 2008; Hanson *et al.*, 2008, 2006; Ishikawa *et al.*, 2012). For ex-

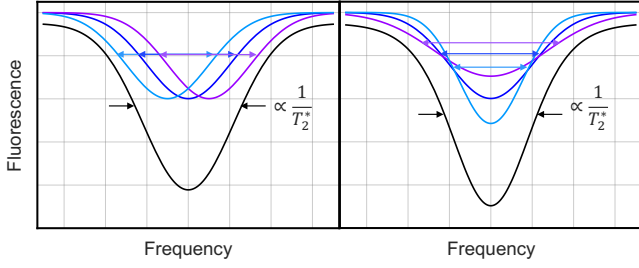


FIG. II.2 Contributions of individual spin resonances to the overall spin ensemble lineshape. The ensemble resonance lineshape (—) is broadened both by the distribution of line centers (left) and the distribution of linewidths (right) of the constituent spins (—, —, —).

ample, an NV^- spin in close proximity to several bath spins will experience faster dephasing than an NV^- spin many lattice sites away from the nearest bath spin.

Although ensemble T_2^* values are also influenced by spin-bath fluctuations, as discussed in Secs. II.D and II.F, an ensemble T_2^* value is not equal to the most common value of $T_2^*\{\text{single}\}$ within the ensemble. For one, the latter is limited by sources of zero-frequency noise that do not contribute to $T_2^*\{\text{single}\}$, such as spatially inhomogeneous magnetic fields, electric fields, strain, or g-factors (de Sousa, 2009). These inhomogeneities cause a spatially-dependent distribution of the single- NV^- resonance line centers, which broadens the ensemble resonance line and thus degrades T_2^* . Figure II.2 depicts broadening contributions to T_2^* from both varying single- NV^- line centers and varying single- NV^- linewidths ($\propto 1/T_2^*\{\text{single}\}$). The relative contribution to an ensemble's T_2^* value from these two types of broadening is expected to be sample-dependent. Although measurements in Ref. (Ishikawa et al., 2012) on a collection of single NV^- centers in a sparse sample found the distribution of line centers to be narrower than the median single- NV^- linewidth, such findings are not expected to hold generally.

However, even in the absence of static field inhomogeneities, the spin-bath-noise-limited T_2^* value of an ensemble is expected to be shorter than the most likely $T_2^*\{\text{single}\}$ value, as the ensemble value is strongly influenced by the small minority of NV^- centers with bath spins on nearby lattice sites (Dobrovitski et al., 2008). In fact, theoretical calculations in Refs. (Dobrovitski et al., 2008; Hall et al., 2014) reveal that single spins and ensembles interacting with surrounding spin baths exhibit free-induction-decay (FID) envelopes with different functional forms (see Appendices A.5 and A.7), a result borne out by experiments (Bauch et al., 2018; Bauch et al., 2019; Maze et al., 2012). In general, the ensemble T_2^* value cannot be predicted from $T_2^*\{\text{single}\}$ of any constituent spin (Dobrovitski et al., 2008), and application of single-spin measurements or theory to ensembles, or vice versa, should be done with great care.

C. Dephasing mechanisms

An NV^- ensemble's spin dephasing time T_2^* can be qualitatively expressed as

$$\frac{1}{T_2^*} \approx \frac{1}{T_2^*\{\text{electronic spin bath}\}} + \frac{1}{T_2^*\{\text{nuclear spin bath}\}} + \frac{1}{T_2^*\{\text{strain gradients}\}} + \frac{1}{T_2^*\{\text{electric field noise}\}} + \frac{1}{T_2^*\{\text{magnetic field gradients}\}} + \frac{1}{T_2^*\{\text{temperature variation}\}} + \frac{1}{T_2^*\{\text{unknown}\}} + \frac{1}{2T_1}, \quad (10)$$

where the symbol notation $T_2^*\{X\}$ denotes the limit to T_2^* solely due to mechanism X. Equation 10 assumes all mechanisms are independent and the associated dephasing rates add linearly. The second assumption is strictly only valid when all dephasing mechanisms lead to single-exponential free-induction-decay envelopes, (i.e., Lorentzian lineshapes); see Appendices A.5, A.7, and A.6. Here we briefly discuss each of these contributions to NV^- ensemble dephasing, and in later sections we examine their scaling, and how each mechanism may be mitigated.

The electronic spin bath consists of paramagnetic impurity defects in the diamond lattice, which couple to NV^- spins via magnetic dipolar interactions. The inhomogeneous spatial distribution and random instantaneous orientation of these bath spins cause dephasing of the NV^- spin ensemble (Bauch et al., 2018; Bauch et al., 2019; Dobrovitski et al., 2008; Hanson et al., 2008). Electronic spin bath dephasing can be broken down into contributions from individual constituent defect populations,

$$\frac{1}{T_2^*\{\text{electronic spin bath}\}} = \frac{1}{T_2^*\{\text{N}_S^0\}} + \frac{1}{T_2^*\{\text{NV}^-\}} + \frac{1}{T_2^*\{\text{NV}^0\}} + \frac{1}{T_2^*\{\text{other electronic spins}\}}. \quad (11)$$

Here $T_2^*\{\text{N}_S^0\}$ denotes the T_2^* limit from dephasing by paramagnetic substitutional nitrogen defects N_S^0 ($S = 1/2$), also called P1 centers, with concentration $[\text{N}_S^0]$ (Cook and Whiffen, 1966; Loubser and van Wyk, 1978; Smith et al., 1959). As substitutional nitrogen is a necessary ingredient for creation of NV^- centers, N_S^0 defects typically persist at concentrations similar to or exceeding NV^- (and NV^0) concentrations, and may account for the majority of electronic spin bath dephasing (Bauch et al., 2018). Sec. II.D examines $T_2^*\{\text{N}_S^0\}$ scaling with $[\text{N}_S^0]$. For NV^- -rich diamonds, dipolar interactions among NV^- spins may also cause dephasing of the ensemble, with associated limit $T_2^*\{\text{NV}^-\}$. Sec. II.G examines the $T_2^*\{\text{NV}^-\}$ scaling with $[\text{NV}^-]$ and other experimental parameters. In NV^- -rich diamonds, the neutral charge state NV^0 ($S = 1/2$) is also present at concentrations similar to $[\text{NV}^-]$ (Hartland, 2014), and may also contribute to dephasing, with limit $T_2^*\{\text{NV}^0\}$. The quantity $T_2^*\{\text{other electronic spins}\}$ encompasses dephasing from the remaining defects in the electronic spin bath, such as negatively charged single vacancies (Baranov et al., 2017), vacancy clusters (Iakubovskii and Stesmans, 2002; Twitchen

et al., 1999b) and hydrogen-containing defects (Edmonds *et al.*, 2012).

The quantity $T_2^*\{\text{nuclear spin bath}\}$ in Eqn. 10 describes NV⁻ ensemble dephasing from nuclear spins in the diamond lattice. In samples with natural isotopic abundance of carbon, the dominant contributor to nuclear spin bath dephasing is the ^{13}C isotope ($I = 1/2$), with concentration $[^{13}\text{C}] = 10700 \pm 800$ ppm (Wieser *et al.*, 2013), so that $T_2^*\{\text{nuclear spin bath}\} \approx T_2^*\{^{13}\text{C}\}$ (Balasubramanian *et al.*, 2009; Dréau *et al.*, 2012; Hall *et al.*, 2014; Zhao *et al.*, 2012). Other nuclear spin impurities exist at much lower concentrations and thus have a negligible effect on dephasing. The $T_2^*\{^{13}\text{C}\}$ scaling with concentration $[^{13}\text{C}]$ is discussed in Sec. II.F and can be minimized through diamond isotope engineering (Balasubramanian *et al.*, 2009; Teraji *et al.*, 2013).

Another major source of NV⁻ ensemble dephasing is non-uniform strain across the diamond lattice. Because strain shifts the NV⁻ spin resonances (Dolde *et al.*, 2011; Jamonneau *et al.*, 2016; Trusheim and Englund, 2016), gradients and inhomogeneities in strain may dephase the ensemble, limiting T_2^* . Strain may vary by more than an order of magnitude within a diamond sample (Bauch *et al.*, 2018), and can depend on myriad diamond synthesis parameters (Gaukroger *et al.*, 2008; Hoa *et al.*, 2014). For a given NV⁻ orientation along any of the $[111]$ diamond crystal axes, strain couples to the NV⁻ Hamiltonian approximately in the same way as an electric field (though with a different coupling strength) (Barson *et al.*, 2017; Doherty *et al.*, 2012; Dolde *et al.*, 2011) (see Appendix A.9 for further discussion). Thus, the quantity $T_2^*\{\text{strain gradients}\}$ may be separated into terms accounting for strain coupling along (\parallel) and transverse to (\perp) the NV⁻ symmetry axis,

$$\frac{1}{T_2^*\{\text{strain gradients}\}} = \frac{1}{T_2^*\{\text{strain}_{\parallel}\}} + \frac{1}{T_2^*\{\text{strain}_{\perp}\}}. \quad (12)$$

Application of a sufficiently strong bias magnetic field mitigates the transverse strain contribution to dephasing (Jamonneau *et al.*, 2016), (see Sec. III.D), while the longitudinal contribution may be canceled by employing double-quantum coherence magnetometry (see Sec. III.B).

Inhomogeneous and fluctuating electric fields also cause NV⁻ ensemble dephasing (Jamonneau *et al.*, 2016), with associated limit $T_2^*\{\text{electric field noise}\}$. This dephasing source may also be broken down into components longitudinal and transverse to the NV⁻ symmetry axis, and the contributions can be suppressed by the same methods as for strain-related dephasing.

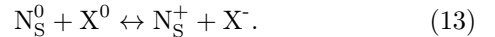
In addition, external magnetic field gradients may cause NV⁻ spin dephasing by introducing spatially-varying shifts in the NV⁻ energy levels across an ensemble volume, with associated limit $T_2^*\{\text{magnetic field gradients}\}$. Design of uniform bias magnetic fields minimizes this contribution to NV⁻ ensemble dephasing, and is largely an engineering challenge given that modern NMR magnets can exhibit sub-ppb uniformities over their cm-scale sample volumes (Vandersypen and Chuang, 2005).

Even though T_2^* is considered the *inhomogeneous* dephasing time, homogeneous time-varying electric and magnetic fields may mask as dephasing mechanisms if these fields fluctuate over the course of multiple interrogation/readout sequences. Such a scenario could result in the unfortunate situation where the measured value of T_2^* depends on the total measurement duration (see Sec. A.2). By the same argument, temperature fluctuations and spatial gradients can also mask as dephasing mechanisms and can artificially limit the measured T_2^* . Temperature variations cause expansion and contraction of the diamond crystal lattice, altering the NV⁻ center's zero-field splitting parameter D ($dD/dT = -74$ kHz/K (Acosta *et al.*, 2010a)) and may also shift the bias magnetic field. Finally, we include a term in Eqn. 10 for as-of-yet unknown mechanisms limiting T_2^* , and note that T_2^* is limited to a theoretical maximum value of $2T_1$ (Levitt, 2008; Myers *et al.*, 2017).

Importantly, Eqn. 10 shows that the value of T_2^* is primarily set by the dominant dephasing mechanism. Therefore, when seeking to extend T_2^* , one should focus on reducing whichever mechanism is dominant until another mechanism becomes limiting. Reference (O’Keeffe *et al.*, 2019) aptly expresses the proper strategy as a “shoot the alligator closest to the boat” approach. For example, if the dephasing due to substitutional nitrogen is decreased by $\sim 10\times$ in a physical experiment, the improvement in T_2^* may only be $2\times$ if, say, strain inhomogeneity becomes a limiting factor; at that point it becomes more fruitful to shift focus towards reducing strain-induced dephasing.

D. Nitrogen limit to T_2^*

In nitrogen-rich diamonds, the majority of electronic spins contributing to the spin bath originate from substitutional nitrogen defects, since N_{S}^0 may donate its unpaired electron to another defect X and become spinless N_{S}^+ , e.g., via the process (Khan *et al.*, 2009),



In these samples, the electronic spin concentration is closely tied to the total concentration of substitutional nitrogen donors $[\text{N}_{\text{S}}^{\text{T}}]$, and thus $T_2^*\{\text{electronic spin bath}\}$ is primarily set by $[\text{N}_{\text{S}}^{\text{T}}]$. In unirradiated nitrogen-rich diamonds, however, N_{S}^0 serves as the primary contributor to the electronic spin bath (Bauch *et al.*, 2018). The N_{S}^0 contribution to dephasing obeys

$$\frac{1}{T_2^*\{\text{N}_{\text{S}}^0\}} = A_{\text{N}_{\text{S}}^0} [\text{N}_{\text{S}}^0] \quad (14)$$

where $[\text{N}_{\text{S}}^0]$ is the concentration of neutral substitutional nitrogen, and $A_{\text{N}_{\text{S}}^0}$ characterizes the magnetic dipole interaction strength between NV⁻ spins and N_{S}^0 spins. The inverse linear scaling of $T_2^*\{\text{N}_{\text{S}}^0\}$ is supported by both theory (Abragam, 1983a; Bauch *et al.*, 2019; Taylor *et al.*, 2008; Wang and Takahashi, 2013; Zhao *et al.*, 2012), and experiment (Bauch *et al.*, 2018; Bauch *et al.*, 2019; van Wyk *et al.*, 1997). However, reported values of the scaling factor $A_{\text{N}_{\text{S}}^0}$ from theoretical spin-bath simulations vary

widely; for example, Ref. (Zhao *et al.*, 2012) predicts $A_{N_S^0} = 56 \text{ ms}^{-1}/\text{ppm}$, whereas Ref. (Wang and Taka-hashi, 2013) predicts $A_{N_S^0} = 560 \text{ ms}^{-1}/\text{ppm}$, a $10\times$ discrepancy. The authors of Ref. (Bauch *et al.*, 2018; Bauch *et al.*, 2019) measure $T_2^*\{N_S^0\}$ on five samples in the range $[N_S^0] = 0.75 - 60 \text{ ppm}$ (see Fig. II.3) and determine $A_{N_S^0} = 101 \pm 12 \text{ ms}^{-1}/\text{ppm}$, such that for a sample with $[N_S^0] = 1 \text{ ppm}$, $T_2^*\{N_S^0\} = 9.9 \pm 1.2 \mu\text{s}$. The experimental value of $A_{N_S^0}$ is consistent with numerical simulations in the same work (Bauch *et al.*, 2019). The authors calculate the second moment of the dipolar-broadened single NV⁻ ODMR linewidth (Abragam, 1983a,b) for 10^4 random spin bath configurations and, by computing the ensemble average over the distribution of single-NV⁻ linewidths (Dobrovitski *et al.*, 2008), find good agreement with the experimental value $A_{N_S^0} = 101 \text{ ms}^{-1}/\text{ppm}$.

Electron paramagnetic resonance (EPR) measurements of nitrogen N_S^0 defects in diamond (van Wyk *et al.*, 1997) from 63 samples also confirm the scaling $1/T_2^* \propto [N_S^0]$ (see Appendix A.6 and Fig. A.3) and the approximate scaling constant $A_{N_S^0}$. With the likely assumption that the dephasing time for ensembles of substitutional nitrogen spins in a nitrogen spin bath can approximate $T_2^*\{N_S^0\}$ for NV⁻ ensembles (Dale, 2015), (see Appendix A.6), the measurements in Ref. (van Wyk *et al.*, 1997) suggest $A_{N_S^0} \approx 130 \text{ ms}^{-1}/\text{ppm}$, which is in good agreement with the measured $A_{N_S^0} = 101 \pm 12 \text{ ms}^{-1}/\text{ppm}$ from Ref. (Bauch *et al.*, 2019) (see Appendices A.5 and A.6).

In addition, the data in Ref. (van Wyk *et al.*, 1997) suggest that dipolar dephasing contributions from ^{13}C at natural isotopic abundance (10700 ppm (Wieser *et al.*, 2013)) and from substitutional nitrogen are equal for $[N_S^0] = 10.8 \text{ ppm}$. The measured values of $A_{N_S^0}$ (Bauch *et al.*, 2018) and $A_{^{13}\text{C}}$ (see Sec. II.F) for NV⁻ ensembles predict the two contributions to be equal at $N_S^0 = 10.3 \text{ ppm}$, which is consistent to within experimental uncertainty.

In Appendix A.4, we present a simple toy model (Kleinsasser *et al.*, 2016) for the case when nitrogen-related defects dominate T_2^* . In this regime, under the assumption that the conversion efficiency of total nitrogen to NV⁻, NV⁰, and N⁺ are independent of the total nitrogen concentration $[N^T]$, the dephasing time T_2^* scales inverse-linearly with $[N^T]$, while the number of collected photons \mathcal{N} scales linearly with $[N^T]$. These scalings result in a shot-noise-limited sensitivity $\eta = 1/\sqrt{\mathcal{N} \cdot T_2^*}$, which is independent of $[N^T]$. However, as discussed in Sec. I.E and Appendix A.3, technical considerations favor lower nitrogen concentrations $[N^T]$, which result in lower photon numbers \mathcal{N} and longer dephasing times T_2^* (Kleinsasser *et al.*, 2016).

E. Nitrogen limit to T_2

Contributions to the NV⁻ spin dephasing time T_2^* from static and slowly-varying inhomogeneities are largely mitigated by employing a $\pi/2 - \pi - \pi/2$ Hahn echo pulse sequence (see Sec. III.A). In contrast to a $\pi/2 - \pi/2$ Ramsey sequence (see Appendix Sec. A.1.a), the added π -pulse re-

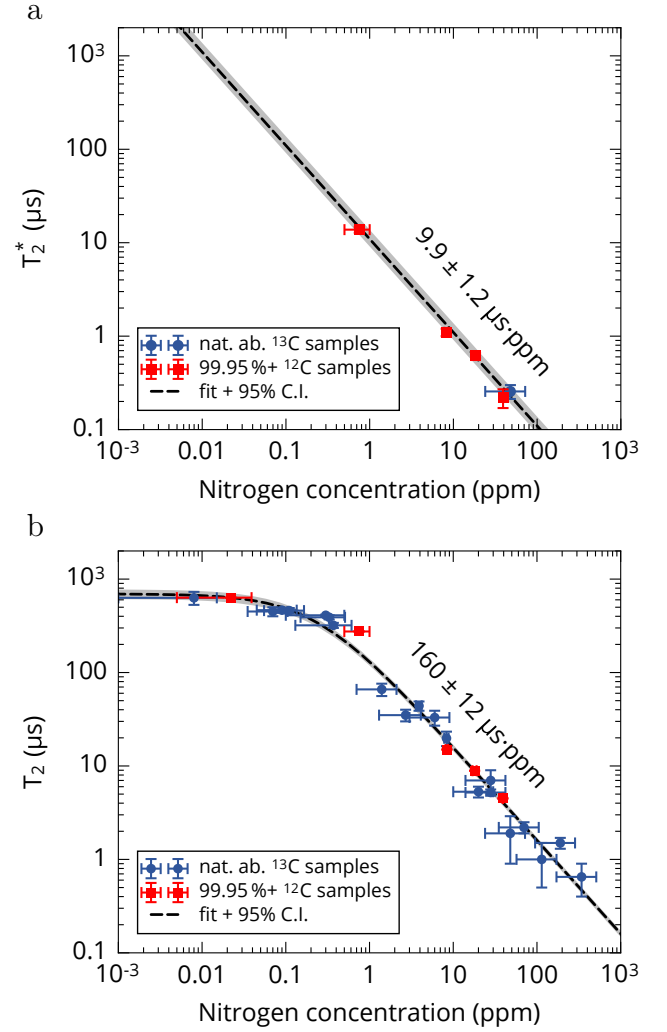


FIG. II.3 Substitutional nitrogen spin bath contribution to ensemble-NV⁻ dephasing time T_2^* and coherence time T_2 . a) Measured spin-bath contribution to T_2^* vs. nitrogen concentration measured by secondary ion mass spectrometry (SIMS) for five diamond samples. Fit yields $1/T_2^*\{N_S^0\} = A_{N_S^0}[N_S^0]$ with $A_{N_S^0} = 101 \pm 12 \text{ ms}^{-1}/\text{ppm}$. b) Measured Hahn echo T_2 vs. nitrogen concentration for 25 diamond samples. Fit yields $1/T_2\{N_S^0\} = B_{N_S^0}[N_S^0]$ with $B_{N_S^0}[N_S^0] = 6.25 \pm 0.47 \text{ ms}^{-1}/\text{ppm}$. Adapted from Ref. (Bauch *et al.*, 2019).

verses the precession direction of the sensor spins halfway through the free precession interval. As a result, any net phase accumulated by the NV⁻ spin state due to a static magnetic field vanishes, as the accumulated phase during the first interval (before the π -pulse) cancels the accumulated phase during the second interval (after the π -pulse). Consequently, the characteristic decay time of the NV⁻ spin state measured through Hahn echo, denoted by T_2 (the coherence time), is substantially longer than the inhomogeneous dephasing time T_2^* , typically exceeding the latter by one to two orders of magnitude (Bauch *et al.*, 2019; de Lange *et al.*, 2010). By design the Hahn echo sequence and its numerous extensions (Gullion *et al.*, 1990; Meiboom and Gill, 1958; Wang *et al.*, 2012) restrict sensing to AC

signals, typically within a narrow bandwidth, preventing their application in DC sensing experiments. Nonetheless, the Hahn echo T_2 plays a crucial role in diamond sample characterization and for AC sensing protocols (Sec. III.A), justifying discussion here.

Like T_2^* , T_2 depends on the nitrogen concentration $[N_S^0]$, which sets both the average dipolar-coupling strength between NV^- and nitrogen bath spins, (i.e., $A_{N_S^0}[N_S^0]$ from Eqn. 14), as well as the average coupling strength between nitrogen bath spins (Bar-Gill *et al.*, 2012; de Sousa, 2009). Furthermore, it can be shown that when nitrogen is the dominant decoherence mechanism, $T_2\{N_S^0\}$ depends inverse linearly on the nitrogen concentration $[N_S^0]$ (Bauch *et al.*, 2019), revealing a close relationship to $T_2^*\{N_S^0\}$. The dependence of $T_2\{N_S^0\}$ on $[N_S^0]$ was recently determined experimentally through NV^- ensemble measurements on 25 diamond samples (see Fig. II.3b), yielding (Bauch *et al.*, 2019)

$$\frac{1}{T_2\{N_S^0\}} = B_{N_S^0}[N_S^0]. \quad (15)$$

Here, $B_{N_S^0} = 6.25 \pm 0.47 \text{ ms}^{-1}/\text{ppm}$, such that an NV^- ensemble in a 1-ppm-nitrogen sample is expected to exhibit $T_2 \simeq 160 \pm 12 \text{ } \mu\text{s}$. The scaling in Eqn. 15 should also be compared to $T_2^*\{N_S^0\}$ (Eqn. 14), with $T_2\{N_S^0\}/T_2^*\{N_S^0\} = B_{N_S^0}/A_{N_S^0} \approx 17$. A straightforward application of these results is the calibration of the total nitrogen spin concentration in diamond samples through T_2^* measurements, T_2 measurements, or both, provided that nitrogen remains the primary source of dephasing and decoherence in such samples. Here, T_2 measurements should be advantageous over T_2^* (or linewidth) measurement schemes, as the latter are more likely to be limited by non-nitrogen dephasing mechanisms (Bauch *et al.*, 2018).

Lastly, we note that the inverse linear scaling of $T_2^*\{N_S^0\}$ and $T_2\{N_S^0\}$ with $[N_S^0]$, as well as the hierarchy $T_2 \gg T_2^*$, are consistent with earlier EPR studies of N_S^0 nitrogen defects in nitrogen-rich diamonds (Stepanov and Takahashi, 2016; van Wyk *et al.*, 1997) and other comparable spin systems in silicon (Abe *et al.*, 2010; Witzel *et al.*, 2010). A direct comparison of T_2 between the different spin systems, however, cannot easily be made and would require accounting for specifics of the different experimental techniques.

F. ^{13}C limit to T_2^*

Dipolar coupling between NV^- electronic and ^{13}C nuclear spins can also limit T_2^* (Balasubramanian *et al.*, 2009; Dobrovitski *et al.*, 2008; Hall *et al.*, 2014; Zhao *et al.*, 2012). Reducing the ^{13}C content below the natural abundance concentration $[^{13}\text{C}] = 10700 \pm 800 \text{ ppm} \approx 1.1\%$ (Wieser *et al.*, 2013) through isotope engineering is the most direct way to mitigate this effect (Balasubramanian *et al.*, 2009; Bauch *et al.*, 2018; Itoh and Watanabe, 2014). In the “dilute” spin limit where $[^{13}\text{C}]/[^{12}\text{C}] \ll 0.01$ (Kittel and Abrahams, 1953), the ^{13}C dephasing contribution is well-approximated

by

$$\frac{1}{T_2^*\{^{13}\text{C}\}} = A_{^{13}\text{C}}[^{13}\text{C}], \quad (16)$$

where $A_{^{13}\text{C}}$ is a constant characterizing the magnetic dipole interaction strength between NV^- spins and ^{13}C nuclear spins, in accordance with theoretical predictions (Abragam, 1983c; Dobrovitski *et al.*, 2008; Hall *et al.*, 2014; Kittel and Abrahams, 1953) (see Appendix section A.8). Although experimental measurements relating T_2^* to $[^{13}\text{C}]$ are only available for single NV^- centers (Balasubramanian *et al.*, 2009; Mizuochi *et al.*, 2009) and not for NV^- ensembles, the scaling in Eqn. 16 is consistent with experimental findings in a similar ensemble spin system; EPR linewidth measurements on substitutional phosphorus spin ensembles in a ^{28}Si crystal exhibit the same scaling for various dilute concentrations of ^{29}Si (Abe *et al.*, 2010; Morishita *et al.*, 2011). Figure 4b in Ref. (Abe *et al.*, 2010) suggests that Eqn. 16 is approximately valid for $[^{29}\text{Si}]/[^{28}\text{Si}] \lesssim 0.05$, so it is feasible that $A_{^{13}\text{C}}$ can be inferred from measurements on diamonds with natural ^{13}C isotopic abundance where $[^{13}\text{C}]/[^{12}\text{C}] \approx 0.0107$. We make this approximation henceforth.

While the value of $A_{^{13}\text{C}}$ is not known precisely for NV^- ensembles, T_2^* measurements in diamond with natural ^{13}C abundance set an approximate upper bound on $A_{^{13}\text{C}}$, since necessarily $1/T_2^* > 1/T_2^*\{^{13}\text{C}\}$. Figure II.4 shows a Ramsey FID for a diamond with natural ^{13}C abundance, which suggests $A_{^{13}\text{C}} \approx 0.100 \text{ ms}^{-1}/\text{ppm}$. With this value for $A_{^{13}\text{C}}$, the expected limit for a 99.999% ^{12}C isotopically enhanced diamond is $T_2^*\{^{13}\text{C}\} \approx 1 \text{ ms}$, making dephasing due to ^{13}C nuclear spins negligible compared to other dephasing mechanisms (see Eqn. 10). Comparing $A_{^{13}\text{C}}$ with the measured $A_{N_S^0} = 101 \text{ ms}^{-1}/\text{ppm}$ for dephasing of NV^- ensembles by substitutional nitrogen (see section II.D), dephasing from natural abundance $[^{13}\text{C}] = 10700 \text{ ppm}$ and substitutional nitrogen with concentration $[N_S^0] = 10.6 \text{ ppm}$ should be equivalent, in good agreement with Ref. (van Wyk *et al.*, 1997), which observes equivalence for $[N_S^0] \approx 10.8 \text{ ppm}$. Conveniently, it is easy to remember that $T_2^*\{^{13}\text{C}\}$ is $1 \text{ } \mu\text{s}$ for natural abundance ^{13}C diamond to better than 10%.

The bound on $A_{^{13}\text{C}}$ derived above can be crudely confirmed utilizing a mix of theoretical predictions from Ref. (Hall *et al.*, 2014) and data from Ref. (Maze *et al.*, 2012). The authors of Ref. (Maze *et al.*, 2012) find the most probable T_2^* for a single NV^- center in natural isotopic diamond to be $T_2^*\{\text{single,mp}\} = 1.8 \pm 0.6 \text{ } \mu\text{s}$ (measured in a 20 G bias field, Fig. 4a in Ref. (Maze *et al.*, 2012)). From relations in Ref. (Hall *et al.*, 2014) we estimate $A_{^{13}\text{C}} \approx 2.2 A_{^{13}\text{C}}^{\text{single,mp}}$, which yields $A_{^{13}\text{C}} = 0.11 \pm 0.04 \text{ ms}^{-1}/\text{ppm}$.

Our measured value $A_{^{13}\text{C}} \approx 0.100 \text{ ms}^{-1}/\text{ppm}$ is also in reasonable agreement with first-principles theoretical calculations by Ref. (Hall *et al.*, 2014), suggesting $A_{^{13}\text{C}} \approx 0.057 \text{ ms}^{-1}/\text{ppm}$ for NV^- ensembles in natural isotopic diamond in tens-of-gauss bias fields. Note that the experimental determination of $A_{^{13}\text{C}}$ outlined in this section represents an upper bound on the true value of $A_{^{13}\text{C}}$ in the dilute (dipolar-broadened) limit; if substantial broadening arises from Fermi-contact contributions in addition to dipolar in-

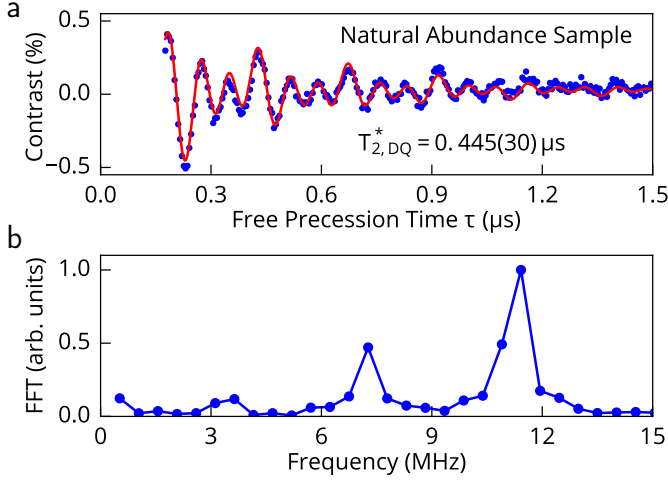


FIG. II.4 T_2^* measurement of a low-nitrogen-content diamond with natural abundance $[^{13}\text{C}] = 10700$ ppm to assess the ^{13}C contribution to dephasing. a) Double quantum Ramsey free induction decay (FID) (\bullet) and associated fit ($-$) suggest T_2^* is 445 ns in the double quantum basis. This data sets a bound $A_{13\text{C}} < 0.105 \text{ ms}^{-1}/\text{ppm}$. Correcting for the test diamond's approximately known $[\text{N}_\text{S}^0] \approx 0.5$ ppm content allows further refinement to $A_{13\text{C}} \approx 0.100 \text{ ms}^{-1}/\text{ppm}$. b) Fourier transform of the FID shown in the top panel. The three peaks arise from hyperfine interactions associated with the NV^- center's ^{14}N nuclear spin $I = 1$ and exhibit intra-peak spacing double that of an equivalent single-quantum Ramsey measurement. The unbalanced peak heights are attributed to nuclear spin polarization induced by the 150 gauss bias magnetic field.

teractions in natural abundance ^{13}C samples, or if $[^{13}\text{C}] = 10700$ ppm does not qualify as the dilute limit (Abragam, 1983c; Kittel and Abrahams, 1953), the value of $A_{13\text{C}}$ given here will be overestimated.

Engineering diamonds for low ^{13}C content may be challenging (Dwyer *et al.*, 2013; Markham *et al.*, 2011; Teraji *et al.*, 2013). The isotopic purity of a diamond grown by plasma-enhanced chemical vapor deposition (PE-CVD) is expected to be limited by the purity of the carbon source gas, which is most commonly methane (CH_4). However, diamonds grown with isotopically enriched methane may exhibit higher fractional ^{13}C content than the source gas due to extraneous carbon sources in the CVD chamber (Dwyer *et al.*, 2013). Nonetheless, Teraji *et al.* achieve $[^{12}\text{C}] = 99.998\%$ as measured by secondary ion mass spectrometry (SIMS) when using isotopically-enhanced methane with 99.999% ^{12}C (i.e., $[^{13}\text{C}] \leq 10$ ppm) (Teraji *et al.*, 2013, 2015). Although such isotopically enhanced methane is currently $10^3 - 10^4$ times more expensive than natural abundance CH_4 , order unity conversion of the methane's carbon content into diamond is attainable (Teraji *et al.*, 2013).

G. NV^- limit to T_2^*

Dipolar interactions among negatively-charged NV^- centers may also limit the dephasing time T_2^* . Dephasing from NV^- - NV^- interactions arises from NV^- spins in both the same and different groups as the NV^- centers used for sens-

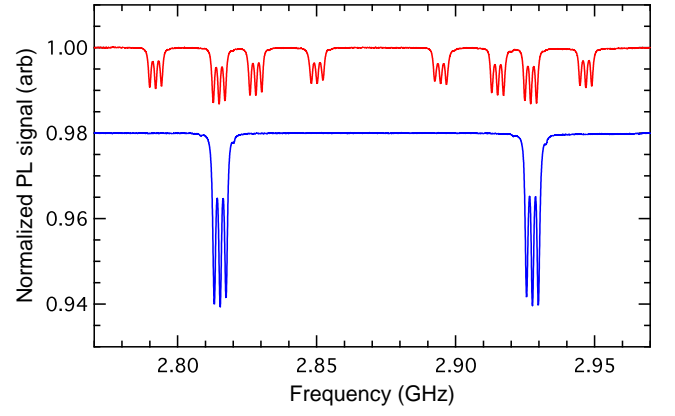


FIG. II.5 ODMR spectra from the same NV^- ensemble in different applied bias magnetic fields. A bias field with a different projection on each of the four NV^- crystallographic orientations separates the $m_s = 0 \leftrightarrow m_s = \pm 1$ spin resonances into distinct groups ($-$). A bias field that projects equally onto all four orientations overlaps the spin resonances ($-$, offset for clarity).

ing, where groups are defined as follows: NV^- centers with approximately the same spin resonance frequency are considered to be in the same group, whereas spins with different resonance frequencies are in different groups (Kucsko *et al.*, 2018). Depending on the strength and angle of the applied bias field, the spin resonances of the four NV^- orientations may be spectrally separated, or two or more may be overlapped, changing the fraction of NV^- spins in the same group (see Fig. II.5). The NV^- - NV^- dipolar contribution to T_2^* is then given by

$$\frac{1}{T_2^*\{\text{NV}^-\}} = \frac{1}{T_2^*\{\text{NV}^-\}_\parallel} + \frac{1}{T_2^*\{\text{NV}^-\}_\#} \quad (17)$$

$$= \varsigma_\parallel A_{\text{NV}_\parallel} [\text{NV}_\parallel] + \varsigma_\# A_{\text{NV}_\#} [\text{NV}_\#].$$

Here the constants A_{NV_\parallel} and $A_{\text{NV}_\#}$ characterize the dipolar interaction strength for pairs of NV^- centers in the same group and different groups respectively; $[\text{NV}_\parallel]$ is the concentration of NV^- spins in the group being used for sensing and $[\text{NV}_\#]$ is the concentration of NV^- spins in other groups, with $[\text{NV}_\parallel] + [\text{NV}_\#] = [\text{NV}_\text{total}]$; and ς_\parallel and $\varsigma_\#$ are dimensionless factors of order unity accounting for (imperfect) initialization of NV^- centers (Doherty *et al.*, 2013). For example, off-resonant NV^- populations polarized into the spinless $m_s = 0$ state during initialization should not contribute to dephasing of the NV^- centers used for sensing, giving $\varsigma_\# \approx 0$.

Flip-flop interactions between NV^- spins in different groups are off-resonant and are thus suppressed, whereas flip-flop interactions can occur resonantly between spins in the same group. The extra interaction terms in the dipole-dipole Hamiltonian for spins in the same group result in a slightly increased dephasing rate (Abragam, 1983a; Kucsko *et al.*, 2018). Following Ref. (Abragam, 1983a), it is expected that $A_{\text{NV}_\parallel} = 3/2 A_{\text{NV}_\#}$.

The lack of published data at present for $T_2^*\{\text{NV}^-\}$ in samples with varying NV^- concentration prevents definitive

determination of $A_{\text{NV}\parallel}$ and $A_{\text{NV}\perp}$. However, both terms can be estimated from the experimentally determined value of $A_{\text{N}_\text{S}^0} = 101 \pm 12 \text{ ms}^{-1}/\text{ppm}$ (Bauch *et al.*, 2019), which describes the scaling of NV^- ensemble T_2^* with substitutional nitrogen concentration (see Sec. II.D). Assuming an NV^- electronic spin bath couples to NV^- sensor spins with approximately the same strength as a substitutional nitrogen spin bath (Hanson *et al.*, 2008), and accounting for the higher spin multiplicity of NV^- centers ($S_{\text{NV}^-} = 1$) compared to substitutional nitrogen spins ($S_{\text{N}_\text{S}^0} = 1/2$), we calculate (Abragam, 1983a)

$$\begin{aligned} A_{\text{NV}\perp} &\simeq \sqrt{\frac{S_{\text{NV}^-}(S_{\text{NV}^-} + 1)}{S_{\text{N}_\text{S}^0}(S_{\text{N}_\text{S}^0} + 1)}} A_{\text{N}_\text{S}^0} \\ &\simeq \sqrt{8/3} A_{\text{N}_\text{S}^0} \\ &\simeq 165 \text{ ms}^{-1}/\text{ppm} \end{aligned} \quad (18)$$

and find $A_{\text{NV}\parallel} = 3/2 A_{\text{NV}\perp} \simeq 247 \text{ ms}^{-1}/\text{ppm}$. Although the value of $T_2^*\{\text{NV}\}$ depends on experimental conditions including optical initialization fraction (determining ς_{\parallel} and ς_{\perp}) and bias magnetic field orientation (setting the ratio $[\text{NV}\parallel]/[\text{NV}\perp]$), the value of $T_2^*\{\text{NV}\}$ for a given NV^- concentration is well approximated (up to a factor of order unity) by the dephasing time $T_2^*\{\text{N}_\text{S}^0\}$ for the same concentration of N_S^0 spins.

Magnetometer operation in the NV^- - NV^- interaction limit may occur as the N-to- NV^- conversion efficiency E_{conv} approaches its theoretical limit of 50% (Felton *et al.*, 2009; Pham *et al.*, 2011) (see Sec. V.A). Under these circumstances, and when other sources of dephasing can be neglected - such as magnetic, electric, and strain gradients as well as ^{13}C nuclear spins (see Sec. II.F) and other paramagnetic defects (see Sec. V.F) - the interaction among NV^- spins becomes the dominant source of dephasing. However, maximal N-to- NV^- conversion efficiency is not necessarily required to operate in the NV^- - NV^- interaction limit. When $E_{\text{conv}} < 50\%$, dephasing due to other paramagnetic impurities may be reduced through spin bath driving techniques described in Sec. III.C. Spin bath driving can also decouple the NV^- centers in different groups from the NV^- centers in the group used for sensing (Bauch *et al.*, 2018), mitigating the second term in Eqn. 17 ($1/T_2^*\{\text{NV}\}_{\perp}$), and leaving only the first term ($1/T_2^*\{\text{NV}\}_{\parallel}$) as a fundamental limit to NV^- ensemble T_2^* .

While this section has focused on the negatively charged NV^- center, NV centers are also present in the neutral charge state NV^0 ($S = 1/2$) (see Sec. V.A). As NV^0 has not been observed in its ground state in EPR, an effect tentatively attributed to resonance line broadening from dynamic Jahn-Teller distortion (Felton *et al.*, 2008), magnetic noise created by NV^0 may be reduced by a motional-narrowing-type effect to less than otherwise expected for a $S = 1/2$ defect (see Sec. III.C). Consequently, the contribution of NV^0 spins to dephasing of NV^- spins, may be smaller than expected. What little, if any, NV^+ present in the sample is expected to be spinless (see Table V.4) and should not contribute substantially to dephasing.

Recently, several protocols have been theoretically proposed to mitigate strong NV^- - NV^- dipolar interactions and extend T_2^* (O’Keeffe *et al.*, 2019) or T_2 (Choi *et al.*, 2017b) while retaining magnetic field sensitivity. In addition, it has been proposed that under certain circumstances the NV^- - NV^- dipolar interaction could enhance magnetometry sensitivity through enabling entanglement of multiple NV^- centers (Choi *et al.*, 2017) (see Sec. VI.D). Harnessing entanglement could enable superior scaling of measurement SNR with number of spins addressed N , exceeding the standard quantum limit $\text{SNR} \propto \sqrt{N}$ and approaching the Heisenberg limit, $\text{SNR} \propto N$. Controlled coupling of NV^- spin pairs (Bernien *et al.*, 2013; Dolde *et al.*, 2013; Hensen *et al.*, 2015; Jakobi *et al.*, 2016; Neumann *et al.*, 2010b; Yamamoto *et al.*, 2013a) has been demonstrated; however, applying entanglement-enhanced techniques to larger ensembles is expected to be challenging.

III. METHODS TO EXTEND T_2^* AND T_2

A. Dynamical decoupling for AC magnetometry

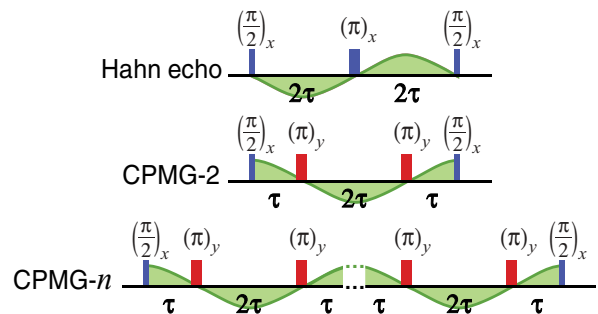


FIG. III.1 Select pulse sequences for AC magnetometry. The Hahn echo sequence includes a refocusing π -pulse midway through the spin interrogation time, allowing phase-sensitive lock-in-type measurements of AC magnetic fields (top). Hahn echo is maximally sensitive to AC fields with nodes coincident with the three MW pulses. Detection of AC fields with the quadrature phase can be achieved using the Carr-Purcell-Meiboom-Gill-2 (CPMG-2) sequence (middle). Employing additional π -pulses (CPMG- n) achieves more efficient decoupling of the NV^- from substitutional nitrogen and other paramagnetic defects in the diamond and provides sensitivity to higher-frequency AC magnetic fields (bottom). From Ref. (Pham *et al.*, 2012a).

While this review primarily addresses the broadband DC sensing modality of ensemble- NV^- magnetometers, many of the sensitivity-improvement techniques described herein can also be applied to detecting narrowband AC magnetic fields. Here we provide a brief overview of standard AC sensing schemes; we discuss several approaches to improving AC magnetic field sensitivity; and we highlight challenges unique to the AC sensing modality.

The Hahn echo (alternatively referred to as the spin echo) protocol, shown in Fig. III.1, builds upon the Ramsey protocol with an additional central MW π -pulse, which refo-

cuses dephasing of the NV⁻ spin ensemble (Hahn, 1950). The decay of spin coherence measured with this pulse sequence is characterized by T_2 , which is typically one to two orders of magnitude longer than T_2^* in NV⁻ ensemble measurements (see Secs. II.C, II.D, and II.E). Furthermore, while the refocusing pulse decouples the NV⁻ spin from DC magnetic fields, its presence makes Hahn echo measurements particularly sensitive to oscillating magnetic fields with period T_B matching the spin interrogation time τ of the pulse sequence. In the ideal case where the three MW pulses are commensurate with the nodes of the AC magnetic field, the shot-noise-limited sensitivity of a Hahn-echo-based measurement is given by (Pham, 2013):

$$\eta_{\text{echo}}^{\text{shot}} \approx \frac{\pi}{2} \frac{\hbar}{g_e \mu_B} \frac{1}{C e^{-(\tau/T_2)^p} \sqrt{\mathcal{N}}} \frac{\sqrt{t_I + \tau + t_R}}{\tau}, \quad (19)$$

where C is the measurement contrast prior to precession (see Sec. I.C), p is a stretched exponential parameter set by ensemble averaging of the local NV⁻ spin environments (see Appendix A.7), and t_I and t_R are the optical initialization and readout times, respectively. For more realistic measurements in which the pulse sequence cannot be phase-locked to the AC magnetic field, the magnetic sensitivity is degraded by $\sqrt{2}$.

The shot-noise-limited sensitivity given by Eqn. 19 has several key differences to that of a Ramsey-based DC sensing protocol (Eqn. 7). First, since typically $T_2 \gg T_2^*$, AC sensing schemes can achieve better sensitivity than DC sensing schemes. Second, choice of spin interrogation time τ is more straightforward for Ramsey schemes than for echo-based schemes. For Ramsey-based sensing of DC or quasi-static fields, $\tau \sim T_2^*$ is optimal (Appendix A.2). In contrast, while $\tau \sim T_2$ is optimal for Hahn-echo-based protocols, τ should also be matched to the period T_B of the AC magnetic field to be measured. As a result the scheme is maximally sensitive to fields of period $T_B \sim T_2$, with a detection bandwidth set by the relevant filter function (Cywiński *et al.*, 2008). Finally, coherent interactions between the NV⁻ spin and other spin impurities in the diamond can modulate the Hahn-echo coherence envelope. At best, these effects introduce collapses and revivals that do not affect T_2 and merely complicate the NV⁻ magnetometer's ability to measure AC magnetic fields of arbitrary frequency. Collapse-and-revival dynamics occur for diamond samples containing a natural abundance of ^{13}C , when the bias magnetic field is aligned to the NV⁻ symmetry axis such that the ^{13}C Larmor precession sets the oscillation frequency. At worst, misalignment between the bias magnetic field and different NV⁻ symmetry axes results in anisotropic hyperfine interactions, which can enhance the nuclear-spin Larmor precession rate for both ^{13}C (as a function of ^{13}C -NV⁻ spacing) and ^{15}N (in ^{15}N -NV-diamonds) (Childress *et al.*, 2006; Maurer *et al.*, 2010). These effects ensemble average to an effectively shorter coherence time T_2 (Stanwix *et al.*, 2010), which degrades AC sensitivity.

Despite these differences, the Ramsey and spin-echo measurement schemes share many of the same components; consequently, many techniques for improving spin readout

fidelity (analyzed in Sec. IV) apply to both DC and AC sensing modalities. For example, ancilla-assisted repetitive readout (Sec. IV.C), level-anticrossing-assisted readout (Sec. IV.D), and improved fluorescence collection methods (Sec. IV.E) increase the number of detected photons per measurement \mathcal{N} ; preferential NV⁻ orientation (Sec. V.G) enhances the measurement contrast C ; and spin-to-charge-conversion (SCC) readout (Sec. IV.A) and NV⁻ charge state optimization (Sec. V.B) increase both C and \mathcal{N} . We note that because typically $T_2 \gg T_2^*$, advanced readout techniques such as repetitive readout and SCC readout presently offer greater sensitivity improvement for AC schemes than for DC schemes, as their long-readout-time requirements introduce smaller fractional overhead in AC measurements with longer spin interrogation times.

Additionally, techniques to extend T_2^* for DC and broadband magnetometry may also improve AC magnetic field sensitivity. For example, double-quantum (DQ) coherence magnetometry (Sec. III.B) is expected to improve AC sensitivity both by introducing a $2\times$ increase in the NV⁻ spin precession rate (Fang *et al.*, 2013; Mamin *et al.*, 2014) and, in certain cases, by extending the NV⁻ coherence time T_2 (Angerer *et al.*, 2015). Similarly, spin bath driving (Sec. III.C) and operation at a sufficiently strong bias magnetic field (Sec. III.D) may extend T_2 by suppressing magnetic and electric/strain noise, respectively.

Another technique for enhancing NV⁻ magnetic sensitivity, unique to the AC sensing modality, is the application of multi-pulse sequences, whose timing is based on the Carr-Purcell-Meiboom-Gill (CPMG) family of pulse sequences well-known in NMR (Cywiński *et al.*, 2008; Pham, 2013) (see Fig. III.1). By applying additional MW π -pulses at a rate of $\frac{1}{2T_B}$, these multi-pulse sequences (i) extend the NV⁻ coherence time T_2 by more effectively decoupling the NV⁻ spins from magnetic noise and (ii) increase the time during which the NV⁻ spins interrogate the AC magnetic field. The coherence time has been found to scale with a power law s ($T_2 \rightarrow T_2^{(k)} = T_2 k^s$) as a function of the number of pulses k (Pham *et al.*, 2012a), where s is set by the noise spectrum of the decohering spin bath and is typically sub-linear. For example, a bath of electronic spins, such as N_S^0 defects in diamond, exhibits a Lorentzian noise spectrum and results in a power-law scaling of the coherence time with $s = 2/3$, when the electronic spin bath is the dominant decoherence source (de Sousa, 2009). The shot-noise-limited multi-pulse sensitivity and the optimal number of pulses k_{opt} for an AC magnetic field with period T_B are given by

$$\eta_{\text{multi}}^{\text{shot}} \approx \frac{\pi \hbar}{2 g_e \mu_B} \frac{1}{C \sqrt{\mathcal{N}}} \exp \left[\left(\frac{k^{(1-s)} T_B}{2 T_2} \right)^p \right] \frac{1}{\sqrt{\frac{k}{2} T_B}}, \quad (20)$$

$$k_{\text{opt}} = \left[\frac{1}{2p(1-s)} \left(\frac{2 T_2}{T_B} \right)^p \right]^{\frac{1}{p(1-s)}}, \quad (21)$$

assuming interrogation time $\tau = \frac{k}{2} T_B$, initialization and readout times $t_I, t_R \lesssim \tau$, and π -pulses commensurate with the nodes of the oscillating magnetic field. As before, the

sensitivity is degraded by $\sqrt{2}$ when measuring AC magnetic fields with unknown or randomly fluctuating phase.

Equations 20 and 21 illustrate that multi-pulse measurement schemes improve sensitivity to magnetic fields with periods $T_B < T_2$ and enable sensing of higher frequencies than can be accessed with Hahn-echo-based measurements. For example, in Ref. (Pham *et al.*, 2012a), Pham *et al.* demonstrate a $10\times$ improvement in ensemble AC sensitivity at 220 kHz by using a multi-pulse sequence, compared to Hahn echo. However, the increased number of control pulses, which are typically imperfect due to NV⁻ hyperfine structure and inhomogeneities in the system, can result in cumulative pulse error and thus degraded AC sensitivity (Wang *et al.*, 2012). Compensating pulse sequences, including schemes in the XY-, concatenated, and BB- n families, may then be employed to restore AC field sensitivity (Farfurnik *et al.*, 2015; Gullion *et al.*, 1990; Low *et al.*, 2014; Rong *et al.*, 2015; Wang *et al.*, 2012).

A final consideration in the application of multi-pulse sequences for enhancing AC magnetometry with NV⁻ centers is that extension of the T_2 coherence time (and thus enhancement of AC magnetic field sensitivity) is eventually limited by the T_1 spin-lattice relaxation time, beyond which increasing the number of π -pulses is ineffective. This limitation can be overcome by reducing the magnetometer operating temperature, thereby suppressing the two-phonon Raman process that dominates NV⁻ spin-lattice relaxation near room temperature and extending T_1 (Jarmola *et al.*, 2012). Multi-pulse sequences performed at 77 K have demonstrated $> 100\times$ extensions in T_2 compared to room temperature measurements (Bar-Gill *et al.*, 2013), and corresponding improvements to AC magnetic field sensitivity are expected.

B. Double-quantum coherence magnetometry

Standard NV⁻ magnetometry techniques, such as CW-ODMR (Sec. I.D.1), pulsed ODMR (Sec. I.D.2), and pulsed Ramsey or echo-type schemes (Sec. III.A), are typically performed in the pseudo-spin- $1/2$ *single-quantum* (SQ) sub-basis of the NV⁻ ground state, with the $m_s = 0$ and either the $m_s = +1$ or $m_s = -1$ spin state ($\Delta m_s = 1$) employed for sensing. In contrast, *double-quantum* (DQ) coherence magnetometry ($\Delta m_s = 2$) works as follows for a Ramsey-type implementation. First, a superposition of both $m_s = +1$ and $m_s = -1$ states (here termed the bright state $|B\rangle$) is prepared. Then, after a free precession interval, the final superposition state is projected onto a population difference between $|0\rangle$ and $|B\rangle$, and the population is read out optically.

Use of the full spin-1 nature of the NV⁻ center and the double-quantum basis $\{-1, +1\}$ allows for several sensing advantages. First, at fixed magnetic field, an NV⁻ spin prepared in a superposition of the $m_s = +1$ and $m_s = -1$ states precesses at twice the rate as in the standard $\{0, \pm 1\}$ basis, enabling enhanced magnetometer sensitivity. Moreover, measurements in the DQ basis are differential, in that noise sources perturbing the $|0\rangle \leftrightarrow | + 1\rangle$ and $|0\rangle \leftrightarrow$

$| - 1\rangle$ transitions in common-mode are effectively rejected. Sources of common-mode noise may include temperature fluctuations, which enter the NV⁻ Hamiltonian via the zero-field splitting parameter D ($\frac{\partial D}{\partial T} \approx -74$ kHz/K) (Acosta *et al.*, 2010a; Kucsko *et al.*, 2013; Toyli *et al.*, 2013); axial strain gradients; axial electric fields; and transverse magnetic fields. For a detailed discussion see Ref. (Bauch *et al.*, 2018).

If the spin bath environment is dominated by magnetic noise, as is common for high-nitrogen and natural ^{13}C abundance diamond samples, measurements in the DQ basis exhibit an increased linewidth and shortened associated dephasing time, as the $2\times$ enhanced sensitivity to magnetic fields causes the spin ensemble to dephase twice as quickly as in the SQ basis, i.e., $T_{2,\text{DQ}}^* \approx T_{2,\text{SQ}}^*/2$. This increased dephasing and decoherence is confirmed experimentally for single NV⁻ centers by the authors of Ref. (Fang *et al.*, 2013), who observe a $2\times$ decrease in T_2^* , and by the authors of Ref. (Mamin *et al.*, 2014), who observe a $\approx 2\times$ decrease in the Hahn-echo coherence time T_2 . Similar results are reported for NV⁻ ensembles (Bauch *et al.*, 2018; Kucsko *et al.*, 2018).

Non-magnetic noise sources such as temperature fluctuations, electric field noise, and inhomogeneous strain may also contribute to spin dephasing (see Sec. II.C). However, measurements in the DQ basis are insensitive to noise sources that shift the $|0\rangle \leftrightarrow | + 1\rangle$ and $|0\rangle \leftrightarrow | - 1\rangle$ spin transitions in common mode. When such noise sources dominate dephasing in the standard basis, the DQ dephasing time $T_{2,\text{DQ}}$ may exceed $T_{2,\text{SQ}}$, allowing for additional sensitivity improvement. For example, DQ measurements reported in Ref. (Bauch *et al.*, 2018) on NV⁻ ensembles demonstrate a $\sim 6\times$ increase in T_2^* (narrowing of linewidth) in an isotopically purified, low-nitrogen diamond, leading to an effective $13\times$ enhancement in phase accumulation per measurement when considering the twice faster precession rate in the DQ basis. In Ref. (Bauch *et al.*, 2018), the standard SQ basis T_2^* is found to be limited by strain inhomogeneities, whereas the T_2^* value measured in the DQ basis is likely primarily limited by interactions with residual ^{13}C nuclear spins (~ 100 ppm). This T_2^* limitation emphasizes the importance of isotopic purification when low-nitrogen samples are employed (see Sec. II.F).

For AC magnetometry, dephasing due to strain inhomogeneities and temperature fluctuations can be largely alleviated by using Hahn echo or similar dynamical decoupling sequences (see Sec. III.A) (Pham, 2013). Nevertheless, double-quantum coherence magnetometry should still yield benefits. First, ensemble AC magnetometry benefits from the expected $\sqrt{2}\times$ sensitivity gain due to twice faster precession (Fang *et al.*, 2013). Second, sensitivity may be further enhanced if $T_{2,\text{DQ}}$ exceeds $T_{2,\text{SQ}}/2$. For example, the authors of Ref. (Angerer *et al.*, 2015) observe $T_{2,\text{SQ}} = 1.66 \pm 0.16$ ms and $T_{2,\text{DQ}} = 2.36 \pm 0.09$ ms for single near-surface NV⁻ center with $T_{2,\text{SQ}}$ likely limited by electric field noise. In addition to magnetic sensing, measurements in the DQ basis can enhance sensitivity for temperature sensing (Toyli *et al.*, 2013) and noise spectroscopy applications (Kim *et al.*, 2015; Myers *et al.*, 2017).

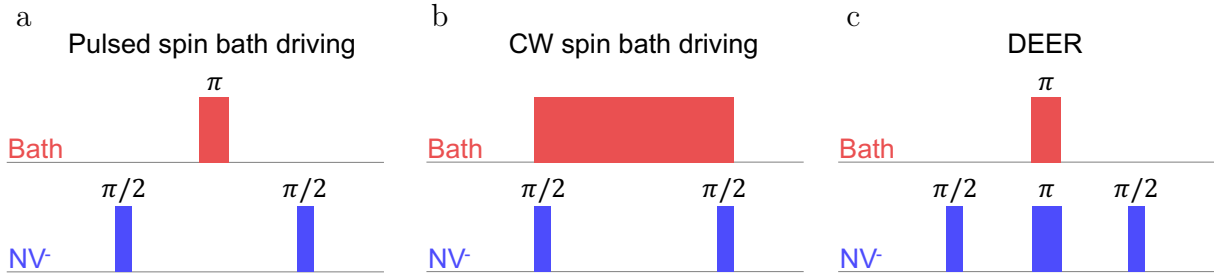


FIG. III.2 Selected pulse sequences for concurrent manipulation of NV^- spins and the surrounding paramagnetic spin bath. a) Pulsed spin bath driving protocol combining a Ramsey sequence on the NV^- center(s) with a central RF π -pulse on the spin bath. b) Continuous spin bath driving protocol combining a Ramsey sequence with continuous resonant RF spin bath drive. c) Double electron-electron resonance (DEER) protocol consisting of a Hahn echo sequence performed on the NV^- center(s) combined with a resonant RF π -pulse performed on the spin bath. Recreated from Ref. (Bauch *et al.*, 2018).

Implementation of double-quantum coherence magnetometry is a straightforward addition to standard pulsed magnetometry. The DQ technique requires applying MW pulses to drive transitions from the $m_s = 0$ state to both the $m_s = +1$ and $m_s = -1$ states. For sufficiently large magnetic fields, these two transitions must be addressed with separate and phase-locked MW frequencies (Angerer *et al.*, 2015; Mamin *et al.*, 2014). At low magnetic, electric, and strain fields, a single MW frequency is adequate (Fang *et al.*, 2013). In either case, care must be taken to ensure that both the upper and lower spin transitions are addressed with adequate MW pulses to achieve an equal superposition of the $m_s = +1$ and $m_s = -1$ states (Bauch *et al.*, 2018; Mamin *et al.*, 2014). While equal Rabi frequencies on the two transitions are desirable, the MW pulse durations may be adjusted to compensate for unequal Rabi frequencies. MW pulses for each spin transition may be applied sequentially (Toyli *et al.*, 2013) or simultaneously (Bauch *et al.*, 2018; Fang *et al.*, 2013; Mamin *et al.*, 2014). Due to the minimal increase in experimental complexity, the ability to suppress common-mode noise sources, and the increased spin precession rate, we expect DQ coherence magnetometry to become standard for high-performance pulsed-measurement DC magnetometers employing NV^- ensembles.

C. Spin bath driving

Residual paramagnetic impurity spins in diamond contribute to NV^- dephasing, thereby reducing T_2^* . This effect can be mitigated by directly driving the impurity spins, which is particularly useful when dynamical decoupling (see Sec. III.A) of the NV^- sensor spins is not applicable, such as in DC sensing protocols. This technique, termed spin bath driving, has been successfully demonstrated with substitutional nitrogen spins N_S^0 ($S = 1/2$) (Bauch *et al.*, 2018; Knowles *et al.*, 2013; de Lange *et al.*, 2012), and, due to the high typical concentrations of N_S^0 spins in NV-rich diamonds, we focus our discussion on this implementation.

In pulsed spin bath driving (see Fig. III.2a), a resonant π -pulse is applied to the N_S^0 spins halfway through the

NV^- Ramsey sequence, decoupling the N_S^0 spins from the NV^- spins in analogy with a refocusing π -pulse in a spin echo sequence (see Fig. III.1) (Bauch *et al.*, 2018; de Lange *et al.*, 2012). Alternatively, the spin bath can be driven continuously (see Fig. III.2b) (Bauch *et al.*, 2018; Knowles *et al.*, 2013; de Lange *et al.*, 2012). In the latter case, the driving Rabi frequency Ω_N must significantly exceed the NV^- - N_S^0 coupling rate γ_N , i.e., satisfy $\Omega_\text{N}/\gamma_\text{N} \gg 1$, to achieve effective decoupling. Under this condition, the nitrogen spins undergo many Rabi oscillations during the characteristic dipolar interaction time $1/\gamma_\text{N}$, where $\gamma_\text{N} \sim 2\pi \times (0.01 - 10)$ MHz for nitrogen concentrations in the 1 – 1000 ppm range (see Sec. II.D). As a result, the NV^- ensemble is decoupled from the nitrogen spin bath and the NV^- dephasing time is enhanced. This situation is similar to motional narrowing observed in many NMR and ESR systems, such as rotation- and diffusion-induced time-averaging of magnetic field inhomogeneities (Abragam, 1983c; Slichter, 1990).

The authors of Ref. (de Lange *et al.*, 2012) perform pulsed spin bath driving in a Type Ib diamond with $[\text{N}^\text{T}] \lesssim 200$ ppm and increase T_2^* for a single NV^- 1.6 \times , from 278 ns to 450 ns. Similarly, in Ref. (Knowles *et al.*, 2013), T_2^* for an individual NV^- is extended from 0.44 μs to 1.27 μs , a 2.9 \times improvement, using continuous spin bath driving in nanodiamonds with $[\text{N}] \lesssim 36$ ppm. An NV^- ensemble study in Ref. (Bauch *et al.*, 2018) finds that if another mechanism, such as lattice strain or magnetic field gradients, is the dominant source of dephasing, spin bath driving becomes less effective, as shown in Fig. III.3 (see also Sec. II.C). Nonetheless, at high nitrogen concentrations ($[\text{N}_\text{S}^\text{T}] \gtrsim 1$ ppm), NV^- ensemble dephasing due to dipolar interaction with nitrogen spins can be greatly reduced by spin bath driving (Bauch *et al.*, 2018), in agreement with single- NV^- results (Knowles *et al.*, 2013; de Lange *et al.*, 2012).

To effectively suppress NV^- dephasing, all nitrogen spin transitions must typically be driven. Elemental nitrogen occurs in two stable isotopes, ^{14}N with 99.6% natural isotopic abundance, and ^{15}N with 0.4% natural isotopic abundance. Diamonds may contain predominantly ^{14}N , where the 99.6% natural abundance purity is typically deemed sufficient, or ^{15}N , which requires isotopic purification. ^{14}N

exhibits nuclear spin $I = 1$ while ^{15}N exhibits nuclear spin $I = 1/2$, resulting in 3 and 2 magnetic-dipole-allowed transitions for each isotope, respectively (Cook and Whiffen, 1966; Loubser and van Wyk, 1978; Smith *et al.*, 1959). Like NV^- centers, substitutional nitrogen defects possess a trigonal symmetry as a result of a Jahn-Teller distortion (Ammerlaan and Burgemeister, 1981; Davies, 1979, 1981). The Jahn-Teller distortion defines a symmetry axis along any of the 4 crystallographic [111] axes leading to 4 groups of N_S^0 spins. For a bias magnetic field B_0 larger than the substitutional nitrogen hyperfine interaction $A_\text{HF} \sim 100$ MHz, m_s and m_I are good quantum numbers, and the ^{14}N spectrum consequently exhibits up to 12 distinct resonances, which need to be driven (Belthangady *et al.*, 2013; de Lange *et al.*, 2012). If B_0 is aligned with any of the diamond [111] axes, the 12 resonances reduce to 6 partially-degenerate groups with approximate amplitude ratio 1:3:1:3:3:1 (see Fig. III.5a). Similarly, the ^{15}N spectrum shows up to 8 distinct resonances, which reduce to 4 partially-degenerate groups with approximate amplitude ratio 1:3:3:1 in an aligned bias field B_0 (see Fig. III.5b). This technique is expected to be easiest to execute when the bias magnetic field B_0 and hyperfine coupling A_HF are not of the same order. When $\frac{g\mu_B}{h}B_0 \sim A_\text{HF}$, additional nuclear-spin-non-conserving transitions arise, resulting in reduced oscillator strength for the nuclear-spin-conserving transitions. Thus, given fixed RF power, the drive efficiency for each addressed transition decreases. Although spin bath driving has to date only been demonstrated in the regime $\frac{g\mu_B}{h}B_0 \gtrsim A_\text{HF}$ (Bauch *et al.*, 2018; Knowles *et al.*, 2013; de Lange *et al.*, 2012), driving in the $\frac{g\mu_B}{h}B_0 \ll A_\text{HF}$ regime is also expected to be effective.

The N_S^0 electron spin resonance spectra for ^{14}N and ^{15}N are readily observed in EPR experiments (see for example Ref. (Smith *et al.*, 1959) and (Drake *et al.*, 2016)). Alternatively, the nitrogen resonance spectra in a diamond can be characterized with NV^- centers using the double electron-electron resonance (DEER) technique (Bauch *et al.*, 2018; de Lange *et al.*, 2012). In this instance, the NV^- electronic spin is made sensitive to decoherence from N_S^0 target impurity spins via application of frequency-selective π -pulses at the targeted spins' resonance frequency. A schematic of the DEER pulse sequence is shown in Fig. III.2c, and the resulting DEER spectra for both nitrogen isotopes are compared in Fig. III.5. Extra resonance features associated with substitutional-nitrogen-related dipole-forbidden transitions and additional paramagnetic spins are also commonly observed, and may reveal additional sources of dephasing.

The experimental requirements for effective spin bath driving typically depend on the substitutional nitrogen concentration. At lower impurity concentrations, reduced spin bath drive strength (i.e., RF power) is needed to mitigate nitrogen-induced dephasing. However, dephasing mechanisms unrelated to nitrogen may exhibit larger relative contributions to T_2^* in this regime, limiting the achievable T_2^* increase from nitrogen spin bath driving. In particular, in samples with nitrogen content $[\text{N}_\text{S}^0] \lesssim 1$ ppm, lattice strain gradients may dominate the ensemble dephasing time, as

is found in Ref. (Bauch *et al.*, 2018). In this instance, strain-insensitive measurement techniques, such as double-quantum coherence magnetometry (see Sec. III.B) must be employed for spin bath driving to extend T_2^* . In the intermediate regime ($[\text{N}_\text{S}^0] \sim 1$ ppm), where strain gradients and NV^- dipolar interactions with the nitrogen spin bath are of similar magnitude, neither spin bath driving nor DQ coherence magnetometry alone can achieve significant enhancement of the dephasing time. However, Ref. (Bauch *et al.*, 2018) demonstrates a $\sim 16\times$ improvement in T_2^* (effectively a $\sim 32\times$ improvement when considering the twice faster precession rate in the DQ basis) for a $[\text{N}_\text{S}^0] \simeq 0.75$ ppm diamond when both techniques are combined, as shown in Fig. III.4. In contrast, employing spin bath driving alone improves the dephasing time only by $\sim 1.1\times$ (see Fig. III.3), as strain-induced dephasing is left unmitigated.

In nitrogen-rich diamonds ($[\text{N}_\text{S}^0] \gtrsim 1$ ppm) achieving the motional narrowing condition $\Omega_\text{N}/\gamma_\text{N} \gg 1$ may be technically difficult; increases in $[\text{N}_\text{S}^0]$ necessitate linear proportional increases in Ω_N , which correspond to quadratic increases in the RF power required (Bauch *et al.*, 2018). We expect both pulsed and continuous spin bath driving in nitrogen-rich samples to be ultimately limited by parasitic effects. These effects include induced AC Zeeman shifts, strain gradients, and sample heating due to the strong applied RF fields (Knowles *et al.*, 2013).

We note that spin bath driving should be applicable to any paramagnetic spin species in diamond, such as electronic dark spins, NV^- centers, or even nuclear spins. The effectiveness of the driving for dilute bath spins (fractional concentration $\ll 0.01$) is expected to depend on the target spin's concentration but not its gyromagnetic ratio, as both Ω_N and γ_N vary linearly with the target spin's gyromagnetic ratio. In other words, species with small gyromagnetic ratios are difficult to drive but also do not contribute much to dephasing for a given concentration (Bauch *et al.*, 2018). Therefore, spin bath driving of the ^{13}C in a natural abundance diamond ($[^{13}\text{C}] = 10700$ ppm) is expected to be quite challenging (Bauch *et al.*, 2019). Lastly, as the nitrogen spin bath contributes to T_2 decoherence (Bar-Gill *et al.*, 2012; Pham *et al.*, 2012a), nitrogen spin bath driving would be expected to extend the Hahn echo T_2 , and, to a lesser extent, coherence times achieved with dynamical decoupling sequences (Bauch *et al.*, 2018), although neither application has been demonstrated at present.

D. Transverse strain and electric field suppression

Spatial and temporal variations in electric fields or in diamond crystal strain can degrade T_2^* , as described in Secs. II.C and III.B. Measurements performed in the NV^- spin's double-quantum basis are insensitive to variations in the *axial* components of the electric field E_z and spin-strain coupling \mathcal{M}_z , as these terms cause common-mode shifts in the spin resonance frequencies (Barson *et al.*, 2017; Glenn *et al.*, 2017). In contrast, broadening due to *transverse* electric fields E_x , E_y and transverse spin-strain couplings \mathcal{M}_x and \mathcal{M}_y may remain in DQ measurements (Barson

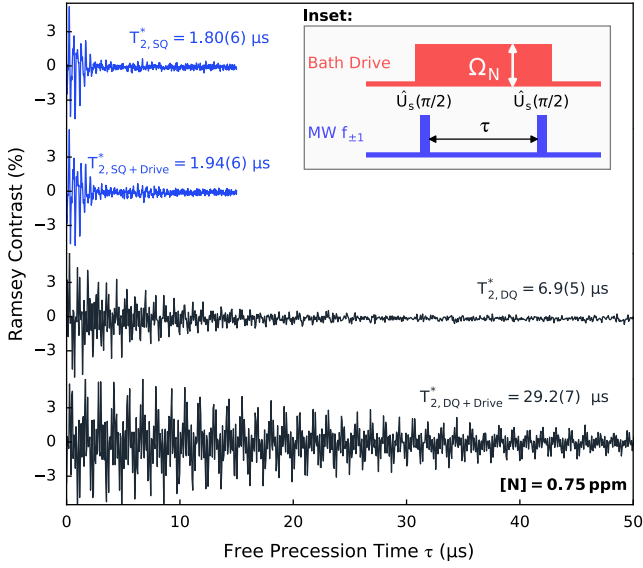


FIG. III.3 Ensemble free induction decay envelopes as measured using SQ and DQ Ramsey magnetometry, with and without continuous spin bath driving (inset). Measurements are shown for the following: in the SQ basis without spin bath driving (—, first from top); in the SQ basis with spin bath driving (—, second from top); in the DQ basis without spin bath driving (—, third from top); in the DQ basis with spin bath driving (—, fourth from top). Measurements in the DQ basis mitigate strain-induced dephasing while spin bath driving mitigates dipolar dephasing from the paramagnetic substitutional nitrogen in the diamond. The data illustrate the synergistic effect of combining DQ coherence magnetometry and spin bath driving; the aggregate approach vastly outperforms either technique employed independently. Even with twice faster precession, T_2^* is extended from 1.8 μs to 29 μs . From Ref. (Bauch *et al.*, 2018).

et al., 2017; Udvarhelyi *et al.*, 2018). However, by operating at a sufficiently strong axial bias magnetic field $B_{0,z}$, the resonance line broadening from E_x , E_y , \mathcal{M}_x , and \mathcal{M}_y can be mitigated (Jamonneau *et al.*, 2016; Schloss *et al.*, 2018), as illustrated in Fig. III.6 and discussed further in Appendix A.9.

The net frequency shifts of the NV^- ground state spin resonances due to transverse strain and electric fields at zero magnetic field are given by

$$\pm \xi_{\perp} = \pm \sqrt{\left(\frac{d_{\perp} E_x}{h} + \mathcal{M}_x\right)^2 + \left(\frac{d_{\perp} E_y}{h} + \mathcal{M}_y\right)^2}, \quad (22)$$

where $d_{\perp} = 0.17 \text{ Hz}/(\text{V}/\text{m})$ (Dolde *et al.*, 2011; Michl *et al.*, 2019; Van Oort and Glasbeek, 1990) is the transverse electric dipole moment of the NV^- ground state spin. Application of an external axial magnetic field $B_{0,z}$ introduces additional magnetic-field-dependent shifts and suppresses the effect of $\pm \xi_{\perp}$ on the spin resonances. When $\beta_z \equiv (g_e \mu_B / h) B_{0,z} \gg \xi_{\perp}$, contributions to T_2^* from temporal fluctuations or spatial variations in ξ_{\perp} (Fang *et al.*, 2013; Jamonneau *et al.*, 2016) are diminished (see Appendix A.9). For the nanodiamonds characterized in Ref. (Jamonneau *et al.*, 2016), with $\xi_{\perp} = 7 \text{ MHz}$, $B_{0,z} \sim 30 \text{ G}$ is required to eliminate the contribution to T_2^* from

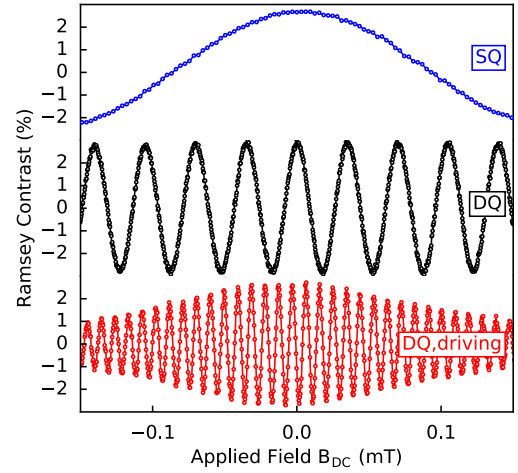


FIG. III.4 Ramsey interference fringes versus an applied test magnetic field, measured in the SQ basis (—, top), DQ basis (—, middle), and DQ basis with N_S^0 spin bath driving (—, bottom). The longer dephasing times achieved when combining DQ coherence magnetometry and spin bath driving allow for denser Ramsey fringes and enhanced sensitivity. The decreased contrast for magnetic fields $> 0.05 \text{ mT}$ in the bottom plot results from magnetic-field-induced detuning of the nitrogen spin resonances with respect to the RF drive frequencies. From Ref. (Bauch *et al.*, 2018).

transverse electric fields and strain. For the lower-strain bulk diamonds used in Refs. (Fang *et al.*, 2013; Jamonneau *et al.*, 2016), with $\xi_{\perp} \sim 10 \text{ kHz}$, $B_{0,z} \lesssim 100 \text{ mG}$ is sufficient.

IV. METHODS TO INCREASE READOUT FIDELITY

A. Spin-to-charge conversion readout

Spin-to-charge conversion (SCC) readout is an alternative to conventional fluorescence-based readout of the NV^- spin state. The technique has been demonstrated for single NVs (Ariyaratne *et al.*, 2018; Hopper *et al.*, 2016; Jaskula *et al.*, 2017; Shields *et al.*, 2015) and for small ensembles in nanodiamonds (Hopper *et al.*, 2018a) and bulk diamond (Jayakumar *et al.*, 2018). In SCC readout, the NV^- center's spin state is mapped optically onto the NV's neutral and negative charge states (NV^0 and NV^-). The charge state, and thus the original NV^- spin information, can then be accurately read out by exploiting differences in the NV^0 and NV^- wavelength-dependent excitation and associated fluorescence (Aslam *et al.*, 2013; Waldherr *et al.*, 2011). Key advantages of SCC readout over conventional spin-state-dependent fluorescence readout are: (i), a slightly increased spin contrast (Jaskula *et al.*, 2017); and (ii), the ability to read out the charge state for extended durations and thus collect more photons per readout, leading to high-fidelity charge-state determination. Larger photon-numbers per readout reduce the relative contribution of shot noise to the measurement, allowing for readout fidelities within order unity of the spin-projection limit $\sigma_R = 1$ (see definition in Sec. I.C).

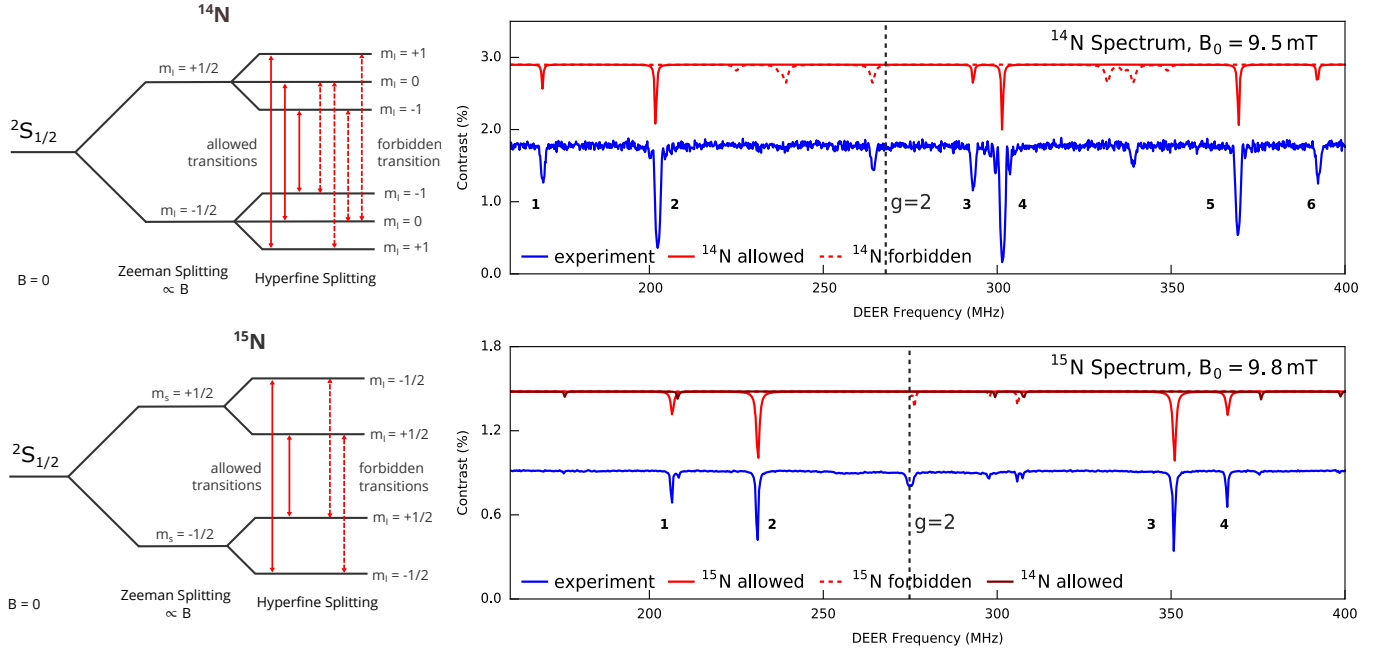


FIG. III.5 Substitutional nitrogen N_S^0 spin energy levels (left panes) and associated double electron-electron resonance (DEER) spectra (right panes), for ^{14}N (top) and ^{15}N (bottom). Simulated spectra depict allowed-transition resonances ($\Delta m_I = 0$) of the primary nitrogen isotope (—), forbidden-transition resonances ($\Delta m_I \neq 0$) of the primary nitrogen isotope (---), and spurious features associated with allowed transitions of impurity isotopes (-.-). The simulated data resonance linewidths and amplitudes are chosen to approximately match the experimental data (—). Spectra are simulated for and experimentally measured in an external magnetic field aligned along the diamond crystallographic [111] axis. Adapted from Ref. (Bauch *et al.*, 2018).

Successful spin-to-charge conversion requires control of the NV charge state. Characterization of charge dynamics under optical excitation (Aslam *et al.*, 2013; Beha *et al.*, 2012; Hacquebard and Childress, 2018; Manson *et al.*, 2018) indicate power- and wavelength-selective photo-ionization processes, which allow for controlled switching between NV^- and NV^0 . For example, green ~ 532 nm light transfers single NV centers preferentially to NV^- with 70 – 75% probability (Aslam *et al.*, 2013; Beha *et al.*, 2012; Waldherr *et al.*, 2011); strong yellow ~ 589 nm (Hopper *et al.*, 2018a) or red ~ 637 nm (Jaskula *et al.*, 2017; Shields *et al.*, 2015) light can selectively ionize NV^- to NV^0 via absorption of two photons by an electron in the triplet ground state; and near-infrared ~ 900 – 1000 nm (Hopper *et al.*, 2016) can similarly ionize NV^- via absorption of two photons by an electron in the singlet metastable state. Readout of the NV^- charge state is commonly performed by applying weak yellow laser light at ~ 594 nm. At intensities well below the NV^- saturation intensity $I_{\text{sat}} \sim 1$ – 3 mW/ μm^2 (Wee *et al.*, 2007), yellow light efficiently excites the NV^- electronic spin transition with zero phonon line (ZPL) at 637 nm without inducing ionization, while hardly exciting the NV^0 transition (with ZPL at 575 nm) (Aslam *et al.*, 2013; Beha *et al.*, 2012; Waldherr *et al.*, 2011). Through introduction of a photon-detection threshold combined with appropriate spectral filtering, NV^- (which fluoresces under the yellow excitation) may thus be distinguished from NV^0 (which produces little if any fluorescence). Figure IV.1a displays a photon-count histogram characteristic of single-NV charge readout reproduced from Ref. (Bluvstein *et al.*, 2019). The clear separation of photon distributions from NV^0 and NV^- at low

excitation powers allows charge-state determination with fidelity $> 99\%$ (Hopper *et al.*, 2018b).

The original work by Ref. (Shields *et al.*, 2015) demonstrates SCC readout on a single NV center in Type IIa diamond nanobeams (see Appendix A.11 for overview of diamond types). First, utilizing green laser light (see Fig. IV.1b) and appropriate MWs, the NV center is prepared in the $m_s = 0$ or one of the $m_s = \pm 1$ spin states of the NV^- triplet electronic ground state. A moderate power, 594 nm yellow “shelving” pulse (145 μW , ~ 0.9 mW/ μm^2) then excites the spin population to the triplet excited state. Due to the spin-dependent intersystem crossing from the triplet excited state, the $m_s = 0$ population is more likely to decay back to the ground state, whereas the $m_s = \pm 1$ population is more likely to be shelved into the metastable singlet states. The spin-to-charge conversion is then realized with a ~ 10 ns high intensity resonant 637-nm pulse (22.5 mW, ~ 140 mW/ μm^2), which ionizes (i.e., converts NV^- to NV^0) the triplet ground state population, corresponding to $m_s = 0$, but leaves the shelved population corresponding to $m_s = \pm 1$ unaffected. Last, the NV charge state is read out by applying weak ~ 594 nm light. The ~ 594 nm light with lower energy than the NV^0 ZPL at 575 nm, ensures that only NV^- is excited while the weak intensity (~ 1 – 10 μW , ~ 6 – 60 $\mu\text{W}/\mu\text{m}^2$, Fig. IV.1a) ensures that NV^- is not ionized during readout.

The single-NV SCC result by Ref. (Shields *et al.*, 2015) achieves a factor over spin projection noise $\sigma_R = 2.76$ ($\mathcal{F} = 1/\sigma_R = 0.36$, see comparison in Tab. I.2). As the fi-

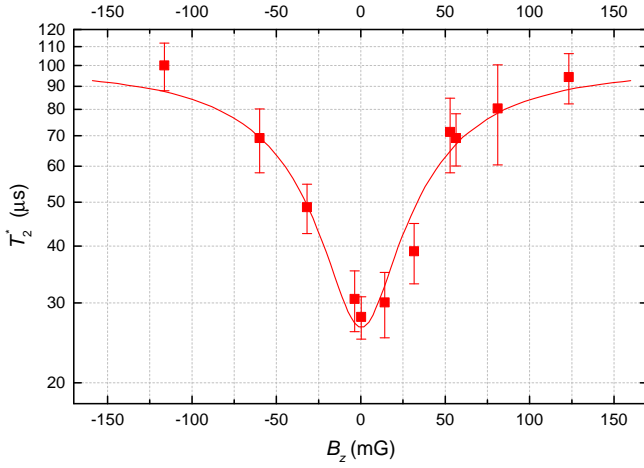


FIG. III.6 Suppression of dephasing from transverse electric fields and strain. For the single NV^- center measured in Ref. (Jamonneau *et al.*, 2016), the dephasing time $T_2^{*\{\text{single}\}}$ at zero magnetic field is limited by electric field fluctuations transverse to the NV^- symmetry axis, E_x and E_y . An applied axial magnetic field suppresses this source of dephasing by decoupling the NV^- center from transverse electric fields and strain. For magnetic fields larger than ~ 100 mG, the value of $T_2^{*\{\text{single}\}}$ is limited by magnetic noise, reaching ~ 100 μs in this isotopically enriched, $[^{13}\text{C}] = 20$ ppm sample. For NV^- ensembles at zero magnetic field, in addition to temporal fluctuations in E_x and E_y that limit $T_2^{*\{\text{single}\}}$, spatial variations in E_x and E_y and in the transverse spin-strain coupling terms \mathcal{M}_x and \mathcal{M}_y may also limit T_2^* for ensembles. Recreated from Ref. (Jamonneau *et al.*, 2016).

delity of the charge readout process itself approaches unity ($\mathcal{F}^{\text{CR}} = 0.975$), the dominant inefficiency is attributed to the imperfect spin-to-charge conversion step ($\mathcal{F}^{\text{SCC}} = 0.37$). Several alternative SCC readout variants have been demonstrated, providing similar sensitivity gains while offering reduced experimental complexity (Hopper *et al.*, 2018a), or utilizing the singlet state for ionization (Hopper *et al.*, 2016). For all SCC readout implementations, however, the improved values of σ_R come at the cost of substantially prolonged spin readout times t_R , which increase the sequence's overhead time and diminish the overall sensitivity improvement (see Sec. I.C). For example, the best reported readout fidelity ($\mathcal{F} = 0.36$) (Shields *et al.*, 2015) is achieved for readout times $t_R = 700$ μs , which exceed conventional fluorescence-based readout times ($t_R \sim 300$ ns) by $\sim 1000\times$. SCC readout is therefore most advantageous for measurement modalities with long sensing intervals (e.g., T_1 relaxometry and AC field sensing), where the penalty due to additional readout overhead is less severe. To date, the best SCC readout demonstrations improve field sensitivity only when interrogation times exceed ~ 10 μs (Hopper *et al.*, 2018a; Shields *et al.*, 2015), which further motivates improvement of spin ensemble properties to achieve sufficiently long dephasing times (see Sec. II.A).

Given the clear success of SCC readout with single NVs, application to NV^- -rich ensembles is a logical progression, especially given the low conventional readout fidelities achieved for NV^- -rich ensembles ($\mathcal{F} \lesssim 0.015$, see Tab. I.2). However, the prospect for SCC readout to substantially im-

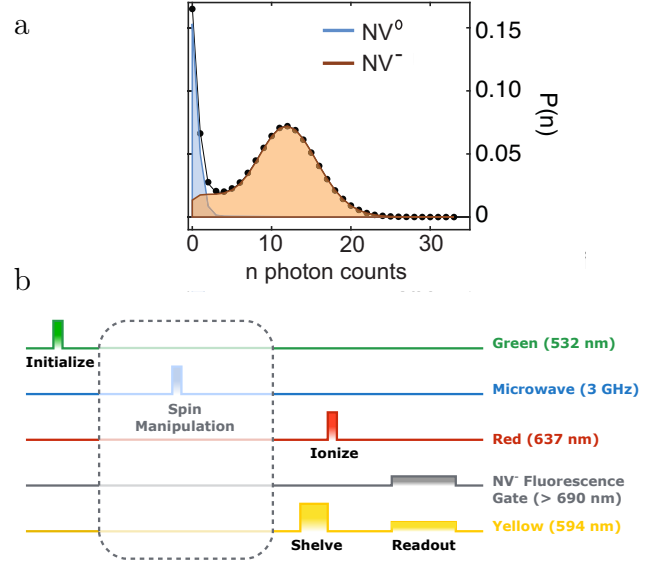


FIG. IV.1 a) Probability histogram depicting photon emission from NV^0 and NV^- under weak yellow excitation. The striking difference in photon emission rate between NV^0 and NV^- allows the NV charge state to be determined with fidelity $\gtrsim 99\%$. Adapted from Ref. (Bluvstein *et al.*, 2019). b) Schematic of the SCC readout protocol used by Shields *et al.* (Shields *et al.*, 2015). Adapted from Ref. (Jaskula *et al.*, 2017).

prove \mathcal{F} in NV^- ensembles likely hinges on whether the additional complex charge dynamics present in NV-rich diamonds can be mitigated (Hopper *et al.*, 2018a). Promising SCC readout results on small NV ensembles in Type Ib nanodiamonds demonstrate $\sigma_R = 20$, compared to $\sigma_R = 70$ with conventional readout in the same setup, allowing the authors to observe improved sensing performance for interrogations times > 6 μs (Hopper *et al.*, 2018a). However, this and other studies (Choi *et al.*, 2017a; Manson *et al.*, 2018) report intricate NV^- and NV^0 charge dynamics absent in single NV experiments. The effectiveness of SCC readout in the complex charge environment inherent to NV-rich ensembles (e.g., due to ionization and charge dynamics of substitutional nitrogen and other impurity defects) warrants further investigation (see Sec. V.B). Nevertheless, SCC readout overcomes one sensing disadvantage specific to ensembles, namely that NV^- orientations not being used for sensing can be preferentially transferred to NV^0 during the ionization step. This results in reduced background fluorescence and potentially allows for an additional $\sim 2\times$ sensitivity improvement relative to conventional NV^- readout. Overall, beyond the long overhead times already discussed, SCC readout's demanding power requirements are expected to further hamper ensemble-based implementation. In particular, high required optical intensities ($\gtrsim 150$ mW/ μm^2) (Hopper *et al.*, 2016, 2018a; Shields *et al.*, 2015) suggest scaling of SCC readout to larger bulk sample sizes ($\gtrsim 100 \times 100$ μm^2) will be challenging.

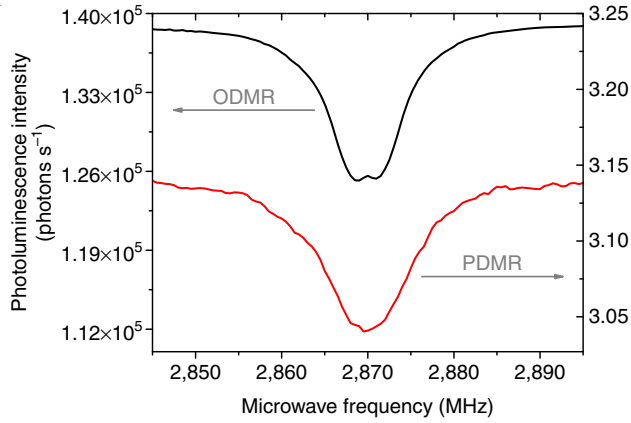


FIG. IV.2 Photoelectrically detected magnetic resonance (PDMR) of NV^- centers. Spectra are simultaneously measured by ODMR (—) and PDMR (—) in the absence of an external magnetic field. From Ref. (Bourgeois *et al.*, 2015).

B. Photoelectric readout

Another method to interrogate the NV^- spin state is photoelectric (PE) readout, which relies on measuring a current of charge carriers resulting from NV^- photo-ionization (Bourgeois *et al.*, 2015, 2017; Gulka *et al.*, 2017; Hrubesch *et al.*, 2017). Since NV^- photo-ionization is spin-state dependent, (see Secs. IV.A and V.B) (Shields *et al.*, 2015), the spin state can be inferred from the photocurrent signal in analogy to fluorescence-based readout. Figure IV.2 shows a photoelectrically detected magnetic resonance (PDMR) spectrum measured simultaneously with an ODMR spectrum, from Ref. (Bourgeois *et al.*, 2015). One promised benefit of PE readout is that the photoelectron collection efficiency can approach unity (Bourgeois *et al.*, 2015).

In PE readout, a bias voltage is applied across electrodes fabricated on the diamond surface. An excitation laser induces NV^- photo-ionization, and the ejected electrons generate a current, which is collected at the electrodes. NV^- photo-ionization may occur via single- or two-photon excitation. Single-photon ionization of the NV^- $^3\text{A}_2$ electronic ground state requires photon energies of 2.7 ± 0.1 eV or higher (wavelength $\lesssim 460$ nm) (Aslam *et al.*, 2013; Bourgeois *et al.*, 2017; Deák *et al.*, 2014; Londero *et al.*, 2018). PE readout implementations employing lower photon energies, such as from 532 nm (2.33 eV) light common for spin-state initialization, ionize the NV^- centers via a two-photon process, namely $^3\text{A}_2 \rightarrow ^3\text{E} \rightarrow \text{conduction band}$ (see Fig. V.1) (Bourgeois *et al.*, 2015, 2017; Gulka *et al.*, 2017; Heremans *et al.*, 2009). Whereas the rate of single-photon ionization scales linearly with optical intensity (Hacquebard and Childress, 2018), two-photon ionization depends quadratically on intensity (Aslam *et al.*, 2013).

Optically illuminating the diamond for PE readout may also induce background photocurrent from ionization of other defects present in the sample. Most unfortunately, 532 nm green light ionizes substitutional nitrogen N_S^0 defects in a single-photon process (Heremans *et al.*, 2009). The background N_S^0 photocurrent may exceed the signal

NV^- photocurrent, resulting in poor NV^- measurement contrast. This problem is exacerbated for excitation intensities well below the NV^- saturation intensity, where two-photon NV^- ionization may be weak compared to single-photon ionization of N_S^0 , and at elevated nitrogen concentrations $[\text{N}_\text{S}^0] \gg [\text{NV}^-]$ (Bourgeois *et al.*, 2017; Londero *et al.*, 2018).

Multiple approaches can partially mitigate the unwanted photocurrent associated with N_S^0 ionization. For example, lock-in techniques can remove the DC background from the nitrogen photocurrent (Gulka *et al.*, 2017). Additionally, a shorter-wavelength laser can be employed to induce single-photon ionization from the NV^- $^3\text{A}_2$ state, thereby improving the NV^- ionization rate relative to that of N_S^0 . However, the authors of Ref. (Bourgeois *et al.*, 2017) observe that under optimized experimental conditions, single-photon ionization using 450 nm light provides no contrast improvement compared to two-photon ionization with 532 nm light.

A variety of challenges accompany implementation of PE readout, both for small NV^- ensembles (Bourgeois *et al.*, 2015, 2017; Gulka *et al.*, 2017; Hrubesch *et al.*, 2017) and for envisioned extensions to larger detection volumes $\gtrsim (100 \mu\text{m})^3$ using NV -rich diamonds. In addition to background photocurrent from ionization of nitrogen and other defects, another expected obstacle to PE readout is electrical cross-talk between MW-delivery electrodes (used to manipulate the NV^- spin states) and photocurrent-detection electrodes (Gulka *et al.*, 2017). Fluctuations in the applied electric field could also add additional measurement noise by coupling to fluctuations in photoelectric collection efficiency.

Scaling PE readout implementations to larger NV^- ensembles may introduce additional challenges. Because the electrodes reside on the diamond surface, collecting photocurrent from NV^- centers located $\gtrsim 100 \mu\text{m}$ deep may prove difficult (Bourgeois *et al.*, 2015). Achieving the necessary bias electric field strength and uniformity over $\gtrsim (100 \mu\text{m})^3$ volumes may also be challenging; bias electric field gradients across large detection volumes could reduce NV^- ensemble T_2^* values. Moreover, the presence of charge traps in NV -rich diamonds might hinder photoelectric collection efficiency (see Sec. V.F), especially from deeper NV^- centers. In addition, Johnson noise in the readout electrodes may induce magnetic field fluctuations that could limit the achievable sensitivity (Kolkowitz *et al.*, 2015).

In certain PE readout implementations, the detected signal amplitude may be increased by photoelectric gain, an intrinsic charge-carrier amplification arising from the diamond's charge dynamics and the electrode boundary conditions (Bourgeois *et al.*, 2015; Hrubesch *et al.*, 2017; Rose, 1963). However, photoelectric gain is expected to be diminished in NV -rich diamonds due to charge traps, non-uniform electric fields, and space-charge limitations (Bourgeois *et al.*, 2015; Bube, 1960; Rose, 1963). The applicability of photoelectric gain to improving PE readout fidelity in ensemble-based extensions remains to be shown. Although PE readout may prove beneficial for certain applications such as integrated quantum devices (Morishita *et al.*, 2018), this technique's utility for ensemble magnetometry in NV -rich diamonds remains uncertain.

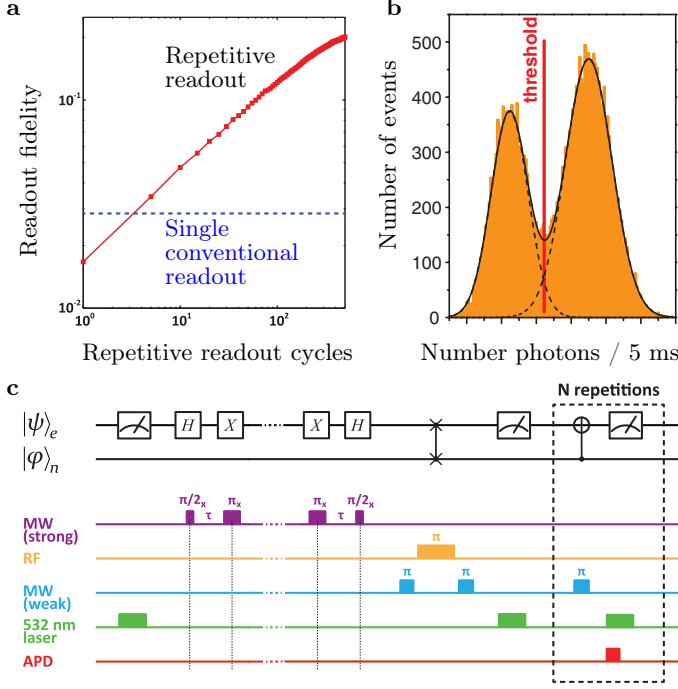


FIG. IV.3 Overview of ancilla-assisted repetitive readout. a) Readout fidelity \mathcal{F} is improved with the number of repetitive readout cycles. Fidelity for repetitive readout (red) is plotted relative to a single conventional readout (blue, dashed). Reproduced from Ref. (Lovchinsky *et al.*, 2016). b) The clear difference in total number of collected photons associated with the initial m_s states allows determination of m_s with fidelity approaching 1 in some implementations. Here $\mathcal{F} \approx 0.92$ in Ref. (Neumann *et al.*, 2010a). Reproduced from Ref. (Neumann *et al.*, 2010a). c) Quantum circuit diagram and magnetometry pulse sequence with detection via ancilla-assisted repetitive readout. Application of an RF π -pulse between two weak MW π -pulses maps the NV⁻ electronic spin superposition onto the ancilla nuclear spin. Subsequently the superposition state may be repeatedly mapped back onto the electronic spin via a weak MW π -pulse and optically read out without destroying the ancilla spin's quantum state. Adapted from Ref. (Lovchinsky *et al.*, 2016).

C. Ancilla-assisted repetitive readout

In conventional readout, the fast ~ 500 ns repolarization of the NV⁻ electronic spin limits the number of photons an NV⁻ emits before all initial spin state information is lost (See Fig. I.2). Even when implementing conventional readout with the best present collection efficiencies, the average number of collected photons per NV⁻ center n_{avg} is less than 1, and for many implementations $n_{\text{avg}} \ll 1$, making photon shot noise the dominant contributor to the parameter σ_R (see Eqn. 4, Tab. I.2, Sec. IV.E). An alternative method to increase the readout fidelity $\mathcal{F} = 1/\sigma_R$ circumvents this problem by instead first mapping the initial NV⁻ electronic spin state information onto an ancilla nuclear spin. In the second step, the ancilla nuclear spin state is mapped back onto the electron spin, which is then detected using conventional fluorescence-based readout. This second step may be repeated many times with each marginal readout improving the aggregate readout fidelity, as shown in Fig. IV.3a,b. While first demonstrated with a nearby ^{13}C nuclear spin as

the ancilla (Jiang *et al.*, 2009), the technique was later realized using the NV⁻ center's ^{14}N (Neumann *et al.*, 2010a) and ^{15}N nuclear spin (Lovchinsky *et al.*, 2016). In the ^{13}C realization (Jiang *et al.*, 2009; Maurer *et al.*, 2012), the coupling to the ancilla spin depends on the distance between the NV⁻ defect and the nearby ^{13}C atom, making the technique difficult to implement for NV⁻ ensembles where this distance varies. This discussion instead focuses on the more scalable realization using the NV⁻ nitrogen nuclear spin as the ancilla, which ensures the electron spin to ancilla spin coupling remains fixed over the NV⁻ ensemble.

Figure IV.3c shows a quantum circuit diagram from Ref. (Lovchinsky *et al.*, 2016) depicting the repetitive readout scheme. After the final MW pulse in an NV⁻ sensing protocol, the NV⁻ electronic spin state (denoted by subscript e) is mapped onto the nitrogen nuclear spin state (subscript n). In Ref. (Lovchinsky *et al.*, 2016), this mapping is achieved using a SWAP gate ($\text{CNOT}_{e|n} - \text{CNOT}_{n|e} - \text{CNOT}_{e|n}$), where CNOT denotes a controlled NOT gate. The SWAP gate consists of a MW π -pulse, then an RF π -pulse, then another MW π -pulse, where the MW pulses flip the electronic spin and the RF pulse flips the nuclear spin. This procedure swaps the electronic and nuclear spin states, importantly, storing the electronic spin state information in the ancilla nuclear spin. Then an optical pulse re-polarizes the electronic spin to $m_s = 0$. Next, a set of repetitive readouts is performed. In each readout, the nuclear spin state is copied back onto the electronic spin with a MW pulse, (a $\text{CNOT}_{e|n}$ gate), and then the electronic spin is optically read out without affecting the nuclear spin state. This process can be repeated many times ($\gtrsim 10^2$), and is limited in principle by the nuclear spin lifetime $T_{1,n}$. In Ref. (Lovchinsky *et al.*, 2016), while the initial RF pulse used in the SWAP gate requires ~ 50 -60 μs , each readout cycle requires only ~ 1 μs . The large number of readouts allow the aggregate readout fidelity $\mathcal{F} = 1/\sigma_R$ to approach 1; notably, Ref. (Neumann *et al.*, 2010a) achieves $\mathcal{F} = 0.92$ ($\sigma_R = 1.1$) as depicted in Fig. IV.3b.

Extending ancilla-assisted repetitive readout to ensembles is expected to be fruitful but necessitates overcoming further challenges. The scheme requires a large magnetic field to minimize coupling between the NV⁻ nuclear and electronic spins, with Refs. (Lovchinsky *et al.*, 2016; Neumann *et al.*, 2010a) employing fields of 2500 gauss and 6500 gauss respectively. Further, the bias magnetic field must be precisely aligned along a single NV⁻ symmetry axis, presently precluding its use for sensing from more than one NV⁻ orientation (Schloss *et al.*, 2018). Even slight angular misalignments introduce measurement back action on the nuclear spin I_z , which spoils $T_{1,n}$ (Neumann *et al.*, 2010a). The reduction in $T_{1,n}$ limits the available readout duration. Ensemble implementations would therefore require highly uniform bias magnetic fields over ensemble sensing volumes, conceivably on the $\sim (100 \mu\text{m})^3$ scale. Engineering such fields is within current technical capability but difficult nevertheless, see II.C and Ref. (Vandersypen and Chuang, 2005). Additionally, the MW and RF control pulses would ideally manipulate the entire ensemble uniformly; spatial inhomogeneities of the control pulses are likely to result in

reduced readout fidelity unless mitigated (Vandersypen and Chuang, 2005). Assuming sufficiently strong and homogeneous B_0 fields and MW driving can be realized, and that the additional overhead time is acceptable, repetitive readout appears to be a promising but technically demanding method to improve \mathcal{F} for ensembles.

D. Level-anticrossing-assisted readout

In conventional readout (Doherty *et al.*, 2013), the readout fidelity $\mathcal{F} = 1/\sigma_R$ depends on the number of photons n_{avg} collected per measurement sequence (see Eqn. 4). The value of n_{avg} is limited by the time the spin population originally in the $m_s = \pm 1$ states spends shelved in the singlet state before decaying to the triplet $m_s = 0$ state. Steiner *et al.* engineer the NV⁻ spin to pass through the singlet state multiple times before repolarization, extending the readout duration per sequence to increase n_{avg} (Steiner *et al.*, 2010), as depicted in Fig. IV.4. Using NV⁻ centers with ^{14}N , which has nuclear spin $I = 1$, three cycles through the singlet state occur during readout, yielding a $\sim 3\times$ increase in n_{avg} and thus a $\sim \sqrt{3}\times$ improvement in the fidelity \mathcal{F} . For NV⁻ centers with ^{15}N with $I = 1/2$, the spin only passes twice through the singlet state before repolarization, yielding only a $\sim \sqrt{2}\times$ improvement in \mathcal{F} .

The technique is implemented as follows: the bias field B_0 is tuned to the excited-state level anticrossing at $B_{\text{LAC}} \approx 500$ G (Fuchs *et al.*, 2008; Neumann *et al.*, 2010a) to allow resonant flip-flops between the NV⁻ center's electronic spin and its ^{14}N nuclear spin ($I = 1$). Operation at the level anticrossing polarizes the nuclear spin into the state $|m_I = +1\rangle$ (Jacques *et al.*, 2009). At completion of a sensing sequence, immediately prior to readout, the NV⁻ electronic spin occupies a superposition of the states $|m_s = 0, m_I = +1\rangle$ and $|m_s = -1, m_I = +1\rangle$. Before the NV⁻ electronic spin state is read out using a conventional green laser pulse, two sequential RF π -pulses flip the nuclear spin into the $m_I = -1$ state, conditional on the electronic spin occupying the $m_s = -1$ state. This CNOT gate relies on the RF drive being resonant with the nuclear transitions between the m_I states for population in the $m_s = -1$ state and off-resonant for population in the $m_s = 0$ state. During readout, the population in $|m_s = -1, m_I = -1\rangle$ cycles through the long-lived singlet state three times before the information stored in the NV⁻ electronic spin is lost, allowing more signal photons to be collected. After the first and second pass through the singlet to the $m_s = 0$ state, an electron-nuclear spin flip-flop returns the electronic spin state to $m_s = -1$, as shown in Fig. 3a of Ref. (Steiner *et al.*, 2010), enabling another cycle through the singlet state. The third pass repolarizes the NV⁻ spin into the stable $|m_s = 0, m_I = +1\rangle$ state.

This technique's utility for magnetic sensing depends on whether the $\leq \sqrt{3}\times$ increase in fidelity \mathcal{F} outweighs the cost of additional overhead time (see Eqn. 2) introduced by the RF pulses. Although the authors of Ref. (Steiner *et al.*, 2010) assert that microsecond-scale RF nuclear spin π -pulses are attainable, achieving such nuclear Rabi fre-

quencies over large ensemble volumes $\sim (100 \mu\text{m})^3$ may prove very difficult, making this method impractical for NV⁻ ensembles with $T_2^* \lesssim 1 \mu\text{s}$. Additional challenges for implementation with NV⁻ ensembles include realizing the requisite uniformity in the MW/RF fields and in the 500 G bias magnetic field over ensemble volumes. Finally, the scheme presently precludes sensing from more than one NV orientation (Schloss *et al.*, 2018).

E. Improved photon collection methods

In the limit of low contrast, the readout fidelity \mathcal{F} is proportional to the square root of the average number of photons collected per NV⁻ per measurement, i.e., $\mathcal{F} \propto \sqrt{\mathcal{N}/N} = \sqrt{n_{\text{avg}}}$ (see Eqn. 4). Under these conditions, sensitivity can be enhanced by increasing the geometric collection efficiency η_{geo} , defined as $\mathcal{N}/\mathcal{N}_{\text{max}}$, where \mathcal{N} and \mathcal{N}_{max} are the number of photons collected and emitted respectively by the NV⁻ ensemble per measurement.

Efficient photon collection in diamond is hindered by total-internal-reflection confinement resulting from diamond's high refractive index of approximately 2.41. For example, air and oil immersion objectives, with numerical apertures of 0.95 and 1.49 respectively, provide calculated collection efficiencies of only 3.7% and 10.4% respectively for photons emitted directly through the (100) diamond surface (Le Sage *et al.*, 2012), as depicted in Fig. IV.5. Although anti-reflection coatings can allow for higher collection efficiencies, present implementations demonstrate only modest improvement (Yeung *et al.*, 2012). While great effort has resulted in high values of η_{geo} for single NV⁻ centers through use of various nano-fabrication approaches (Babinec *et al.*, 2010; Choy *et al.*, 2013, 2011; Häberle *et al.*, 2017; Hadden *et al.*, 2010; Li *et al.*, 2015; Marseglia *et al.*, 2011; Momenzadeh *et al.*, 2015; Neu *et al.*, 2014; Riedel *et al.*, 2014; Schröder *et al.*, 2011; Shields *et al.*, 2015; Yeung *et al.*, 2012), such methods do not easily translate to large ensembles.

Successful approaches for bulk ensemble magnetometers have so far focused on collecting NV⁻ fluorescence that has undergone total internal reflection in the diamond (Le Sage *et al.*, 2012; Wolf *et al.*, 2015). While absorption of NV⁻ fluorescence by various defects may limit η_{geo} (Khan *et al.*, 2013, 2009) for some diamonds, nitrogen (Weerdts and Collins, 2008) and NV⁻ centers (Fraczek *et al.*, 2017) are expected to hardly absorb in the NV⁻ PL band $\sim 600 - 850$ nm. A collection efficiency of 39% is demonstrated in Ref. (Le Sage *et al.*, 2012) by detecting fluorescence from the four sides of a rectangular diamond chip surrounded by four photodiodes (see Fig. IV.6). However, the increased experimental complexity associated with employing four detectors in contact with the diamond may be problematic for certain applications. In another approach, Wolf *et al.* employ a trapezoidally-cut diamond chip and a parabolic concentrator to improve collection efficiency (Wolf *et al.*, 2015). Although the authors calculate η_{geo} to be between 60% and 65%, this result is not confirmed experimentally. Ma *et al.* (Ma *et al.*, 2018) demon-

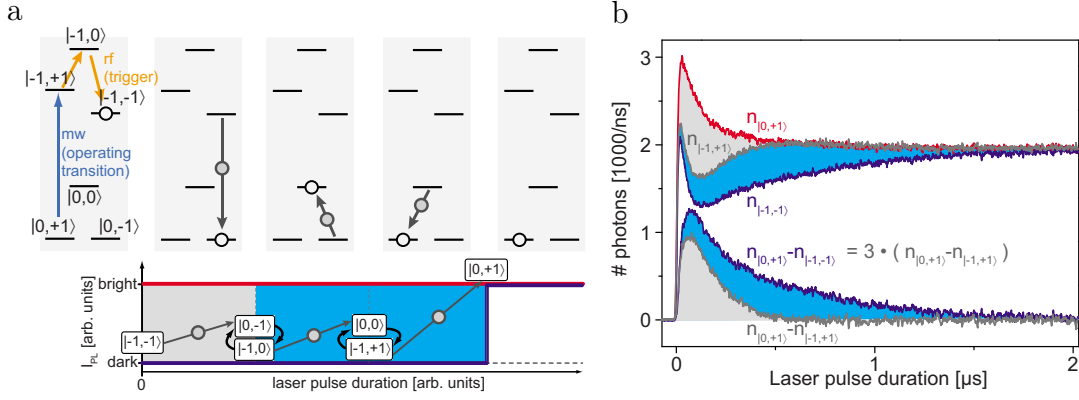


FIG. IV.4 Level-anticrossing-assisted readout as demonstrated in Ref. (Steiner *et al.*, 2010). At the excited-state level anticrossing near $B = 500$ G, green optical excitation polarizes NV^- into the spin state $|m_s = 0, m_I = +1\rangle$. a) Upon completion of a sensing sequence, two RF pulses transfer population in the electronic spin state $|m_s = -1\rangle$ from the nuclear spin state $|m_I = +1\rangle$ to $|m_I = -1\rangle$ without affecting the $|m_s = 0\rangle$ state. During optical readout, this population passes three times through the singlet states before being repolarized to $|m_s = 0, m_I = +1\rangle$, increasing the time over which the state-dependent fluorescence contrast persists. b) Time-resolved photon detection comparing conventional readout (gray) and LAC-assisted readout (blue). The optimal readout duration is extended by $3\times$ and the difference in detected photon number between the two spin states is increased by $3\times$. From Ref. (Steiner *et al.*, 2010).

strate a collection efficiency of 40% by eliminating all air interfaces between the diamond and detector, in conjunction with coupling prisms which direct light exiting the diamond's four side faces to the detector.

In the future, collection efficiency in bulk NV-diamond magnetometers is expected to improve to near 100%, limited only by losses due to absorption. For example, light lost from the top and sides of the diamond in Ref. (Wolf *et al.*, 2015) could be redirected to the detector by coating these sides of the diamond with a metallic (Choy *et al.*, 2011) or dielectric reflector (Boesch *et al.*, 2016). The authors of Ref. (Wolf *et al.*, 2015) might also see an improvement in collection efficiency by designing an optimized parabolic concentrator rather than using a commercially available part. Hypothetical geometries for light collection using parabolic or ellipsoidal reflectors are discussed in Ref. (Boesch *et al.*, 2016). Whereas multiple-reflection methods are suitable for bulk magnetometers, increasing η_{geo} by collecting light undergoing multiple reflections in the diamond may substantially complicate accurate image reconstruction for NV^- magnetic imaging microscopes (Le Sage *et al.*, 2013; Pham *et al.*, 2011; Steiner *et al.*, 2010).

F. Near-infrared absorption readout

The sensitivity of conventional fluorescence-based readout is limited by shot noise on the collected photons due to low fluorescence contrast C (see Eqn. 3). As an alternative to fluorescence-based readout, population in one or both NV^- singlet states may be directly probed via absorption, giving a probabilistic measure of the initial m_s spin state prior to readout. While the upper singlet state $^1\text{A}_1$ lifetime of $\lesssim 1$ ns at room temperature (Acosta *et al.*, 2010b) is likely too short for such an approach to be effective, the lower singlet state ^1E lifetime $\sim 140 - 220$ ns at room temperature (Acosta *et al.*, 2010b; Gupta *et al.*, 2016; Robledo

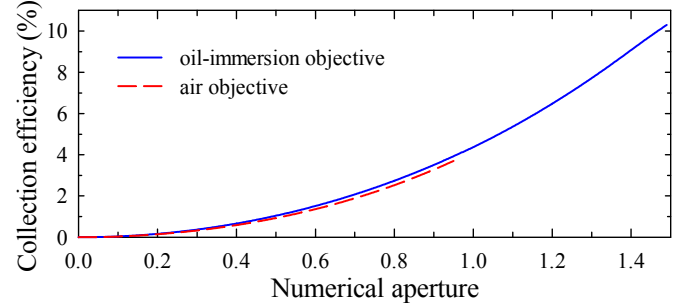


FIG. IV.5 Calculated collection efficiencies of NV^- fluorescence by oil-immersion or air microscope objectives through the (100) surface of a diamond chip, as a function of numerical aperture. Figure and caption from Ref. (Le Sage *et al.*, 2012).

et al., 2011) makes measuring the ^1E population via absorption on the $^1\text{E} \leftrightarrow ^1\text{A}_1$ transition at 1042 nm viable.

Near-infrared (NIR) absorption has attractive benefits for certain applications: a) Contrast (and therefore sensitivity) is not reduced by background fluorescence from non- NV^- defects (such as NV^0). b) The directional nature of the 1042 nm probe light allows maximal collection efficiency (ignoring absorptive losses) to be obtained more easily than in a fluorescence-based measurement; for example, this benefit was exploited in the first demonstration of microwave-free magnetometry with NV^- centers (Wickenbrock *et al.*, 2016). c) Owing to the upper singlet $^1\text{A}_1$ lifetime of $\lesssim 1$ ns (Acosta *et al.*, 2010b), the saturation intensity of the $^1\text{E} \leftrightarrow ^1\text{A}_1$ transition is unusually large ($I_{1042}^{\text{sat}} \sim 50$ megawatts/cm² (Dumeige *et al.*, 2013)), allowing high intensity 1042 nm probe radiation to be used, so that fractional shot noise is reduced to well below that of an equivalent fluorescence-based measurement (Acosta, 2011). d) NIR absorption readout is nondestructive, allowing for a single NV^- center in the ^1E singlet state to absorb multiple 1042 nm photons before eventual decay to the $^3\text{A}_2$ triplet. In principle such absorption by a single NV^- center can al-

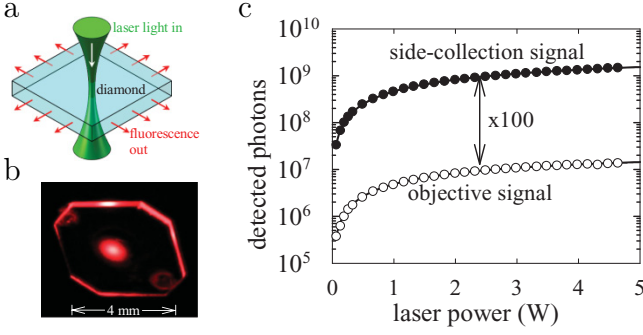


FIG. IV.6 Fluorescence side-collection method (Le Sage *et al.*, 2012). a) Green optical excitation is applied normal to the large face of the diamond chip, and red fluorescence is collected from the sides. b) Red fluorescence from actual diamond chip. c) The depicted implementation results in a $100\times$ increase in detected photons relative to a 0.4 numerical aperture air objective. Figures are reproduced from Ref. (Le Sage *et al.*, 2012).

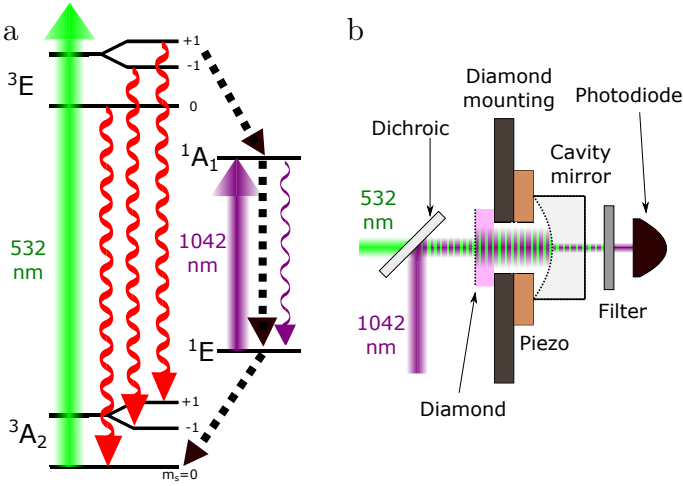


FIG. IV.7 Near-infrared (NIR) absorption readout. a) Level diagram for the NV^- center. Population accumulating in the ^1E singlet state is probed via absorption of 1042 nm radiation resonantly addressing the $^1\text{E} \leftrightarrow ^1\text{A}_1$ transition. b) Miniature NIR cavity-enhanced diamond magnetometer as described in Ref. (Chatzidrosos *et al.*, 2017). Dashed black lines depict surfaces forming the dual-wavelength optical cavity. Components pertaining to MW delivery are omitted for clarity.

low readout fidelity near the spin-projection limit, even in the presence of non-negligible optical losses.

NIR absorption readout has been successfully implemented in several proof-of-principle magnetometers. In the first demonstration (Acosta *et al.*, 2010), a diamond containing $[\text{NV}^-] \sim 16$ ppm is continuously illuminated with 532 nm radiation (driving the $^3\text{A}_2 \leftrightarrow ^3\text{E}$ transition to optically polarize the NV^- spin state) and 1042 nm NIR radiation (resonantly addressing the $^1\text{E} \leftrightarrow ^1\text{A}_1$ transition), as shown in Fig. IV.7a. MW radiation transfers population between the ground state Zeeman sublevels. In this first demonstration (Acosta *et al.*, 2010), a single pass of the 1042 nm radiation through the diamond sample resulted in a peak-to-peak contrast of ~ 0.003 at room temperature.

The contrast can be enhanced by increasing the num-

ber of NV^- defects interacting with each 1042 nm photon, such as by employing a higher NV^- density or a larger diamond. Alternatively, for a fixed number of NV^- centers, the 1042 nm radiation can be recirculated through the diamond. An NIR absorption magnetometer employing an optical cavity to increase the 1042 nm interaction length is analyzed in Ref. (Dumeige *et al.*, 2013) and experimentally realizes a peak-to-peak contrast of 7.1% in Ref. (Jensen *et al.*, 2014) when the bias magnetic field is directed along the [100] crystallographic direction (making the magnetic resonances of all four NV^- orientations degenerate). For this demonstration, the diamond is anti-reflection coated (Yeung *et al.*, 2012) and placed in the center of a dual-wavelength optical cavity, which allows recirculation of both 1042 nm and 532 nm radiation. The more efficient use of the 532 nm light enabled by the cavity allows both a larger NV^- ensemble to be addressed and a higher degree of spin initialization into the $m_s = 0$ state. Ultimately the device in Ref. (Jensen *et al.*, 2014) achieves a sensitivity of $2.5 \text{ nT}/\sqrt{\text{Hz}}$, well above the shot-noise limit of $70 \text{ pT}/\sqrt{\text{Hz}}$.

A notable recent implementation of NIR absorption (Chatzidrosos *et al.*, 2017) is depicted in Fig. IV.7b. One diamond face forms a reflector while the addition of a dual-wavelength concave mirror results in an optical cavity with a finesse of 160 and a cylindrical sensing volume of $\sim 76 \mu\text{m}$ diameter and $\sim 390 \mu\text{m}$ length (Chatzidrosos *et al.*, 2017). With 500 mW of 532 nm radiation and 80 mW of 1042 nm radiation, a DC magnetic field sensitivity of $28 \text{ pT}/\sqrt{\text{Hz}}$ is achieved with this compact setup, with a bandwidth of about 530 Hz. The shot-noise-limited sensitivity is $22 \text{ pT}/\sqrt{\text{Hz}}$ and the spin-projection-noise-limited sensitivity is $0.43 \text{ pT}/\sqrt{\text{Hz}}$.

The NIR absorption approach is hindered, however, by several non-idealities, which so far limit readout fidelity to values far from the spin projection noise limit, similar to conventional optical readout (i.e., $\sigma_R = 65$ for the NIR absorption approach in Ref. (Chatzidrosos *et al.*, 2017) versus $\sigma_R \approx 67$ for conventional readout in Ref. (Le Sage *et al.*, 2012)). First, the predominantly non-radiative decay of the $^1\text{A}_1$ singlet greatly reduces the absorption cross section σ_{1042} of the $^1\text{E} \leftrightarrow ^1\text{A}_1$ transition compared to a radiative-decay-only transition (Acosta *et al.*, 2010b; Rogers *et al.*, 2008). Estimates suggest $\sigma_{1042} = 3_{-1}^{+3} \times 10^{-18} \text{ cm}^2$ (Dumeige *et al.*, 2013; Jensen *et al.*, 2014; Kehayias *et al.*, 2013), whereas the purely radiative $^3\text{A}_2 \leftrightarrow ^3\text{E}$ transition is measured to have a much larger absorption cross section $\sigma_{532} = (3.1 \pm 0.8) \times 10^{-17} \text{ cm}^2$ for 532 nm excitation (Wee *et al.*, 2007). Realizing the full potential of this method requires 1042 nm laser intensities of order $I_{1042}^{\text{sat}} \sim 50 \text{ MW}/\text{cm}^2$ (Jensen *et al.*, 2014). This saturation intensity appears to limit interrogation cross sections to $\lesssim 100 \mu\text{m}^2$ for $\sim 100 \text{ mW}$ -scale 1042 nm radiation powers, assuming a cavity finesse of ~ 160 . Laser intensities of this magnitude may lead to undesirable ionization dynamics (see Sec. V.B). Second, as described in Ref. (Dumeige *et al.*, 2013), non-resonant losses for 1042 nm radiation compromise sensitivity by reducing the effective achievable collection efficiency. For example, in Ref. (Chatzidrosos

et al., 2017), 80 mW of 1042 nm radiation input to the dual-wavelength cavity results in 4.2 mW transmitted to the detector. Third, the NIR absorption has only been demonstrated for dense ensembles with $[NV^T] \sim 10$ ppm to ensure appreciable 1042 nm absorption; the performance of this method for diamonds with more dilute NV^- concentrations and longer T_2^* values remains unknown, and will likely depend on the scaling of cavity finesse with $[N^T]$ or $[NV^T]$ density.

While NIR absorption readout is effective and may find preference for certain applications (Chatzidrosos *et al.*, 2017; Wickenbrock *et al.*, 2016), without further advances enabling readout fidelity enhancement, (e.g., reduced 1042 nm non-resonant absorption or reduced non-radiative 1A_1 singlet decay rate), this method will remain approximately on par with conventional fluorescence readout while requiring the non-trivial overhead of an NIR single frequency laser and an optical cavity.

G. Green absorption readout

Alternatively, NV^- readout may be achieved by monitoring absorption of green probe laser radiation, which off-resonantly drives the triplet $^3A_2 \leftrightarrow ^3E$ transition (Bauch, 2010; Walsworth, 2017). When resonant MWs drive the $m_s = 0 \leftrightarrow m_s = -1$ or $m_s = 0 \leftrightarrow m_s = +1$ ground state spin transitions and facilitate population transfer to the NV^- singlet states, it is expected that the 3A_2 state will be depleted, resulting in *increased* green probe transmission and *decreased* red fluorescence. For absorption measurements (both NIR and green), the change in transmitted light upon resonant MW drive is expected to mirror the change in fluorescence light up to a scaling constant, since transmission is minimal when fluorescence is maximal and vice versa (Bauch, 2010). Data consistent with this understanding is shown in Fig. IV.8 for NV^- centers illuminated with 514 nm light.

The absorption contrast, denoted C_{absorb} , may differ substantially in magnitude from the fluorescence contrast C_{fluor} (see Fig. IV.8). Because absorption measurements monitor transmitted light, the detected signal (and thus C_{absorb}) depends on the optical depth of the absorbing material. For example, even for the idealized case where $C_{\text{fluor}} = 1$, if only a small fraction of the incident light is absorbed in the absence of MWs, the change in transmission upon application of resonant MWs will necessarily also be small, yielding a low absorption contrast C_{absorb} . Additionally, the absorption contrast may be further decreased due to the presence of non-radiative decay pathways.

Observed magnitudes of C_{absorb} in the literature are lower than C_{fluor} by $\sim 3\times$ (Bauch, 2010; Le Sage and Arai, 2011) or more. For example, the authors of Refs. (Ahmadi *et al.*, 2017, 2018a,b) use a CW-ODMR-based magnetometer employing a resonant optical cavity to recycle the green excitation light through the diamond multiple times, and observe $C_{\text{fluor}} \sim 0.01$, (which is typical), while measuring $C_{\text{absorb}} \sim 10^{-6}$. In Ref. (Ahmadi *et al.*, 2018a) the same experimental setup performs magnetometry simultaneously

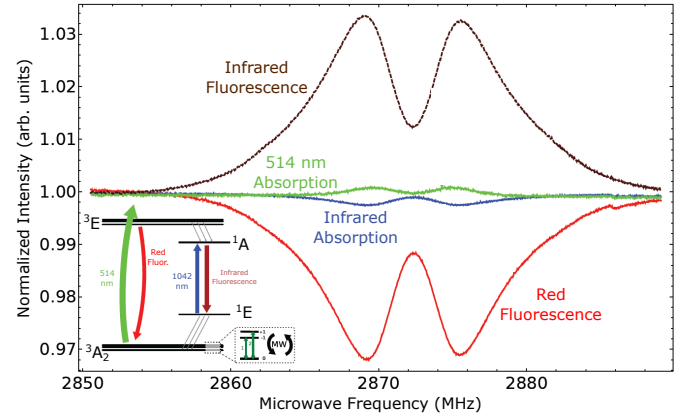


FIG. IV.8 Simultaneous measurement of absorption and fluorescence on both the triplet and singlet NV^- electronic transitions (see inset lower left). For both transitions, the absorption and fluorescence features have opposite signs and mirror one another up to a scaling factor. Adapted from Ref. (Bauch, 2010).

using both green absorption and red fluorescence, as shown in Fig. IV.9. The green absorption yields ~ 100 nT/ $\sqrt{\text{Hz}}$ sensitivity while the conventional readout based on red fluorescence reaches ~ 400 pT/ $\sqrt{\text{Hz}}$, about $250\times$ better. As with NIR absorption readout (see Sec. IV.F), recycling the green excitation light via a resonant optical cavity can increase the absorption signal by (i) addressing a larger NV^- population, (ii) improving initialization into the $m_s = 0$ state, or (iii) enhancing C_{absorb} . Although effectively implemented absorption readout may achieve higher optical collection efficiency than fluorescence detection, the low realized absorption contrasts are a current major drawback.

Furthermore, absorption behavior for 532 nm probe radiation can result in *increased* probe laser transmission under resonant MW application (Bauch, 2010; Le Sage and Arai, 2011), leading to an anomalous inversion of the green absorption signal. This deviation from expected behavior has been independently observed in multiple research groups (Bauch, 2010; Le Sage and Arai, 2011). The anomalous C_{absorb} reveals a strong wavelength and power dependence (Bauch, 2010), which suggests that green absorption readout is hindered by an unknown effect competing with and sometimes dominating otherwise expected behavior. The wavelength and power dependence of this effect suggests NV^0/NV^- charge dynamics could play a role. Further investigation of this behavior might reveal presently unknown NV dynamics. Overall, given the low absorption contrast C_{absorb} , and yet unknown mechanism of anomalous absorption behavior, the utility of green absorption readout remains questionable.

H. Laser threshold magnetometry

Another approach for bulk NV^- magnetometry is the creation of a NV -diamond-based laser threshold magnetometer, as suggested by Ref. (Jeske *et al.*, 2016). Lasing is induced on the NV^- $^3E(v=0) \leftrightarrow ^3A_2(v' \geq 1)$ transition; then, when a magnetic-field-dependent population accumu-

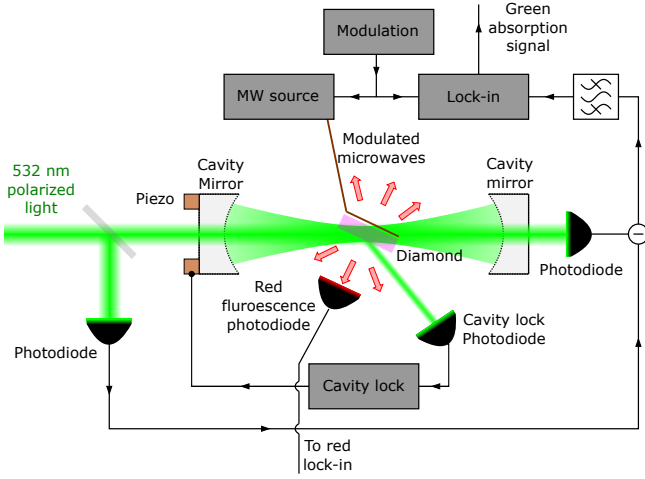


FIG. IV.9 Cavity-enhanced magnetometry based on green absorption as demonstrated in Refs. (Ahmadi *et al.*, 2018a,b). A power build-up cavity allows green excitation light to pass through the diamond sample multiple times, increasing the effective path length. The red fluorescence is measured simultaneously along with the green absorption. Adapted from Ref. (Ahmadi *et al.*, 2018b).

lates in the singlet state, the lasing threshold increases, and the laser's output power is reduced. As theoretically outlined (Jeske *et al.*, 2017; Savitski, 2017), the laser threshold approach has a number of benefits relative to generic CW-ODMR methods (Sec. I.D.1): (i), effective contrast is enhanced near the lasing threshold due to competition between stimulated and spontaneous emission, (ii) collection efficiency is substantially improved by virtue of the lasing process. Although the emission cross sections for NV^- and NV^0 have been measured (Fraczek *et al.*, 2017), and stimulated emission from NV^- was recently demonstrated (Jeske *et al.*, 2017), substantial work remains to address potential problems. For example, absorption by substitutional nitrogen or other defects may obstruct the lasing process (Dodson *et al.*, 2011), and it will need to be shown that other sources of noise affecting the lasing threshold or output power can be either controlled or normalized out (Jeske *et al.*, 2016). More concerning, however, is that both theory (DeGiorgio and Scully, 1970) and experiment (Lim *et al.*, 2002) find large laser field fluctuations in the vicinity of the lasing threshold.

V. DIAMOND MATERIAL ENGINEERING

A. Conversion efficiency

In an idealized case in which all other parameters are held constant, increasing the NV^- density in a fixed detection volume will result in enhanced sensitivity. Since the NV^- density is limited by the density of nitrogen introduced into the diamond, the N-to- NV^- conversion efficiency

$$E_{\text{conv}} \equiv \frac{[NV^-]}{[N^T]} \quad (23)$$

must be increased in order to achieve a high density of NV^- spins while minimizing the concentration of residual paramagnetic substitutional nitrogen. Converting a substitutional nitrogen N_S into a NV^- defect requires both introducing a vacancy to a lattice site adjacent to a substitutional nitrogen (to create the NV), and capturing an electron (to change the NV center's charge state to NV^-). We denote the efficiency with which nitrogen atoms in the diamond are converted to NVs as

$$\chi = \frac{[NV^T]}{[N^T]}, \quad (24)$$

where $[N^T] = [N_S^0] + [N_S^+] + [NV^-] + [NV^0] + [NV^+] + [N^{\text{other}}]$ accounts for the concentration of substitutional nitrogen N_S in the neutral and ionized charge states, NV centers in all three charge states, and other nitrogen-containing defects in the diamond, such as NVH (see Sec. V.F). We define the fraction of NV centers residing in the negative charge state as the charge state efficiency ζ ,

$$\zeta = \frac{[NV^-]}{[NV^T]} = \frac{[NV^-]}{[NV^-] + [NV^0] + [NV^+]}, \quad (25)$$

so that $E_{\text{conv}} = \chi \cdot \zeta$. Although Refs. (Hauf *et al.*, 2014; Pfender *et al.*, 2017) show evidence for NV^+ , this state has so far required application of external voltages for observation. The rest of this section therefore assumes $[NV^+]$ is negligible and can be ignored.

As the N-to- NV^T conversion efficiency χ is determined by the physical location of nitrogen and vacancies in the diamond lattice, the value of χ is expected to be invariant under ambient conditions. Modification of χ requires conditions severe enough to rearrange atoms within the diamond lattice, such as irradiation, implantation, high temperature, or high pressure. With suitable electron irradiation and subsequent annealing, N-to- NV^T conversion efficiencies approaching 1 can be achieved, although such high values are not necessarily desirable (see Secs. V.D and V.E).

In contrast, the charge state efficiency ζ depends on local conditions in the diamond and can be affected by external fields and optical illumination. Increasing ζ benefits sensitivity in two ways: first, by increasing the NV^- concentration and thus the number of collected photons \mathcal{N} from the NV^- ensemble; and second, by decreasing the concentration of NV^0 and the associated background fluorescence, which improves measurement contrast. In the following section we discuss factors contributing to the charge state efficiency and methods to optimize it for sensing.

B. NV charge state efficiency

The charge state efficiency ζ from Eqn. 25, depends on many factors both internal and external to the diamond. For both native NVs (Iakoubovskii *et al.*, 2000) and NVs created by irradiation and annealing of nitrogen-rich diamonds (Mita, 1996), the NV^- and NV^0 charge states can coexist in a single sample. In general, for a given sample and experimental procedure, the steady-state charge state

efficiency is difficult to predict. Contributing factors include the concentration of substitutional nitrogen and other defects serving as charge donors or acceptors (Groot-Berning *et al.*, 2014) and their microscopic distributions (Collins, 2002; Doi *et al.*, 2016); the wavelength, intensity, and duty cycle of optical illumination (Aslam *et al.*, 2013; Doi *et al.*, 2016; Ji and Dutt, 2016; Manson and Harrison, 2005); the application of a bias voltage (Doi *et al.*, 2014; Grotz *et al.*, 2012; Kato *et al.*, 2013; Schreyvogel *et al.*, 2014); and, for near-surface NVs, the diamond surface termination (Chu *et al.*, 2014; Cui and Hu, 2013; Fu *et al.*, 2010; Groot-Berning *et al.*, 2014; Hauf *et al.*, 2011; Kageura *et al.*, 2017; Newell *et al.*, 2016; Osterkamp *et al.*, 2015; Rondin *et al.*, 2010; Santori *et al.*, 2009; Yamano *et al.*, 2017). The charge state efficiency is likely affected by the conditions of diamond growth, as well as the irradiation dose (Mita, 1996) (see Sec. V.D), the annealing duration and temperature, and possibly the operation temperature (Manson and Harrison, 2005). Moreover, the value of the charge state efficiency ζ during an NV⁻ sensing procedure can be difficult to measure. NVs may be reversibly converted between NV⁻ and NV⁰ by various optical and non-optical processes (Aslam *et al.*, 2013; Bourgeois *et al.*, 2017; Khan *et al.*, 2009). Because ζ is strongly affected by the illumination laser intensity and wavelength (Aslam *et al.*, 2013; Bourgeois *et al.*, 2017), characterization of ζ by methods such as Fourier-transform infrared spectroscopy (FTIR), ultraviolet-visible (UV-Vis) spectroscopy, and electron paramagnetic resonance (EPR) may be misrepresentative of NV charge state behavior under the optical illumination employed in most NV-diamond sensing devices.

1. Non-optical effects on NV charge state efficiency

Here we discuss the charge state efficiency ζ in nitrogen-rich diamond in the absence of optical illumination. For shallow NVs, the charge state is strongly affected by the surface chemical termination (Cui and Hu, 2013; Fu *et al.*, 2010; Groot-Berning *et al.*, 2014; Hauf *et al.*, 2011; Rondin *et al.*, 2010). Based on the work in Ref. (Groot-Berning *et al.*, 2014), surface termination should provide enhanced charge state stability to a depth of at least 60 nm and possibly farther (Malinauskas *et al.*, 2008; Santori *et al.*, 2009). The charge state efficiency ζ can also be controlled electrically (Doi *et al.*, 2014; Forneris *et al.*, 2017; Grotz *et al.*, 2012; Hauf *et al.*, 2014; Karaveli *et al.*, 2016; Kato *et al.*, 2013; Murai *et al.*, 2018; Schreyvogel *et al.*, 2015, 2014). Because diamond is an approximately 5.47 eV wide band gap insulator (Wort and Balmer, 2008), Ref. (Collins, 2002) contends that an NV center's charge state depends less on the position of the Fermi level and more on the distance to the nearest charge donor. In nitrogen-rich diamonds, these donors are mainly substitutional nitrogen defects N_S, and the charge state efficiency ζ is seen to increase with the concentration [N_S] (Collins, 2002; Manson and Harrison, 2005). Other defects in the diamond lattice can alter ζ as well; for example, in Ref. (Groot-Berning *et al.*, 2014), the NVs in separate implanted regions containing phosphorus (an elec-

tron donor) and boron (an electron acceptor), were seen to have increased, and respectively decreased, NV charge state efficiencies.

Introduction of electron donors other than nitrogen into diamond might appear to be a promising avenue for increasing the NV charge state efficiency. For example, phosphorus (Doi *et al.*, 2016; Groot-Berning *et al.*, 2014; Murai *et al.*, 2018), with donor level 0.6 eV below the conduction band (Katagiri *et al.*, 2004), is a shallower donor than nitrogen, which lies 1.7 eV below the conduction band (Farer, 1969; Wort and Balmer, 2008). However, creating n-doped diamond through introduction of phosphorus has proven difficult (Kalish, 1999), likely due to an unidentified acceptor introduced along with the phosphorus (Jones *et al.*, 1996). Moreover, irradiation and annealing to create NV centers is expected to also create phosphorus-vacancies (PVs), which are predicted to be deep acceptors (Jones *et al.*, 1996). PVs in diamond will compete with NVs for electrons, undermining the benefit of the phosphorus donors to the charge state efficiency. Additionally, PL emission at wavelengths overlapping the NV⁻ PL spectrum was observed in phosphorus-doped diamond (Cao *et al.*, 1995), further complicating the use of phosphorus in NV-diamond sensing.

The irradiation and annealing procedures applied to increase the N-to-NV^T conversion efficiency χ can also affect the charge state efficiency ζ . In Type Ib diamonds grown by high-pressure-high-temperature (HPHT) synthesis (see Sec. V.C), with [N_S] \gtrsim 50 ppm, ζ approaching 1 is seen after low- and moderate-dose irradiation and annealing (Manson and Harrison, 2005; Mita, 1996). As discussed in Sec. V.D, at higher irradiation doses, the NV⁰ concentration is seen to abruptly increase (Mita, 1996), which can be attributed to the combination of an insufficient concentration of nitrogen defects N_S available to donate electrons to the increasing overall NV population, and an increase in deep acceptor states such as multi-vacancy defects (Pu *et al.*, 2001; Twitchen *et al.*, 1999b).

2. Optical effects on NV charge state efficiency

Optical illumination of diamond may also change the NV charge state efficiency ζ through ionization of NV⁻ to NV⁰ and also recombination of NV⁰ back to NV⁻ (Aslam *et al.*, 2013; Hopper *et al.*, 2016, 2018a; Manson and Harrison, 2005; Waldherr *et al.*, 2011). The steady-state value of ζ is seen to depend on the illumination intensity and wavelength, although most of the reported measurements have been taken on single NV centers (Aslam *et al.*, 2013; Hopper *et al.*, 2016; Waldherr *et al.*, 2011). For example, an excitation wavelength band from 510 nm to 540 nm was found to produce the most favorable single-NV charge state efficiency in steady state compared to longer and shorter wavelengths (Aslam *et al.*, 2013). In particular, when single NVs were illuminated by 532 nm light at intensities typical for pulsed sensing protocols (Hopper *et al.*, 2016; Waldherr *et al.*, 2011) or similar wavelength light at lower intensities (Aslam *et al.*, 2013), a charge state efficiency

$\zeta \sim 70\text{-}75\%$ was observed. However, the value of ζ under these conditions is likely to differ for dense NV ensembles (Manson and Harrison, 2005; Meirzada *et al.*, 2018). For example, measurements in Ref. (Manson and Harrison, 2005) on an NV ensemble in a diamond with $[N_S^T] \sim 70$ ppm and $[NV^T] \sim 1$ ppm show the charge state efficiency dropping to $\sim 50\%$ as the 532 nm power approaches the saturation power of the NV^- optical transition. More study is required to determine the relative contributions to the NV ensemble ζ of optical charge-state switching, the presence of nearby charge donors/acceptors, and other effects.

Recently, several studies on single NV centers have shown improved optical initialization to NV^- by applying near-infrared radiation (NIR) in combination with the 532 nm green excitation light (Chen *et al.*, 2017; Hopper *et al.*, 2016; Ji and Dutt, 2016). This enhanced charge-state initialization has been demonstrated with 780 nm CW radiation (Chen *et al.*, 2017), 1064 nm CW radiation (Ji and Dutt, 2016), and 900 nm-1000 nm pulsed radiation, achieving in the third case $\zeta > 90\%$ (Hopper *et al.*, 2016). The effect is theoretically explained as follows: after absorption of a green photon to enter the electronically excited state, an NV^0 absorbs an NIR photon, which promotes a hole to the valence band and forms NV^- (Hopper *et al.*, 2016; Ji and Dutt, 2016). The mechanism, visualized schematically in Fig. V.1, is the same as the two-photon ionization and recombination of NV^- and NV^0 by 532 nm radiation, but with the second absorbed photon being an NIR photon. In Ref. (Hopper *et al.*, 2016) the NV^0 -to- NV^- recombination process is found to occur with up to a $\sim 7\times$ higher likelihood than the analogous ionization process converting NV^- to NV^0 , wherein the excited-state NV^- absorbs an NIR photon, promoting an electron to the conduction band.

NIR-enhancement of charge state efficiency is expected to be compatible with pulsed initialization and readout. However, when employing 532 nm intensities $I \approx I_{\text{sat}} \approx 2.7 \text{ mW}/\mu\text{m}^2$ (Wee *et al.*, 2007) typical for pulsed experiments, Ref. (Hopper *et al.*, 2016) finds enhancements in ζ to be lessened compared to operation at lower green intensity. Furthermore, if the charge switching rate under green-plus-NIR illumination approaches or exceeds the optical spin polarization rate, spin readout fidelity could be degraded by the increased photoionization during the readout pulse. Refs. (Ji and Dutt, 2016) and (Chen *et al.*, 2017) report charge switching rates near $\sim 1 \mu\text{s}^{-1}$, approaching the singlet state decay rate of $4 \mu\text{s}^{-1}$ (Acosta *et al.*, 2010b). Nonetheless, Hopper *et al.* achieve enhanced charge state initialization with much lower charge switching rates of $\sim 10 \text{ ms}^{-1}$.

Further work is required to determine if this technique can be extended to increase the charge state efficiency ζ in NV ensembles. Ref. (Meirzada *et al.*, 2018) observes no enhancement in the NV^- PL from NIR-plus-green illumination compared to green-only excitation for NV centers in bulk diamond. Moreover, even if NIR-plus-green illumination can enhance the ensemble value of ζ , the power requirements may limit the technique's application to large ensembles. Although the required NIR power for confocal setups addressing single NV^- centers or small ensembles is

modest ($\sim \text{mW}$), the NIR intensity is $\gtrsim 10\times$ higher than the typical 532 nm intensities used for NV^- spin initialization ($I_{\text{NIR}} \approx 23 I_{\text{sat}}^{532 \text{ nm}}$ in Ref. (Hopper *et al.*, 2016)). Thus, when applying the technique to macroscopic ensemble volumes, the maximum addressable ensemble size will quickly be limited by the available laser power. For example, a $(50 \mu\text{m})^2$ spot would require $\gtrsim 100 \text{ W}$ of NIR (Wee *et al.*, 2007). At present, NIR-enhancement of charge state efficiency appears unlikely to yield substantial improvements to ensemble- NV^- magnetometer sensitivities.

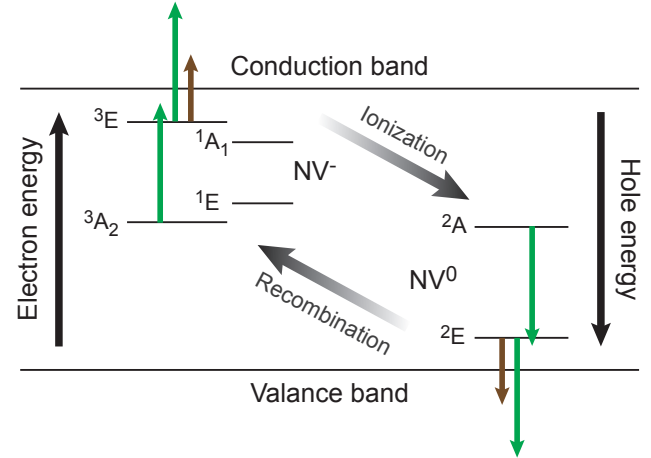


FIG. V.1 Energy level diagrams for NV^- and NV^0 , representing optical ionization and recombination processes through either absorption of two 532 nm photons (green arrows) or a 532 nm photon and an NIR photon (brown arrows)

C. Diamond synthesis and high pressure high temperature treatment

Fabricated bulk diamonds are commonly synthesized using one of two methods. In high pressure high temperature (HPHT) synthesis, a process mimicking natural diamond formation, a carbon source material is mechanically compressed (pressure $> 5 \text{ GPa}$) and heated (temperatures $\gtrsim 1250^\circ\text{C}$) to create conditions where diamond is the thermodynamically favored carbon allotrope. Dissolving the carbon source (typically graphite) in a metal "solvent-catalyst" can increase the growth rate, decrease the required temperature and pressure, and allow for better composition control. Consequently, solvent-catalysts are nearly always employed. A small seed diamond facilitates the growth; the dissolved carbon precipitates out of the metal catalyst solution and crystallizes onto the seed diamond, growing the size. Nitrogen easily incorporates into the diamond lattice, and is historically the primary impurity element in HPHT diamonds. However, nitrogen content in HPHT-synthesized diamonds can be reduced by varying the atomic composition of the metal solvent catalyst to "getter" the nitrogen, and recent advances in getter technology have allowed direct creation of electronic grade HPHT diamond with $[N_S^0] \lesssim 5 \text{ ppb}$ (D'Haenens-Johansson *et al.*, 2015; Tallaire *et al.*, 2017b). References (Dobrinets

et al., 2013; Kanda, 2000; Palyanov *et al.*, 2015) discuss HPHT synthesis in detail.

Plasma-enhanced chemical vapor deposition (PE-CVD) diamond synthesis (Angus *et al.*, 1968) is a popular alternative to HPHT synthesis, and can leverage established semiconductor fabrication techniques. In the most widespread variant of this method, employing homo-epitaxial growth, a diamond seed is exposed to a hydrocarbon plasma consisting of approximately 95 - 99% hydrogen, with the balance composed of carbon and possibly other species such as oxygen or argon. Methane is the most popular carbon source. Radicalized carbon atoms bond with the growth surface, forming a mixture of sp^2 and sp^3 bonded orbitals. Although hydrogen etches both sp^2 and sp^3 bonded carbon, the etch rate for sp^2 bonded carbon is much greater (Schwander and Partes, 2011) and, if the hydrogen etching and carbon deposition rates are carefully tuned, diamond synthesis can be achieved (Angus *et al.*, 1968). Unlike HPHT synthesis, PE-CVD (alternatively simply called CVD) synthesis can easily allow the production of thin or delta doped layers from nanometer to micron scale (McLellan *et al.*, 2016; Ohno *et al.*, 2012), masked synthesis of diamond structures (Zhang and Hu, 2016), or layered epitaxial growth required for PIN (Kato *et al.*, 2013) or NIN structures (Murai *et al.*, 2018).

In the past 15 years, the majority of NV-diamond literature has employed diamonds grown by PE-CVD. First, much early work focused on single NV^- centers; and most HPHT-synthesized diamonds were not available at that time with the requisite low nitrogen concentration ($\lesssim 100$ ppb), as HPHT impurity control can be challenging (Gaukroger *et al.*, 2008; Martineau *et al.*, 2009). Second, the layered deposition inherent to CVD allows straightforward growth of epitaxial layers (as would be required for magnetic imaging devices) and the application of semi-conductor techniques to control diamond composition. Third, the PE-CVD method was historically more popular with commercial collaborators (such as Element Six and Apollo Diamond) responsible for producing the majority of scientific diamonds containing NV^- centers.

In addition, several challenges accompany direct HPHT synthesis of high-quality NV-diamonds. For one, solvent-catalyst incorporation into the diamond lattice may result in metal inclusions with size visible to the naked eye. Such inclusions could be particularly problematic for magnetic sensing applications, since the common materials employed in the solvent catalyst alloys are the ferromagnetic elements Fe, Co, and Ni (Palyanov *et al.*, 2015). The purity of HPHT-synthesized diamonds may be limited by the solid precursor materials, which may not be available with as high chemical or isotopic purity as the gas-phase precursor elements employed for CVD synthesis. Finally, the HPHT process is not intrinsically amenable to fabrication of NV^- -rich layers, as are needed for imaging applications. In spite of these challenges, HPHT-fabricated diamonds with good characteristics for ensemble- NV^- DC magnetometry - including long T_2^* ($\gtrsim 2$ μ s), high E_{conv} ($\sim 30\%$), and $[N^T] \sim 1$ -4 ppm - have been recently reported in the literature (Grezes *et al.*, 2015; Stürner *et al.*, 2019; Wolf *et al.*,

2015) (see Table V.1).

While the exact motivation for HPHT diamond synthesis is not always explicitly stated (Teraji *et al.*, 2013), HPHT synthesis may circumvent undesired characteristics inherent to CVD-synthesized diamonds (Charles *et al.*, 2004; Hartland, 2014). A serious disadvantage of CVD synthesis is the incorporation of unwanted impurities and charge traps into the lattice (see Sec. V.F). In addition, CVD-grown diamonds may display undesirable strain non-uniformities or contain a high dislocation density. For example, CVD-grown diamonds sometimes exhibit a brown coloration, which is attributed to vacancy cluster incorporation during synthesis (Hounscome *et al.*, 2006; Khan *et al.*, 2013). As vacancy clusters, chains, and rings are typically paramagnetic (Baker, 2007; Iakoubovskii and Stesmans, 2002; Lomer and Wild, 1973; Yamamoto *et al.*, 2013b), these clusters can increase NV^- ensemble dephasing, reducing T_2^* . Additionally, since such vacancy chains and clusters are deeper electron acceptors than NV^- (Edmonds *et al.*, 2012; Khan *et al.*, 2009), their presence may decrease measurement contrast (Tallaire *et al.*, 2017a). Naturally occurring diamond that has not undergone irradiation rarely contains vacancies (Mainwood, 1999), suggesting that vacancies and vacancy clusters should be uncommon in well-synthesized HPHT diamond. As point defects, dislocations, and other extended defects are believed to be the dominant sources of strain in Type IIa diamonds (Fisher *et al.*, 2006), HPHT-synthesized diamonds may also exhibit lower strain than their CVD-grown counterparts. While dislocation densities of $\approx 10^4$ - 10^6 cm^{-2} are typical in CVD-grown diamonds (Achard *et al.*, 2014), certain HPHT-synthesized diamonds can demonstrate dislocation densities of ≈ 100 - 1000 cm^{-2} (Martineau *et al.*, 2009; Tallaire *et al.*, 2017b) and substantially lower strain (D’Haenens-Johansson *et al.*, 2015, 2014).

Although more research is needed, it is observed that the high quantity of hydrogen present during CVD growth can result in hydrogen incorporation into the diamond lattice (Charles *et al.*, 2004; Goss *et al.*, 2014), (see Sec. V.F). In contrast, diamonds synthesized directly by HPHT are unlikely to have hydrogen defects, as only one hydrogen-related defect has been found to incorporate into HPHT-synthesized diamond (Hartland, 2014).

Alternatively, mixed-synthesis approaches can combine the strengths of CVD and HPHT. One popular method is HPHT treatment, where an existing CVD diamond is heated and subjected to high pressure, resulting in atomic-scale reconfigurations of atoms in the lattice while leaving the macro-scale diamond largely unchanged (Dobrinets *et al.*, 2013). HPHT treatment effectively removes single vacancies (Collins *et al.*, 2000; Dobrinets *et al.*, 2013) and causes vacancy clusters to dissociate (Collins *et al.*, 2000; Dobrinets *et al.*, 2013) or aggregate (Bangert *et al.*, 2009). Thus, this method is effective to treat CVD-grown diamonds, which can exhibit vacancies and vacancy clusters (Charles *et al.*, 2004; Hartland, 2014; Khan *et al.*, 2013). The approach of applying HPHT treatment to CVD diamonds was proposed in Ref. (Twitchen *et al.*, 2010) and realized by the author of Ref. (Hartland, 2014), wherein a

CVD-grown diamond was HPHT treated after synthesis but prior to irradiation and subsequent annealing (see Secs. V.D and V.E). The diamond produced in Ref. (Hartland, 2014) exhibits a notably high 30% conversion efficiency $E_{\text{conv}} = [\text{NV}^-]/[\text{N}^T]$ as shown in Table V.5. A similar process pioneered by Lucent Diamonds employs HPHT treatment of diamonds prior to irradiation and annealing (Vins, 2007). This process results in a final material with an intense red hue and photoluminescence dominated by NV^- emission (Dobrinets *et al.*, 2013; Wang *et al.*, 2005), suggesting that HPHT treatment can be effective to increase the charge state efficiency ζ , likely by eliminating charge traps.

However, HPHT treatment cannot address all diamond deficiencies, CVD-related or otherwise. For example, should a CVD-synthesized diamond incorporate high concentrations of hydrogen or other elemental impurities into the diamond lattice during growth, HPHT treatment is ineffective to remove these impurities (Charles *et al.*, 2004). Such treatment is also limited to diamonds with balanced aspect ratios, as thin plates or rods will likely crack under the high applied pressure.

In addition to HPHT treatment of existing diamonds, other mixed-synthesis approaches have also been pursued. For example, utilizing type IIa HPHT seeds for CVD growth rather than CVD-grown seeds can yield material with lower strain and reduced densities of dislocations and other unwanted defects (Gaukroger *et al.*, 2008; Hoa *et al.*, 2014; Martineau *et al.*, 2009; Tallaire *et al.*, 2017b). Another mixed-synthesis method exploits the fine composition control and high chemical purities available with CVD synthesis to create the carbon precursor for HPHT synthesis (Teraji *et al.*, 2013). The diamond composition can thus be carefully controlled, and HPHT synthesis can take advantage of high-purity or isotopically enriched gaseous sources (e.g., methane or $^{15}\text{N}_2$).

Given the prominent role lattice defects and elemental impurities play in determining the charge state efficiency and coherence times for NV^- , additional research focused on synthesizing sensing-optimized diamonds is warranted.

D. Electron irradiation

For unmodified as-grown CVD diamond, realized conversion efficiency values E_{conv} can be far less than unity, as shown in Table V.2, where the majority of substitutional nitrogen is not converted to NV^- (Edmonds *et al.*, 2012; Hartland, 2014). In fact, for some CVD diamonds (see Table V.3) the concentration of grown-in monovacancies is insufficient to achieve good E_{conv} for total nitrogen concentration $[\text{N}^T] \gtrsim 1$ ppm regardless of location; even if every monovacancy were adjacent to a substitutional nitrogen, the conversion efficiency E_{conv} would still be low (Deák *et al.*, 2014; Mainwood, 1999). However, the monovacancy concentration can be augmented after growth by irradiating the diamond with energetic particles. The high-energy irradiating particles knock carbon atoms out of the diamond lattice, creating both interstitial carbon atoms and monovacancies (Newton *et al.*, 2002; Twitchen *et al.*, 1999a). Al-

though theoretical calculations have not yet completely converged with experimental observations (Deák *et al.*, 2014; Zaitsev *et al.*, 2017), the widely accepted model posits that upon subsequent annealing (discussed in Sec. V.E), diffusing vacancies are captured by substitutional nitrogen atoms, forming NV centers (Acosta *et al.*, 2009). Primary considerations in the irradiation process are the particle type, energy, and dose.

The irradiation of diamond has been performed using a variety of particles: protons, ionized deuterium atoms, neutrons, and electrons (Ashbaugh III, 1988). Gamma ray irradiation from ^{60}Co has also been used (Ashbaugh III, 1988; Campbell and Mainwood, 2000). Many of these particles are suboptimal for NV creation, however, where only single monovacancies V^0 are desired, and other created defects are likely deleterious. A particular problem for certain irradiation methods is the production of “knock-on-atoms” (Campbell and Mainwood, 2000; Davies *et al.*, 2001), where the irradiating particle has sufficient energy not only to displace an initial carbon atom from the lattice, but to impart enough kinetic energy to that carbon that it displaces additional carbon atoms, resulting in localized lattice damage (Buchan *et al.*, 2015). Although annealing (see Sec. V.E) can partially alleviate such damage, the lattice damage can never be completely repaired (Balmer *et al.*, 2009; Fávaro de Oliveira *et al.*, 2017, 2016; Lobaev *et al.*, 2017; Twitchen *et al.*, 2010) and may result in unwanted paramagnetic defects or charge traps. For irradiation with protons, neutrons, or ionized deuterium atoms, damage from such knock-on-atoms can be severe. Similar lattice damage occurs from ion implantation of various species such as nitrogen (Fávaro de Oliveira *et al.*, 2017; Naydenov *et al.*, 2010; Yamamoto *et al.*, 2013b), carbon (Naydenov *et al.*, 2010; Schwartz *et al.*, 2011), and helium nuclei (Himics *et al.*, 2014; Kleinsasser *et al.*, 2016; McCloskey *et al.*, 2014; Schwartz *et al.*, 2011; Waldermann *et al.*, 2007). Electrons, with their lower mass, transfer less kinetic energy to the carbon atoms and are therefore better suited to creating isolated monovacancies. Electron irradiation is favored over gamma ray irradiation because the former can be accomplished in hours whereas the latter, when implemented using ^{60}Co , can take weeks (Collins, 2007). In summary, electron irradiation is preferred to create NV^- ensembles optimized for sensing applications (Campbell *et al.*, 2002; Twitchen *et al.*, 2010; Uedono *et al.*, 1999), as this method allows for evenly distributed monovacancies to be created throughout the diamond in a timely manner, with less lattice damage than alternative methods.

Theoretical calculations predict monovacancy creation requires electron energies $\gtrsim 165$ keV (Campbell *et al.*, 2002), which is consistent with experimental data wherein vacancy creation is observed for electron irradiation along the [100] direction at 180 keV but not 170 keV (Koike *et al.*, 1992). Crude estimates suggest electron irradiation energies between 0.5 and 0.8 MeV will create mainly single vacancies (Loubser and van Wyk, 1978; Mitchell, 1965) and avoid producing multi-vacancy complexes. While this estimate is consistent with Ref. (Dannefaer *et al.*, 1992) where divacancies are detected after irradiation with 3.5 MeV electrons,

Reference	T_2^*	T_2	E_{conv}	$[\text{NV}^-]$	$[\text{NV}^0]$	$[\text{N}^{\text{T}}]$	^{13}C	Synthesis
(Grezes <i>et al.</i> , 2015)	$\sim 2.6 \mu\text{s}$	$84 \mu\text{s}$	29%	0.4 ppm	0.4 ppm	1.4 ppm	300 ppm	HPHT
(Wolf <i>et al.</i> , 2015)	-	$\sim 50 \mu\text{s}$	30%	0.9 ppm	-	3 ppm	-	HPHT
(Zheng <i>et al.</i> , 2018)	$\geq 1.4 \mu\text{s}$	-	-	$\sim 0.9 \text{ ppm}$	-	$> 2.9 \text{ ppm}$	300 ppm	HPHT
(Hartland, 2014)	-	-	28%	1.2 ppm	0.7 ppm	4.1 ppm	10700 ppm	CVD+HPHT
This work	$1.55 \mu\text{s}$	$15.7 \mu\text{s}$	$\sim 30\%$	$\sim 3 \text{ ppm}$	-	$\sim 10 \text{ ppm}$	100 ppm	CVD
(Barry <i>et al.</i> , 2016)	580 ns	$5.1 \mu\text{s}$	6.3%	$\sim 1.7 \text{ ppm}$	-	27 ppm	10 ppm	CVD
(Schloss <i>et al.</i> , 2018)	450 ns	$7 \mu\text{s}$	$\sim 14\%$	3.8 ppm	2.0 ppm	$\sim 28 \text{ ppm}$	10700 ppm	CVD

TABLE V.1 Partial literature survey of diamonds with properties well-suited to ensemble- NV^- magnetometry. Diamonds with long T_2^* , high N-to- NV^- conversion efficiency E_{conv} , and $[\text{NV}^-] \gtrsim 1 \text{ ppm}$, are expected to be particularly favorable for high sensitivity magnetometry applications. Dashed lines (-) indicate values not reported or unknown.

E_{conv}	$[\text{N}^{\text{T}}]$	Growth location	Reference
0.0007 – 0.005	$3 \times 10^{-7} - 3 \times 10^{-5}$	Element Six	(Edmonds <i>et al.</i> , 2012)
0.0006 – 0.03	$3.5 \times 10^{-7} - 2.4 \times 10^{-6}$	Apollo Diamond Inc.	(Edmonds <i>et al.</i> , 2012)
0.02 – 0.03	4×10^{-6}	Warwick University	(Hartland, 2014)

TABLE V.2 Realized values of E_{conv} for unmodified CVD diamond.

$[\text{V}^0 + \text{V}^-]$	Reference
6×10^{-8}	(Rutledge and Gleason, 1998)
$\lesssim 2 \times 10^{-8}$	(Twitchen <i>et al.</i> , 2010)
$\lesssim 3 \times 10^{-11}$	(Mainwood, 1999)

TABLE V.3 Native fractional content of monovacancies in bulk CVD diamond

Ref. (Twitchen *et al.*, 2010), however, finds no evidence of vacancy pairs after irradiation with 4.6 MeV electrons, suggesting that several-MeV irradiation energies may be safe. The optimal irradiation energy may also depend on sample geometries; thicker diamonds should require higher energies to ensure vacancies are created uniformly through the entire thickness (Campbell and Mainwood, 2000; Twitchen *et al.*, 2010). For small ensembles close to the diamond surface, an electron microscope can provide the needed irradiation (Farfurnik *et al.*, 2017; Kim *et al.*, 2012; McLellan *et al.*, 2016; Schwartz *et al.*, 2012). More study is required to resolve remaining discrepancies between experimental data and detailed simulations of the electron irradiation process (Campbell *et al.*, 2002; Campbell and Mainwood, 2000). For example, recent measurements of monovacancy density profiles versus depth, as judged by GR1 intensities in 1 MeV electron irradiated diamonds (Zaitsev *et al.*, 2017), are inconsistent with Monte Carlo simulations in Refs. (Campbell *et al.*, 2002; Campbell and Mainwood, 2000).

The irradiation dose should also be approximately matched to the diamond’s total nitrogen concentration $[\text{N}^{\text{T}}]$ as suggested in Sec. V.A; if too many vacancies are created, then $> 50\%$ of N_s will be converted to NV^0 , and the number of electrons donated by the remaining N_s will be insufficient to convert every NV^0 to NV^- . Figure 2 in Ref. (Mita,

1996) illustrates the importance of matching the irradiation dose to $[\text{N}^{\text{T}}]$ to achieve maximal E_{conv} . When determining irradiation dose, in-situ recombination between a vacancy and an interstitial carbon should be accounted for (Campbell and Mainwood, 2000; Davies *et al.*, 2001). Current estimates suggest approximately 30% (Campbell and Mainwood, 2000) to 50% (Davies *et al.*, 2001) of initially created vacancies are immediately lost to spontaneous recombination. For example, using 1 MeV electrons (generating $\sim 2 \times 10^{-4}$ vacancies/electron/ μm according to Ref. (Campbell and Mainwood, 2000), and assuming 40% of vacancies recombine immediately and two nitrogens are required to make a single NV^- center, we expect a sample with $[\text{N}^{\text{T}}] \sim 1 \text{ ppm}$ to require a dose of $7.3 \times 10^{16} \text{ cm}^{-2}$. However, fine-tuning of the irradiation dose is often done empirically, suggesting either the presence of dynamics more complicated than those included in the simple model presented here (i.e., the presence of other vacancy traps, the formulation of divacancies, loss at surfaces, etc.) or errors in the measured electron flux or substrate temperature (Campbell and Mainwood, 2000). For example, while the production rate of neutral monovacancies from irradiation with 2 MeV electrons is found to be temperature-independent from room temperature to $\sim 300 \text{ }^\circ\text{C}$, the rate decreases notably for higher temperatures (Newton *et al.*, 2002).

E. Low pressure high temperature annealing

For the successful creation of NV^- centers, substitutional nitrogen and monovacancies must be relocated to occupy adjacent sites in the diamond lattice. This process can be accomplished via diffusion at elevated temperature, i.e., annealing. Since monovacancies migrate in the neutral charge state V^0 (Breuer and Briddon, 1995) with an activation energy of $E_a = 2.3 \pm 0.3 \text{ eV}$ (Davies *et al.*, 1992; Mainwood, 1999), compared to measured values of $E_a = 4.8\text{--}6.2 \text{ eV}$ for

substitutional nitrogen (Deák *et al.*, 2014; Dobrinets *et al.*, 2013; Jones *et al.*, 2015), neutral monovacancies diffuse throughout the lattice during annealing until they reach the more immobile nitrogens. The negatively charged monovacancy's higher activation energy (Breuer and Briddon, 1995) ensures that monovacancy diffusion occurs predominantly in the neutral charge state (Breuer and Briddon, 1995), although a negative monovacancy can convert to a neutral monovacancy in a reversible charge transfer process (Davies *et al.*, 1992). The diffusion constant D of the neutral monovacancy is (Hu *et al.*, 2002; Orwa *et al.*, 2012)

$$D = D_0 e^{-E_a/k_B T}, \quad (26)$$

where k_B is the Boltzmann constant, T is the temperature, and D_0 is a diffusion prefactor (see Appendix A.10). The diffusion constant D has been measured to be $\sim 1.1 \text{ nm}^2/\text{s}$ (Baranov *et al.*, 2017; Jelesko and Wrachtrup, 2008; Martin *et al.*, 1999) at 750 °C, suggesting D_0 is in good agreement with theoretical calculations (Fletcher and Brown, 1953) and with an independently measured upper bound (Acosta *et al.*, 2009). Other sources, however find or employ different values for D_0 or E_a (Hu *et al.*, 2002; Onoda *et al.*, 2017; Orwa *et al.*, 2012), suggesting that further measurements are warranted. Once an NV center is formed, the deeper binding energy of the nitrogen-vacancy bond relative to the neutral vacancy ensures that the bound vacancy does not diffuse away (Goss *et al.*, 2005; Hartland, 2014).

The procedure described here is commonly termed low pressure high temperature (LPHT) annealing to distinguish it from high pressure high temperature (HPHT) annealing (discussed in Sec. V.C). Given the role of diffusion in LPHT treatment, the annealing temperature and annealing duration are important control parameters. A temperature of ~ 800 °C is usually employed (Botsoa *et al.*, 2011), given that monovacancies become mobile around 600 °C (Davies *et al.*, 1992; Kiflawi *et al.*, 2007; Uedono *et al.*, 1999; ?), and annealing times of several hours are typical, e.g., 2 hours in Ref. (Acosta *et al.*, 2009), 4 hours in Ref. (Lawson *et al.*, 1998), 8 hours in Ref. (Twitcheen *et al.*, 2010), 12 hours in Ref. (Barry *et al.*, 2016), and 16 hours in Ref. (Fraczek *et al.*, 2017). Diamonds with lower values of $[\text{N}^{\text{T}}]$ are expected to require longer annealing times due to the greater initial distances between vacancies and substitutional nitrogens. A study by Element Six found no observable deleterious changes in diamond properties between samples that were annealed at ~ 800 °C for ~ 8 hours and samples that were annealed at the same temperature for longer periods (Twitcheen *et al.*, 2010). This ~ 800 °C annealing step is typically performed under vacuum or in a non-oxidizing, inert gaseous environment to avoid graphitization (Dobrinets *et al.*, 2013). Under vacuum, present understanding is that diamond graphitization begins roughly around 1500 °C (Davies and Evans, 1972).

Although the 800 °C LPHT treatment is effective to create NVs, unwanted defects may form as well. For example, diffusing monovacancies can combine to form divacancies (Twitcheen *et al.*, 1999b), which are immobile at 800 °C. As deeper electron acceptors than NVs (Deák *et al.*, 2014;

Miyazaki *et al.*, 2014), the presence of divacancies reduces E_{conv} . To mitigate divacancy formation, electron irradiation with in-situ (i.e., simultaneous) annealing has been proposed (Nöbauer *et al.*, 2013). Under such conditions, single vacancies are continuously created in an environment consisting primarily of substitutional nitrogen (and, as the process progresses, NVs), thereby reducing divacancy formation. Although preliminary work in Ref. (Nöbauer *et al.*, 2013) finds electron irradiation with in-situ annealing increases T_2^* , no increase in E_{conv} is observed, and further investigation is warranted.

Following NV formation, further LPHT annealing above 800 °C may reduce strain or paramagnetic impurities resulting from lattice damage. For example, divacancies can combine into other defects at ~ 900 °C (Twitcheen *et al.*, 1999b). Reduction of a given defect species may be effected by consolidation into other larger defect species, which may be paramagnetic (Baker, 2007; Hartland, 2014; Lomer and Wild, 1973; Yamamoto *et al.*, 2013b). Annealing to temperatures of 1000 °C to 1200 °C is shown to extend the T_2 of both single NV^- centers (Naydenov *et al.*, 2010; Yamamoto *et al.*, 2013b) and ensembles (Tetienne *et al.*, 2018) created by ion implantation. As this increase is attributed to a reduction in paramagnetic multi-vacancy defects (Tetienne *et al.*, 2018; Yamamoto *et al.*, 2013b), improvement in T_2^* is expected as well, though this expectation has not been systematically confirmed in experiment. Practically, this additional LPHT treatment is limited by the temperature at which NVs anneal out, which is typically around 1400 °C to 1500 °C (Hartland, 2014; Pinto *et al.*, 2012; Zaitsev, 2001) and can vary depending on the presence of other defect species within the diamond (Zaitsev, 2001). While a systematic study of annealing temperatures and durations is warranted for engineering optimal samples for ensemble-NV $^-$ sensing, a standard recipe for samples is at least several hours at ~ 800 °C followed by several more hours at ~ 1200 °C (Breeze *et al.*, 2018; Chu *et al.*, 2014; Fraczek *et al.*, 2017). Some example calculations for annealing are detailed in Appendix A.10.

F. Other common impurities in synthetic or treated single crystal diamond

Unwanted species in the diamond lattice can degrade magnetometer performance by decreasing the NV charge state efficiency $\zeta = [\text{NV}^-]/[\text{NV}^{\text{T}}]$, creating local magnetic noise, or reducing the fraction of substitutional nitrogen N_S converted to NV^- . This section restricts detailed discussion to multivacancy clusters and NVH (Khan *et al.*, 2013), species present in diamond at sufficient concentrations to likely affect NV spin and charge dynamics. Extended discussion of other defects can be found in Refs. (Deák *et al.*, 2014; Newton, 2007); see also Table V.4 for relevant defects commonly found in diamond.

Multivacancy clusters are common in some diamonds grown by chemical vapor deposition (CVD) (Hounscome *et al.*, 2006; Pu *et al.*, 2000), and are believed to cause the brown coloration in CVD-grown diamond (Fujita *et al.*,

Diamond defect	Ground state spin
N_S^0	$S = 1/2$
N_S^+	$S = 0$
NV^+	$S = 0$
NV^0	$S = 1/2$
NV^-	$S = 1$
NVH^-	$S = 1/2$
NVH^0	$S = 0$
N_2V^-	$S = 1/2$
N_3V^0	$S = 1/2$
N_2VH^0	$S = 1/2$
VH^0	$S = 1/2$
VH^-	$S = 1$
V_nH^-	$S = 1$
V^+	$S = 1/2$ (Baranov <i>et al.</i> , 2017)
V^0	$S = 0$ (Baranov <i>et al.</i> , 2017)
V^-	$S = 3/2$ (Baranov <i>et al.</i> , 2017)
VV^-	$S = 3/2$ (Kirui <i>et al.</i> , 2013)
VV^0	$S = 1$ (Twitchen <i>et al.</i> , 1999b)

TABLE V.4 Common defects in diamond and their ground state electronic spin.

2009; Hounscome *et al.*, 2006). During CVD synthesis, the diamond surface can become rough and stepped. When these steps are rapidly covered with additional deposited material, small voids, i.e., clusters of vacancies, can be left in the diamond (Hounscome *et al.*, 2006; Khan *et al.*, 2013). Multivacancy cluster incorporation has been observed to increase at high growth rates (Hounscome *et al.*, 2006), and may be correlated with nitrogen content (Pu *et al.*, 2000). Using positron annihilation, the authors of Ref. (Dannefaer *et al.*, 1993) found the density of multivacancy clusters was found to be roughly $10^{17} - 10^{18} \text{ cm}^{-3}$ for their growth conditions. Such vacancy clusters can trap electrons (Campbell *et al.*, 2002; Deák *et al.*, 2014; Edmonds *et al.*, 2012; Jones *et al.*, 2007), reducing the ratio of NV^- to NV^0 and also generating magnetic noise resulting from their trapped unpolarized electron spins. The neutral divacancy V_2^0 (Deák *et al.*, 2014; Lea-wilson *et al.*, 1995; Slepetz and Kertesz, 2014; Twitchen *et al.*, 1999b) and neutral multivacancy chains (V_n^0 , $n \geq 3$) are paramagnetic (Baker, 2007; Iakoubovskii and Stesmans, 2002; Lomer and Wild, 1973), and increase environmental magnetic noise. Irradiation or implantation followed by annealing can also produce such defects (Naydenov *et al.*, 2010; Yamamoto *et al.*, 2013b). Low pressure high temperature annealing is effective to remove certain multivacancy clusters. However, as the removal of multivacancy clusters is effected by aggregating these species together or combining them with other defects, the reduction of smaller multivacancy defects may be accompanied by an increase in larger multivacancy clusters or other defects. High pressure high temperature (HPHT) treatment effectively removes single vacancies (Dobrinets *et al.*, 2013) and causes some vacancy clusters to dissociate (Dobrinets *et al.*, 2013), which may aggregate to form

different multivacancy clusters (Bangert *et al.*, 2009). See Sec. V.C.

Another common impurity in diamond is hydrogen, which gives rise to many defects (Dobrinets *et al.*, 2013; Goss *et al.*, 2014; Zaitsev, 2001). For typical CVD diamond growth, the plasma is composed predominantly of hydrogen ($\gtrsim 95\%$) (Tokuda, 2015), which can incorporate into single crystal diamond at concentrations as high as 1000 ppm (Sakaguchi *et al.*, 1999). The hydrogen incorporation rate into the lattice is partially dependent upon the diamond growth recipe (Tang *et al.*, 2004), and further investigation into the hydrogen quantity incorporated and methods to mitigate hydrogen incorporation is warranted. Hydrogen-related defects may influence the NV charge state (Hauf *et al.*, 2011; Lyons and de Walle, 2016). Additionally, at high enough concentrations the nuclear spin of hydrogen may result in non-negligible dephasing or decoherence. At present we are unaware of any published method to effectively remove hydrogen from the bulk diamond lattice (Charles *et al.*, 2004; Hartland, 2014).

The presence of hydrogen in the diamond lattice can enable formation of the NVH defect (Glover *et al.*, 2003), wherein the hydrogen occupies the vacancy of an NV. In as-grown nitrogen-enriched CVD diamond, the ratio of $([N_S^+] + [N_S^0]) : [NVH^-] : [NV^-]$ was found to be approximately 300:30:1 in Ref. (Edmonds *et al.*, 2012) and 52:7:1 in Ref. (Hartland, 2014). The NVH species is undesirable because: (i) it lowers the conversion efficiency of incorporated nitrogen to NV centers; (ii) it reduces the concentration of substitutional nitrogen N_S available to donate electrons to turn NV^0 defects into NV^- ; (iii) NVH competes with NV as an electron acceptor; (iv) NVH^- is paramagnetic, causing magnetic noise; and (v) the hydrogen in NVH may rapidly tunnel among the three adjacent carbon atoms at GHz frequencies, resulting in high-frequency magnetic or electric noise (Edmonds, 2008).

No known treatment can transform existing NVH defects into NV defects. The NVH complex is stable against annealing up to approximately 1600 °C but anneals out completely by 1800 °C (Hartland, 2014; Khan *et al.*, 2013). However, removal of NVH via annealing is not associated with increased NV concentration; rather, further isochronal annealing to 2000 °C and 2200 °C is accompanied by increases in N_2VH^0 and N_3VH^0 species (Hartland, 2014), suggesting the NVH concentration is reduced via aggregation of NVH with one or more nitrogen atoms. NVH^0 exhibits absorption at 3123 cm^{-1} (Cann, 2009) but is otherwise not known to be optically active.

Diamonds subject to temperatures at which substitutional nitrogen or interstitial nitrogen become mobile may exhibit defects consisting of aggregated nitrogen, such as N_2 (Boyd *et al.*, 1994; Tucker *et al.*, 1994; ?), N_2V (Green *et al.*, 2015), N_2VH (Hartland, 2014), N_3V (Green *et al.*, 2017), N_3VH (Hartland, 2014; Liggins, 2010), N_4V (Bursill and Glaisher, 1985), or other aggregated nitrogen defects (Goss *et al.*, 2004). The presence of aggregated nitrogen defects reduces the quantity of nitrogen available to form NV centers or donate electrons to NV^0 to form NV^- , and can cause additional paramagnetic noise. Other

defects such as VH (Glover, 2003; Glover *et al.*, 2004), V_2H (Cruddace, 2007; Shaw *et al.*, 2005), and OV (Cann, 2009; Hartland, 2014) have been identified in synthetic diamond and may act as charge acceptors or create additional paramagnetic noise. However most defects discussed in this paragraph are observed at concentrations low enough to be neglected for diamonds fabricated for NV^- magnetometry, as shown in Table V.5, reproduced from Ref. (Hartland, 2014). Additional defect species are inferred to exist from charge conservation arguments but have not been directly observed (Khan *et al.*, 2009). More research is needed to better understand defects in synthetic diamond grown for magnetometry applications.

G. Preferential orientation

In naturally occurring and many fabricated diamonds, NV^- centers are distributed evenly among all four crystallographic orientations. However, under certain circumstances, CVD-grown diamond can exhibit preferential orientation of NV^- centers along certain crystallographic axes (Edmonds *et al.*, 2012; Pham *et al.*, 2012b). Several research groups have achieved almost perfect alignment of all NV^- centers along the a single [111] axis. Michl *et al.* demonstrated 94% alignment (Michl *et al.*, 2014), Lesik *et al.* demonstrated 97% alignment (Lesik *et al.*, 2014), and Fukui *et al.* demonstrated 99% alignment (Fukui *et al.*, 2014). The mechanism for preferential orientation is explained in Ref. (Miyazaki *et al.*, 2014).

An ensemble- NV^- magnetometer utilizing a single NV^- orientation in a diamond with no preferential orientation suffers from reduced measurement contrast due to unwanted PL from NV^- centers of other orientations. A diamond with 100% preferential orientation may allow a $4\times$ increase in contrast. In practice, though, the enhancement is typically somewhat less than $4\times$, since polarized excitation light can already be used to selectively address particular NV^- orientations (Lesik *et al.*, 2014), and high bias fields can suppress fluorescence from off-axis NV^- centers (Epstein *et al.*, 2005; Tetienne *et al.*, 2012).

Diamonds grown with preferential orientation have at least two main drawbacks. First, NV^- concentrations for preferentially grown diamonds in the literature are currently relatively low (Fukui *et al.*, 2014; Lesik *et al.*, 2014; Michl *et al.*, 2014), typically around 10^{12} cm^{-3} although concentrations up to 10^{15} cm^{-3} have been achieved (Tahara *et al.*, 2015). Second, it appears that the N-to- NV^- conversion efficiency cannot be increased through irradiation and subsequent annealing without destroying the preferential alignment, although conflicting evidence on this topic has been reported (Fukui *et al.*, 2014). Since electron irradiation followed by annealing can increase the N-to- NV^- conversion efficiency by $\sim 10\times$ to $100\times$, preferential orientation is not currently believed to be a viable method to achieve better ensemble magnetometry sensitivity. However it is possible that future technical advances or treatment could alter this understanding. Additionally, preferential orientation precludes the implementation of vector magne-

tometry (Schloss *et al.*, 2018).

VI. MISCELLANEOUS SENSING TECHNIQUES

A. Rotary echo magnetometry

Broadband magnetometry can also be performed using a MW pulse scheme called rotary echo (Aiello *et al.*, 2013; Mkhitarian and Dobrovitski, 2014; Mkhitarian *et al.*, 2015). In this technique pioneered by Aiello *et al.* (Aiello *et al.*, 2013), rotary echoes are produced by periodic reversals of the driving field. The simplest protocol inverts the phase of the driving field to reverse the sign of the Rabi oscillations. The rotary echo technique may have utility for certain niche applications such as event detection (Aiello *et al.*, 2013), but the method so far yields worse sensitivity than a Ramsey protocol. Like other dynamical-decoupling-type methods, rotary echo can be tailored to reject noise at certain frequencies and also has applications for certain narrowband AC sensing, such as detection of individual nuclear spins (Mkhitarian *et al.*, 2015).

B. Geometric phase magnetometry

In the presence of particular DC and RF magnetic fields, an NV^- spin may accumulate a measurable geometric phase (Berry, 1984) in addition to a dynamical phase. Following demonstrations of control and readout of an NV^- center's geometric phase (Arroyo-Camejo *et al.*, 2014; Maclaurin *et al.*, 2012; Yale *et al.*, 2016; Zhou *et al.*, 2017; Zu *et al.*, 2014), the authors of Ref. (Arai *et al.*, 2018) implemented geometric phase measurements for DC magnetometry. In their protocol, depicted in Fig. VI.1, the phase of a MW Rabi drive is swept adiabatically around a closed phase-space loop during two intervals separated by a central π -pulse. Whereas the π -pulse cancels the dynamic phase accumulated during the sequences, the acquired geometric phase depends on the strength of the DC magnetic field. While this technique enables wide-dynamic-range field sensing by avoiding a 2π phase ambiguity inherent to Ramsey magnetometry, it is unlikely to enhance sensitivity with respect to optimized Ramsey.

C. Ancilla-assisted upconversion magnetometry

A clever and novel magnetometry scheme pioneered by Ajoy *et al.* in Ref. (?) utilizes frequency upconversion via an ancilla nuclear spin to make broadband measurements of an external magnetic field. The method works as follows: A large magnetic field is aligned along the NV^- internuclear axis and tuned to near the ground state level anti-crossing (GSLAC) at ≈ 1024 gauss, allowing the relative strengths of the Zeeman term and the hyperfine coupling of the NV^- electronic spin to the ancilla nuclear spin to be precisely tuned. In this regime, the NV^- electronic spin is first-order insensitive to magnetic fields perpendicular to the NV^- symmetry axis. However, an applied transverse magnetic field

Defect	As-grown	1500 °C anneal	Irradiation	800 °C anneal
$[N_S^0]$ (ppb)	1620 (160)	1100 (100)	200 (20)	120 (15)
$[N_S^+]$ (ppb)	1500 (150)	2200 (250)	3000 (300)	1000 (100)
$[NV^0]$ (ppb)	≤ 10	≤ 10	≤ 10	695 (70)
$[NV^-]$ (ppb)	60 (5)	40 (5)	35 (5)	1160 (120)
$[NVH^0]$ (ppb)	500 (50)	310 (30)	380 (40)	290 (30)
$[NVH^-]$ (ppb)	405 (40)	200 (20)	obscured	20 (5)
$[N_2VH^0]$ (ppb)	< 0.1	22 (3)	obscured	24 (5)
$[V_nH^-]$ (ppb)	3.1 (1)	≤ 0.1	25 (3)	41 (4)

TABLE V.5 Concentrations of quantifiable defects in sample GG1 in the as-grown state and after each treatment stage. Table reproduced from Ref. (Hartland, 2014).

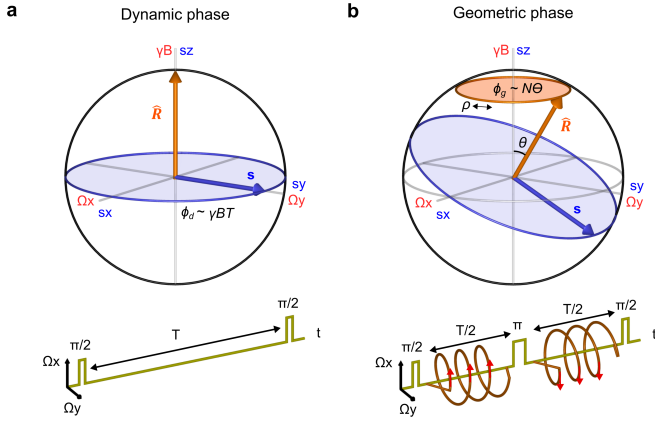


FIG. VI.1 Comparison of dynamic and geometric phase magnetometry. For dynamic phase magnetometry (i.e., Ramsey), the Bloch vector (blue arrow), is optically prepared and then rotated by a $\pi/2$ -pulse to the equator. The Bloch vector then precesses about the fixed Larmor vector (orange arrow) before being mapped into a population difference by a second $\pi/2$ -pulse and read out optically. b) For geometric-phase magnetometry, the Bloch vector is optically prepared and then rotated to the equator. Additional off-resonant driving then rotates the Larmor vector about the z-axis. As the spins precess, a geometric phase proportional to the product of the solid angle (orange disk) and the number of Larmor vector rotations is acquired in addition to the dynamic phase. To cancel the dynamic phase while continuing geometric phase accrual, a π -pulse and a reversal of the off-resonant drive are inserted at the sequence midpoint. Lastly, the Bloch vector is mapped onto a population difference by a second $\pi/2$ -pulse and read out optically. From Ref. (Arai *et al.*, 2018).

B_{\perp} modulates the strength of the hyperfine interaction, resulting in amplitude modulation of the electronic spin energy level at the nuclear spin precession frequency. The modulation deviation is proportional to B_{\perp} . Thus, by performing standard AC magnetometry at the nuclear spin precession frequency, the magnitude of the perpendicular magnetic field B_{\perp} can be detected.

The technique is intriguing because (i), it allows the effective gyromagnetic ratio of the sensor to be tuned and (ii), it enables the use of AC magnetometry techniques including dynamical-decoupling protocols to sense DC fields for durations on the order of T_2 or longer (see Sec. III.A). However, the method is expected (and observed) to upmodulate both

magnetic signals and magnetic noise, including spin bath noise, to the AC measurement band. Further, the improved dephasing times are achieved primarily by decreasing the effective gyromagnetic ratio (i.e., the ratio relating B_{\perp} to an energy level shift) relative to the native NV^- electronic gyromagnetic ratio. Although the scheme enables vector sensing from a single NV^- center and may be compatible with NV^- spin ensembles, the method presently precludes sensing from multiple NV^- orientations. So far there has been no experimental demonstration of improved sensitivity using this method relative to that of an optimized Ramsey-type equivalent. The requirement for ≈ 1000 gauss axial fields is also disadvantageous and likely prevents utilization of off-axis NV^- centers for sensing.

D. Techniques for the strong NV^- - NV^- interaction regime

Dipolar interactions among NV^- spins contribute to ensemble- NV^- dephasing, as described in Sec. 2.7. When NV^- centers comprise the majority of spin defects in diamond, or when a different majority spin species is decoupled from the NV^- centers via spin bath driving, NV^- - NV^- interactions may degrade relaxation times T_2^* , T_2 , and T_1 (Choi *et al.*, 2017a), limiting the sensitivity of both DC and AC magnetometers. Measurement protocols that decouple or leverage these like-spin interactions while retaining sensitivity to magnetic signals offer an avenue to surpass this sensitivity limit.

Proposed techniques to improve sensitivity in the limit of strong NV^- - NV^- interactions may be separated into two categories. Protocols in the first category mitigate dipolar interactions between like spins to extend either the dephasing time T_2^* (O’Keeffe *et al.*, 2019) for DC sensing or the coherence time T_2 (Choi *et al.*, 2017b) for AC sensing. However, these techniques partially decouple the spins from the fields to be sensed, which may counteract the sensitivity enhancement from T_2^* or T_2 extension. Protocols in the second category harness like-spin interactions to generate entangled many-body states. Measurements of an entangled spin state comprising N spins can beat the standard quantum limit for spin projection noise ($\eta \propto 1/\sqrt{N}$, see Eqn. 1), and may approach the Heisenberg limit ($\eta \propto 1/N$) (Choi *et al.*, 2017).

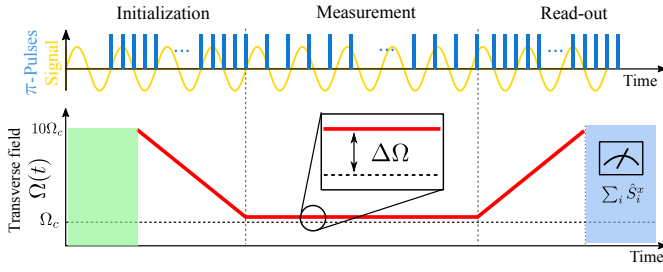


FIG. VI.2 Schematic diagram of entanglement-enhanced sensing protocol proposed in Ref. (Choi *et al.*, 2017). During the initialization, measurement, and readout steps, the amplitude of a transverse magnetic field Ω and the repetition frequency of additional transverse-magnetic-field π -pulses are tuned. In the initialization stage, a correlated many-body spin state is generated as Ω is decreased toward a quantum critical point at Ω_c . At the end of the measurement period, an axial AC magnetic field signal is mapped onto the total magnetization of the ensemble, which for NV^- centers can be detected using conventional readout. From Ref. (Choi *et al.*, 2017).

To illuminate the promise and challenges associated with entanglement-enhanced techniques, we focus on the specific protocol proposed in Ref. (Choi *et al.*, 2017). The technique, which is expected to be applicable to NV^- centers, utilizes strong like-spin interactions to create quantum correlated states sensitive to AC magnetic fields. The proposed scheme, outlined schematically in Fig. VI.2 generates entanglement within a 2D array of spins by first polarizing the individual spins along a transverse magnetic field (which for NV^- centers may be a MW-frequency field) and then adiabatically decreasing the field toward a quantum critical point. For the measurement to be compatible with global NV^- ensemble readout, the system approaches the quantum critical point, generating entanglement, without crossing over the quantum phase transition to a Greenberger-Horne-Zeilinger (GHZ) state. In the measurement step, periodic transverse-magnetic-field π -pulses are applied to the ensemble, allowing axial AC magnetic fields to excite the many-body system. The number of excitations detected after the transverse field is increased to its original value provides a measure of the strength of the AC magnetic field.

Importantly, the entangled state's coherence time, denoted \bar{T}_2 , is no longer limited by like-spin interactions, but by external noise. That is, if the coherence time T_2 is separated into contributions from NV^- - NV^- dipolar interactions and from other noise (including spin-lattice relaxation) as

$$\frac{1}{\bar{T}_2} = \frac{1}{T_2\{\text{NV}^-\text{NV}^-\}} + \frac{1}{T_2\{\text{other}\}}, \quad (27)$$

then the entangled state's coherence time \bar{T}_2 is only a function of $T_2\{\text{other}\}$. Therefore, when NV^- - NV^- interactions dominate, \bar{T}_2 may be comparable to or exceed T_2 , yielding improved AC magnetic field sensitivity via both the increased coherence time and reduced readout noise.

However, when the noise on each spin in the entangled ensemble is independent, \bar{T}_2 is expected to diminish linearly with the number of entangled spins N (i.e., $\bar{T}_2 \propto 1/N$), which at best cancels the sensitivity enhancement obtained

from the $1/\sqrt{N}$ reduction in spin projection noise compared to the standard quantum limit. Even without improved AC magnetic sensitivity, the scheme is expected to provide an increased measurement bandwidth by enabling faster field sampling than conventional sensing. When the dominant noise limiting the NV^- ensemble's spin coherence time is instead set by spatially-correlated noise, such as dipolar interactions with nearby magnetic dipoles of a different species (Choi *et al.*, 2017), enhanced AC magnetic field sensitivity from reduced spin projection noise may again be possible. Although the protocol may also be compatible with broadband DC magnetometry, the scaling of the correlated ensemble's effective T_2^* with entangled number of spins N remains unclear. Further investigation is required to determine if this protocol could yield a sensitivity improvement over conventional DC magnetometry.

While the approach proposed in Ref. (Choi *et al.*, 2017) represents an important milestone towards magnetometry enhanced by NV^- - NV^- dipolar interactions, the protocol is expected to be challenging to execute. First, the mean NV^- - NV^- separation distance $\langle r_{\text{NV}^-, \text{NV}^-} \rangle$ must be small compared to the average distance to the nearest paramagnetic defect $\langle r_{\text{NV}^-, \text{other}} \rangle$, but large compared to the thickness L of any (quasi) two-dimensional NV^- layer, i.e., $\langle r_{\text{NV}^-, \text{other}} \rangle > \langle r_{\text{NV}^-, \text{NV}^-} \rangle > L$. This hierarchy indicates that for a typical NV^- -rich diamond with $\langle r_{\text{NV}^-, \text{NV}^-} \rangle \sim 10$ nm, the NV^- layer thickness L should be less than a few nanometers. Shallow nitrogen implantation into diamond (Glenn *et al.*, 2017; Pham *et al.*, 2011) or nitrogen delta-doping during CVD growth (Ohno *et al.*, 2012; Osterkamp *et al.*, 2015) can yield layers that approach the appropriate thickness. Crucially, this 2D requirement restricts the practical NV^- ensemble size, which may limit achievable sensitivity (see Sec. I.E and Appendix A.3) when considering wide-field imaging and bulk magnetometry applications. Second, since the preparation and readout steps require a slow adiabatic field ramp, the practical requirement that these steps occur within time \bar{T}_2 limits the degree of achievable entanglement. Consequently, the protocol will mostly likely entangle sub-ensembles much smaller than the total ensemble size. Disorder (i.e., static field inhomogeneity) in the ensemble, e.g., from the random positioning of NV^- centers, also restricts the maximum entangled sub-ensemble size. Both of these mechanisms are expected to increase the measurement's spin projection noise above the Heisenberg limit, further restricting the parameter regime where sensitivity enhancements are possible.

In spite of the serious challenges and limitations, the proposed technique remains a promising first step toward practical schemes harnessing the full quantum nature of NV^- ensembles for sensitivity enhancement. While ensemble- NV^- sensing at the standard quantum limit is expected to outperform entanglement-enhanced schemes in the near future, further development of these techniques remains an important endeavor toward enabling long-term sensitivity improvements approaching fundamental limits.

VII. CONCLUSION AND OUTLOOK

This work constitutes a comprehensive survey of methods for improving broadband magnetometry from DC to ~ 100 kHz using ensembles of NV^- centers. We highlight the Ramsey-type sensing protocol as most promising (Secs. I.C and I.D), and we identify key factors limiting achievable magnetic-field sensitivity of such devices (Sec. I.E). Parameters given particularly close examination include the spin dephasing time T_2^* , which dictates the magnetic-field sensing time (Secs. II and III); the spin readout fidelity (Sec. IV); and the host diamond material properties (Sec. V). Below, we summarize our analyses within these broad categories, and we recommend areas where future study could lead to improvements in magnetometer sensitivity and performance.

Measurements employing Ramsey-type protocols with NV^- ensembles are limited by T_2^* , which presently remains orders of magnitude shorter than the physical limit of $2T_1$. The magnetic field sensitivity improves nearly linearly with T_2^* extension when the measurement overhead time is significant ($t_O \gtrsim T_2^*$), as is common for present-day ensemble- NV^- magnetometers. Therefore, this work focuses on understanding limitations to T_2^* and methods to extend T_2^* in NV^- -rich diamonds. Among the factors limiting T_2^* are magnetic-field, electric-field, and strain gradients. External bias-magnetic-field gradients may be mitigated through experimental design. Whereas internal strain and electric-field gradients can be more difficult to eliminate outright, the NV^- ensemble can be made insensitive to such gradients through operation at sufficiently strong bias magnetic fields (Sec. III.D) and employment of double-quantum coherence magnetometry (Sec. III.B). Ensemble- NV^- T_2^* values may also be limited by dipolar interactions with the diamond's inhomogeneous paramagnetic spin bath. We determine the individual contributions to T_2^* from substitutional nitrogen N_S^0 electronic spins (Sec. II.D), ^{13}C nuclear spins (Sec. II.F), and NV^- spins (Sec. II.G). Recent experiments determine T_2 - and T_2^* -dependencies on nitrogen concentration to better than 10% (Bauch *et al.*, 2018; Bauch *et al.*, 2019). We suggest reducing the unwanted bath-spin concentrations through (i) diamond growth using isotopically-purified ^{12}C (Sec. II.F), and (ii) diamond treatment via optimized electron irradiation and annealing procedures (Sec. V). We also identify spin bath driving using strong, resonant RF fields as an effective measure to decouple N_S^0 and other impurity spins from the NV^- ensemble (Sec. III.C). Recent work implementing spin bath driving combined with double-quantum coherence magnetometry in NV^- ensembles demonstrates T_2^* extension by more than $16\times$ (Bauch *et al.*, 2018). We expect continued progress on this front; one avenue opened up when T_2^* is increased to the NV^- - NV^- dipolar interaction limit is the exploration of enhanced sensing techniques harnessing quantum entanglement (Choi *et al.*, 2017) (Sec. VI.D).

In Sec. IV we survey existing techniques to improve ensemble- NV^- readout fidelity $\mathcal{F} = 1/\sigma_R$, which, for conventional fluorescence-based readout, is currently limited to ~ 0.015 (see Table I.2). We analyze methods that allow

readout fidelities for single NV^- centers and small ensembles in nanodiamonds to approach the spin projection limit, including spin-to-charge conversion readout (Sec. IV.A) and ancilla-assisted repetitive readout (Sec. IV.C). However, no demonstrated method has substantially outperformed conventional fluorescence-based readout for large NV^- ensembles (Table I.2). Nonetheless, we anticipate that with careful experimental design and advances in diamond-sample engineering, fidelity-enhancement methods so far limited to single spins or small ensembles may be extended to large NV^- ensembles. Additionally, given that any method employing optical readout benefits from increased collection efficiency, such optimizations (Sec. IV.E) remain worthwhile for improving magnetometer sensitivity.

As optimal sensing techniques require co-development with diamond samples tailored to these techniques, this work reviews diamond fabrication and relevant material properties in Sec. V. In particular, we focus on methods to engineer lab-grown diamond samples optimized for ensemble- NV^- magnetometry. We analyze growth via chemical vapor deposition, high-pressure-high-temperature synthesis, and mixed-synthesis methods (Sec. V.C). We examine how diamond synthesis and treatment can be used to engineer high N-to- NV^- conversion efficiencies E_conv , and we investigate methods to improve and stabilize the charge state efficiency $\zeta = [\text{NV}^-]/[\text{NV}^\text{T}]$ (Sec. V.B). We also investigate undesired defects commonly found in NV^- -rich diamond samples (Sec. V.F). These defects, including multi-vacancy clusters and hydrogen-related impurities, may both trap charges in the diamond and contribute to the dipolar spin bath, reducing both E_conv and T_2^* .

Although present understanding of diamond synthesis, treatment, and characterization is extensive and spans multiple decades, further work is needed to reproducibly create NV^- -rich diamond samples with low strain, low concentrations of unwanted impurities, and high NV^- concentrations. In particular, advancing diamond materials science to enable longer native T_2^* values is a worthwhile pursuit; e.g., although the NV^- center's sensitivity to strain can be reduced (Secs. III.B and III.D), employing low-strain host diamonds is preferable regardless. Importantly, a robust and optimized protocol for diamond irradiation and annealing that takes nitrogen concentration into account should be established (Secs. V.D and V.E). Furthermore, widespread access to high-quality scientific diamonds is imperative and would greatly accelerate advances in NV -diamond-related research. Presently, diamonds with natural carbon isotopic abundance, suboptimal nitrogen concentrations, and undesired strain and surface characteristics are widely employed by the community solely because most research groups lack access to optimized diamond samples.

In addition, many aspects of NV physics, and charge dynamics for ensembles in particular, remain poorly understood and warrant further investigation. We anticipate that additional knowledge could be harnessed to improve sensor performance, similar to how the study of NV^- and NV^0 ionization characteristics under low optical intensity by Aslam *et al.* (Aslam *et al.*, 2013) prompted the development of spin-to-charge conversion readout. Further examination of

charge dynamics under magnetometer operating conditions (e.g., high optical intensity) is expected to yield fruitful insights. For NV-rich diamonds, systematic studies of (i) NV⁻ ionization (both from the singlet and triplet excited states), and (ii) recombination from the NV⁰ excited state versus optical wavelength and intensity, would be particularly useful. Such studies would address present knowledge gaps and could inform diamond-engineering protocols to better stabilize the NV⁻ charge state in ensemble-based devices. These investigations could also lay the groundwork for new sensitivity-enhancement techniques tailored to ensembles. In addition, continued basic research into the NV⁻ center is warranted. For example, while four electronic states of NV⁻ have been observed, two additional predicted states have not yet been experimentally confirmed (Jensen *et al.*, 2017).

We also expect unanticipated creative ideas to emerge that further enhance readout fidelity, dephasing time T_2^* , and overall magnetic field sensitivity. Ensemble-NV⁻ magnetometers are already relevant in wide-varying sensing applications, thanks to key advances made over the past decade, which we have summarized here. Moreover, NV-diamond quantum sensing is a quickly developing platform, well positioned to continue improving, with significant advancements possible before fundamental limits are reached. By combining the knowledge collected here with likely future advances, we expect further expansion of applications of quantum sensors based on NV⁻ ensembles in diamond.

Acknowledgments

The authors thank Eisuke Abe, Victor Acosta, Scott Alsid, Ashok Ajoy, Keigo Arai, Nithya Arunkumar, Ania Bleszynski-Jayich, Dolev Bluvstein, Danielle Braje, Dominik Bucher, Alexei Bylinskii, Paola Cappellaro, Soonwon Choi, Alexandre Cooper, Colin Connolly, Andrew Edmonds, Michael Geis, David Glenn, Ben Green, Kohei Itoh, Jean-Christophe Jaskula, Pauli Kehayias, Mark Ku, Junghyun Lee, David LeSage, Igor Lovchinsky, Matthew Markham, Claire McLellan, Idan Meirzada, Gavin Morley, Mark Newton, Michael O’Keeffe, David Phillips, Emma Rosenfeld, Brendan Shields, Swati Singh, and Daniel Twitchen for helpful comments and discussions. This material is based upon work supported by, or in part by, the United States Army Research Laboratory and the United States Army Research Office under Grant No. W911NF-15-1-0548; the National Science Foundation Electronics, Photonics and Magnetic Devices (EPMD), Physics of Living Systems (PoLS), and Integrated NSF Support Promoting Interdisciplinary Research and Education (INSPIRE) programs under Grants No. ECCS-1408075, No. PHY-1504610, and No. EAR-1647504, respectively; Air Force Office of Scientific Research award FA9550-17-1-0371; Defense Advanced Research Projects Agency Quantum Assisted Sensing and Readout (DARPA QuASAR) program under Contract No. HR0011-11-C-0073; and Lockheed Martin under Contract No. A32198. J. M. S. was partially supported by a Fannie and John Hertz Foundation Graduate Fellow-

ship and a NSF Graduate Research Fellowship under Grant No. 1122374.

Appendix A: APPENDIX

1. Derivations

a. Ramsey DC magnetic field measurement

The following is a derivation of a Ramsey-type pulsed magnetometry sequence (see Fig. 1.3) using a magnetic dipole moment. Here the magnetic moment is taken to be an NV⁻ center’s ground-state electronic spin, although this discussion applies to any two-level system sensitive to magnetic fields, including atomic vapors and other solid state defects. Although the NV⁻ ground state spin is a triplet with $S = 1$, a bias magnetic field B_0 can be applied along the NV⁻ symmetry axis to split the $m_s = +1$ and $m_s = -1$ energy levels so that resonant MWs may selectively drive the $m_s = 0$ to $m_s = +1$ (or $m_s = 0$ to $m_s = -1$) transition. Any off-axis magnetic field component B_\perp can be ignored so long as $(\gamma_e B_\perp)^2 / [(2\pi D)^2 \pm (\gamma_e B_0)^2] \ll 1$, where $D = 2.87$ GHz is the zero-field splitting and $\gamma_e = g_e \mu_B / \hbar$ is the gyromagnetic ratio of the NV⁻ electronic spin. Here the NV⁻ center’s nuclear spin is also ignored as well as static electric or strain fields. This two-level subspace can be described as a pseudo-spin-1/2 system with $|m_s = +1\rangle = |\uparrow\rangle$ and $|m_s = 0\rangle = |\downarrow\rangle$ and Hamiltonian

$$H = (2\pi D + \gamma_e B) S_z \\ = \frac{\hbar}{2} \begin{pmatrix} 2\pi D + \gamma_e B & 0 \\ 0 & -2\pi D - \gamma_e B \end{pmatrix}, \quad (\text{A1})$$

where S_z is the operator for the z-projection of the pseudo-spin; and $B = B_0 + B_{\text{sense}}$ is the total magnetic field projection along the NV⁻ symmetry axis, taken here to be the z-axis, which is the sum of the applied bias field and an unknown DC field to be sensed. Here terms in the Hamiltonian proportional to the identity matrix have been dropped, as they introduce only a global phase to the states’ time evolution. In the bias field B_0 the spin resonance frequency is $\omega_0 = 2\pi D + \gamma_e B_0$. Spin operators are expressed in the S_z basis in terms of the Pauli matrices $\vec{S} = \frac{\hbar}{2} \vec{\sigma}$, yielding

$$H = \frac{\hbar \omega_0}{2} \sigma_z + \frac{\hbar}{2} \gamma_e B_{\text{sense}} \sigma_z. \quad (\text{A2})$$

As described herein, a Ramsey sequence consists of two $\pi/2$ -pulses of an oscillating magnetic field resonant with the transition between $|\downarrow\rangle$ and $|\uparrow\rangle$, which are separated by a free precession time τ . The sequence begins at time $t = 0$, with the spin polarized to $|\psi(0)\rangle = |\downarrow\rangle$. An oscillating magnetic field oriented perpendicular to the NV⁻ symmetry axis $\vec{B}_1(t) = B_1 \cos(\omega t) \hat{y}$ with angular frequency $\omega \approx \omega_0$ is turned on abruptly. Without loss of generality \vec{B} is assumed to be polarized along the y-axis. For $B_1 \gg B_{\text{sense}}$, the second term in H can be dropped, thereby ignoring effects of the unknown DC sensing field while the oscillating

field is on. The Hamiltonian for the system driven by this oscillating field, denoted H_{driv} , becomes

$$H_{\text{driv}} = \frac{\hbar\omega_0}{2}\sigma_z + \frac{\hbar}{2}\gamma_e B_1 \cos(\omega t)\sigma_y. \quad (\text{A3})$$

We proceed in the interaction picture, with $H_0 = \frac{\hbar\omega_0}{2}\sigma_z$ and $H_1 = \frac{\hbar}{2}\gamma_e B_1 \cos(\omega t)\sigma_y$. This step is equivalent to transforming into a rotating frame with angular frequency ω_0 . The interaction-picture state vector $|\psi(t)\rangle$ is defined in terms of the Schrödinger-picture state vector $|\tilde{\psi}(t)\rangle$ as $|\tilde{\psi}(t)\rangle = U_0^\dagger(t)|\psi(t)\rangle$ with $U_0(t) = e^{-iH_0 t/\hbar}$. This state evolves according to $|\tilde{\psi}(t)\rangle = \tilde{U}_1(t)|\tilde{\psi}(0)\rangle$ where $\tilde{U}_1(t) = e^{-i\tilde{H}_1 t/\hbar}$, with

$$\begin{aligned} \tilde{H}_1 &= U_0^\dagger(t)H_1U_0(t) \\ &= \frac{\hbar}{4}\gamma_e B_1 \begin{pmatrix} 0 & -i(e^{-i(\omega_0+\omega)t} + e^{-i(\omega_0-\omega)t}) \\ i(e^{i(\omega_0-\omega)t} + e^{i(\omega_0+\omega)t}) & 0 \end{pmatrix}. \end{aligned} \quad (\text{A4})$$

The transformed interaction Hamiltonian \tilde{H}_1 is simplified by assuming resonant driving of the spin with $\omega = \omega_0$ and by making the rotating wave approximation, dropping off-resonant terms rotating at $2\omega_0$, to yield

$$\tilde{H}_1 \approx \frac{\hbar}{4}\gamma_e B_1 \sigma_y. \quad (\text{A5})$$

This Hamiltonian causes the spin system to undergo Rabi oscillations at angular frequency $\Omega = \gamma_e B_1/2$. The oscillating field $\vec{B}_1(t)$ is turned off abruptly after a duration $\tau_{\frac{\pi}{2}} = \frac{\pi}{2\Omega} = \frac{\pi}{\gamma_e B_1}$, so that

$$\begin{aligned} |\tilde{\psi}(\tau_{\frac{\pi}{2}})\rangle &= \exp\left(-i\frac{\gamma_e B_1 \sigma_y \tau_{\frac{\pi}{2}}}{4}\right)|\tilde{\psi}(0)\rangle \\ &= \exp\left(-i\frac{\pi}{4}\sigma_y\right)|\downarrow\rangle \\ &= \frac{1}{\sqrt{2}} \begin{pmatrix} 1 & -1 \\ 1 & 1 \end{pmatrix} \begin{pmatrix} 0 \\ 1 \end{pmatrix} \\ &= \frac{1}{\sqrt{2}}(-|\uparrow\rangle + |\downarrow\rangle), \end{aligned} \quad (\text{A6})$$

which uses the identity $e^{-i\theta\hat{n}\cdot\vec{\sigma}} = \cos(\theta)I - i\sin(\theta)(\hat{n}\cdot\vec{\sigma})$ where \hat{n} is a unit vector on the Bloch sphere. This constitutes a $\pi/2$ -pulse on the spin.

Next, the magnetic moment undergoes free precession in the absence of $\vec{B}_1(t)$ for a sensing time τ . During this time the system Hamiltonian returns to H from Eqn. A1. We continue to use the interaction picture with $H_0 = \frac{\hbar\omega_0}{2}\sigma_z$, and with new interaction Hamiltonian H'_1 determined by $\vec{B}_{\text{sense}} = B_{\text{sense}}\hat{z}$ as

$$H'_1 = \frac{\hbar}{2}\gamma_e B_{\text{sense}}\sigma_z. \quad (\text{A7})$$

Recognizing that H'_1 commutes with H_0 , the transformed interaction Hamiltonian $\tilde{H}'_1 \equiv U_0^\dagger(t)H'_1U_0(t) = H'_1$, and

thus the interaction-picture state vector $|\tilde{\psi}(t)\rangle$ evolves under H'_1 into

$$\begin{aligned} |\tilde{\psi}(\tau_{\pi/2} + \tau)\rangle &= e^{-iH'_1\tau/\hbar}|\tilde{\psi}(\tau_{\pi/2})\rangle \\ &= \frac{1}{\sqrt{2}}(-e^{-i\phi/2}|\uparrow\rangle + e^{i\phi/2}|\downarrow\rangle), \end{aligned} \quad (\text{A8})$$

where $\phi = \gamma_e B_{\text{sense}}\tau$ is the phase accumulated due to B_{sense} . (If $B_{\text{sense}} = 0$, the state vector $|\tilde{\psi}(t)\rangle$ accumulates no phase, as H'_1 vanishes and the entire Hamiltonian $H = H_0$.)

To complete the sequence, a second oscillating field $\vec{B}_2(t) = \vec{B}_2 \cos(\omega_0 t)$, is applied for a $\pi/2$ -pulse. As with the first $\pi/2$ -pulse, $B_{\text{sense}} \ll B_2$ is assumed so that additional spin state evolution due to B_{sense} can be ignored. The polarization of $\vec{B}_2(t)$ is chosen to be along \hat{n} in the x-y plane at an angle ϑ with respect \hat{y} , the polarization direction of the first $\pi/2$ -pulse $\vec{B}_1(t)$. After again making the rotating wave approximation, the transformed interaction Hamiltonian, \tilde{H}''_1 is given by

$$\tilde{H}''_1 \approx \frac{\hbar}{4}\gamma_e B_2 (\cos(\vartheta)\sigma_y - \sin(\vartheta)\sigma_x) \quad (\text{A9})$$

and

$$\begin{aligned} |\tilde{\psi}(\tau_{\frac{\pi}{2}} + \tau + \tau_{\frac{\pi}{2}})\rangle &= e^{-i\tilde{H}''_1\tau_{\frac{\pi}{2}}/\hbar}|\tilde{\psi}(\tau_{\frac{\pi}{2}} + \tau)\rangle \\ &= \frac{1}{\sqrt{2}} \begin{pmatrix} 1 & -e^{-i\vartheta} \\ e^{i\vartheta} & 1 \end{pmatrix} \cdot \frac{1}{\sqrt{2}} \begin{pmatrix} -e^{-i\phi/2} \\ e^{i\phi/2} \end{pmatrix}, \end{aligned} \quad (\text{A10})$$

which, up to a global phase, is equal to

$$|\tilde{\psi}\rangle = \cos\left(\frac{\phi - \vartheta}{2}\right)|\uparrow\rangle - ie^{i\vartheta}\sin\left(\frac{\phi - \vartheta}{2}\right)|\downarrow\rangle. \quad (\text{A11})$$

The phase accumulated during τ is thus mapped on to a population difference between the $|\uparrow\rangle$ and $|\downarrow\rangle$ states. The value of B_{sense} is determined by measuring the observable $\tilde{S}_z = S_z$ and relating that to ϕ .

$$\begin{aligned} \langle\tilde{S}_z\rangle &= \frac{\hbar}{2}\langle\tilde{\psi}|\sigma_z|\tilde{\psi}\rangle \\ &= \frac{\hbar}{2}\left(\cos^2\left(\frac{\phi - \vartheta}{2}\right) - \sin^2\left(\frac{\phi - \vartheta}{2}\right)\right) \\ &= \frac{\hbar}{2}\cos(\phi - \vartheta) \\ &= \frac{\hbar}{2}\cos(\gamma_e B_{\text{sense}}\tau - \vartheta). \end{aligned} \quad (\text{A12})$$

The cosinusoidal fluctuations in $\langle\tilde{S}_z\rangle$ are termed Ramsey fringes. Common choices of ϑ are 0 and $\pi/2$. The case where $\vartheta = 0$ (respectively, $\vartheta = \pi/2$) is commonly called cosine (sine) magnetometry, as the observable $\langle\tilde{S}_z\rangle$ varies as the cosine (sine) of B_{sense} for fixed τ . For ensembles of NV⁻ centers, $\langle\tilde{S}_z\rangle$ is measured by reading out the spin-state-dependent fluorescence over a predetermined readout window of several hundred nanoseconds (see Fig. I.2), as discussed in Sec. I.C and later in Appendix A.1.c.

For small B_{sense} such that $\phi \ll 2\pi$, Eqn. A12 can be linearized about $\phi = 0$ for any value of ϑ except $\vartheta = 0$.

The values of B_{sense} and ϕ can then be related to a small change in the observable $\delta\langle S_z \rangle = \langle S_z \rangle|_{\phi} - \langle S_z \rangle|_0$ as follows:

$$B_{\text{sense}} = \frac{\phi}{\gamma_e \tau} \approx \frac{1}{\gamma_e \tau} \frac{\delta\langle S_z \rangle}{\frac{d\langle S_z \rangle}{d\phi}|_0} \approx \frac{1}{\gamma_e \tau} \frac{\frac{2}{\hbar} \langle S_z \rangle|_{\phi} - \cos(\vartheta)}{\sin(\vartheta)}. \quad (\text{A13})$$

For $\vartheta = 0$ the linear term $\delta\langle S_z \rangle$ vanishes, as the slope of the Ramsey fringe goes to zero; a small B_{sense} produces to lowest order a quadratic change in $\langle S_z \rangle$. For $\vartheta = \pi/2$, the slope of the Ramsey fringe is maximized, and Eqn. A13 reduces to

$$B_{\text{sense}} \approx \frac{2}{\hbar \gamma_e \tau} \langle S_z \rangle. \quad (\text{A14})$$

b. Spin-projection-noise-limited sensitivity

The spin-projection-noise-limited magnetic field sensitivity is defined as the field δB at which the size of the signal $\delta\langle S_z \rangle$ due to δB is equal to the uncertainty in the signal, i.e., when $\delta\langle S_z \rangle = \Delta S_z$, where $\Delta S_z = \sqrt{\langle S_z^2 \rangle - \langle S_z \rangle^2}$ is the standard deviation of a series of identical measurements of δB . For a precession time τ , this minimum field is

$$\delta B_{\text{sp}} = \frac{1}{\gamma_e \tau} \frac{\Delta S_z}{\left| \frac{d\langle S_z \rangle}{d\phi} \right|}. \quad (\text{A15})$$

When M uncorrelated consecutive measurements are taken, each with precession time τ over a total measurement time t_{meas} , the minimum field is reduced by the factor $\sqrt{1/M} = \sqrt{\tau/t_{\text{meas}}}$, yielding

$$\delta B_{\text{sp}} = \frac{1}{\gamma_e} \frac{1}{\sqrt{\tau t_{\text{meas}}}} \frac{\Delta S_z}{\left| \frac{d\langle S_z \rangle}{d\phi} \right|}. \quad (\text{A16})$$

The spin-projection-noise-limited sensitivity of a Ramsey magnetometry measurement is then

$$\eta_{\text{sp}} = \delta B_{\text{sp}} \sqrt{t_{\text{meas}}} = \frac{1}{\gamma_e \sqrt{\tau}} \frac{\Delta S_z}{\left| \frac{d\langle S_z \rangle}{d\phi} \right|}. \quad (\text{A17})$$

The quotient $\frac{\Delta S_z}{\left| \frac{d\langle S_z \rangle}{d\phi} \right|}$ is calculated:

$$\langle S_z \rangle = \frac{\hbar}{2} \cos(\phi - \vartheta), \quad (\text{A18})$$

$$\frac{d\langle S_z \rangle}{d\phi} = -\frac{\hbar}{2} \sin(\phi - \vartheta), \quad (\text{A19})$$

$$\begin{aligned} \langle S_z^2 \rangle &= \frac{\hbar^2}{4} \langle \psi | \sigma_z^2 | \psi \rangle \\ &= \frac{\hbar^2}{4} \left(\cos^2 \left(\frac{\phi - \vartheta}{2} \right) + \sin^2 \left(\frac{\phi - \vartheta}{2} \right) \right) \\ &= \frac{\hbar^2}{4}, \end{aligned} \quad (\text{A20})$$

$$\begin{aligned} \Delta S_z &= \sqrt{\langle S_z^2 \rangle - \langle S_z \rangle^2} \\ &= \sqrt{\frac{\hbar^2}{4} (1 - \cos^2(\phi - \vartheta))} \\ &= \frac{\hbar}{2} |\sin(\phi - \vartheta)|, \end{aligned} \quad (\text{A21})$$

$$\frac{\Delta S_z}{\left| \frac{d\langle S_z \rangle}{d\phi} \right|} = 1. \quad (\text{A22})$$

This result is independent of the value of ϕ or ϑ . The projection noise is always equal to the slope of the Ramsey fringe. That is, a magnetometer limited by spin projection noise has the same signal-to-noise ratio regardless of where on the Ramsey fringe the measurement is taken. The spin-projection-noise-limited sensitivity is simply

$$\eta_{\text{sp}} = \delta B_{\text{sp}} \sqrt{t_{\text{meas}}} = \frac{1}{\gamma_e \sqrt{\tau}}. \quad (\text{A23})$$

For sensing with an ensemble of N independent spins, the sensitivity $\eta_{\text{sp}}^{\text{ensemble}} = \eta_{\text{sp}}/\sqrt{N}$ such that

$$\eta_{\text{sp}}^{\text{ensemble}} = \frac{1}{\gamma_e \sqrt{N \tau}}. \quad (\text{A24})$$

c. Photon-shot-noise-limited sensitivity

The above discussion considered a direct measurement of S_z . The measurement technique for NV⁻ spins - optical readout - instead indirectly probes the spin through measuring the spin-state-dependent fluorescence. Shot noise in the collected fluorescence must be incorporated into the measurement uncertainty and sensitivity.

To phenomenologically introduce Poisson fluctuations from the fluorescence photons into the sensitivity, the optical readout procedure is treated as a mapping of the spin eigenstates onto two light field modes: $|m_s = +1\rangle = |\uparrow\rangle \rightarrow |\beta\rangle$ and $|m_s = 0\rangle = |\downarrow\rangle \rightarrow |\alpha\rangle$, where $|\alpha\rangle$ and $|\beta\rangle$ are coherent states defined by $\hat{a}|\alpha\rangle = \alpha|\alpha\rangle$ and $\hat{b}|\beta\rangle = \beta|\beta\rangle$. We define $a = |\alpha|^2$ as the mean number of photons in $|\alpha\rangle$ and $b = |\beta|^2$ as the mean number of photons in $|\beta\rangle$. Since the

$|m_s = 0\rangle$ state produces more fluorescent photons during readout than the $|m_s = +1\rangle$ state, $a > b$. The final spin state $|\tilde{\psi}\rangle$ from Eqn. A11 is mapped onto the photon field state

$$|\psi_{\text{ph}}\rangle = \cos\left(\frac{\phi - \vartheta}{2}\right)|\beta\rangle - ie^{i\vartheta}\sin\left(\frac{\phi - \vartheta}{2}\right)|\alpha\rangle. \quad (\text{A25})$$

A measurement of the spin state has become a measurement of the number of photons collected from the two light fields $\hat{N} = \hat{a}^\dagger \hat{a} + \hat{b}^\dagger \hat{b}$. Defining $\varphi = \phi - \vartheta$,

$$\begin{aligned} \langle \hat{N} \rangle &= \langle \psi_{\text{ph}} | (\hat{a}^\dagger \hat{a} + \hat{b}^\dagger \hat{b}) | \psi_{\text{ph}} \rangle = b \cos^2\left(\frac{\varphi}{2}\right) + a \sin^2\left(\frac{\varphi}{2}\right) \\ &= b \left(\frac{1 + \cos(\varphi)}{2} \right) + a \left(\frac{1 - \cos(\varphi)}{2} \right). \end{aligned} \quad (\text{A26})$$

where the two light fields are assumed to be noninterfering so that $\hat{a}|\beta\rangle = \hat{b}|\alpha\rangle = 0$ and $\langle \alpha | \beta \rangle = \langle \beta | \alpha \rangle = 0$.

The sensitivity of a magnetometer employing optical readout is written in the same way as the spin-projection-noise-limited sensitivity given in Eqn. A17, but with the observable S_z replaced by \hat{N} :

$$\eta_{\text{opt}} = \delta B_{\text{opt}} \sqrt{t_{\text{meas}}} = \frac{1}{\gamma_e \sqrt{\tau}} \frac{\Delta \hat{N}}{|d\langle \hat{N} \rangle / d\phi|}, \quad (\text{A27})$$

where $\Delta \hat{N} = \sqrt{\langle \hat{N}^2 \rangle - \langle \hat{N} \rangle^2}$. The derivative of $\langle \hat{N} \rangle$ with respect to ϕ is

$$\frac{d\langle \hat{N} \rangle}{d\phi} = \frac{d\langle \hat{N} \rangle}{d\varphi} = \frac{(a-b)}{2} \sin(\varphi). \quad (\text{A28})$$

Recalling the operator commutation relation $[\hat{a}, \hat{a}^\dagger] = 1$, $\Delta \hat{N}$ is calculated:

$$\begin{aligned} \langle \hat{N}^2 \rangle &= \langle (\hat{a}^\dagger \hat{a} + \hat{b}^\dagger \hat{b})(\hat{a}^\dagger \hat{a} + \hat{b}^\dagger \hat{b}) \rangle \\ &= \langle \psi_{\text{ph}} | (\hat{a}^\dagger \hat{a} \hat{a}^\dagger \hat{a} + \hat{b}^\dagger \hat{b} \hat{b}^\dagger \hat{b}) | \psi_{\text{ph}} \rangle \\ &= \langle \psi_{\text{ph}} | (\hat{a}^\dagger (\hat{a}^\dagger \hat{a} + 1) \hat{a} + \hat{b}^\dagger (\hat{b}^\dagger \hat{b} + 1) \hat{b}) | \psi_{\text{ph}} \rangle \\ &= b(b+1) \left(\frac{1 + \cos(\varphi)}{2} \right) + a(a+1) \left(\frac{1 - \cos(\varphi)}{2} \right), \end{aligned} \quad (\text{A29})$$

$$\begin{aligned} \langle \hat{N} \rangle^2 &= b^2 \left(\frac{1/2 + \cos(\varphi)}{2} \right) + a^2 \left(\frac{1/2 - \cos(\varphi)}{2} \right) \\ &\quad + \left(\frac{b^2}{4} + \frac{a^2}{4} \right) \cos^2(\varphi) + \frac{ba}{2} \sin^2(\varphi), \end{aligned} \quad (\text{A30})$$

$$\begin{aligned} \Delta \hat{N} &= \sqrt{\langle \hat{N}^2 \rangle - \langle \hat{N} \rangle^2} \\ &= \sqrt{\left(\frac{b^2}{4} - \frac{ba}{2} + \frac{a^2}{4} \right) \sin^2(\varphi) + b \left(\frac{1 + \cos(\varphi)}{2} \right) + a \left(\frac{1 - \cos(\varphi)}{2} \right)} \text{ and} \\ &= \sqrt{\frac{(a-b)^2}{4} \sin^2(\varphi) + b \cos^2\left(\frac{\varphi}{2}\right) + a \sin^2\left(\frac{\varphi}{2}\right)}. \end{aligned} \quad (\text{A31})$$

Using Eqns. A31 and A28, the sensitivity reduces to

$$\frac{\Delta \hat{N}}{|d\langle \hat{N} \rangle / d\phi|} = \sqrt{\frac{\frac{(a-b)^2}{4} \sin^2(\varphi) + b \cos^2\left(\frac{\varphi}{2}\right) + a \sin^2\left(\frac{\varphi}{2}\right)}{\frac{(a-b)^2}{4} \sin^2(\varphi)}}. \quad (\text{A32})$$

Note that in the case of very strong coherent states, such that $a(a+1) \approx a^2$ and $b(b+1) \approx b^2$, Eqn. A32 approaches the spin-projection noise limit of $\frac{\Delta \hat{N}}{|d\langle \hat{N} \rangle / d\phi|} = 1$.

For the case $\varphi = \pi/2$, the sensitivity is optimized, yielding

$$\frac{\Delta \hat{N}}{|d\langle \hat{N} \rangle / d\phi|} = \sqrt{\frac{\frac{(a-b)^2}{4} + \frac{a+b}{2}}{\frac{(a-b)^2}{4}}} = \sqrt{1 + \frac{2(a+b)}{(a-b)^2}}. \quad (\text{A33})$$

We identify $C = \frac{a-b}{a+b}$ as the measurement contrast, (i.e., the fringe visibility), and $n_{\text{avg}} = \frac{a+b}{2}$ as the average number of photons collected per measurement (per spin, if the measurement is on an ensemble). The contrast C depends on the degree of initial polarization of the spin state and the readout duration. Measurement contrast also diminishes with increased free precession time due to spin dephasing and decoherence, parameterized by T_2^* , as shown in Eqn. 5. However, since this degradation affects both the shot-noise and spin-projection-noise terms in the measurement sensitivity η_{opt} , it is included explicitly rather than incorporated into C . Thus, the sensitivity for a Ramsey measurement on a single spin with both photon shot noise and spin-projection noise is given by

$$\eta_{\text{opt}} = \delta B_{\text{opt}} \sqrt{t_{\text{meas}}} = \frac{1}{\gamma_e e^{-(\tau/T_2^*)^p} \sqrt{\tau}} \sqrt{1 + \frac{1}{C^2 n_{\text{avg}}}}. \quad (\text{A34})$$

(See Appendix A.7 for discussion of the stretched exponential parameter p .) When sensing with an ensemble of N independent spins, the sensitivity is given by

$$\eta_{\text{opt}}^{\text{ensemble}} = \eta_{\text{opt}} / \sqrt{N}. \quad (\text{A35})$$

In conventional NV⁻ optical readout, contrast is low ($\lesssim 15\%$), and the number of photons n_{avg} collected per spin is limited by the ratio of the optical cycling rate to the singlet-state decay rate to be $\lesssim 15$ (Dréau *et al.*, 2011; Taylor *et al.*, 2008), and is often much less due to imperfect collection efficiency. Thus, $C^2 n_{\text{avg}} \ll 1$, and shot noise becomes the dominant contribution to the magnetic field sensitivity, with

$$\eta_{\text{shot}} \approx \frac{1}{\gamma_e} \frac{1}{C e^{-(\tau/T_2^*)^p} \sqrt{n_{\text{avg}} \tau}}. \quad (\text{A36})$$

$$\eta_{\text{shot}}^{\text{ensemble}} \approx \frac{1}{\gamma_e} \frac{1}{C e^{-(\tau/T_2^*)^p} \sqrt{N n_{\text{avg}} \tau}}. \quad (\text{A37})$$

d. Overhead time

The sensitivity equations above have neglected any optical initialization or readout time, as well as the finite duration of the two $\pi/2$ -pulses of the Ramsey sequence. Grouping all of these factors into an experimental dead time t_O , we find the sensitivity factor for M measurements each with sensing time τ over a total time t_{meas} is $\sqrt{1/M} = \sqrt{(\tau + t_O)/t_{\text{meas}}}$, yielding a sensitivity limited by shot noise and spin-projection noise of

$$\eta_{\text{opt}} = \delta B_{\text{opt}} \sqrt{t_{\text{meas}}} = \frac{1}{\gamma_e e^{-(\tau/T_2^*)^p}} \frac{\sqrt{\tau + t_O}}{\tau} \sqrt{1 + \frac{1}{C^2 n_{\text{avg}}}}. \quad (\text{A38})$$

2. Optimal precession time

The optimal precession time τ to achieve best Ramsey magnetometry sensitivity (Eqn. 7) depends on the value of the stretched exponential parameter p , the initialization time t_I , and the readout time t_R . By defining the overhead time per measurement as $t_O = t_I + t_R$, Eqn. 7 reduces to

$$\eta \propto \frac{1}{e^{-(\tau/T_2^*)^p}} \frac{\sqrt{t_O + \tau}}{\tau}. \quad (\text{A39})$$

For $t_O \ll T_2^*$, sensitivity is optimized when $\tau \approx T_2^*/2$ for $1 \leq p \leq 2$. Particularly, for $t_O = 0$ and $p = 1$ or $p = 2$ (see Appendix A.7), sensitivity is exactly optimized for $\tau = T_2^*/2$. As t_O increases from zero, the optimal precession time increases as well, asymptotically approaching $\tau = T_2^*$ when $t_O \gg T_2^*$ for $p = 1$. Figure A.1 shows the optimal precession time τ for various combinations of p and t_O . For clarity the optimal precession time is normalized to the dephasing time in the employed measurement basis (DQ or SQ). Equation A39, and thus Fig. A.1, also apply for Hahn echo (Eqn. 19) with T_2^* replaced by T_2 (see Section III.A).

In practice, additional experimental factors warrant consideration when choosing the Ramsey free precession time τ . For example, because time-varying electric and magnetic fields and temperature may mask as dephasing mechanisms, the measured value of T_2^* depends on the measurement duration. Thus, if the time required to measure the value of T_2^* is significantly longer than the duration of a magnetic field measurement, field fluctuations may artificially reduce the measured value of T_2^* compared to the value relevant for sensing. This spoiled T_2^* measurement could lead to a suboptimal choice of τ (Bauch *et al.*, 2018). Therefore, care should be taken when choosing the appropriate free precession time τ for a magnetometry experiment.

3. Considerations for increasing sensor number

Increasing the number N of interrogated NV⁻ centers by increasing either the interrogation volume or the NV⁻ density may be partially effective to improve magnetic field sensitivity. In this instance, the number of photons detected per measurement \mathcal{N} increases with the number of sensors

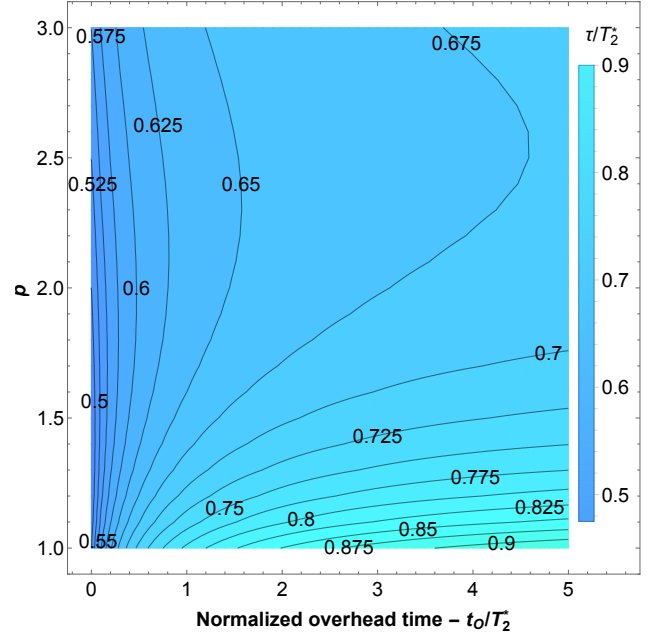


FIG. A.1 Optimal precession time τ for a pulsed magnetometry protocol. The contour plot shows the precession time τ to achieved optimal sensitivity in units of T_2^* , for different stretched exponential parameters p and different overhead times t_O .

N . However, a series of practical factors may hinder this strategy. First, sensitivity enhancement exhibits sublinear scaling with N and the associated number of photons detected per measurement \mathcal{N} , i.e., $\eta \propto \frac{1}{\sqrt{\mathcal{N}}}$, making significant sensitivity improvements from increasing N difficult.

Additional technical difficulties may arise when increasing N , such as the photon number requirement for optical initialization. Assuming that each interrogated NV⁻ center requires m photons for optical initialization, each measurement is expected to require an energy of

$$E_{\text{init}} = Nm \frac{hc}{\lambda}, \quad (\text{A40})$$

where h is Planck's constant, c is the speed of light and λ is the excitation wavelength. If measurements are performed every T_2^* , the required mean power is

$$P_{\text{init}} = \frac{Nm}{T_2^*} \frac{hc}{\lambda}. \quad (\text{A41})$$

For example, initialization of all 1.76×10^{14} NV⁻ centers in a 1 mm³ diamond with 1 ppm [NV⁻] would require $E_{\text{init}} = 200$ μ J, using a crude guess of $m = 3$ (see Table A.3). Assuming $T_2^* = 1$ μ s, the required power is $P_{\text{init}} = 200$ W. Eqn. A41 illustrates that achieving a sensitivity improvement by increasing the NV⁻ ensemble size will increase P_{init} unless T_2^* is increased as well. For experimental approaches employing an acousto-optic modulator to gate a CW laser, the required CW laser power will be higher as many photons are wasted.

Another difficulty encountered when increasing the number of interrogated NV⁻ centers N (and thus detected photon number \mathcal{N}) is that reaching the shot noise limit can become challenging for large values of \mathcal{N} . For example, the

absolute noise contributed by some systematic (not stochastic) noise sources scales linearly with the number of photons detected, i.e., $\propto k_1 \mathcal{N}$, where $k_1 \ll 1$. In comparably proportional units, shot noise scales as $\propto \sqrt{\mathcal{N}}$. For $\mathcal{N} > \frac{1}{k_1^2}$, the systematic noise will be larger than shot noise. Primary examples of such noise sources include laser intensity noise in all implementations, timing jitter in the readout pulse length for Ramsey and pulsed ODMR, and MW amplitude noise in CW-ODMR.

Lastly, increases in interrogation volume or NV⁻ density are both accompanied by unique challenges independent of those associated with increases in sensor number N . For example, larger sensing volumes require better engineering to ensure the bias magnetic field and MW field are uniform over the sensing volume (Abe and Sasaki, 2018; Eisenach et al., 2018). Alternatively, increasing NV⁻ density necessarily positions NV⁻ spins (and all other nitrogen-related paramagnetic spins) closer together, which results in increased dipolar dephasing and shorter associated T_2^* values, canceling the sensitivity improvement from addressing more NV⁻ spins.

4. Choosing nitrogen concentration in diamond samples

The following discussion parallels the clear analysis presented in Ref. (Kleinsasser et al., 2016), which the reader is encouraged to review. Equation 10 can be simplified by grouping all non-nitrogen-related broadening mechanisms together, yielding

$$\frac{1}{T_2^*} = \frac{1}{T_2^* \{N_S^0\}} + \frac{1}{T_2^* \{NV^-\}} + \frac{1}{T_2^* \{NV^0\}} + \frac{1}{T_2^* \{\text{other}\}}, \quad (\text{A42})$$

where we have ignored typically less common defects in fully treated diamond (i.e., irradiated, annealed, etc.) such as NVH⁻, N₂V⁻, etc. (Hartland, 2014); and $T_2^* \{\text{other}\}$ denotes the T_2^* limit from all non-nitrogen-related dephasing mechanisms. The above equation can be rewritten as

$$\frac{1}{T_2^*} = A_{N_S^0} [N^T] [1 - E_{\text{conv}} - E_{\text{conv}}^0 - E_{\text{conv}}^{N_S^+}] + A_{NV^-} [N^T] [E_{\text{conv}}] + A_{NV^0} [N^T] [E_{\text{conv}}^0] + \frac{1}{T_2^* \{\text{other}\}} \quad (\text{A43})$$

where $E_{\text{conv}} \equiv [NV^-]/[N^T]$, $E_{\text{conv}}^0 \equiv [NV^0]/[N^T]$, and $E_{\text{conv}}^{N_S^+} \equiv [N_S^+]/[N^T]$ are the conversion efficiencies from the total nitrogen concentration $[N^T]$ to $[NV^-]$, $[NV^0]$, and $[N_S^+]$ respectively. The A_X coefficients characterize the magnetic dipole interaction strength between NV⁻ spins and spin species X. The value of $A_{N_S^0}$ is defined in Eqn. 14, the value of A_{NV^-} is defined in Section II.G and in this section for reasons of compactness we do not differentiate between $A_{NV_{\parallel}^-}$ and $A_{NV_{\perp}^-}$. The value of A_{NV^0} is defined so that the NV⁻ dephasing from NV⁰ satisfies $\frac{1}{T_2^* \{NV^0\}} = A_{NV^0} [NV^0]$. Under the assumption that E_{conv} , E_{conv}^0 , $E_{\text{conv}}^{N_S^+}$ are indepen-

dent of $[N^T]$, consolidation yields

$$\frac{1}{T_2^*} = \kappa [N^T] + \frac{1}{T_2^* \{\text{other}\}}, \quad (\text{A44})$$

where $\kappa = A_{N_S^0} [1 - E_{\text{conv}} - E_{\text{conv}}^0 - E_{\text{conv}}^{N_S^+}] + A_{NV^-} [E_{\text{conv}}] + A_{NV^0} [E_{\text{conv}}^0]$. The detected number of PL photons per measurement is $\mathcal{N} \propto [N^T] E_{\text{conv}} V n_{\text{avg}}$ where V is the interrogation volume. For simplicity we consider the limit where initialization and readout times t_I and t_R are negligible, so that sensitivity is

$$\eta \propto \sqrt{\frac{1}{\mathcal{N} T_2^*}} = \sqrt{\frac{1}{E_{\text{conv}} V n_{\text{avg}}}} \times \sqrt{\kappa + \frac{1}{[N^T] T_2^* \{\text{other}\}}}, \quad (\text{A45})$$

which suggests that for $[N^T] \gg \frac{1}{\kappa T_2^* \{\text{other}\}}$, sensitivity is independent of $[N^T]$. Qualitatively, this can be interpreted as follows: when T_2^* is limited by nitrogen-related dephasing mechanisms (i.e., NV⁻, NV⁰, N_S⁺), and again assuming E_{conv} , E_{conv}^0 , and $E_{\text{conv}}^{N_S^+}$ are independent of $[N^T]$, decreasing $[N^T]$ increases T_2^* by the same fractional quantity that the NV ensemble photoluminescence \mathcal{N} is decreased. However, when T_2^* is limited by other broadening mechanisms unrelated to nitrogen, decreasing $[N^T]$ decreases the collected fluorescence \mathcal{N} without any corresponding T_2^* increase. The implications here are significant: this analysis suggests that while there is not a unique value of $[N^T]$ for maximal sensitivity, there is a minimum value. In other words, if nitrogen-related broadening is a small contributor to T_2^* , the nitrogen content should be increased; the increased resulting PL will favorably offset the increase in T_2^* , resulting in overall enhanced sensitivity.

A few points are in order regarding the above analysis. Experimental considerations can also set an upper bound on the most desirable total nitrogen concentration $[N^T]$. For example the larger detected photon number \mathcal{N} associated with a higher values of $[N^T]$ can present technical challenges (see Appendix A.3). Moreover, the above analysis considers the simple limit where the initialization and readout time are negligible; accounting for this fixed overhead time (see Eqns. 2, 6, and 7) favors trading off nitrogen concentration density for longer values of T_2^* , in order to reduce the fractional overhead time devoted to initialization and readout. Overall, combined experimental and theoretical considerations suggest that for best sensitivity nitrogen content should be decreased until nitrogen-related broadening is similar to non-nitrogen related broadening, i.e., $\kappa [N^T] \approx \frac{1}{T_2^* \{\text{other}\}}$.

5. Spin resonance linewidth and T_2^*

The quantity T_2^* , which characterizes the time scale of the free induction decay (FID), is inversely proportional to the natural spin resonance linewidth in the absence of power broadening. Exact conversion between T_2^* and linewidth requires knowledge of the functional form of the FID or the resonance lineshape (Abragam, 1983c; Kwan and Yen,

1979). Ramsey fringes decaying with an FID envelope $\propto e^{-t/T_2^*}$ indicate a Lorentzian spin resonance profile with full width at half maximum (FWHM) $\Gamma = \frac{1}{\pi T_2^*}$, as shown by the Fourier transform pair:

$$\begin{aligned}\mathcal{F}_t[e^{2\pi i f_0 t} e^{-t/T_2^*}](f) &= \frac{1}{\pi} \frac{\frac{1}{2\pi T_2^*}}{\left(\frac{1}{2\pi T_2^*}\right)^2 + (f - f_0)^2} \\ &= \frac{1}{\pi} \frac{\Gamma/2}{(\Gamma/2)^2 + (f - f_0)^2},\end{aligned}\quad (\text{A46})$$

valid for $t \geq 0$, where f_0 is the Ramsey fringe frequency.

A Gaussian decay envelope $\propto e^{-(t/T_2^*)^2}$ corresponds to a resonance with a Gaussian profile, with standard deviation $\sigma = \frac{1}{\sqrt{2\pi T_2^*}}$ as shown by the Fourier transform pair:

$$\begin{aligned}\mathcal{F}_t[e^{2\pi i f_0 t} e^{-(t/T_2^*)^2}](f) &= \sqrt{\pi T_2^*} e^{-(\pi T_2^* (f - f_0))^2} \\ &= \frac{1}{\sigma \sqrt{2\pi}} e^{-(f - f_0)^2 / (2\sigma^2)}.\end{aligned}\quad (\text{A47})$$

6. Estimating T_2^* from spin resonance linewidths of N_S^0

Although sensor performance is dictated by T_2^* of the NV^- ensemble, T_2^* values of other paramagnetic defects within the diamond, such as substitutional nitrogen defects, can provide useful information on sources of NV^- spin dephasing. Such T_2^* values can be extracted from linewidth measurements, for example from electron paramagnetic resonance (EPR). Accurate conversion from EPR linewidth to paramagnetic-defect T_2^* enables leveraging of existing diamond EPR data (van Wyk *et al.*, 1997) to better understand the contributions of different noise sources to NV^- ensemble T_2^* values.

EPR linewidths are commonly tabulated by their peak-to-peak widths ΔB , where ΔB denotes the magnetic field spacing between extrema of the resonance line first derivative (Poole, 1996). In (linear) frequency units, this peak-to-peak width is $\delta = \frac{g\mu_B}{h} \Delta B$. Accurately relating δ and T_2^* requires the resonance lineshape to be known (Kwan and Yen, 1979). For example, a Lorentzian profile with full width at half maximum (FWHM) Γ , expressed in frequency units, has $\delta = \Gamma/\sqrt{3}$ and $\Gamma = \frac{1}{\pi T_2^*}$ (see Appendix A.5). Combining these relations yields $T_{2\text{Lor}}^* = \frac{1}{\sqrt{3}\pi\delta}$. A Gaussian lineshape with the same measured peak-to-peak linewidth δ has standard deviation $\sigma = \delta/2$ and $\sigma = \frac{1}{\sqrt{2\pi T_2^*}}$ (see Appendix A.5). Thus, $T_{2\text{Gau}}^* = \frac{\sqrt{2}}{\pi\delta}$, which is $\sqrt{6}\times$ longer than $T_{2\text{Lor}}^*$. A visual comparison of these relationships is displayed in Fig. A.2.

Diamond EPR literature results may report values of δ without giving the associated resonance lineshape, preventing accurate determination of T_2^* from δ . For example, linewidth measurements in Ref. (van Wyk *et al.*, 1997) on substitutional nitrogen defects N_S^0 in diamond indicate a scaling $1/T_2^*\{N_S^0\} = A_{N_S^0}[N_S^0]$ with varying nitrogen concentration $[N_S^0]$, but the scaling factor $A_{N_S^0}$ cannot be accurately determined without knowledge of the lineshape.

Theoretical and experimental results on dipolar-coupled spin systems suggest a Lorentzian resonance lineshape when spin-bath interactions are the dominant source of line-broadening (Abragam, 1983c; Dobrovitski *et al.*, 2008; Hall *et al.*, 2014; Kittel and Abrahams, 1953). Furthermore, Ramsey measurements with NV^- spin ensembles show FID envelopes well fit by $e^{-(t/T_2^*)^p}$ with $p \sim 1$, corresponding to a Lorentzian lineshape (see Appendix A.7, Fig. A.2 and Ref. (Bauch *et al.*, 2018)) when T_2^* is expected to be spin-bath limited.

Assuming a Lorentzian profile when converting δ values from Ref. (van Wyk *et al.*, 1997) to T_2^* values yields $A_{N_S^0} \approx 130 \text{ ms}^{-1}/\text{ppm}$ for nitrogen spins in a nitrogen spin bath (see Fig. A.3). This calculated scaling factor is considered to be an upper bound because (i), a Gaussian or Voigt profile would result in a smaller value of $A_{N_S^0}$ than that calculated by assuming a Lorentzian profile, as $1/T_{2\text{Gau}}^* = 1/(\sqrt{6}\times T_{2\text{Lor}}^*)$; and (ii), other sources of broadening may contribute to the EPR linewidths observed in Ref. (van Wyk *et al.*, 1997). In the latter case the true contribution to dephasing from dipolar interactions between N_S^0 spins would be smaller than that estimated from the measured δ . Nitrogen-spin-bath induced dephasing of N_S^0 and of NV^- are expected to be similar, as the dipolar coupling between two N_S^0 spins is similar to the dipolar coupling between a N_S^0 and an NV^- for equivalent separation (Hanson *et al.*, 2008). Thus, the spin-bath-limited linewidth of nitrogen defects in diamond measured via EPR can serve as a proxy for the spin-bath limited linewidth of NV^- centers. The value of $A_{N_S^0} \approx 130 \text{ ms}^{-1}/\text{ppm}$ for N_S^0 from the data in Ref. (van Wyk *et al.*, 1997) serves as an independent estimate of $A_{N_S^0}$ for NV^- centers in a nitrogen spin bath. This value is in reasonable agreement with the measured $A_{N_S^0} \approx 101 \text{ ms}^{-1}/\text{ppm}$ for NV^- ensembles from Ref. (Bauch *et al.*, 2018).

7. Stretched exponential parameter

Equations A46 and A47 show that the spin resonance lineshape can be parameterized by the stretched exponential parameter p of the free induction decay (FID) envelope $e^{-(t/T_2^*)^p}$. We note that for the idealized case of a purely Lorentzian lineshape, $p = 1$, and for a purely Gaussian lineshape, $p = 2$. The exact ODMR lineshape and value of p are well characterized for single spins under a variety of environmental conditions (Dobrovitski *et al.*, 2008; Hall *et al.*, 2014; Hanson *et al.*, 2008; Maze *et al.*, 2012; de Sousa, 2009). For example, a single spin experiencing dipolar coupling to a surrounding bath of spins displays an FID envelope with stretched exponential parameter $p = 2$ (Dobrovitski *et al.*, 2008; Hall *et al.*, 2014; Maze *et al.*, 2012; de Sousa, 2009) (Gaussian ODMR lineshape, see Table A.1 and Fig. A.2). Meanwhile, NV^- ensembles with linewidth limited by dipolar coupling to a spin bath are predicted (Dobrovitski *et al.*, 2008; Hall *et al.*, 2014) and measured (Bauch *et al.*, 2018; MacQuarrie *et al.*, 2015) to exhibit FID envelopes with $p = 1$ (Lorentzian ODMR lineshape, see Table A.1 and Fig. A.2). However, experimental Ramsey measurements

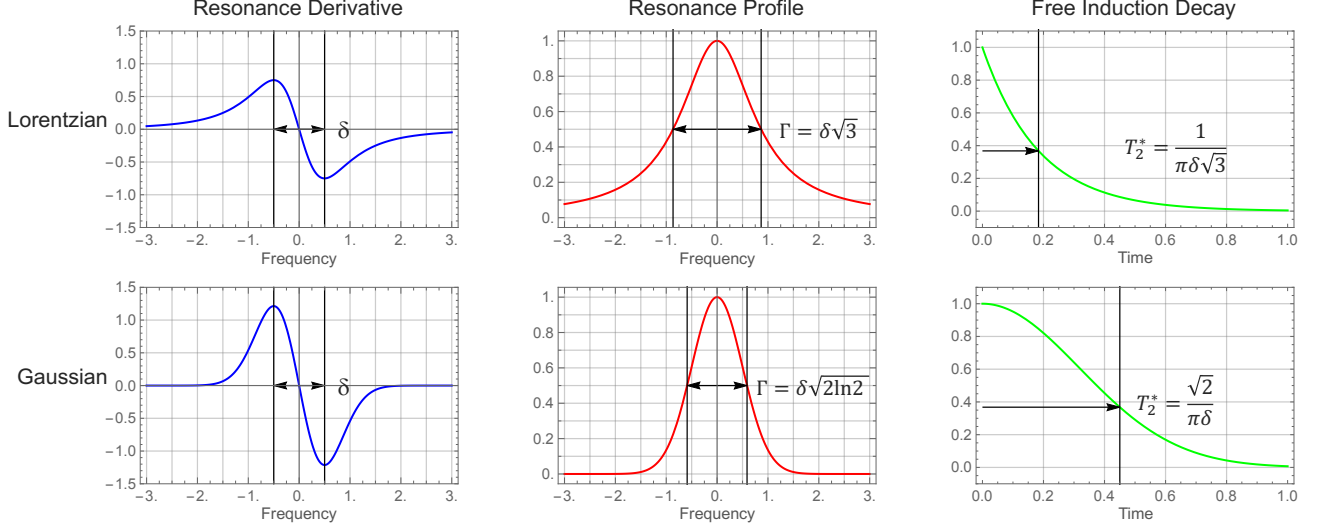


FIG. A.2 Resonance derivatives (—), resonance profiles (—), and free induction decay (FID) envelopes (—) for Lorentzian and Gaussian lineshape profiles with the same peak-to-peak widths δ . Full-width-at-half-max linewidths Γ and FID decay envelope times T_2^* are indicated and expressed in terms of the peak-to-peak width δ , a commonly reported parameter characterizing linewidth in electron paramagnetic resonance (EPR) data.

Ramsey T_2^* decay	p	Reference (experiment)	Reference (theory)
Single NV ⁻	2	(Maze <i>et al.</i> , 2012)	(Dobrovitski <i>et al.</i> , 2008; Hall <i>et al.</i> , 2014; de Sousa, 2009)
NV ⁻ ensemble	1	(Bauch <i>et al.</i> , 2018; MacQuarrie <i>et al.</i> , 2015)	(Dobrovitski <i>et al.</i> , 2008; Hall <i>et al.</i> , 2014)

TABLE A.1 Stretched exponential parameters p associated with free induction decay envelopes for single NV⁻ centers and NV⁻ ensembles in dipolar-coupled spin baths

on NV⁻ ensembles may sometimes exhibit decay envelopes with $p \neq 1$, suggesting the presence of other broadening mechanisms such as strain gradients, magnetic field gradients, or temperature fluctuations (Bauch *et al.*, 2018). A noninteger p for an ensemble may also indicate the presence of more complex dephasing and decoherence dynamics, including spatial inhomogeneity, than can be encompassed by a single decay time constant. In some cases the decay may be better described by a sum (Cao, 1994) or a product of multiple decay curves with different values of T_2^* and p . For example, a product of two FID decays, one with $p = 1$ and one with $p = 2$, corresponds to a Voigt profile lineshape. Allowing p to vary when fitting FID envelopes crudely accounts for these sorts of lineshape variations while only requiring a single additional fit parameter. Therefore, Ramsey FID measurements exhibiting $1 \leq p \leq 2$ for some NV⁻ ensembles may suggest contributions to the ODMR lines from both Lorentzian and Gaussian broadening mechanisms (Bauch *et al.*, 2018).

Hahn echo T_2 decays of single NV⁻ spins have been predicted (de Sousa, 2009) and measured (de Lange *et al.*, 2010) to exhibit a stretched exponential parameter $p = 3$ when T_2 is limited by spin-bath noise. In contrast, Hahn echo decay envelopes for ensembles of NV⁻ spins have been seen to exhibit p varying from ~ 0.5 to 3, depending on the dominant contributors to the spin bath and the bias magnetic field angle (Bauch *et al.*, 2019; Stanwix *et al.*, 2010).

8. Isotopic purity confusion in the literature

In Sec. II.F, we discussed the T_2^* limit imposed by $[^{13}\text{C}]$, which is described by an inverse linear scaling in Eqn. 16, reproduced below,

$$\frac{1}{T_2^*\{^{13}\text{C}\}} = A_{^{13}\text{C}} [^{13}\text{C}], \quad (\text{A48})$$

where $A_{^{13}\text{C}} \approx 0.100 \text{ ms}^{-1}/\text{ppm}$. Although such inverse linear scaling with $[^{13}\text{C}]$ is predicted by several theoretical calculations (see Refs. (Abragam, 1983c; Dobrovitski *et al.*, 2008; Hall *et al.*, 2014; Kittel and Abrahams, 1953)), some experiments based on single NV⁻ centers (incorrectly we believe) suggest an inverse square root scaling (Balasubramanian *et al.*, 2009; Mizuochi *et al.*, 2009), i.e.,

$$\frac{1}{T_2^*\{\text{single}\}\{^{13}\text{C}\}} = A_{^{13}\text{C}}^{\{\text{single}\}} \sqrt{[^{13}\text{C}]}. \quad (\text{A49})$$

for single NV⁻ centers in the dilute limit ($[^{13}\text{C}]/[^{12}\text{C}] \ll 0.01$). In Ref. (Mizuochi *et al.*, 2009), the data were derived from mean T_2^* values taken from many single NV⁻ defects in the diamond. However, Eqn. A49 conflicts with theoretical calculations by both Dobrovitski *et al.* (Dobrovitski *et al.*, 2008) and Hall *et al.* (Hall *et al.*, 2014) explicitly for single NV⁻ centers. Both sources instead suggest that for the mean single NV⁻ center,

$$\frac{1}{T_2^*\{\text{single}\}\{^{13}\text{C}\}} = A_{^{13}\text{C}}^{\{\text{single}\}} [^{13}\text{C}], \quad (\text{A50})$$

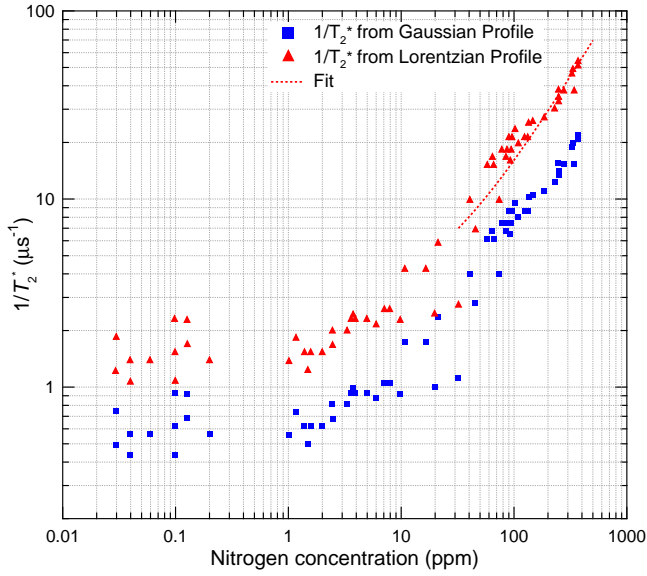


FIG. A.3 Bounds on $1/T_2^*$ associated with EPR linewidth measurements of N_S^0 defects (P1 centers) from Ref. (van Wyk *et al.*, 1997) in diamonds with a range of nitrogen impurity concentrations, calculated assuming Gaussian (■) and Lorentzian (▲) EPR lineshapes. A fit to the function $1/T_2^* = A_{N_S^0} [N_S^0] + b$ assuming a Lorentzian lineshape (···) yields $A_{N_S^0} \approx 130 \text{ ms}^{-1}/\text{ppm}$ for nitrogen spins in a nitrogen spin bath (see main text).

similar to Eqn. 16.

We hypothesize that the origin of this discrepancy is omission of nitrogen broadening in the study from Ref. (Mizuochi *et al.*, 2009), as summarized in Table A.2. Using the relation $1/T_2^{\{\text{single}\}}\{N_S^0\} = A_{N_S^0}^{\{\text{single}\}} [N_S^0]$ (see Sec. II.D), we roughly estimate $A_{N_S^0}^{\{\text{single}\}} = 56 \text{ ms}^{-1}/\text{ppm}$ from Ref. (Zhao *et al.*, 2012). For the lowest ^{13}C sample in the data from Ref. (Mizuochi *et al.*, 2009), which has $[N_S^0] \sim 1 \text{ ppm}$, this estimate predicts a nitrogen-limited $T_2^{\{\text{single}\}}\{N_S^0\}$ of $\sim 18 \text{ } \mu\text{s}$, close to the actual reported T_2^* measurement. Neglecting the additional nitrogen contribution to $T_2^{\{\text{single}\}}$ for the lowest ^{13}C sample likely caused Mizuochi *et al.* to overestimate the contribution of ^{13}C to T_2^* and draw incorrect conclusions on the scaling of T_2^* with $[^{13}\text{C}]$.

Reference (Balasubramanian *et al.*, 2009) report linewidths of 210 kHz and 55 kHz for diamonds with 1.1% and 0.3% ^{13}C respectively, data which is clearly consistent with Eqn. 16. However the authors of Ref. (Balasubramanian *et al.*, 2009) interpret their data using formalism appropriate for $^{13}\text{C} \gtrsim 10\%$ (Abragam, 1983c), which results in them employing Eqn. A49.

As discussed in Sec. II.F, Eqn. 16 has been experimentally verified in the dilute limit in a similar system (Abe *et al.*, 2010). Given that the mean single-NV⁻ FID time is longer than the ensemble FID time by $\sim 2\times$ in diamond with natural abundance ^{13}C (see Section II.F and Ref. (Maze *et al.*, 2012)), if Eqn. A49 were also correct, then at sufficiently low ^{13}C concentration, an NV⁻ ensemble would dephase more slowly than its constituent spins.

This prediction conflicts with the present understanding that $T_2^{\{\text{single}\}}\{^{13}\text{C}\} > T_2^*\{^{13}\text{C}\}$ regardless of concentration (see Sec. II.B).

9. Linear Stark and Zeeman regimes

Here we describe coupling of electric fields, strain, and magnetic fields to the NV⁻ spin resonances in the regimes of both low and high axial bias magnetic field $B_{0,z}$. This treatment draws heavily on equations and analysis in Ref. (Jamonneau *et al.*, 2016). While understanding of strain's effect on the NV⁻ spin continues to evolve (Barfuss *et al.*, 2018; Barson *et al.*, 2017; Doherty *et al.*, 2013; Udvarhelyi *et al.*, 2018), we take the NV⁻ ground state spin Hamiltonian in the presence of a bias magnetic field \vec{B}_0 , an electric field \vec{E} , and intrinsic crystal strain to be (Doherty *et al.*, 2013; Udvarhelyi *et al.*, 2018)

$$\begin{aligned} H/h = & (D + \mathcal{M}_z + d_{\parallel} E_z) S_z^2 \\ & + \frac{g_e \mu_B}{h} (B_{0,z} S_z + B_{0,x} S_x + B_{0,y} S_y) \\ & + \left(\frac{d_{\perp} E_x}{h} + \mathcal{M}_x \right) (S_y^2 - S_x^2) \\ & + \left(\frac{d_{\perp} E_y}{h} + \mathcal{M}_y \right) (S_x S_y + S_y S_x) \\ & + \mathcal{N}_x (S_x S_z + S_z S_x) + \mathcal{N}_y (S_y S_z + S_z S_y). \end{aligned} \quad (\text{A51})$$

Here S_i with $i = x, y, z$ are the dimensionless spin-1 projection operators; D is the NV⁻ zero field splitting ($\approx 2.87 \text{ GHz}$ at room temperature); $d_{\parallel} = 3.5 \times 10^{-3} \text{ Hz}/(\text{V}/\text{m})$ and $d_{\perp} = 0.17 \text{ Hz}/(\text{V}/\text{m})$ are the axial and transverse electric dipole moments (Dolde *et al.*, 2011; Michl *et al.*, 2019; Van Oort and Glasbeek, 1990); and $\mathcal{M}_z, \mathcal{M}_x, \mathcal{M}_y, \mathcal{N}_x$, and \mathcal{N}_y are spin-strain coupling parameters.

The Hamiltonian can be simplified when D is large compared to all other coupling terms, i.e., in the regime of low magnetic field, electric field, and strain. In particular, energy level shifts associated with transverse magnetic field components $B_{0,x}$ and $B_{0,y}$ (Jamonneau *et al.*, 2016), and with spin-strain coupling parameters \mathcal{N}_x and \mathcal{N}_y , are suppressed by D and thus may be neglected from the Hamiltonian (Kehayias *et al.*, 2019). This low-field Hamiltonian H_{LF} is given by

$$\begin{aligned} H_{\text{LF}}/h = & (D + \mathcal{M}_z + d_{\parallel} E_z) S_z^2 + \frac{g_e \mu_B}{h} B_{0,z} S_z \\ & + \left(\frac{d_{\perp} E_x}{h} + \mathcal{M}_x \right) (S_y^2 - S_x^2) \\ & + \left(\frac{d_{\perp} E_y}{h} + \mathcal{M}_y \right) (S_x S_y + S_y S_x). \end{aligned} \quad (\text{A52})$$

We focus on the interplay between different terms in H_{LF} that shift the NV⁻ spin resonance frequencies in opposite directions, including $B_{0,z}$, E_x , E_y , \mathcal{M}_x , and \mathcal{M}_y . In contrast, dephasing associated with variations in terms that shift the resonance frequencies in common-mode (D , E_z , and \mathcal{M}_z), can be mitigated by employing double-quantum coherence magnetometry (see Sec. III.B) and are ignored herein. In

^{13}C (ppm)	Measured $T_2^{*\{\text{single}\}}$ (μs) (Mizuochi <i>et al.</i> , 2009)	Synthesis	$[\text{N}_\text{S}]$ (ppm)	Calculated $T_2^{*\{\text{single}\}}\{^{13}\text{C}\}$ (μs) (This work)	Calculated $T_2^{*\{\text{single}\}}\{\text{N}_\text{S}^0\}$ (μs) (This work)
10700	3.3	CVD	< 0.001	2.3	$\gtrsim 18000$
3500	6.2	CVD	< 0.001	7	$\gtrsim 18000$
300	18	HPHT	~ 1	82	~ 18

TABLE A.2 The three diamonds used in Ref. (Mizuochi *et al.*, 2009). The calculated value of $T_2^{*\{\text{single}\}}\{^{13}\text{C}\}$ is derived using the mean value of $T_2^* = 2.3 \mu\text{s}$ for single NV⁻ centers in a natural abundance ^{13}C sample measured with a bias field of 20 G from Ref. (Maze *et al.*, 2012), so that $T_2^{*\{\text{single}\}}\{^{13}\text{C}\} = 2.3 \mu\text{s} \times \frac{0.0107}{[^{13}\text{C}]}$. The calculated value of $T_2^{*\{\text{single}\}}\{\text{N}_\text{S}^0\}$ is estimated using the simulation in Fig. 1 of Ref. (Zhao *et al.*, 2012) which predicts $T_2^{*\{\text{single}\}}\{\text{N}_\text{S}^0\} = 18 \pm 1 \text{ ps}/[\text{N}_\text{S}^0]$.

addition to shifting the spin resonance frequencies, transverse electric fields, E_x and E_y , and transverse spin-strain coupling terms, \mathcal{M}_x and \mathcal{M}_y , mix the $m_s = \pm 1$ spin states into

$$|+\rangle = \cos\left(\frac{\theta}{2}\right)|+1\rangle + e^{i\phi}\sin\left(\frac{\theta}{2}\right)|-1\rangle, \quad (\text{A53})$$

$$|-\rangle = \sin\left(\frac{\theta}{2}\right)|+1\rangle - e^{i\phi}\cos\left(\frac{\theta}{2}\right)|-1\rangle, \quad (\text{A54})$$

where $\tan(\phi) = (d_\perp E_y + \mathcal{M}_y)/(d_\perp E_x + \mathcal{M}_x)$ and $\tan(\theta) = \xi_\perp/\beta_z$. Here $\beta_z = (g_e\mu_B/h)B_{0,z}$ represents the magnetic field coupling to the NV⁻ spin and $\xi_\perp = \sqrt{(d_\perp E_x/h + \mathcal{M}_x)^2 + (d_\perp E_y/h + \mathcal{M}_y)^2}$ combines the effects of transverse strain and electric fields. The transition frequencies $|0\rangle \leftrightarrow |+\rangle$ and $|0\rangle \leftrightarrow |-\rangle$ are

$$\nu_\pm = D + \mathcal{M}_z + d_\parallel E_z \pm \sqrt{\xi_\perp^2 + \beta_z^2}, \quad (\text{A55})$$

and the coupling strength of transverse strain and electric fields to the NV⁻ spin resonance frequencies is given by

$$\frac{\partial \nu_\pm}{\partial \xi_\perp} = \frac{\pm 1}{\sqrt{1 + \left(\frac{\beta_z}{\xi_\perp}\right)^2}}. \quad (\text{A56})$$

In the linear Stark regime, characterized by $\beta_z \ll \xi_\perp$, the spin eigenstates become, approximately, equal superpositions of $|+1\rangle$ and $|-1\rangle$, and the transition frequencies exhibit maximal sensitivity to variations in ξ_\perp :

$$\left|\frac{\partial \nu_\pm}{\partial \xi_\perp}\right|_{\beta_z \ll \xi_\perp} = 1 - \frac{1}{2}\left(\frac{\beta_z}{\xi_\perp}\right)^2 + \mathcal{O}\left[\left(\frac{\beta_z}{\xi_\perp}\right)^4\right]. \quad (\text{A57})$$

In contrast, in the linear Zeeman regime, characterized by $\beta_z \gg \xi_\perp$, the spin eigenstates become, approximately, $|+1\rangle$ and $|-1\rangle$, and sensitivity to strain/electric fields is suppressed by the ratio $\frac{\xi_\perp}{\beta_z}$:

$$\left|\frac{\partial \nu_\pm}{\partial \xi_\perp}\right|_{\beta_z \gg \xi_\perp} = \frac{\xi_\perp}{\beta_z} - \frac{1}{2}\left(\frac{\xi_\perp}{\beta_z}\right)^3 + \mathcal{O}\left[\left(\frac{\xi_\perp}{\beta_z}\right)^5\right]. \quad (\text{A58})$$

By performing magnetic sensing in the linear Zeeman regime, spatial and temporal variations in transverse electric fields and strain couple less strongly to the NV⁻ spin, and thus their contribution to T_2^* is diminished. The linear

Zeeman regime is best suited for high-sensitivity magnetometry not only because of the T_2^* extension from suppressed sensitivity to variations in ξ_\perp , but also because magnetic field changes couple most strongly to ν_\pm in this regime:

$$\left|\frac{\partial \nu_\pm}{\partial \beta_z}\right|_{\beta_z \gg \xi_\perp} = 1 - \frac{1}{2}\left(\frac{\xi_\perp}{\beta_z}\right)^2 + \mathcal{O}\left[\left(\frac{\xi_\perp}{\beta_z}\right)^4\right]. \quad (\text{A59})$$

Experiments that must operate at near-zero \vec{B}_0 for other reasons, such as to protect ferromagnetic samples, should use low-strain diamonds to avoid operating in the unfavorable regime where $\beta_z \ll \xi_\perp$ (Backlund *et al.*, 2017; Fu *et al.*, 2014; Glenn *et al.*, 2017; Zheng *et al.*, 2018). In this linear Stark regime, not only is sensitivity to magnetic signals suppressed by the ratio $\frac{\beta_z}{\xi_\perp}$,

$$\left|\frac{\partial \nu_\pm}{\partial \beta_z}\right|_{\beta_z \ll \xi_\perp} = \frac{\beta_z}{\xi_\perp} - \frac{1}{2}\left(\frac{\beta_z}{\xi_\perp}\right)^3 + \mathcal{O}\left[\left(\frac{\beta_z}{\xi_\perp}\right)^5\right], \quad (\text{A60})$$

but also T_2^* may be shortened by electric field and strain variations.

10. Example annealing calculations

We present some calculations to estimate parameters necessary for LPHT annealing to form NV centers. Using $D_0 = 1.6 \times 10^{-3} \text{ cm}^2/\text{s}$ (Fletcher and Brown, 1953) for the diffusion constant, $E_a = 2.3 \text{ eV}$ for the activation energy, and $T = 800 \text{ }^\circ\text{C}$ for the annealing temperature, we expect $D = 2.5 \text{ nm}^2/\text{s}$. When annealing at $T = 800 \text{ }^\circ\text{C}$ and $t_{\text{anneal}} = 12 \times 3600 \text{ s}$, a single vacancy in a perfect lattice is expected (based on the model presented here) to have made $\sim 2.7 \times 10^7$ lattice jumps, visited 1.5×10^7 distinct lattice sites (Fastenau, 1982; Vineyard, 1963), and diffused a root-mean-square distance of $\langle r_{\text{rms}} \rangle \approx .8 \mu\text{m}$, assuming $\langle r_{\text{rms}} \rangle = \sqrt{6Dt_{\text{anneal}}}$. The uncertainties in these estimates are dominated by the $\pm 0.3 \text{ eV}$ uncertainty in E_a (Davies *et al.*, 1992; Mainwood, 1999), which can lead to an order of magnitude variation in D for $T = 800 \text{ }^\circ\text{C}$. Ignoring small repulsive forces between substitutional nitrogen and mono-vacancies (Davies *et al.*, 1992), a vacancy is expected to visit $\sim 10^6/4$ lattice sites in a 1 ppm $[\text{N}_\text{S}]$ diamond to form an NV. The factor 4 arises from the four closest sites to a

substitutional nitrogen while the 10^6 arises because only 1 out of every 10^6 lattice sites is occupied by a substitutional nitrogen. Because the number of distinct lattice sites visited is substantially greater than the number of sites needed to form an NV center (i.e., $\frac{1.5 \times 10^7}{10^6/4} \gg 1$), the chosen values of T and t_{anneal} are expected to ensure adequate NV center formation. The simple analysis stated here is complicated by the uncertainty in D_0 and E_a , as well as the presence of other vacancies, vacancy aggregates, dislocations, surfaces, etc., which can also trap vacancies, but are beyond the scope of this paper.

11. The diamond type classification system

We briefly overview the “diamond type” classification system introduced in the 1930s and outlined in Refs. (Robertson *et al.*, 1933, 1936). In spite of the system’s shortcomings, it has been widely adopted by the gemstone community and is partially used by the scientific community today. In the mid-1930’s the authors of Refs. (Robertson *et al.*, 1933, 1936) noted that although the vast majority of natural diamonds exhibited absorption lines in the 225–300 nm band and near 8 μm , these same absorption features were absent in a small minority of diamonds. The authors further observed that diamonds lacking these same absorption features tended to exhibit lower birefringence and higher photoconductivity relative to their peers (Robertson *et al.*, 1933, 1936). In 1959 the authors of Ref. (Kaiser and Bond, 1959) attributed the observed infrared absorption features to carbon-nitrogen molecular vibrations, signaling the presence of nitrogen. Nitrogen was found to be the most common impurity occurring in natural diamonds, which made its presence or absence a logical basis for diamond classification.

In this nitrogen-based diamond classification system, all diamonds are categorized into one of two primary types: Type I diamonds contain measurable quantities of nitrogen while Type II diamonds do not, as shown in Fig. A.4. There is no wide consensus on what constitutes “measurable” in an age of ever-advancing characterization tools, although a common definition is a quantity detectable with an FTIR spectrometer (Breeding and Shigley, 2009). Most sources suggest a delineation somewhere between 0.5 ppm (Zaitsev, 2001) and 20 ppm (Dischler, 2012; Gaillou *et al.*, 2012). This delineation uncertainty is particularly unfortunate for the NV community, as many diamonds employed for ensemble NV experiments fall in this range.

Type I diamonds can be further classified by the specific nitrogen complexes incorporated into the carbon lattice. For example, Type Ia diamonds contain aggregated nitrogen impurities, and describe the vast majority of natural diamonds ($\gtrsim 95\%$, depending on the delineation nitrogen concentration (Breeding and Shigley, 2009; Zaitsev, 2001)). Typical nitrogen concentrations in natural Type Ia diamonds are in the hundreds of ppm (e.g., 500 ppm (Zaitsev, 2001)) but can be as high as 3000 ppm (Neves and Nazaré, 2001). If the aggregated nitrogen predominantly forms A centers consisting of two substitutional nitrogens

located adjacent in the diamond lattice, the diamond is classified as Type IaA. If the aggregated nitrogen predominantly forms B centers consisting of four substitutional nitrogens surrounding a lattice vacancy, the diamond is classified as Type IaB. In contrast, diamonds containing predominantly isolated single nitrogen impurities are classified as Type Ib and make up about 0.1% of all natural diamonds (Zaitsev, 2001). As higher nitrogen density promotes aggregation, Type Ib diamonds typically exhibit nitrogen concentrations at or below the 100 ppm level (Zaitsev, 2001), less than typical for Type Ia diamonds (Zaitsev, 2001).

Type II diamonds containing no “measurable” nitrogen can be additionally classified as well. Type IIa diamonds contain no other measurable impurities and make up the majority of gem-grade diamonds in spite of comprising only 1 to 2% of natural diamonds. These diamonds are the most optically transparent diamonds: while Type IIa diamonds with low levels of impurities may exhibit pale shades of yellow, pink, or purple; extremely pure Type IIa diamonds are colorless (Zaitsev, 2001). Nearly all single NV experiments employ Type IIa diamonds. As boron is another common impurity in natural diamond, Type II diamonds with “measurable” boron are categorized as Type IIb. These diamonds make up about 0.1% of all natural diamonds and may exhibit a bluish or greyish hue.

Although the diamond type classification system was developed for natural diamonds, it appropriately describes synthetic diamonds as well. CVD-grown diamonds without nitrogen doping are Type IIa. Man made HPHT diamonds of Type IaA, Ib, IIa, and IIb have been created. Further diamond types exist: see Ref. (Zaitsev, 2001).

Reference	(Tetienne <i>et al.</i> , 2012)	(Gupta <i>et al.</i> , 2016)	(Robledo <i>et al.</i> , 2011)	(Acosta <i>et al.</i> , 2010b)	
NV ⁻ centers probed	4	3	2	ensemble	units
Values reported	avg. (max, min)	avg. (max, min)	avg.		
$^3E(m_s=0) \rightarrow ^3A_2(m_s=0)$	67.9 (63.2, 69.1)	66.16 (66.08, 66.43)	64.2	-	μs^{-1}
$^3E(m_s=\pm 1) \rightarrow ^3A_2(m_s=\pm 1)$	67.9 (63.2, 69.1)	66.16 (66.08, 66.43)	64.9	-	μs^{-1}
$^3E(m_s=0) \rightarrow ^1A_1$	5.7 (5.2, 10.8)	11.1 (10.9, 11.2)	11.2	-	μs^{-1}
$^3E(m_s=\pm 1) \rightarrow ^1A_1$	49.9 (48.6, 60.7)	91.8 (89.3, 92.9)	80.0	-	μs^{-1}
$^1E \rightarrow ^3A_2(m_s=0)$	1.0 (0.7, 1.5)	4.87 (4.75, 4.90)	3.0	-	μs^{-1}
$^1E \rightarrow ^3A_2(m_s=\pm 1)$	0.75 (0.4, 1.4)	2.04 (2.03, 2.13)	2.6	-	μs^{-1}
1A_1 lifetime	-	144.5 (144.3, 145.3)	178 ± 6	219 ± 3	ns

TABLE A.3 NV⁻ decay rates measured at room temperature. Averages over measured NV⁻ centers are weighted by reported uncertainties. Dashed lines (-) indicate values not reported. Branching ratios can be derived from the given data.

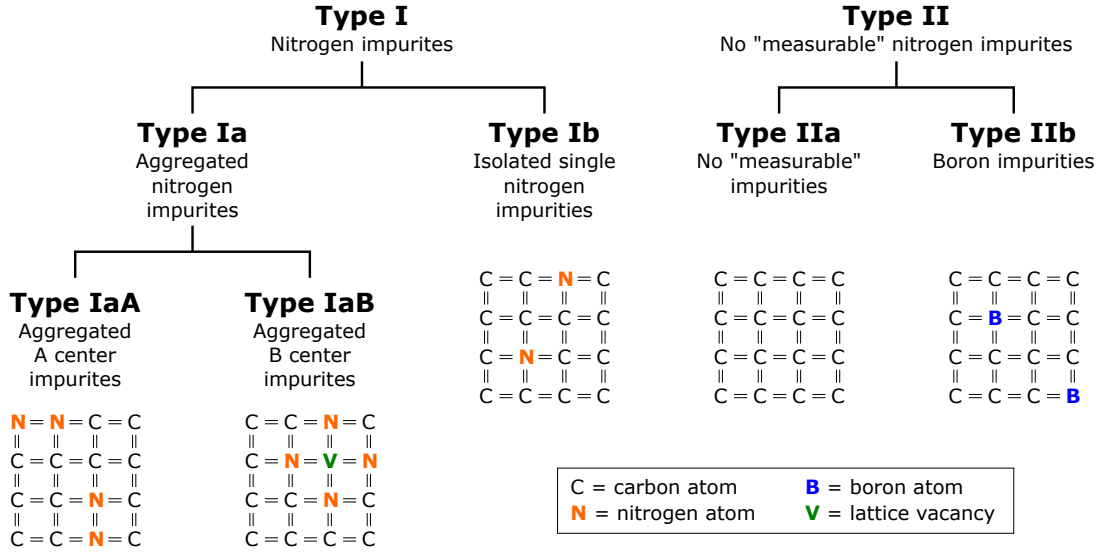


FIG. A.4 The diamond type classification system as described in the main text. Adapted from Ref. (Breeding and Shigley, 2009)

Acronym	Description
CPMG	Carr-Purcell-Meiboom-Gill (pulse sequences)
CW	Continuous wave
CVD	Chemical vapor deposition
DEER	Double electron-electron resonance
EPR	Electron paramagnetic resonance
ESLAC	Excited-state level anti-crossing
ESR	Electron spin resonance
FID	Free induction decay
GSLAC	Ground state level anti-crossing
HPHT	High pressure high temperature
LAC	Level anti-crossing
LPHT	Low pressure high temperature
MW	Microwave
NIR	Near-infrared
NMR	Nuclear magnetic resonance
NQR	Nuclear quadrupole resonance
ODMR	Optically detected magnetic resonance
PDMR	Photoelectrically detected magnetic resonance
PE	Photoelectric (readout)
PL	Photoluminescence
QND	Quantum non-demolition
RF	Radiofrequency
SCC	Spin-to-charge conversion

TABLE A.4 Frequently used acronyms

Quantity	Symbol	Units	Notes
Longitudinal (spin-lattice) relaxation time	T_1	s	
Coherence time (transverse relaxation time)	T_2	s	
Dephasing time (free induction decay time)	T_2^*	s	
Single-NV ⁻ dephasing time	$T_2^{*\{\text{single}\}}$	s	
Magnetic field sensitivity	η	T/ $\sqrt{\text{Hz}}$	
Interrogation time (free-precession time for Ramsey)	τ	s	
Initialization, readout, and overhead time	t_I, t_R, t_O	s	$t_O \equiv t_I + t_R$
Stretched exponential parameter	p	-	
Static (bias) & microwave magnetic field	B_0 & B_1	T	
Electronic spin gyromagnetic ratio	γ_e	s ⁻¹ /T	$\equiv g_e \mu_B / \hbar$
Readout fidelity	\mathcal{F}	-	$\equiv 1/\sigma_R$
Factor above spin projection noise	σ_R	-	$\equiv 1/\mathcal{F}$
Rabi frequency	Ω_R	s ⁻¹	
ODMR center frequency & linewidth	ν & $\Delta\nu$	Hz	
Dephasing or decay rate	Γ	s ⁻¹	
Measurement contrast (fringe visibility)	C	-	
CW-ODMR contrast, pulsed ODMR contrast	$C_{\text{CW}}, C_{\text{pulsed}}$	-	
Number of sensors (NV ⁻ centers in ensemble)	N	-	
Average collected photons per readout per NV ⁻	n_{avg}	-	
Average collected photons per readout from an NV ⁻ ensemble	\mathcal{N}	-	
Concentration of species X	$[X]$	cm ⁻³ or ppm	
Negative, neutral & total NV concentration	$[\text{NV}^-], [\text{NV}^0], [\text{NV}^T]$	cm ⁻³ or ppm	
Total nitrogen concentration in the lattice	$[\text{N}^T]$	cm ⁻³ or ppm	
Neutral, positive, total substitutional nitrogen concentration	$[\text{N}_S^0], [\text{N}_S^+], [\text{N}_S^T]$	cm ⁻³ or ppm	
Contribution to T_2^* from mechanism X	$T_2^{*\{X\}}$	s	
Dipolar interaction strength between N _S ⁰ and NV ⁻	$A_{\text{N}_S^0}$	s ⁻¹ /ppm	
Dipolar interaction strength between ¹³ C and NV ⁻	$A_{13\text{C}}$	s ⁻¹ /ppm	
Dipolar interaction strength between NV ⁻ spins in the same group (same resonance frequency)	$A_{\text{NV}^-_{\parallel}}$	s ⁻¹ /ppm	
Dipolar interaction strength between NV ⁻ spins in different groups (different resonance frequencies)	$A_{\text{NV}^-_{\nparallel}}$	s ⁻¹ /ppm	
Proportionality factor for N _S ⁰ contribution to T_2	$B_{\text{N}_S^0}$	s ⁻¹ /ppm	
Hamiltonian	H	J	
Electronic spin, electronic spin projection	S, m_s	-	
Nuclear spin, nuclear spin projection	I, m_I	-	
NV ⁻ ground state spin eigenstates	$\{ 0\rangle, -1\rangle, +1\rangle\}$	-	
Zero field splitting parameter	D	Hz	≈ 2.87 GHz
Spin-strain coupling parameters	$\mathcal{M}_z, \mathcal{M}_x, \mathcal{M}_y, \mathcal{N}_x, \mathcal{N}_y$	Hz	
Electric field components	E_x, E_y, E_z	V/m	
NV ⁻ transverse, axial (longitudinal) electric dipole moment	d_{\perp}, d_{\parallel}	Hz/(V/m)	
Transverse strain and electric field coupling parameter	ξ_{\perp}	Hz	
Axial magnetic field coupling parameter	β_z	Hz	$\equiv \frac{g\mu_B}{\hbar} B_z$
Total N-to-NV ⁻ conversion efficiency	E_{conv}	-	$\equiv [\text{NV}^-]/[\text{N}^T]$
N-to-NV conversion efficiency	χ	-	$\equiv [\text{NV}^T]/[\text{N}^T]$
NV-to-NV ⁻ charge state efficiency	ζ	-	$\equiv [\text{NV}^-]/[\text{NV}^T]$

TABLE A.5 Frequently used symbols

REFERENCES

- Abe, E., and K. Sasaki (2018), *J. Appl. Phys.* **123** (16), 161101.
- Abe, E., A. M. Tyryshkin, S. Tojo, J. J. L. Morton, W. M. Witzel, A. Fujimoto, J. W. Ager, E. E. Haller, J. Isoya, S. A. Lyon, M. L. W. Thewalt, and K. M. Itoh (2010), *Phys. Rev. B* **82**, 121201.
- Abragam, A. (1983a), *The Principles of Nuclear Magnetism* (Clarendon Press, Oxford) Chap. 4.
- Abragam, A. (1983b), *The Principles of Nuclear Magnetism* (Clarendon Press, Oxford) Chap. 3.
- Abragam, A. (1983c), *The Principles of Nuclear Magnetism* (Clarendon Press, Oxford).
- Achard, J., A. Tallaie, V. Mille, M. Naamoun, O. Brinza, A. Boussadi, L. William, and A. Gicquel (2014), *Phys. Status Solidi A* **211** (10), 2264.
- Acosta, V. M. (May 2011), *Optical Magnetometry with Nitrogen-Vacancy Centers in Diamond*, Ph.D. thesis (University of California Berkeley).
- Acosta, V. M., E. Bauch, A. Jarmola, L. J. Zipp, M. P. Ledbetter, and D. Budker (2010), *Appl. Phys. Lett.* **97** (17), 174104.
- Acosta, V. M., E. Bauch, M. P. Ledbetter, C. Santori, K.-M. C. Fu, P. E. Barclay, R. G. Beausoleil, H. Linget, J. F. Roch, F. Treussart, S. Chemerisov, W. Gawlik, and D. Budker (2009), *Phys. Rev. B* **80**, 115202.
- Acosta, V. M., E. Bauch, M. P. Ledbetter, A. Waxman, L.-S. Bouchard, and D. Budker (2010a), *Phys. Rev. Lett.* **104**, 070801.
- Acosta, V. M., A. Jarmola, E. Bauch, and D. Budker (2010b), *Phys. Rev. B* **82** (20), 201202.
- Ahmadi, S., H. A. R. El-Ella, J. O. B. Hansen, A. Huck, and U. L. Andersen (2017), *Phys. Rev. Applied* **8**, 034001.
- Ahmadi, S., H. A. R. El-Ella, A. M. Wojciechowski, T. Gehring, J. O. B. Hansen, A. Huck, and U. L. Andersen (2018a), in *Conference on Lasers and Electro-Optics* (Optical Society of America) p. JF3B.2.
- Ahmadi, S., H. A. R. El-Ella, A. M. Wojciechowski, T. Gehring, J. O. B. Hansen, A. Huck, and U. L. Andersen (2018b), *Phys. Rev. B* **97**, 024105.
- Aiello, C. D., M. Hirose, and P. Cappellaro (2013), *Nat. Commun.* **4**, 1419.
- Ammerlaan, C. A. J., and E. A. Burgemeister (1981), *Phys. Rev. Lett.* **47** (13), 954.
- Angerer, A., T. Nöbauer, G. Wachter, M. Markham, A. Stacey, J. Majer, J. Schmiedmayer, and M. Trupke (2015), ArXiv e-prints [arXiv:1509.01637](https://arxiv.org/abs/1509.01637) [quant-ph].
- Angus, J. C., H. A. Will, and W. S. Stanko (1968), *J. Appl. Phys.* **39** (6), 2915.
- Arai, K., C. Belthangady, H. Zhang, N. Bar-Gill, S. J. DeVience, P. Cappellaro, and R. L. Walsworth (2015), *Nat. Nanotechnol.* **10** (10), 859.
- Arai, K., J. Lee, C. Belthangady, D. R. Glenn, H. Zhang, and R. L. Walsworth (2018), *Nat. Commun.* **9** (1), 4996.
- Ariyaratne, A., D. Bluvstein, B. A. Myers, and A. C. B. Jayich (2018), *Nat. Commun.* **9** (1), 2406.
- Arroyo-Camejo, S., A. Lazarev, S. W. Hell, and G. Balasubramanian (2014), *Nat. Commun.* **5**, 4870.
- Ashbaugh III, C. E. (1988), *Gems Gemol.* **24** (4).
- Aslam, N., M. Pfender, P. Neumann, R. Reuter, A. Zappe, F. Fávoro de Oliveira, A. Denisenko, H. Sumiya, S. Onoda, J. Isoya, and J. Wrachtrup (2017), *Science* **357** (6346), 67.
- Aslam, N., G. Waldherr, P. Neumann, F. Jelezko, and J. Wrachtrup (2013), *New J. Phys.* **15** (1), 013064.
- Babinec, T. M., H. J. M., M. Khan, Y. Zhang, J. R. Maze, P. R. Hemmer, and M. Loncar (2010), *Nat. Nanotechnol.* **5** (3), 195.
- Backlund, M. P., P. Kehayias, and R. L. Walsworth (2017), *Phys. Rev. Applied* **8**, 054003.
- Baker, J. (2007), *Diam. Relat. Mater.* **16** (2), 216.
- Balasubramanian, G., I. Y. Chan, R. Kolesov, M. Al-Hmoud, J. Tisler, C. Shin, C. Kim, A. Wojcik, P. R. Hemmer, A. Krueger, T. Hanke, A. Leitenstorfer, R. Bratschitsch, F. Jelezko, and J. Wrachtrup (2008), *Nature* **455**, 648.
- Balasubramanian, G., P. Neumann, D. Twitchen, M. Markham, R. Kolesov, N. Mizuochi, J. Isoya, J. Achard, J. Beck, J. Tisler, V. Jacques, P. R. Hemmer, F. Jelezko, and J. Wrachtrup (2009), *Nat. Mater.* **8** (5), 383.
- Balmer, R. S., J. R. Brandon, S. L. Clewes, H. K. Dhillon, J. M. Dodson, I. Friel, P. N. Inglis, T. D. Madgwick, M. L. Markham, T. P. Mollart, N. Perkins, G. A. Scarsbrook, D. J. Twitchen, A. J. Whitehead, J. J. Wilman, and S. M. Woolard (2009), *J. Phys.: Condens. Matter* **21** (36), 364221.
- Bangert, U., R. Barnes, M. H. Gass, A. L. Bleloch, and I. S. Godfrey (2009), *J. Phys.: Condens. Matter* **21** (36), 364208.
- Bar-Gill, N., L. M. Pham, C. Belthangady, D. Le Sage, P. Cappellaro, J. R. Maze, M. D. Lukin, A. Yacoby, and R. Walsworth (2012), *Nat. Commun.* **3**, 858.
- Bar-Gill, N., L. M. Pham, A. Jarmola, D. Budker, and R. L. Walsworth (2013), *Nat. Commun.* **4**, 1743.
- Baranov, P. G., H. J. von Bardeleben, F. Jelezko, and J. Wrachtrup (2017), “Retrospectives: Magnetic resonance studies of intrinsic defects in semiconductors,” in *Magnetic Resonance of Semiconductors and Their Nanostructures: Basic and Advanced Applications* (Springer, Vienna) pp. 179–211.
- Barfuss, A., M. Kasperczyk, J. Kölbl, and P. Maletinsky (2018), ArXiv e-prints [arXiv:1810.07190](https://arxiv.org/abs/1810.07190) [cond-mat.mes-hall].
- Barry, J. F., M. J. Turner, J. M. Schloss, D. R. Glenn, Y. Song, M. D. Lukin, H. Park, and R. L. Walsworth (2016), *Proc. Natl. Acad. Sci.* **113** (49), 14133.
- Barson, M. S. J., P. Peddibhotla, P. Ovarthaiyapong, K. Ganesan, R. L. Taylor, M. Gebert, Z. Mielens, B. Koslowski, D. A. Simpson, L. P. McGuinness, J. McCallum, S. Prawer, S. Onoda, T. Ohshima, A. C. Bleszynski Jayich, F. Jelezko, N. B. Manson, and M. W. Doherty (2017), *Nano Lett.* **17** (3), 1496.
- Bauch, E. (2010), *Nitrogen-Vacancy Defects in Diamond for sub-millimeter Magnetometry*, Master’s thesis (Technische Universität Berlin and University of California Berkeley).
- Bauch, E., C. A. Hart, J. M. Schloss, M. J. Turner, J. F. Barry, P. Kehayias, S. Singh, and R. L. Walsworth (2018), *Phys. Rev. X* **8**, 031025.
- Bauch, E., S. Singh, J. Lee, C. H. Hart, J. M. Schloss, M. J. Turner, J. F. Barry, L. M. Pham, N. Bar-Gill, and R. L. Walsworth (2019), in prep.
- Beha, K., A. Batalov, N. B. Manson, R. Bratschitsch, and A. Leitenstorfer (2012), *Phys. Rev. Lett.* **109**, 097404.
- Belthangady, C., N. Bar-Gill, L. M. Pham, K. Arai, D. Le Sage, P. Cappellaro, and R. L. Walsworth (2013), *Phys. Rev. Lett.* **110**, 157601.
- Bernien, H., B. Hensen, W. Pfaff, G. Koolstra, M. S. Blok, L. Robledo, T. H. Taminiau, M. Markham, D. J. Twitchen, L. Childress, and R. Hanson (2013), *Nature* **497**, 86.
- Berry, M. V. (1984), *Proc. R. Soc. London, Ser. A* **392** (1802), 45.
- Bluvstein, D., Z. Zhang, and A. C. B. Jayich (2019), *Phys. Rev. Lett.* **122**, 076101.
- Boesch, B. P., G. S. Bruce, J. D. Cammerata, D. N. Coar, L. N. Egan, B. N. Fisk, W. Lew, A. Manickam, S. M. Sekelsky, J. B. Stetson, P. G. Kaup, J. L. Miller, J. C. Russo, and E. S. Stockman (2016), “DNV magnetic field detector,” WO Patent 2016/118791 Al.
- Boss, J. M., K. Chang, J. Armijo, K. Cujia, T. Rosskopf, J. R. Maze, and C. L. Degen (2016), *Phys. Rev. Lett.* **116**, 197601.

- Boss, J. M., K. S. Cujia, J. Zopes, and C. L. Degen (2017), *Science* **356** (6340), 837.
- Botsoa, J., T. Sauvage, M.-P. Adam, P. Desgardin, E. Leoni, B. Courtois, F. Treussart, and M.-F. Barthe (2011), *Phys. Rev. B* **84**, 125209.
- Bourgeois, E., A. Jarmola, P. Siyushev, M. Gulka, J. Hruby, F. Jelezko, D. Budker, and M. Nesladek (2015), *Nat. Commun.* **6**, 8577.
- Bourgeois, E., E. Londero, K. Buczak, J. Hruby, M. Gulka, Y. Balasubramaniam, G. Wachter, J. Stursa, K. Dobes, F. Aumayr, M. Trupke, A. Gali, and M. Nesladek (2017), *Phys. Rev. B* **95**, 041402.
- Boyd, S. R., I. Kiflawi, and G. S. Woods (1994), *Philos. Mag. B* **69** (6), 1149.
- Breeding, C. M., and J. E. Shigley (2009), *Gems Gemol.* **45** (2), 96.
- Breeze, J. D., E. Salvadori, J. Sathian, N. M. Alford, and C. W. M. Kay (2018), *Nature* **555**, 493.
- Breuer, S. J., and P. R. Briddon (1995), *Phys. Rev. B* **51**, 6984.
- Bube, R. (1960), *Photoconductivity of solids* (Wiley).
- Buchan, J. T., M. Robinson, H. J. Christie, D. L. Roach, D. K. Ross, and N. A. Marks (2015), *J. Appl. Phys.* **117** (24), 245901.
- Bucher, D. B., D. R. Glenn, H. Park, M. D. Lukin, and R. L. Walsworth (2018), ArXiv e-prints [arXiv:1810.02408](https://arxiv.org/abs/1810.02408) [physics.app-ph].
- Budker, D., and M. Romalis (2007), *Nat. Phys.* **3** (4), 227.
- Bursill, L. A., and R. W. Glaisher (1985), *Am. Mineral.* **70**, 608.
- Cai, J., F. Jelezko, M. B. Plenio, and A. Retzker (2013), *New J. Phys.* **15** (1), 013020.
- Campbell, B., W. Choudhury, A. Mainwood, M. Newton, and G. Davies (2002), *Nucl. Instrum. Methods Phys. Res., Sect. A* **476** (3), 680.
- Campbell, B., and A. Mainwood (2000), *Phys. Status Solidi A* **181** (1), 99.
- Cann, B. L. (2009), *Magnetic resonance studies of point defects in diamond*, Ph.D. thesis (University of Warwick).
- Cao, G. Z., F. A. J. M. Driessen, G. J. Bauhuis, L. J. Giling, and P. F. A. Alkemade (1995), *J. Appl. Phys.* **78** (5), 3125.
- Cao, J. (1994), *J. Magn. Reson., Ser B* **103** (3), 296.
- Casola, F., T. van der Sar, and A. Yacoby (2018), *Nat. Rev. Mater.* **3**, 17088.
- Charles, S. J., J. E. Butler, B. N. Feygelson, M. E. Newton, D. L. Carroll, J. W. Steeds, H. Darwish, C.-S. Yan, H. K. Mao, and R. J. Hemley (2004), *Phys. Status Solidi A* **201** (11), 2473.
- Chatzidrosos, G., A. Wickenbrock, L. Bougas, N. Leefer, T. Wu, K. Jensen, Y. Dumeige, and D. Budker (2017), *Phys. Rev. Applied* **8**, 044019.
- Chen, X.-D., S. Li, A. Shen, Y. Dong, C.-H. Dong, G.-C. Guo, and F.-W. Sun (2017), *Phys. Rev. Applied* **7**, 014008.
- Childress, L., M. V. Gurudev Dutt, J. M. Taylor, A. S. Zibrov, F. Jelezko, J. Wrachtrup, P. R. Hemmer, and M. D. Lukin (2006), *Science* **314** (5797), 281.
- Choi, J., S. Choi, G. Kucsko, P. C. Maurer, B. J. Shields, H. Sumiya, S. Onoda, J. Isoya, E. Demler, F. Jelezko, N. Y. Yao, and M. D. Lukin (2017a), *Phys. Rev. Lett.* **118**, 093601.
- Choi, S., N. Y. Yao, and M. D. Lukin (2017b), *Phys. Rev. Lett.* **119**, 183603.
- Choi, S., N. Y. Yao, and M. D. Lukin (2017), ArXiv e-prints [arXiv:1801.00042](https://arxiv.org/abs/1801.00042) [quant-ph].
- Choy, J. T., I. Bulu, B. J. M. Hausmann, E. Janitz, I.-C. Huang, and M. Loncar (2013), *Appl. Phys. Lett.* **103** (16), 161101.
- Choy, J. T., B. J. M. Hausmann, T. M. Babinec, I. Bulu, M. Khan, P. Maletinsky, A. Yacoby, and M. Loncar (2011), *Nat. Photonics* **5** (12), 738.
- Chu, Y., N. de Leon, B. Shields, B. Hausmann, R. Evans, E. Togan, M. J. Burek, M. Markham, A. Stacey, A. Zibrov, A. Yacoby, D. Twitchen, M. Loncar, H. Park, P. Maletinsky, and M. Lukin (2014), *Nano Lett.* **14** (4), 1982.
- Clevenson, H., M. E. Trusheim, C. Teale, T. Schroder, D. Braje, and D. Englund (2015), *Nat. Phys.* **11** (5), 393.
- Collins, A. T. (2002), *J. Phys.: Condens. Matter* **14** (14), 3743.
- Collins, A. T. (2007), *New Diamond and Frontier Carbon Technology* **17**.
- Collins, A. T., H. Kanda, and H. Kitawaki (2000), *Diam. Relat. Mater.* **9** (2), 113.
- Cook, R. J., and D. H. Whiffen (1966), *Proc. R. Soc. London, Ser. A* **295** (1441), 99.
- Cruddace, R. (2007), *Magnetic resonance and optical studies of point defects in single crystal CVD diamond*, Ph.D. thesis (University of Warwick).
- Cui, S., and E. L. Hu (2013), *Appl. Phys. Lett.* **103** (5), 051603.
- Cywiński, L., R. M. Lutchyn, C. P. Nave, and S. Das Sarma (2008), *Phys. Rev. B* **77**, 174509.
- Dale, M. W. (2015), *Colour Centres on Demand in Diamond*, Ph.D. thesis (University of Warwick).
- Dannefaer, S., T. Bretagnon, and D. Kerr (1993), *Diam. Relat. Mater.* **2** (12), 1479.
- Dannefaer, S., P. Mascher, and D. Kerr (1992), *Diam. Relat. Mater.* **1** (5), 407.
- Davies, G. (1976), *J. Phys. C: Solid State Phys.* **9** (19), L537.
- Davies, G. (1979), *J. Phys. C: Solid State Phys.* **12** (13), 2551.
- Davies, G. (1981), *Rep. Prog. Phys.* **44** (7), 787.
- Davies, G., B. Campbell, A. Mainwood, M. Newton, M. Watkins, H. Kanda, and T. Anthony (2001), *Phys. Status Solidi A* **186** (2), 187.
- Davies, G., and T. Evans (1972), *Proc. R. Soc. London, Ser. A* **328** (1574), 413.
- Davies, G., and M. F. Hamer (1976), *Proc. R. Soc. London, Ser. A* **348** (1653), 285.
- Davies, G., S. C. Lawson, A. T. Collins, A. Mainwood, and S. J. Sharp (1992), *Phys. Rev. B* **46**, 13157.
- Davis, H. C., P. Ramesh, A. Bhatnagar, A. Lee-Gosselin, J. F. Barry, D. R. Glenn, R. L. Walsworth, and M. G. Shapiro (2018), *Nat. Commun.* **9** (1), 131.
- Deák, P., B. Aradi, M. Kaviani, T. Frauenheim, and A. Gali (2014), *Phys. Rev. B* **89**, 075203.
- Degen, C. L. (2008), *Appl. Phys. Lett.* **92** (24), 243111.
- Degen, C. L., F. Reinhard, and P. Cappellaro (2017), *Rev. Mod. Phys.* **89**, 035002.
- DeGiorgio, V., and M. O. Scully (1970), *Phys. Rev. A* **2**, 1170.
- DeVience, S. J., L. M. Pham, I. Lovchinsky, A. O. Sushkov, N. Bar-Gill, C. Belthangady, F. Casola, M. Corbett, H. Zhang, M. Lukin, H. Park, A. Yacoby, and R. L. Walsworth (2015), *Nat. Nanotechnol.* **10**, 129.
- D'Haenens-Johansson, U. F., A. Katrusha, P. Johnson, W. Wang, *et al.* (2015), *Gems Gemol.* **51** (3).
- D'Haenens-Johansson, U. F., K. S. Moe, P. Johnson, S. Y. Wong, R. Lu, and W. Wang (2014), *Gems Gemol.* **50** (1).
- Dischler, B. (2012), *Handbook of Spectral Lines in Diamond: Volume 1: Tables and Interpretations*, Vol. 1 (Springer).
- Dobrinets, I. A., V. G. Vins, and A. M. Zaitsev (2013), *HPHT-Treated Diamonds: Diamonds Forever* (Springer).
- Dobrovitski, V. V., A. E. Feiguin, D. D. Awschalom, and R. Hanson (2008), *Phys. Rev. B* **77** (24), 245212.
- Dodson, J., J. R. Brandon, H. Dhillon, I. Friel, S. L. Geoghegan, T. Mollart, P. Santini, G. Scarsbrook, D. Twitchen, A. J. Whitehead, J. J. Wilman, and H. de Wit (2011), *Proc. of SPIE* **8016**, 80160L.
- Doherty, M. W., F. Dolde, H. Fedder, F. Jelezko, J. Wrachtrup, N. B. Manson, and L. C. L. Hollenberg (2012), *Phys. Rev. B* **85**, 205203.
- Doherty, M. W., N. B. Manson, P. Delaney, F. Jelezko,

- J. Wrachtrup, and L. C. Hollenberg (2013), *Phys. Rep.* **528** (1), 1.
- Doherty, M. W., V. V. Struzhkin, D. A. Simpson, L. P. McGuinness, Y. Meng, A. Stacey, T. J. Karle, R. J. Hemley, N. B. Manson, L. C. L. Hollenberg, and S. Prawer (2014), *Phys. Rev. Lett.* **112**, 047601.
- Doi, Y., T. Fukui, H. Kato, T. Makino, S. Yamasaki, T. Tashima, H. Morishita, S. Miwa, F. Jelezko, Y. Suzuki, and N. Mizuochi (2016), *Phys. Rev. B* **93**, 081203.
- Doi, Y., T. Makino, H. Kato, D. Takeuchi, M. Ogura, H. Okushi, H. Morishita, T. Tashima, S. Miwa, S. Yamasaki, P. Neumann, J. Wrachtrup, Y. Suzuki, and N. Mizuochi (2014), *Phys. Rev. X* **4**, 011057.
- Dolde, F., H. Fedder, M. W. Doherty, T. Nobauer, F. Rempp, G. Balasubramanian, T. Wolf, F. Reinhard, L. C. L. Hollenberg, F. Jelezko, and J. Wrachtrup (2011), *Nat. Phys.* **7** (6), 459.
- Dolde, F., I. Jakobi, B. Naydenov, N. Zhao, S. Pezzagna, C. Trautmann, J. Meijer, P. Neumann, F. Jelezko, and J. Wrachtrup (2013), *Nat. Phys.* **9** (3), 139.
- Drake, M., E. Scott, and J. A. Reimer (2016), *New J. Phys.* **18** (1), 13011.
- Dréau, A., M. Lesik, L. Rondin, P. Spinicelli, O. Arcizet, J.-F. Roch, and V. Jacques (2011), *Phys. Rev. B* **84** (19), 195.
- Dréau, A., J.-R. Maze, M. Lesik, J.-F. Roch, and V. Jacques (2012), *Phys. Rev. B* **85**, 134107.
- Dumeige, Y., M. Chipaux, V. Jacques, F. Treussart, J.-F. Roch, T. Debuisschert, V. M. Acosta, A. Jarmola, K. Jensen, P. Kehayias, and D. Budker (2013), *Phys. Rev. B* **87**, 155202.
- Dwyer, K. J., J. M. Pomeroy, and D. S. Simons (2013), *Appl. Phys. Lett.* **102** (25), 254104.
- Edmonds, A. M. (2008), *Magnetic resonance studies of point defects in single crystal diamond*, *Ph.D. thesis* (University of Warwick).
- Edmonds, A. M., U. F. S. D’Haenens-Johansson, R. J. Crundace, M. E. Newton, K.-M. C. Fu, C. Santori, R. G. Beausoleil, D. J. Twitchen, and M. L. Markham (2012), *Phys. Rev. B* **86**, 035201.
- Eisenach, E. R., J. F. Barry, L. M. Pham, R. G. Rojas, D. R. Englund, and D. A. Braje (2018), *Rev. Sci. Instrum.* **89** (9), 094705.
- El-Ella, H. A. R., S. Ahmadi, A. M. Wojciechowski, A. Huck, and U. L. Andersen (2017), *Opt. Express* **25** (13), 14809.
- Epstein, R. J., F. M. Mendoza, Y. K. Kato, and D. D. Awschalom (2005), *Nat. Phys.* **1**, 94.
- Fang, K., V. M. Acosta, C. Santori, Z. Huang, K. M. Itoh, H. Watanabe, S. Shikata, and R. G. Beausoleil (2013), *Phys. Rev. Lett.* **110**, 130802.
- Farchi, E., Y. Ebert, D. Farfurnik, G. Haim, R. Shaar, and N. Bar-Gill (2017), *Spin* **07** (03), 1740015.
- Farfurnik, D., N. Alfasi, S. Masis, Y. Kauffmann, E. Farchi, Y. Romach, Y. Hovav, E. Buks, and N. Bar-Gill (2017), *Appl. Phys. Lett.* **111** (12), 123101.
- Farfurnik, D., A. Jarmola, L. M. Pham, Z. H. Wang, V. V. Dobrovitski, R. L. Walsworth, D. Budker, and N. Bar-Gill (2015), *Phys. Rev. B* **92**, 060301.
- Farrer, R. (1969), *Solid State Commun.* **7** (9), 685.
- Fastenau, R. (Jun 1982), *Diffusion limited reactions in crystalline solids*, *Ph.D. thesis* (Technische Hogeschool Delft).
- Fávaro de Oliveira, F., D. Antonov, Y. Wang, P. Neumann, S. A. Momenzadeh, T. Häußermann, A. Pasquarelli, A. Denisenko, and J. Wrachtrup (2017), *Nat. Commun.* **8**, 15409.
- Fávaro de Oliveira, F., S. A. Momenzadeh, D. Antonov, J. Scharpf, C. Osterkamp, B. Naydenov, F. Jelezko, A. Denisenko, and J. Wrachtrup (2016), *Nano Lett.* **16** (4), 2228.
- Fedder, H., F. Dolde, F. Rempp, T. Wolf, P. Hemmer, F. Jelezko, and J. Wrachtrup (2011), *Appl. Phys. B* **102** (3), 497.
- Felton, S., B. L. Cann, A. M. Edmonds, S. Liggins, R. J. Crundace, M. E. Newton, D. Fisher, and J. M. Baker (2009), *J. Phys.: Condens. Matter* **21**, 364212.
- Felton, S., A. M. Edmonds, M. E. Newton, P. M. Martineau, D. Fisher, and D. J. Twitchen (2008), *Phys. Rev. B* **77**, 081201.
- Fescenko, I., A. Laraoui, J. Smits, N. Mosavian, P. Kehayias, J. Seto, L. Bougas, A. Jarmola, and V. M. Acosta (2018), ArXiv e-prints [arXiv:1808.03636](https://arxiv.org/abs/1808.03636) [cond-mat.mes-hall].
- Fisher, D., D. J. F. Evans, C. Glover, C. J. Kelly, M. J. Sheehy, and G. C. Summerton (2006), *Diam. Relat. Mater.* **15**, 1636.
- Fletcher, R. C., and W. L. Brown (1953), *Phys. Rev.* **92**, 585.
- Forneris, J., S. Ditalia Tchernij, A. Tengattini, E. Enrico, V. Grilj, N. Skukan, G. Amato, L. Boarino, M. Jakšić, and P. Olivero (2017), *Carbon* **113**, 76.
- Fraczek, E., V. G. Savitski, M. Dale, B. G. Breeze, P. Diggle, M. Markham, A. Bennett, H. Dhillon, M. E. Newton, and A. J. Kemp (2017), *Opt. Mater. Express* **7** (7), 2571.
- Fu, K.-M. C., C. Santori, P. E. Barclay, and R. G. Beausoleil (2010), *Appl. Phys. Lett.* **96** (12), 121907.
- Fu, R. R., B. P. Weiss, E. A. Lima, R. J. Harrison, X.-N. Bai, S. J. Desch, D. S. Ebel, C. Suavet, H. Wang, D. Glenn, D. Le Sage, T. Kasama, R. L. Walsworth, and A. T. Kuan (2014), *Science* **346** (6213), 1089.
- Fuchs, G. D., V. V. Dobrovitski, R. Hanson, A. Batra, C. D. Weis, T. Schenkel, and D. D. Awschalom (2008), *Phys. Rev. Lett.* **101**, 117601.
- Fujita, N., R. Jones, S. Öberg, and P. Briddon (2009), *Diam. Relat. Mater.* **18** (5–8), 843.
- Fukui, T., Y. Doi, T. Miyazaki, Y. Miyamoto, H. Kato, T. Matsumoto, T. Makino, S. Yamasaki, R. Morimoto, N. Tokuda, M. Hatano, Y. Sakagawa, H. Morishita, T. Tashima, S. Miwa, Y. Suzuki, and N. Mizuochi (2014), *Appl. Phys. Express* **7** (5), 055201.
- Gaillou, E., J. E. Post, D. Rost, and J. E. Butler (2012), *Am. Mineral.* **97** (1), 1.
- Gaukroger, M., P. Martineau, M. Crowder, I. Friel, S. Williams, and D. Twitchen (2008), *Diam. Relat. Mater.* **17** (3), 262.
- Glenn, D. R., D. B. Bucher, J. Lee, M. D. Lukin, H. Park, and R. L. Walsworth (2018), *Nature* **555** (7696), 351.
- Glenn, D. R., R. R. Fu, P. Kehayias, D. Le Sage, E. A. Lima, B. P. Weiss, and R. L. Walsworth (2017), *Geochim. Geophys. Geosyst.* **18** (8), 3254.
- Glenn, D. R., K. Lee, H. Park, R. Weissleder, A. Yacoby, M. D. Lukin, H. Lee, R. L. Walsworth, and C. B. Connolly (2015), *Nat. Methods* **12** (8), 736.
- Glover, C. (2003), *A Study of Defects in Single Crystal CVD Diamond*, *Ph.D. thesis* (University of Warwick).
- Glover, C., M. E. Newton, P. Martineau, D. J. Twitchen, and J. M. Baker (2003), *Phys. Rev. Lett.* **90**, 185507.
- Glover, C., M. E. Newton, P. M. Martineau, S. Quinn, and D. J. Twitchen (2004), *Phys. Rev. Lett.* **92**, 135502.
- Goldman, M. L., M. W. Doherty, A. Sipahigil, N. Y. Yao, S. D. Bennett, N. B. Manson, A. Kubanek, and M. D. Lukin (2015a), *Phys. Rev. B* **91**, 165201.
- Goldman, M. L., A. Sipahigil, M. W. Doherty, N. Y. Yao, S. D. Bennett, M. Markham, D. J. Twitchen, N. B. Manson, A. Kubanek, and M. D. Lukin (2015b), *Phys. Rev. Lett.* **114**, 145502.
- Goss, J. P., P. R. Briddon, V. Hill, R. Jones, and M. J. Rayson (2014), *J. Phys.: Condens. Matter* **26** (14), 145801.
- Goss, J. P., P. R. Briddon, S. Papagiannidis, and R. Jones (2004), *Phys. Rev. B* **70**, 235208.
- Goss, J. P., P. R. Briddon, M. J. Rayson, S. J. Sque, and R. Jones (2005), *Phys. Rev. B* **72**, 035214.
- Green, B. L., B. G. Breeze, and M. E. Newton (2017), *J. Phys.:*

- Condens. Matter* **29** (22), 225701.
- Green, B. L., M. W. Dale, M. E. Newton, and D. Fisher (2015), *Phys. Rev. B* **92**, 165204.
- Grezes, C., B. Julsgaard, Y. Kubo, W. L. Ma, M. Stern, A. Bienfait, K. Nakamura, J. Isoya, S. Onoda, T. Ohshima, V. Jacques, D. Vion, D. Esteve, R. B. Liu, K. Mølmer, and P. Bertet (2015), *Phys. Rev. A* **92**, 020301.
- Grinolds, M. S., M. Warner, K. De Greve, Y. Dovzhenko, L. Thiel, R. L. Walsworth, S. Hong, P. Maletinsky, and A. Yacoby (2014), *Nat. Nanotechnol.* **9**, 279.
- Groot-Berning, K., N. Raatz, I. Dobrinets, M. Lesik, P. Spinicelli, A. Tallaie, J. Achard, V. Jacques, J.-F. Roch, A. M. Zaitsev, J. Meijer, and S. Pezzagna (2014), *Phys. Status Solidi A* **211** (10), 2268.
- Grosz, A., M. J. Haji-Sheikh, and S. C. Mukhopadhyay (2017), *High Sensitivity Magnetometers* (Springer).
- Grotz, B., M. V. Hauf, M. Dankerl, B. Naydenov, S. Pezzagna, J. Meijer, F. Jelezko, J. Wrachtrup, M. Stutzmann, F. Reinhard, and J. A. Garrido (2012), *Nat. Commun.* **3**, 729.
- Gulka, M., E. Bourgeois, J. Hruby, P. Siyushev, G. Wachter, F. Aumayr, P. R. Hemmer, A. Gali, F. Jelezko, M. Trupke, and M. Nesladek (2017), *Phys. Rev. Applied* **7**, 044032.
- Gullion, T., D. B. Baker, and M. S. Conradi (1990), *J. Magn. Reson.* **89** (3), 479.
- Gupta, A., L. Hacquebard, and L. Childress (2016), *J. Opt. Soc. Am. B* **33** (3), B28.
- Häberle, T., T. Oeckinghaus, D. Schmid-Lorch, M. Pfender, F. F. de Oliveira, S. A. Momenzadeh, A. Finkler, and J. Wrachtrup (2017), *Rev. Sci. Instrum.* **88** (1), 013702.
- Hacquebard, L., and L. Childress (2018), *Phys. Rev. A* **97**, 063408.
- Hadden, J. P., J. P. Harrison, A. C. Stanley-Clarke, L. Marseglia, Y. L. D. Ho, B. R. Patton, J. L. O'Brien, and J. G. Rarity (2010), *Appl. Phys. Lett.* **97** (24), 241901.
- Hahn, E. L. (1950), *Phys. Rev.* **80**, 580.
- Hall, L. T., J. H. Cole, and L. C. L. Hollenberg (2014), *Phys. Rev. B* **90**, 075201.
- Hall, L. T., P. Kehayias, D. A. Simpson, A. Jarmola, A. Stacey, D. Budker, and L. C. L. Hollenberg (2016), *Nat. Commun.* **7**, 10211.
- Hämäläinen, M., R. Hari, R. J. Ilmoniemä, J. Knuutila, and O. V. Lounasmaa (1993), *Rev. Mod. Phys.* **65** (2), 413.
- Hanson, R., V. V. Dobrovitski, A. E. Feiguin, O. Gywat, and D. D. Awschalom (2008), *Science* **320** (5874), 352.
- Hanson, R., F. M. Mendoza, R. J. Epstein, and D. D. Awschalom (2006), *Phys. Rev. Lett.* **97**, 087601.
- Hartland, C. B. (2014), *A Study of Point Defects in CVD Diamond Using Electron Paramagnetic Resonance and Optical Spectroscopy*, Ph.D. thesis (University of Warwick).
- Hauf, M. V., B. Grotz, B. Naydenov, M. Dankerl, S. Pezzagna, J. Meijer, F. Jelezko, J. Wrachtrup, M. Stutzmann, F. Reinhard, and J. A. Garrido (2011), *Phys. Rev. B* **83**, 081304.
- Hauf, M. V., P. Simon, N. Aslam, M. Pfender, P. Neumann, S. Pezzagna, J. Meijer, J. Wrachtrup, M. Stutzmann, F. Reinhard, and J. Garrido (2014), *Nano Lett.* **14** (5), 2359.
- Hensen, B., H. Bernien, A. E. Dréau, A. Reiserer, N. Kalb, M. S. Blok, J. Ruitenbergh, R. F. L. Vermeulen, R. N. Schouten, C. Abellán, W. Amaya, V. Pruneri, M. W. Mitchell, M. Markham, D. J. Twitchen, D. Elkouss, S. Wehner, T. H. Taminiau, and R. Hanson (2015), *Nature* **526**, 682.
- Heremans, F. J., G. D. Fuchs, C. F. Wang, R. Hanson, and D. D. Awschalom (2009), *Appl. Phys. Lett.* **94** (15), 152102.
- Himics, L., S. Tóth, M. Veres, Z. Balogh, and M. Koós (2014), *Appl. Phys. Lett.* **104** (9), 093101.
- Hoa, L. T. M., T. Ouisse, D. Chaussende, M. Naamoun, A. Tallaie, and J. Achard (2014), *Cryst. Growth Des.* **14** (11), 5761.
- Hobbs, P. C. (2011), *Building electro-optical systems: making it all work* (Wiley).
- Hopper, D. A., R. R. Grote, A. L. Exarhos, and L. C. Bassett (2016), *Phys. Rev. B* **94**, 241201.
- Hopper, D. A., R. R. Grote, S. M. Parks, and L. C. Bassett (2018a), *ACS Nano* **12** (5), 4678.
- Hopper, D. A., H. J. Shulevitz, and L. C. Bassett (2018b), *Micromachines* **9** (9).
- Hounscome, L. S., R. Jones, P. M. Martineau, D. Fisher, M. J. Shaw, P. R. Briddon, and S. Öberg (2006), *Phys. Rev. B* **73**, 125203.
- Hrubesch, F. M., G. Braunbeck, M. Stutzmann, F. Reinhard, and M. S. Brandt (2017), *Phys. Rev. Lett.* **118**, 037601.
- Hsieh, S., P. Bhattacharyya, C. Zu, T. Mittiga, T. J. Smart, F. Machado, B. Kobrin, T. O. Höhn, N. Z. Rui, M. Kamrani, S. Chatterjee, S. Choi, M. Zaletel, V. V. Struzhkin, J. E. Moore, V. I. Levitas, R. Jeanloz, and N. Y. Yao (2018), ArXiv e-prints [arXiv:1812.08796](https://arxiv.org/abs/1812.08796) [cond-mat.mes-hall].
- Hu, X., Y. Dai, R. Li, H. Shen, and X. He (2002), *Solid State Commun.* **122** (1), 45.
- Iakubovskii, K., G. J. Adriaenssens, and M. Nesladek (2000), *J. Phys.: Condens. Matter* **12** (2), 189.
- Iakubovskii, K., and A. Stesmans (2002), *Phys. Rev. B* **66** (4), 045406.
- Ishikawa, T., K.-M. C. Fu, C. Santori, V. M. Acosta, R. G. Beausoleil, H. Watanabe, S. Shikata, and K. M. Itoh (2012), *Nano Lett.* **12** (4), 2083.
- Itano, W. M., J. C. Bergquist, J. J. Bollinger, J. M. Gilligan, D. J. Heinzen, F. L. Moore, M. G. Raizen, and D. J. Wineland (1993), *Phys. Rev. A* **47**, 3554.
- Itoh, K. M., and H. Watanabe (2014), *MRS Commun.* **4** (4), 143.
- Ivány, V., T. Simon, J. R. Maze, I. A. Abrikosov, and A. Gali (2014), *Phys. Rev. B* **90**, 235205.
- Jacques, V., P. Neumann, J. Beck, M. Markham, D. Twitchen, J. Meijer, F. Kaiser, G. Balasubramanian, F. Jelezko, and J. Wrachtrup (2009), *Phys. Rev. Lett.* **102**, 057403.
- Jakobi, I., S. A. Momenzadeh, F. F. de Oliveira, J. Michl, F. Ziem, M. Schreck, P. Neumann, A. Denisenko, and J. Wrachtrup (2016), *J. Phys.: Conf. Ser.* **752** (1), 012001.
- Jamonneau, P., M. Lesik, J. P. Tetienne, I. Alvizu, L. Mayer, A. Dréau, S. Kosen, J.-F. Roch, S. Pezzagna, J. Meijer, T. Teraji, Y. Kubo, P. Bertet, J. R. Maze, and V. Jacques (2016), *Phys. Rev. B* **93**, 024305.
- Jarmola, A., V. M. Acosta, K. Jensen, S. Chemerisov, and D. Budker (2012), *Phys. Rev. Lett.* **108**, 197601.
- Jaskula, J.-C., E. Bauch, S. Arroyo-Camejo, M. D. Lukin, S. W. Hell, A. S. Trifonov, and R. L. Walsworth (2017), *Optics Express* **25** (10), 11048.
- Jaskula, J.-C., B. J. Shields, E. Bauch, M. D. Lukin, A. S. Trifonov, and R. L. Walsworth (2017), ArXiv e-prints [arXiv:1711.02023](https://arxiv.org/abs/1711.02023) [quant-ph].
- Jayakumar, H., S. Dhomkar, J. Henshaw, and C. A. Meriles (2018), *Appl. Phys. Lett.* **113** (12), 122404.
- Jelezko, F., and J. Wrachtrup (2008), "Single defect centers in diamond," in *Physics and Applications of CVD Diamond* (Wiley) pp. 257–281.
- Jensen, K., P. Kehayias, and D. Budker (2017), in *Smart Sensors, Measurement and Instrumentation: High Sensitivity Magnetometers*, Vol. 19, pp. 553–576.
- Jensen, K., N. Leefer, A. Jarmola, Y. Dumeige, V. M. Acosta, P. Kehayias, B. Patton, and D. Budker (2014), *Phys. Rev. Lett.* **112** (16), 160802.
- Jeske, J., J. H. Cole, and A. D. Greentree (2016), *New J. Phys.* **18** (1), 013015.
- Jeske, J., D. W. M. Lau, X. Vidal, L. P. McGuinness, P. Reineck, B. C. Johnson, M. W. Doherty, J. C. McCallum, S. Onoda,

- F. Jelezko, T. Ohshima, T. Volz, J. H. Cole, B. C. Gibson, and A. D. Greentree (2017), *Nat. Commun.* **8**, 14000.
- Ji, P., and M. V. G. Dutt (2016), *Phys. Rev. B* **94**, 024101.
- Jiang, L., J. S. Hodges, J. R. Maze, P. Maurer, J. M. Taylor, D. G. Cory, P. R. Hemmer, R. L. Walsworth, A. Yacoby, A. S. Zibrov, and M. D. Lukin (2009), *Science* **326** (5950), 267.
- Jones, R., J. Goss, H. Pinto, and D. Palmer (2015), *Diam. Relat. Mater.* **53**, 35.
- Jones, R., L. S. Hounscome, N. Fujita, S. Öberg, and P. R. Briddon (2007), *Phys. Status Solidi A* **204** (9), 3059.
- Jones, R., J. E. Lowther, and J. Goss (1996), *Appl. Phys. Lett.* **69**, 2489.
- Kageura, T., K. Kato, H. Yamano, E. Suaebah, M. Kajiji, S. Kawai, M. Inaba, T. Tanii, M. Haruyama, K. Yamada, S. Onoda, W. Kada, O. Hanaizumi, T. Teraji, J. Isoya, S. Kono, and H. Kawarada (2017), *Appl. Phys. Express* **10** (5), 055503.
- Kaiser, W., and W. Bond (1959), *Phys. Rev.* **115** (4), 857.
- Kalish, R. (1999), *Carbon* **37** (5), 781.
- Kanda, H. (2000), *Braz. J. Phys.* **30**, 482.
- Karaveli, S., O. Gaathon, A. Wolcott, R. Sakakibara, O. A. Shemesh, D. S. Peterka, E. S. Boyden, J. S. Owen, R. Yuste, and D. Englund (2016), *Proc. Natl. Acad. Sci.* **113** (15), 3938.
- Katagiri, M., J. Isoya, S. Koizumi, and H. Kanda (2004), *Appl. Phys. Lett.* **85** (26), 6365.
- Kato, H., M. Wolfer, C. Schreyvogel, M. Kunzer, W. Müller-Sebert, H. Obloh, S. Yamasaki, and C. Nebel (2013), *Appl. Phys. Lett.* **102** (15), 151101.
- Kehayias, P., M. W. Doherty, D. English, R. Fischer, A. Jarmola, K. Jensen, N. Leefer, P. Hemmer, N. B. Manson, and D. Budker (2013), *Phys. Rev. B* **88**, 165202.
- Kehayias, P., A. Jarmola, N. Mosavian, I. Fescenko, F. M. Benito, A. Laraoui, J. Smits, L. Bougas, D. Budker, A. Neumann, S. R. J. Brueck, and V. M. Acosta (2017), *Nat. Commun.* **8** (1), 188.
- Kehayias, P. K., M. J. Turner, R. Trubko, J. M. Schloss, C. A. Hart, D. Glenn, M. Wesson, and R. L. R. Walsworth (2019), in prep.
- Khan, R. U. A., B. L. Cann, P. M. Martineau, J. Samartseva, J. J. P. Freeth, S. J. Sibley, C. B. Hartland, M. E. Newton, H. K. Dhillon, and D. J. Twitchen (2013), *J. Phys.: Condens. Matter* **25** (27), 275801.
- Khan, R. U. A., P. M. Martineau, B. L. Cann, M. E. Newton, and D. J. Twitchen (2009), *J. Phys.: Condens. Matter* **21** (36), 364214.
- Kiflawi, I., A. T. Collins, K. Iakoubovskii, and D. Fisher (2007), *J. Phys.: Condens. Matter* **19** (4), 046216.
- Kim, E., V. M. Acosta, E. Bauch, D. Budker, and P. R. Hemmer (2012), *Appl. Phys. Lett.* **101** (8), 082410.
- Kim, M., H. J. Mamin, M. H. Sherwood, K. Ohno, D. D. Awschalom, and D. Rugar (2015), *Phys. Rev. Lett.* **115**, 087602.
- Kirschner, F. K. K., F. Flicker, A. Yacoby, N. Y. Yao, and S. J. Blundell (2018), *Phys. Rev. B* **97**, 140402.
- Kirui, J., J. van Wyk, and M. Hoch (2013), *Diam. Relat. Mater.* **39**, 78.
- Kitching, J. (2018), *Appl. Phys. Rev.* **5** (3), 031302.
- Kittel, C., and E. Abrahams (1953), *Phys. Rev.* **90**, 238.
- Kleinsasser, E. E., M. M. Stanfield, J. K. Q. Banks, Z. Zhu, W.-D. Li, V. M. Acosta, H. Watanabe, K. M. Itoh, and K.-M. C. Fu (2016), *Appl. Phys. Lett.* **108** (20), 202401.
- Knowles, H. S., D. M. Kara, and M. Atatüre (2013), *Nat. Mater.* **13**, 21.
- Koike, J., D. M. Parkin, and T. E. Mitchell (1992), *Appl. Phys. Lett.* **60** (12), 1450.
- Kolkowitz, S., A. Safira, A. A. High, R. C. Devlin, S. Choi, Q. P. Unterreithmeier, D. Patterson, A. S. Zibrov, V. E. Manucharyan, H. Park, and M. D. Lukin (2015), *Science* **347** (6226), 1129.
- Kucsko, G., S. Choi, J. Choi, P. C. Maurer, H. Zhou, R. Landig, H. Sumiya, S. Onoda, J. Isoya, F. Jelezko, E. Demler, N. Y. Yao, and M. D. Lukin (2018), *Phys. Rev. Lett.* **121**, 023601.
- Kucsko, G., P. C. Maurer, N. Y. Yao, M. Kubo, H. J. Noh, P. K. Lo, H. Park, and M. D. Lukin (2013), *Nature* **500** (7460), 54.
- Kwan, C. L., and T. F. Yen (1979), *Anal. Chem.* **51** (8), 1225.
- de Lange, G., T. van der Sar, M. Blok, Z.-H. Wang, V. Dobrovitski, and R. Hanson (2012), *Sci. Rep.* **2**, 382.
- de Lange, G., Z. H. Wang, D. Ristè, V. V. Dobrovitski, and R. Hanson (2010), *Science* **330** (6000), 60.
- Lawson, S. C., D. Fisher, D. C. Hunt, and M. E. Newton (1998), *J. Phys.: Condens. Matter* **10** (27), 6171.
- Le Sage, D., and K. Arai (2011), personal communication.
- Le Sage, D., K. Arai, D. R. Glenn, S. J. DeVience, L. M. Pham, L. Rahn-Lee, M. D. Lukin, A. Yacoby, A. Komeili, and R. L. Walsworth (2013), *Nature* **496** (7446), 486.
- Le Sage, D., L. M. Pham, N. Bar-Gill, C. Belthangady, M. D. Lukin, A. Yacoby, and R. L. Walsworth (2012), *Phys. Rev. B* **85**, 121202.
- Lea-wilsonf, M. A., J. N. Lomer, and J. A. V. Wyk (1995), *Philos. Mag. B* **72** (1), 81.
- Lesik, M., J.-P. Tetienne, A. Tallaie, J. Achard, V. Mille, A. Gicquel, J.-F. Roch, and V. Jacques (2014), *Appl. Phys. Lett.* **104** (11), 113107.
- Levitt, M. H. (2008), *Spin Dynamics: Basics of Nuclear Magnetic Resonance*, 2nd ed. (John Wiley & Sons) Chap. 11.
- Li, L., E. H. Chen, J. Zheng, S. L. Mouradian, F. Dolde, T. Schröder, S. Karaveli, M. L. Markham, D. J. Twitchen, and D. Englund (2015), *Nano Lett.* **15** (3), 1493.
- Liggins, S. (2010), *Identification of point defects in treated single crystal diamond*, Ph.D. thesis (University of Warwick).
- Lim, T.-S., J.-L. Chern, and K. Otsuka (2002), *Opt. Lett.* **27** (12), 1037.
- Liu, Y.-X., A. Ajoy, and P. Cappellaro (2019), *Phys. Rev. Lett.* **122**, 100501.
- Lobaev, M., A. Gorbachev, S. Bogdanov, A. Vikharev, D. Radishev, V. Isaev, V. Chernov, and M. Drozdov (2017), *Diam. Relat. Mater.* **72**, 1.
- Lomer, J. N., and A. M. A. Wild (1973), *Radiat. Eff.* **17** (1-2), 37.
- Londero, E., E. Bourgeois, M. Nesladek, and A. Gali (2018), *Phys. Rev. B* **97**, 241202.
- Loretz, M., S. Pezzagna, J. Meijer, and C. L. Degen (2014), *Appl. Phys. Lett.* **104** (3), 033102.
- Loretz, M., T. Rosskopf, and C. L. Degen (2013), *Phys. Rev. Lett.* **110**, 017602.
- Loubser, J. H. N., and J. A. van Wyk (1978), *Rep. Prog. Phys.* **41** (8), 1201.
- Lovchinsky, I., J. D. Sanchez-Yamagishi, E. K. Urbach, S. Choi, S. Fang, T. I. Andersen, K. Watanabe, T. Taniguchi, A. Bylinskii, E. Kaxiras, P. Kim, H. Park, and M. D. Lukin (2017), *Science* **355** (6324), 503.
- Lovchinsky, I., A. O. Sushkov, E. Urbach, N. P. de Leon, S. Choi, K. De Greve, R. Evans, R. Gertner, E. Bersin, C. Müller, L. McGuinness, F. Jelezko, R. L. Walsworth, H. Park, and M. D. Lukin (2016), *Science* **351** (6275), 836.
- Low, G. H., T. J. Yoder, and I. L. Chuang (2014), *Phys. Rev. A* **89**, 022341.
- Lyons, J. L., and C. G. V. de Walle (2016), *J. Phys.: Condens. Matter* **28** (6), 06LT01.
- Ma, Z., S. Zhang, Y. Fu, H. Yuan, Y. Shi, J. Gao, L. Qin, J. Tang, J. Liu, and Y. Li (2018), *Opt. Express* **26** (1), 382.
- Maclaurin, D., M. W. Doherty, L. C. L. Hollenberg, and A. M. Martin (2012), *Phys. Rev. Lett.* **108**, 240403.

- MacQuarrie, E. R., T. A. Gosavi, A. M. Moehle, N. R. Jungwirth, S. A. Bhawe, and G. D. Fuchs (2015), *Optica* **2** (3), 233.
- Maertz, B. J., A. P. Wijnheijmer, G. D. Fuchs, M. E. Nowakowski, and D. D. Awschalom (2010), *Appl. Phys. Lett.* **96** (9), 092504.
- Mainwood, A. (1999), *Phys. Status Solidi A* **172** (1), 25.
- Malinauskas, T., K. Jarasiunas, E. Ivakin, V. Ralchenko, A. Gontar, and S. Ivakhnenko (2008), *Diam. Relat. Mater.* **17** (7), 1212.
- Mamin, H. J., M. H. Sherwood, M. Kim, C. T. Rettner, K. Ohno, D. D. Awschalom, and D. Rugar (2014), *Phys. Rev. Lett.* **113** (3), 030803.
- Manson, N. B., and J. P. Harrison (2005), *Diam. Relat. Mater.* **14**, 1705.
- Manson, N. B., M. Hedges, M. S. J. Barson, R. Ahlefeldt, M. W. Doherty, H. Abe, T. Ohshima, and M. J. Sellars (2018), *New J. Phys.* **20** (11), 113037.
- Marblestone, A., B. Zamft, Y. Maguire, M. Shapiro, T. Cybulski, J. Glaser, D. Amodei, P. B. Stranges, R. Kalhor, D. Dalrymple, D. Seo, E. Alon, M. Maharbiz, J. Carmenta, J. Rabaey, E. Boyden, G. Church, and K. Kording (2013), *Front. in Comput. Neurosci.* **7**, 137.
- Markham, M., J. Dodson, G. Scarsbrook, D. Twitchen, G. Balasubramanian, F. Jelezko, and J. Wrachtrup (2011), *Diam. Relat. Mater.* **20** (2), 134.
- Marseglia, L., J. P. Hadden, A. C. Stanley-Clarke, J. P. Harrison, B. Patton, Y. L. D. Ho, B. Naydenov, F. Jelezko, J. Meijer, P. R. Dolan, J. M. Smith, J. G. Rarity, and J. L. O'Brien (2011), *Appl. Phys. Lett.* **98** (13), 133107.
- Martin, J., R. Wannemacher, J. Teichert, L. Bischoff, and B. Köhler (1999), *Appl. Phys. Lett.* **75** (20), 3096.
- Martineau, P. M., M. P. Gaukroger, K. B. Guy, S. C. Lawson, D. J. Twitchen, I. Friel, J. O. Hansen, G. C. Summerton, T. P. G. Addison, and R. Burns (2009), *J. Phys.: Condens. Matter* **21** (36), 364205.
- Maurer, P. C., G. Kucsko, C. Latta, L. Jiang, N. Y. Yao, S. D. Bennett, F. Pastawski, D. Hunger, N. Chisholm, M. Markham, D. J. Twitchen, J. I. Cirac, and M. D. Lukin (2012), *Science* **336** (6086), 1283.
- Maurer, P. C., J. R. Maze, P. L. Stanwix, L. Jiang, A. V. Gorshkov, A. A. Zibrov, B. Harke, J. S. Hodges, A. S. Zibrov, A. Yacoby, D. Twitchen, S. W. Hell, R. L. Walsworth, and M. D. Lukin (2010), *Nat. Phys.* **6**, 912.
- Maze, J. R., A. Dréau, V. Waselowski, H. Duarte, J.-F. Roch, and V. Jacques (2012), *New J. Phys.* **14** (10), 103041.
- Maze, J. R., P. L. Stanwix, J. S. Hodges, S. Hong, J. M. Taylor, P. Cappellaro, L. Jiang, M. V. G. Dutt, E. Togan, A. S. Zibrov, A. Yacoby, R. L. Walsworth, and M. D. Lukin (2008), *Nature* **455** (7213), 644.
- McCloskey, D., D. Fox, N. O'Hara, V. Usov, D. Scanlan, N. McEvoy, G. S. Duesberg, G. L. W. Cross, H. Z. Zhang, and J. F. Donegan (2014), *Appl. Phys. Lett.* **104** (3), 031109.
- McLellan, C. A., B. A. Myers, S. Kraemer, K. Ohno, D. D. Awschalom, and A. C. Bleszynski Jayich (2016), *Nano Lett.* **16** (4), 2450.
- Meiboom, S., and D. Gill (1958), *Rev. Sci. Instrum.* **29** (8), 688.
- Meirzada, I., Y. Hovav, S. A. Wolf, and N. Bar-Gill (2018), *Phys. Rev. B* **98**, 245411.
- Michl, J., J. Steiner, A. Denisenko, A. Buelau, A. Zimmermann, K. Nakamura, H. Sumiya, S. Onoda, P. Neumann, J. Isoya, and J. Wrachtrup (2019), ArXiv e-prints [arXiv:1901.01614](https://arxiv.org/abs/1901.01614) [cond-mat.mes-hall].
- Michl, J., T. Teraji, S. Zaiser, I. Jakobi, G. Waldherr, F. Dolde, P. Neumann, M. W. Doherty, N. B. Manson, J. Isoya, and J. Wrachtrup (2014), *Appl. Phys. Lett.* **104** (10), 102407.
- Mita, Y. (1996), *Phys. Rev. B* **53**, 11360.
- Mitchell, E. W. J. (1965), "Radiation damage in diamond," in *Physical Properties of Diamond*, edited by R. Berman (Clarendon Press, Oxford).
- Miyazaki, T., Y. Miyamoto, T. Makino, H. Kato, S. Yamasaki, T. Fukui, Y. Doi, N. Tokuda, M. Hatano, and N. Mizuochi (2014), *Appl. Phys. Lett.* **105** (26), 261601.
- Mizuochi, N., P. Neumann, F. Rempp, J. Beck, V. Jacques, P. Siyushev, K. Nakamura, D. J. Twitchen, H. Watanabe, S. Yamasaki, F. Jelezko, and J. Wrachtrup (2009), *Phys. Rev. B* **80**, 041201.
- Mkhitarian, V. V., and V. V. Dobrovitski (2014), *Phys. Rev. B* **89**, 224402.
- Mkhitarian, V. V., F. Jelezko, and V. V. Dobrovitski (2015), *Sci. Rep.* **5**, 15402.
- Momenzadeh, S. A., R. J. Stöhr, F. F. de Oliveira, A. Brunner, A. Denisenko, S. Yang, F. Reinhard, and J. Wrachtrup (2015), *Nano Lett.* **15** (1), 165.
- Morishita, H., E. Abe, W. Akhtar, L. S. Vlasenko, A. Fujimoto, K. Sawano, Y. Shiraki, L. Dreher, H. Riemann, N. V. Abrosimov, P. Becker, H.-J. Pohl, M. L. W. Thewalt, M. S. Brandt, and K. M. Itoh (2011), *Appl. Phys. Express* **4** (2), 021302.
- Morishita, H., S. Kobayashi, M. Fujiwara Hiromitsu Kato Toshiharu Makino Satoshi Yamasaki, and N. Mizuochi (2018), ArXiv e-prints [arXiv:1803.01161](https://arxiv.org/abs/1803.01161) [cond-mat.mes-hall].
- Mrózek, M., D. Rudnicki, P. Kehayias, A. Jarmola, D. Budker, and W. Gawlik (2015), *EPJ Quantum Technology* **2** (1), 22.
- Murai, T., T. Makino, H. Kato, M. Shimizu, T. Murooka, E. D. Herbschleb, Y. Doi, H. Morishita, M. Fujiwara, M. Hatano, S. Yamasaki, and N. Mizuochi (2018), *Appl. Phys. Lett.* **112** (11), 111903.
- Myers, B. A., A. Ariyaratne, and A. C. B. Jayich (2017), *Phys. Rev. Lett.* **118**, 197201.
- Naydenov, B., F. Reinhard, A. Lämmle, V. Richter, R. Kalish, U. F. S. D'Haenens-Johansson, M. Newton, F. Jelezko, and J. Wrachtrup (2010), *Appl. Phys. Lett.* **97** (24), 242511.
- Neu, E., P. Appel, M. Ganzhorn, J. Miguel-Sánchez, M. Lesik, V. Mille, V. Jacques, A. Tallaie, J. Achard, and P. Maletinsky (2014), *Appl. Phys. Lett.* **104** (15), 153108.
- Neumann, P., J. Beck, M. Steiner, F. Rempp, H. Fedder, P. R. Hemmer, J. Wrachtrup, and F. Jelezko (2010a), *Science* **329** (5991), 542.
- Neumann, P., I. Jakobi, F. Dolde, C. Burk, R. Reuter, G. Waldherr, J. Honert, T. Wolf, A. Brunner, J. H. Shim, D. Suter, H. Sumiya, J. Isoya, and J. Wrachtrup (2013), *Nano Lett.* **13** (6), 2738.
- Neumann, P., R. Kolesov, V. Jacques, J. Beck, J. Tisler, A. Batalov, L. Rogers, N. B. Manson, G. Balasubramanian, F. Jelezko, and J. Wrachtrup (2009), *New J. Phys.* **11** (1), 013017.
- Neumann, P., R. Kolesov, B. Naydenov, J. Beck, F. Rempp, M. Steiner, V. Jacques, G. Balasubramanian, M. L. Markham, D. J. Twitchen, S. Pezzagna, J. Meijer, J. Twamley, F. Jelezko, and J. Wrachtrup (2010b), *Nat. Phys.* **6** (4), 249.
- Neves, A., and M. H. Nazaré (2001), *Properties, growth and applications of diamond*, 26 (Institution of Engineering and Technology).
- Newell, A. N., D. A. Dowdell, and D. H. Santamore (2016), *J. Appl. Phys.* **120** (18), 185104.
- Newton, M., B. Campbell, D. Twitchen, J. Baker, and T. Anthony (2002), *Diam. Relat. Mater.* **11** (3-6), 618.
- Newton, M. E. (2007), *EPR, ENDOR and EPR Imaging of Defects in Diamond* (Royal Society of Chemistry) Chap. 6.
- Nöbauer, T., A. Angerer, B. Bartels, M. Trupke, S. Rotter, J. Schmiedmayer, F. Mintert, and J. Majer (2015), *Phys. Rev. Lett.* **115**, 190801.
- Nöbauer, T., K. Buczak, A. Angerer, S. Putz, G. Steinhauser,

- J. Akbarzadeh, H. Peterlik, J. Majer, J. Schmiedmayer, and M. Trupke (2013), ArXiv e-prints [arXiv:1309.0453 \[quant-ph\]](https://arxiv.org/abs/1309.0453).
- Ohno, K., F. Joseph Heremans, L. C. Bassett, B. A. Myers, D. M. Toyli, A. C. Bleszynski Jayich, C. J. Palmström, and D. D. Awschalom (2012), *Appl. Phys. Lett.* **101** (8), 082413.
- O’Keeffe, M. F., L. Horesh, J. F. Barry, D. A. Braje, and I. L. Chuang (2019), *New Journal of Physics* **21** (2), 023015.
- Onoda, S., K. Tatsumi, M. Haruyama, T. Teraji, J. Isoya, W. Kada, T. Ohshima, and O. Hanaizumi (2017), *Phys. Status Solidi A* **214** (11), 1700160.
- Orwa, J., K. Ganesan, J. Newnham, C. Santori, P. Barclay, K. Fu, R. Beausoleil, I. Aharonovich, B. Fairchild, P. Olivero, A. Greentree, and S. Prawer (2012), *Diam. Relat. Mater.* **24**, 6.
- Osterkamp, C., J. Lang, J. Scharpf, C. Müller, L. P. McGuinness, T. Diemant, R. J. Behm, B. Naydenov, and F. Jelezko (2015), *Appl. Phys. Lett.* **106** (11), 113109.
- Palyanov, Y. N., I. N. Kupriyanov, A. F. Khokhryakov, and V. G. Ralchenko (2015), “Crystal growth of diamond,” in *Handbook of Crystal Growth: Bulk Crystal Growth: Second Edition*, Vol. 2, pp. 671–713.
- Pelliccione, M., B. A. Myers, L. M. A. Pascal, A. Das, and A. C. Bleszynski Jayich (2014), *Phys. Rev. Applied* **2**, 054014.
- Pfender, M., N. Aslam, P. Simon, D. Antonov, G. Thiering, S. Burk, F. Fávaro de Oliveira, A. Denisenko, H. Fedder, J. Meijer, J. A. Garrido, A. Gali, T. Teraji, J. Isoya, M. W. Doherty, A. Alkauskas, A. Gallo, A. Grüneis, P. Neumann, and J. Wrachtrup (2017), *Nano Lett.* **17** (10), 5931.
- Pham, L. M. (2013), *Magnetic Field Sensing with Nitrogen-Vacancy Color Centers in Diamond*, Ph.D. thesis (Harvard University).
- Pham, L. M., N. Bar-Gill, C. Belthangady, D. Le Sage, P. Cappellaro, M. D. Lukin, A. Yacoby, and R. L. Walsworth (2012a), *Phys. Rev. B* **86**, 045214.
- Pham, L. M., N. Bar-Gill, D. Le Sage, C. Belthangady, A. Stacey, M. Markham, D. J. Twitchen, M. D. Lukin, and R. L. Walsworth (2012b), *Phys. Rev. B* **86** (12), 121202.
- Pham, L. M., S. J. DeVience, F. Casola, I. Lovchinsky, A. O. Sushkov, E. Bersin, J. Lee, E. Urbach, P. Cappellaro, H. Park, A. Yacoby, M. Lukin, and R. L. Walsworth (2016), *Phys. Rev. B* **93**, 045425.
- Pham, L. M., D. L. Sage, P. L. Stanwix, T. K. Yeung, D. Glenn, A. Trifonov, P. Cappellaro, P. R. Hemmer, M. D. Lukin, H. Park, A. Yacoby, and R. L. Walsworth (2011), *New J. Phys.* **13** (4), 045021.
- Pinto, H., R. Jones, D. W. Palmer, J. P. Goss, P. R. Briddon, and S. Öberg (2012), *Phys. Status Solidi A* **209** (9), 1765.
- Plakhotnik, T., M. W. Doherty, J. H. Cole, R. Chapman, and N. B. Manson (2014), *Nano Lett.* **14** (9), 4989.
- Poole, C. P. (1996), *Electron Spin Resonance: A Comprehensive Treatise on Experimental Techniques*, edited by 2nd (Courier Corporation).
- Popa, I., T. Gaebel, M. Domhan, C. Wittmann, F. Jelezko, and J. Wrachtrup (2004), *Phys. Rev. B* **70** (20), 201203.
- Pu, A., V. Avalos, and S. Dannefaer (2001), *Diam. Relat. Mater.* **10** (3), 585.
- Pu, A., T. Bretagnon, D. Kerr, and S. Dannefaer (2000), *Diam. Relat. Mater.* **9** (8), 1450.
- Rabi, I. I. (1937), *Phys. Rev.* **51**, 652.
- Rajendran, S., N. Zobrist, A. O. Sushkov, R. Walsworth, and M. Lukin (2017), *Phys. Rev. D* **96**, 035009.
- Ramsey, N. F. (1950), *Phys. Rev.* **78**, 695.
- Riedel, D., D. Rohner, M. Ganzhorn, T. Kaldewey, P. Appel, E. Neu, R. J. Warburton, and P. Maletinsky (2014), *Phys. Rev. Applied* **2**, 064011.
- Robertson, R., J. J. Fox, and A. E. Martin (1933), *Philos. Trans. R. Soc. London, Ser. A* **232** (707-720), 463.
- Robertson, R., J. J. Fox, and A. E. Martin (1936), *Proc. R. Soc. Lond. A* **157** (892), 579.
- Robledo, L., H. Bernien, T. v. d. Sar, and R. Hanson (2011), *New J. Phys.* **13** (2), 025013.
- Rogers, L. J., S. Armstrong, M. J. Sellars, and N. B. Manson (2008), *New J. Phys.* **10** (10), 103024.
- Romach, Y., C. Müller, T. Unden, L. J. Rogers, T. Isoda, K. M. Itoh, M. Markham, A. Stacey, J. Meijer, S. Pezzagna, B. Naydenov, L. P. McGuinness, N. Bar-Gill, and F. Jelezko (2015), *Phys. Rev. Lett.* **114**, 017601.
- Rondin, L., G. Dantelle, A. Slablab, F. Grosshans, F. Treussart, P. Bergonzo, S. Perruchas, T. Gacoin, M. Chaigneau, H.-C. Chang, V. Jacques, and J.-F. Roch (2010), *Phys. Rev. B* **82**, 115449.
- Rondin, L., J.-P. Tetienne, T. Hingant, J.-F. Roch, P. Maletinsky, and V. Jacques (2014), *Rep. Prog. Phys.* **77** (5), 056503.
- Rong, X., J. Geng, F. Shi, Y. Liu, K. Xu, W. Ma, F. Kong, Z. Jiang, Y. Wu, and J. Du (2015), *Nat. Commun.* **6**, 8748.
- Rose, A. (1963), *Concepts in photoconductivity and allied problems* (Interscience Publishers).
- Roskopf, T., A. Dussaux, K. Ohashi, M. Loretz, R. Schirhagl, H. Watanabe, S. Shikata, K. M. Itoh, and C. L. Degen (2014), *Phys. Rev. Lett.* **112**, 147602.
- Rugar, D., H. J. Mamin, M. H. Sherwood, M. Kim, C. T. Rettnner, K. Ohno, and D. D. Awschalom (2015), *Nat. Nanotechnol.* **10**, 120.
- Rutledge, K. M., and K. K. Gleason (1998), “Characterization methods,” in *Handbook of Industrial Diamonds and Diamond Films*, Chap. 9 (CRC Press).
- Sakaguchi, I., M. Nishitani-Gamo, K. P. Loh, H. Haneda, and T. Ando (1999), *J. Appl. Phys.* **86** (3), 1306.
- Santori, C., P. E. Barclay, K.-M. C. Fu, and R. G. Beausoleil (2009), *Phys. Rev. B* **79**, 125313.
- Savitski, V. G. (2017), *J. Phys. D: Appl. Phys.* **50** (47), 475602.
- Schirhagl, R., K. Chang, M. Loretz, and C. L. Degen (2014), *Annu. Rev. Phys. Chem.* **65** (1), 83.
- Schloss, J. M., J. F. Barry, M. J. Turner, and R. L. Walsworth (2018), *Phys. Rev. Applied* **10**, 034044.
- Schmitt, S., T. Gefen, F. M. Stürner, T. Unden, G. Wolff, C. Müller, J. Scheuer, B. Naydenov, M. Markham, S. Pezzagna, J. Meijer, I. Schwarz, M. Plenio, A. Retzker, L. P. McGuinness, and F. Jelezko (2017), *Science* **356** (6340), 832.
- Schoenfeld, R. S., and W. Harneit (2011), *Phys. Rev. Lett.* **106** (3), 030802.
- Schreyvogel, C., V. Polyakov, R. Wunderlich, J. Meijer, and C. E. Nebel (2015), *Sci. Rep.* **5**, 12160.
- Schreyvogel, C., M. Wolfer, H. Kato, M. Schreck, and C. E. Nebel (2014), *Sci. Rep.* **4**, 3634.
- Schröder, T., F. Gädeke, M. J. Banholzer, and O. Benson (2011), *New J. Phys.* **13** (5), 055017.
- Schwander, M., and K. Partes (2011), *Diam. Relat. Mater.* **20** (9), 1287.
- Schwartz, J., S. Aloni, D. F. Ogletree, and T. Schenkel (2012), *New J. Phys.* **14** (4), 043024.
- Schwartz, J., P. Michaelides, C. D. Weis, and T. Schenkel (2011), *New J. Phys.* **13** (3), 035022.
- Shao, L., M. Zhang, M. Markham, A. M. Edmonds, and M. Loncar (2016), *Phys. Rev. Applied* **6**, 064008.
- Shaw, M. J., P. R. Briddon, J. P. Goss, M. J. Rayson, A. Kerridge, A. H. Harker, and A. M. Stoneham (2005), *Phys. Rev. Lett.* **95**, 105502.
- Shi, F., Q. Zhang, P. Wang, H. Sun, J. Wang, X. Rong, M. Chen, C. Ju, F. Reinhard, H. Chen, J. Wrachtrup, J. Wang, and J. Du (2015), *Science* **347** (6226), 1135.
- Shields, B. J., Q. P. Unterreithmeier, N. P. de Leon, H. Park, and M. D. Lukin (2015), *Phys. Rev. Lett.* **114** (13), 136402.

- Shin, C. S., C. E. Avalos, M. C. Butler, D. R. Trease, S. J. Seltzer, J. Peter Mustonen, D. J. Kennedy, V. M. Acosta, D. Budker, A. Pines, and V. S. Bajaj (2012), *J. Appl. Phys.* **112** (12), 124519.
- Simpson, D. A., J.-P. Tetienne, J. M. McCoey, K. Ganesan, L. T. Hall, S. Petrou, R. E. Scholten, and L. C. L. Hollenberg (2016), *Sci. Rep.* **6**, 22797.
- Slepetz, B., and M. Kertesz (2014), *Phys. Chem. Chem. Phys.* **16**, 1515.
- Slichter, C. P. (1990), *Principles of Magnetic Resonance* (Springer, Berlin, Heidelberg).
- Smith, W. V., P. P. Sorokin, I. L. Gelles, and G. J. Lasher (1959), *Phys. Rev.* **115** (6), 1546.
- Smits, J., J. Damron, P. Kehayias, A. F. McDowell, N. Mosavian, I. Fescenko, N. Ristoff, A. Laraoui, A. Jarmola, and V. M. Acosta (2019), ArXiv e-prints [arXiv:1901.02952](https://arxiv.org/abs/1901.02952) [physics.ins-det].
- de Sousa, R. (2009), “Electron spin as a spectrometer of nuclear-spin noise and other fluctuations,” in *Electron Spin Resonance and Related Phenomena in Low-Dimensional Structures* (Springer Berlin Heidelberg) pp. 183–220.
- Stanwix, P. L., L. M. Pham, J. R. Maze, D. Le Sage, T. K. Yeung, P. Cappellaro, P. R. Hemmer, A. Yacoby, M. D. Lukin, and R. L. Walsworth (2010), *Phys. Rev. B* **82** (20), 201201.
- Staudacher, T., F. Shi, S. Pezzagna, J. Meijer, J. Du, C. A. Meriles, F. Reinhard, and J. Wrachtrup (2013), *Science* **339** (6119), 561.
- Steiner, M., P. Neumann, J. Beck, F. Jelezko, and J. Wrachtrup (2010), *Phys. Rev. B* **81**, 035205.
- Steinert, S., F. Dolde, P. Neumann, A. Aird, B. Naydenov, G. Balasubramanian, F. Jelezko, and J. Wrachtrup (2010), *Rev. Sci. Instrum.* **81** (4), 043705.
- Steinert, S., F. Ziem, L. T. Hall, A. Zappe, M. Schweikert, N. Götz, A. Aird, G. Balasubramanian, L. Hollenberg, and J. Wrachtrup (2013), *Nat. Commun.* **4**, 1607.
- Stepanov, V., and S. Takahashi (2016), *Phys. Rev. B* **94** (2), 024421.
- Stürner, F. M., A. Brenneis, J. Kassel, U. Wostradowski, R. Rölver, T. Fuchs, K. Nakamura, H. Sumiya, S. Onoda, J. Isoya, and F. Jelezko (2019), *Diam. Relat. Mater.* **93**, 59.
- Sushkov, A. O., N. Chisholm, I. Lovchinsky, M. Kubo, P. K. Lo, S. D. Bennett, D. Hunger, A. Akimov, R. L. Walsworth, H. Park, and M. D. Lukin (2014), *Nano Lett.* **14** (11), 6443.
- Tahara, K., H. Ozawa, T. Iwasaki, N. Mizuochi, and M. Hatano (2015), *Appl. Phys. Lett.* **107** (19), 193110.
- Tallaire, A., L. Mayer, O. Brinza, M. A. Pinault-Thaury, T. Debuisschert, and J. Achard (2017a), *Appl. Phys. Lett.* **111** (14), 143101.
- Tallaire, A., V. Mille, O. Brinza, T. N. T. Thi, J. Brom, Y. Loguinov, A. Katrusha, A. Koliadin, and J. Achard (2017b), *Diam. Relat. Mater.* **77**, 146.
- Tang, C., A. Neves, and A. Fernandes (2004), *Diam. Relat. Mater.* **13** (1), 203.
- Taylor, J. M., P. Cappellaro, L. Childress, L. Jiang, D. Budker, P. R. Hemmer, A. Yacoby, R. Walsworth, and M. D. Lukin (2008), *Nat. Phys.* **4** (10), 810.
- Teraji, T., T. Taniguchi, S. Koizumi, Y. Koide, and J. Isoya (2013), *Appl. Phys. Express* **6** (5), 055601.
- Teraji, T., T. Yamamoto, K. Watanabe, Y. Koide, J. Isoya, S. Onoda, T. Ohshima, L. J. Rogers, F. Jelezko, P. Neumann, J. Wrachtrup, and S. Koizumi (2015), *Phys. Status Solidi A* **212** (11), 2365.
- Tetienne, J.-P., N. Dotschuk, D. A. Broadway, A. Stacey, D. A. Simpson, and L. C. L. Hollenberg (2017), *Sci. Adv.* **3** (4).
- Tetienne, J.-P., R. W. de Gille, D. A. Broadway, T. Teraji, S. E. Lillie, J. M. McCoey, N. Dotschuk, L. T. Hall, A. Stacey, D. A. Simpson, and L. C. L. Hollenberg (2018), *Phys. Rev. B* **97**, 085402.
- Tetienne, J.-P., T. Hingant, L. Rondin, A. Cavaillès, L. Mayer, G. Dantelle, T. Gacoin, J. Wrachtrup, J.-F. Roch, and V. Jacques (2013), *Phys. Rev. B* **87**, 235436.
- Tetienne, J.-P., L. Rondin, P. Spinicelli, M. Chipaux, T. Debuisschert, J.-F. Roch, and V. Jacques (2012), *New J. Phys.* **14** (10), 103033.
- Thiering, G., and A. Gali (2018), *Phys. Rev. B* **98**, 085207.
- Tokuda, N. (2015), “Homoeptaxial diamond growth by plasma-enhanced chemical vapor deposition,” in *Novel Aspects of Diamond: From Growth to Applications*, edited by N. Yang (Springer International Publishing, Cham) pp. 1–29.
- Toyli, D. M., C. F. de las Casas, D. J. Christle, V. V. Dobrovitski, and D. D. Awschalom (2013), *Proc. Natl. Acad. Sci.* **110** (21), 8417.
- Toyli, D. M., D. J. Christle, A. Alkauskas, B. B. Buckley, C. G. Van de Walle, and D. D. Awschalom (2012), *Phys. Rev. X* **2**, 031001.
- Trusheim, M. E., and D. Englund (2016), *New J. Phys.* **18** (12), 123023.
- Tucker, O. D., M. E. Newton, and J. M. Baker (1994), *Phys. Rev. B* **50**, 15586.
- Twitchen, D., D. Hunt, M. Newton, J. Baker, T. Anthony, and W. Banholzer (1999a), *Physica B: Condens. Matter* **273–274**, 628.
- Twitchen, D. J., S. L. Geoghegan, and N. Perkins (2010), “Method for treating single crystal CVD diamond and product obtained,” WO Patent 2010/149775 A1.
- Twitchen, D. J., M. E. Newton, J. M. Baker, T. R. Anthony, and W. F. Banholzer (1999b), *Phys. Rev. B* **59**, 12900.
- Udvarhelyi, P., V. O. Shkolnikov, A. Gali, G. Burkard, and A. Pályi (2018), *Phys. Rev. B* **98**, 075201.
- Uedono, A., K. Mori, N. Morishita, H. Itoh, S. Tanigawa, S. Fujii, and S. Shikata (1999), *J. Phys.: Condens. Matter* **11** (25), 4925.
- van der Sar, T., F. Casola, R. Walsworth, and A. Yacoby (2015), *Nat. Commun.* **6**, 7886.
- Van Oort, E., and M. Glasbeek (1990), *Chem. Phys. Lett.* **168** (6), 529.
- Vandersypen, L. M. K., and I. L. Chuang (2005), *Rev. Mod. Phys.* **76**, 1037.
- Vanier, J., and C. Audoin (1989), *The Quantum Physics of Atomic Frequency Standards* (A. Hilger).
- Vineyard, G. H. (1963), *J. Math. Phys.* **4** (9), 1191.
- Vins, V. (2007), “Technique of production of fancy red diamonds,” U.S. Patent 2007/0053823 A1.
- Waldermann, F., P. Olivero, J. Nunn, K. Surmacz, Z. Wang, D. Jaksch, R. Taylor, I. Walmsley, M. Draganski, P. Reichart, A. Greentree, D. Jamieson, and S. Prawer (2007), *Diam. Relat. Mater.* **16** (11), 1887.
- Waldherr, G., J. Beck, M. Steiner, P. Neumann, A. Gali, T. Frauenheim, F. Jelezko, and J. Wrachtrup (2011), *Phys. Rev. Lett.* **106**, 157601.
- Walsworth, R. (2017), “Absorption-based detection of spin impurities in solid-state spin systems,” U.S. Patent 9,658,301 B2.
- Wang, Q., C. P. Smith, M. S. Hall, C. M. Breeding, and T. M. Moses (2005), *Gems Gemol.* **41** (1).
- Wang, Z.-H., G. de Lange, D. Ristè, R. Hanson, and V. V. Dobrovitski (2012), *Phys. Rev. B* **85**, 155204.
- Wang, Z.-H., and S. Takahashi (2013), *Phys. Rev. B* **87**, 115122.
- Wee, T.-L., Y.-K. Tzeng, C.-C. Han, H.-C. Chang, W. Fann, J.-H. Hsu, K.-M. Chen, and Y.-C. Yu (2007), *J. Phys. Chem. A* **111** (38), 9379.
- Weerdt, F. D., and A. Collins (2008), *Diam. Relat. Mater.* **17** (2), 171.
- Wickenbrock, A., H. Zheng, L. Bougas, N. Leefer, S. Afach,

- A. Jarmola, V. M. Acosta, and D. Budker (2016), *Appl. Phys. Lett.* **109** (5), 053505.
- Wieser, M. E., N. Holden, T. B. Coplen, J. K. Böhlke, M. Berglund, W. A. Brand, P. De Bièvre, M. Gröning, R. D. Loss, J. Meija, T. Hirata, T. Prohaska, R. Schoenberg, G. O Connor, T. Walczyk, S. Yoneda, and X.-K. Zhu (2013), *Pure Appl. Chem.* **85** (5), 1047.
- Witzel, W. M., M. S. Carroll, A. Morello, Ł. Cywiński, and S. Das Sarma (2010), *Phys. Rev. Lett.* **105** (18), 187602.
- Wolf, T., P. Neumann, K. Nakamura, H. Sumiya, T. Ohshima, J. Isoya, and J. Wrachtrup (2015), *Phys. Rev. X* **5**, 041001.
- Wood, J. D. A., D. A. Broadway, L. T. Hall, A. Stacey, D. A. Simpson, J.-P. Tetienne, and L. C. L. Hollenberg (2016), *Phys. Rev. B* **94**, 155402.
- Wort, C. J., and R. S. Balmer (2008), *Mater. Today* **11** (1), 22.
- Wu, Y., F. Jelezko, M. B. Plenio, and T. Weil (2016), *Angew. Chem. Int. Ed.* **55** (23), 6586.
- van Wyk, J. A., E. C. Reynhardt, G. L. High, and I. Kiflawi (1997), *J. Phys. D: Appl. Phys.* **30** (12), 1790.
- Yale, C. G., F. J. Heremans, B. B. Zhou, A. Auer, G. Burkard, and D. D. Awschalom (2016), *Nat. Photonics* **10**, 184.
- Yamamoto, T., C. Müller, L. P. McGuinness, T. Teraji, B. Naydenov, S. Onoda, T. Ohshima, J. Wrachtrup, F. Jelezko, and J. Isoya (2013a), *Phys. Rev. B* **88** (20), 201201.
- Yamamoto, T., T. Umeda, K. Watanabe, S. Onoda, M. L. Markham, D. J. Twitchen, B. Naydenov, L. P. McGuinness, T. Teraji, S. Koizumi, F. Dolde, H. Fedder, J. Honert, J. Wrachtrup, T. Ohshima, F. Jelezko, and J. Isoya (2013b), *Phys. Rev. B* **88**, 075206.
- Yamano, H., S. Kawai, K. Kato, T. Kageura, M. Inaba, T. Okada, I. Higashimata, M. Haruyama, T. Tani, K. Yamada, S. Onoda, W. Kada, O. Hanaizumi, T. Teraji, J. Isoya, and H. Kawarada (2017), *Jpn. J. Appl. Phys.* **56** (4S), 04CK08.
- Yeung, T. K., D. L. Sage, L. M. Pham, P. L. Stanwix, and R. L. Walsworth (2012), *Appl. Phys. Lett.* **100** (25), 251111.
- Zaitsev, A., K. Moe, and W. Wang (2017), *Diam. Relat. Mater.* **71**, 38.
- Zaitsev, A. M. (2001), *Optical Properties of Diamond* (Springer, Berlin).
- Zhang, X., and E. L. Hu (2016), *Appl. Phys. Lett.* **109** (8), 081101.
- Zhao, N., S.-W. Ho, and R.-B. Liu (2012), *Phys. Rev. B* **85**, 115303.
- Zheng, H., J. Xu, G. Iwata, T. Lenz, J. Michl, B. Yavkin, K. Nakamura, H. Sumiya, T. Ohshima, J. Isoya, J. Wrachtrup, A. Wickenbrock, and D. Budker (2018), ArXiv e-prints [arXiv:1811.11498](https://arxiv.org/abs/1811.11498) [physics.app-ph].
- Zhou, B. B., P. C. Jerger, V. O. Shkolnikov, F. J. Heremans, G. Burkard, and D. D. Awschalom (2017), *Phys. Rev. Lett.* **119**, 140503.
- Zu, C., W. B. Wang, L. He, W. G. Zhang, C. Y. Dai, F. Wang, and L. M. Duan (2014), *Nature* **514**, 72.